Charles University in Prague
Faculty of Mathematics and Physics

DOCTORAL THESIS

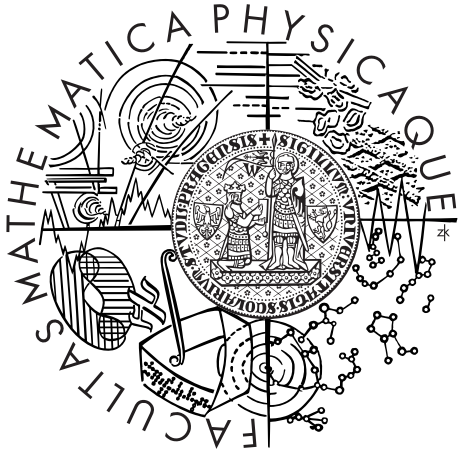

David Schmoranzer

Investigation of cryogenic helium flows using mechanical oscillators

Department of Low Temperature Physics

Supervisor: Professor RNDr. Ladislav Skrbek, DrSc.
Field of Study: Physics
Specialization: Condensed Matter and Material Research (F3)

Prague 2011

Acknowledgments

I would like to take this opportunity to thank all my friends and colleagues whose help during the work that eventually led to the writing of this Thesis was invaluable, and without whom it would hardly be possible to present it in its current form. My thanks belong to Míša Kráľová for her kindness and patience during my first years in the Laboratory of Superfluidity, as well as for her immense contribution to the results on classical and superfluid turbulence presented here. Tim Chagovets has my gratitude for helping me improve many practical skills, from mechanical design, through precise soldering and general cryogenics related expertise, to various programming techniques. To Marco La Mantia, I am grateful for his help with the measurements of acoustic emission by tuning forks, for the ensuing data processing, and for sharing his expertise from outside our cryogenics-based environment. I would also like to thank Simone Babuin and Mathias Stammeier for many interesting discussions within and beyond the field of physics, and generally for making our laboratory a more pleasant place to work at. When finishing his Master's degree, Michal Šindler has contributed to some of the measurements on the transition to turbulence in superfluid helium, which I appreciate. Veronika Pilcová has my thanks for her meticulous measurements of the transition to turbulence using room temperature visualization techniques, which required both extreme care and extreme amounts of time. Our younger students, Daniel Duda and Emil Varga, are commended for their help with practical tasks in the laboratory, such as calibration of thermometers, and I appreciate their genuine interest in low temperature physics. To Miloš Rotter, I am indebted for many a piece of his kindly given advice, for sharing his extensive knowledge of cryogenics, thermometry, vacuum systems and other related topics, as well as for his immense practical help. Josef Šebek deserves my gratitude for his valuable help in the laboratory, for using his organizational abilities to the benefit of all his co-workers, as well as for sharing his knowledge of specialized fields, such as dilution refrigeration. I would like to thank Franta Soukup and Miloš Pfeffer for their willingness to discuss advanced electronics with laymen such as myself, and for providing our laboratory with many pieces of equipment that would be beyond reach without their skills. Our technicians, namely Ladislav Doležal, Petr Vacek, Bohumil Vejr, and Jiří Boháč are commended for their highly appreciated mechanical skills, for many insightful ideas regarding construction and design, and for their excellent service of cryogenic liquids.

From my colleagues abroad, my special thanks belong to Matti Krusius, Volodya Eltsov and Mikko Paalanen, who offered me the possibility to visit their laboratory twice, welcomed me in a friendly manner, and allowed me to take part in an interesting scientific project that would not have been accessible otherwise – the measurements of Andreev reflection on quantized vortices in ^{3}He–B. During these two visits, my guide in Finland, in the world of ^{3}He experiments, and around the laboratory was Jaakko Hosio, to whom I am deeply grateful for many hours of his time, for his immense contribution to the Andreev reflection measurements, and for his friendship. For the excellent numerical simulations of excitation motion, my thanks belong to Jere Mäkinen. Together with all of them, Rob de Graaf, Petri Heikkinen, Elias Pentti, Anssi Salmela, Risto Hanninen and other members of the Low Temperature Laboratory at Aalto University have my

thanks for many useful discussions and for making my two visits an enjoyable experience.

Grisha Sheshin from the B. Verkin Institute in Kharkov deserves my thanks for his help with some of the experiments during his visit in Prague and together with his colleagues from Kharkov, I. Gritsenko and A. Zadorozhko, they have my gratitude for their contribution to the measurements of acoustic emission. I would also like to thank Phillipe Roche for explaining to me the specific issues related to sensitive measurements of pressure and velocity spectra in turbulent normal and superfluid helium, as well as for his effort to help us with the Prague washing machine experiment during his visit. My gratitude also belongs to Henri Godfrin, who welcomed me at Institut Néel in Grenoble and allowed me to study microfabrication techniques in an effort to develop sensitive detectors of superfluid turbulence, and Sébastien Dufresnes, who guided me through the clean room and chemical processes necessary to achieve this goal.

Finally, my biggest debt of gratitude is towards my supervisor Ladislav Skrbek, for many hours of his time eagerly spent in discussions of interesting physical problems, for introducing me to the international cryogenic fluid dynamics community and providing me with opportunities to work and learn abroad, for his friendly attitude and his willingness to help whenever it was needed, as well as for many other lessons a student might have the opportunity to learn from a good teacher.

For their moral support and friendship, I would like to thank all my friends from the Prague choir Sebranka, my fellow aikidoka, and many others whom I have met on my travels and in my life. Special thanks belong to my mother, who had understanding for my professional undertakings and showed her constant support. And to my fiancée Eva, I am eternally grateful for making my life pleasant and complete, and for standing by me unconditionally throughout all the good as well as all the difficult times.

Název práce: Studium proudění kryogenního helia pomocí mechanických oscilátorů
Autor: David Schmoranzer
Katedra: Katedra fyziky nízkých teplot
Vedoucí disertační práce: Prof. RNDr. Ladislav Skrbek, DrSc.

Abstrakt: Tato práce sjednocuje výsledky kryogenních experimentů zaměřených na studium přechodu k turbulenci v klasických a supratekutých kryogenních kapalinách za použití velmi citlivého detektoru – vibrující křemenné ladičky. V případě klasických tekutin bylo experimentálně potvrzeno očekávané škálování kritické rychlosti u_0^{crit} s kinematickou viskozitou, ν a frekvencí ω dle $u_0^{\mathrm{crit}} \propto \sqrt{\nu\,\omega}$, a to v nebývalém rozsahu kinematických viskozit přesahujícím dvě dekády. Výsledky těchto kryogenních měření jsou dále potvrzeny vizualizací dynamicky podobných proudění pomocí Bakerovy techniky a roztoku Kalliroscope za pokojové teploty. Pro přechod k turbulenci v supratekutém heliu byl navržen fenomenologický model, popisující vznikající vazbu mezi normální a supratekutou složkou, který dobře odpovídá nejen našim experimentálním pozorováním, ale i výsledkům jiných skupin. Jakožto dodatečný mechanismus disipace energie, který by mohl potenciálně komplikovat měření kvantové turbulence za velmi nízkých teplot byla zkoumána emise zvuku vyvolaná pohybem oscilujících těles, a byly zformulovány tři modely umožňující tyto ztráty kvantifikovat v případě křemenných ladiček. Tyto ladičky byly s výhodou využity i při měření Andrejevova rozptylu excitací na pravidelně uspořádané mříži kvantovaných vírů v ^{3}He–B, čímž byl položen základ pro interpretaci dalších měření kvantové turbulence v supratekutých fázích ^{3}He touto metodou.

Klíčová slova: křemenná ladička, kryogenní helium, supratekutost, turbulence

Title: Investigations of cryogenic helium flows using mechanical oscillators
Author: David Schmoranzer
Department: Department of Low Temperature Physics
Supervisor: Professor RNDr. Ladislav Skrbek, DrSc.

Abstract: This Thesis brings together the results of several cryogenic experiments centered around the investigations of the transition to turbulence in cryogenic normal fluids and superfluids performed using a very sensitive detector – the oscillating quartz tuning fork. In classical fluids, the expected scaling of the critical velocity, u_0^{crit}, with the kinematic viscosity, ν, and frequency, ω, as $u_0^{\mathrm{crit}} \propto \sqrt{\nu\,\omega}$ was confirmed experimentally in an unprecedented range of kinematic viscosity exceeding two decades. Additional evidence supporting our interpretation of the cryogenic measurements was found from room temperature visualization of dynamically similar flows using the Baker technique and Kalliroscope. For superfluid helium, a phenomenological model describing the gradual coupling between the normal and superfluid components occurring at the transition to turbulence was proposed, describing our results as well as those obtained by other groups. As an additional dissipation mechanism potentially hindering future turbulence measurements at very low temperatures, acoustic emission by oscillating structures was studied experimentally, and three models were put forward allowing to calculate its magnitude in the case of emission by quartz tuning forks. Finally, the tuning forks were also used successfully to detect Andreev reflection on a well-defined array of quantized vortices in ^{3}He–B, providing basis for further measurements of quantum turbulence in ^{3}He superfluids using the same method.

Keywords: quartz tuning fork, cryogenic helium, superfluidity, turbulence

Preface

This Thesis aims to bring together the results of multiple cryogenic experiments performed with oscillating objects in normal liquid and superfluid phases of both isotopes of helium. All these experiments are joined by two common purposes. The first and principal one is to investigate the peculiar behaviour of superfluids at low temperatures, especially the dynamics of quantized vortices, the interplay between the normal and superfluid components during the transition to turbulence in the superfluid phases of helium, and various mechanisms of energy transport and dissipation. The second and less obvious purpose is to provide a full characterisation of an extremely popular experimental instrument often used in these types of investigations – the quartz tuning fork, and moreover, to provide hints on the behaviour of other oscillating bodies commonly used in cryogenic fluid dynamics research.

The experiments, forming the basis of this work, have been performed in two locations. Investigations of the ^{4}He isotope have been carried out in the Prague Laboratory of Superfluidity, within the Joint Low Temperature Laboratory established between the Faculty of Mathematics and Physics of the Charles University in Prague and the Institute of Physics of the Czech Academy of Sciences. An independent study requiring very low temperatures in superfluid ^{3}He–B was realised in cooperation with the Low Temperature Laboratory of Aalto Univeristy, School of Science based in Espoo, Finland (formerly the Helsinki University of Technology), during the course of two consecutive visits by the Author.

The Thesis is structured as follows. Chapter 1 gives an elementary introduction into the topics of superfluidity, including the differences between ^{3}He and ^{4}He and emphasizing the phenomenon of Andreev reflection in ^{3}He–B. The same Chapter also provides a description of the main detection technique used throughout the work, i.e., measurement of the resonant properties of a quartz tuning fork oscillator. Chapters 2 and 3 deal in detail with the transition to turbulence detected by the quartz tuning fork in classical fluids and superfluid ^{4}He, while Chapter 4 is focused on acoustic emission by the tuning fork as a potentially important dissipation mechanism. In Chapter 5, we will describe the investigations of Andreev reflection on a well-defined arrangement of quantized vortices in ^{3}He–B, and the main body of the Thesis is then completed with the Conclusions presented in Chapter 6. Appendix A, containing a collection of the Author's published papers on the topics under discussion, is included for the reader's convenience.

Author's contribution

The Author began working with tuning fork oscillators in ^{4}He in the Prague Laboratory of Superfluidity under the guidance of Ladislav Skrbek at the end of 2005, and the early measurements have already been used as a part of his Master's Thesis. The work presented here is a result of the joint effort of many people cooperating in cryogenic fluid dynamics research, and here, we shall clarify the role of the Author in this endeavour and acknowledge the contribution of his colleagues.

The investigations of the transition to classical turbulence in He I and He gas presented in Chapter 2 have been carried out together with Michaela Kráľová (née Blažková), and it is fair to say that it was her who acquired most of the data. The Author took part in the installation of the tuning forks and in the measurements themselves as well, his role being that of a younger student being trained in the process. The Author later contributed in a larger extent to the data processing and the general preparation of the resulting publication [1], included here in Appendix A as attachment A1.

In the experiments on room temperature visualisation by Baker and Kalliroscope techniques presented in the same Chapter, in a sense, the Author's role had been reversed, as he was doing his best to help and guide a younger student, Veronika Pilcová, to collect and process the data for her Bachelor's Thesis. Here, the Author contributed mainly to the construction of the apparatus, to the data analysis by providing some input in terms of the theories of hydrodynamics, although in a lesser extent then his and Veronika's supervisor, Ladislav Skrbek. While it was Veronika, who, after adequate training, took almost all of the data, the Author assisted in the process and contributed significantly by developing multiple software tools, including an image processor, that have been used in analysing the input from the camera recording the position of the oscillating body. The final processing of the visualisation data as well as reprocessing of the data from classical turbulence in He I, for the resulting publication [2] (included as attachment A2) was also the Author's responsibility to a large extent, but he benefited greatly from the help from Michaela Kráľová regarding the cryogenic data.

The experiments with quartz tuning forks on the transition to turbulence in He II as presented in Chapter 3 was a task jointly given to the Author and to Michaela Kráľová. Here, the Author was already more heavily involved in the measurements and in the analysis as well, especially after Michaela had taken her maternity leave in 2008. In devising the model presented in Ref. [3] (included here as A3), the roles of Professors W. F. Vinen and L. Skrbek were irreplaceable, the Author and Michaela were mainly involved in raw data processing and testing various working versions of the mentioned model.

Regarding the studies of acoustic emission presented in Chapter 4, the first idea of the importance of this phenomenon came to the Author from the data measured in the Kharkov dilution refrigerator with Prague high frequency tuning forks (resonating at 77 kHz and 100 kHz). The measurements in Kharkov were performed by Grigoriy Sheshin and his colleagues I. Gritsenko and A. Zadorozhko, and they kindly shared their results looking for a reasonable interpretation. The Author realized that the observed frequency dependence of the linear drag force

can be explained neither by viscosity nor by ballistic drag at low temperature, and that another phenomenon must be responsible, guessing at acoustic emission, as was suggested by the steep frequency dependence. The subsequent Prague experiments were performed and analysed mainly by the Author, although he was helped significantly by Marco La Mantia, at that time a new postdoc in Prague. The three models of acoustic emission by tuning forks presented in Ref. [4] (attachment A4) were fully developed by the Author based on the work of Sillitto [5], Clubb *et al.* [6] and on the Landau-Lifschitz course of hydrodynamics [7], and the text of the mentioned publication is also of his making, although, of course, with appropriate corrections from the other authors, and according to the suggestions of the referees, who have contributed to the final form of the paper significantly.

The Andreev reflection measurements performed in Helsinki and presented in Chapter 5 were the first chance for the Author to acquaint himself with the physics of ^{3}He, and consequently, he was concerned mainly with minor technical tasks, such as the selection, preparation and characterisation of the tuning forks used, and some rather straightforward data analysis. Most of the important work around the experiment was done by members of the ROTA group, namely by Jaakko Hosio, Petri Heikkinen, Rob de Graaf, Volodya Eltsov and Matti Krusius. The computer simulation of the motion of thermal excitations was performed by Jere Mäkinen. Nevertheless, the Author took part in the measurements as well, obtaining one series of results at several different rotation velocities of the cryostat, and was responsible for the analysis of the thermal relaxation processes. The results can be found in Ref. [8], included as attachment A5.

Finally, a brief note about other experiments not included in this Thesis that the Author took part in. The most prominent one was the "Prague washing machine", which was intended to study turbulent flows of normal and superfluid ^{4}He between two counter-rotating discs (von Kármán geometry). The detection methods were to be tuning forks, second sound attenuation, and a Pitot tube fitted with a pressure probe to measure velocity fluctuations. Unfortunately, due to an excessive number of technical difficulties, ranging from problems with the drive of the discs, to insufficient sensitivity of the pressure probe and the readout electronics, this experiment never yielded the expected results despite almost two years of effort and the help of other colleagues who had experience with similar measurements, especially Philippe Roche. Whether this particular experiment will be revisited someday remains to be seen. Other performed studies include cavitation in normal and superfluid ^{4}He [9, 10], and the behaviour of tuning fork oscillators in externally driven flows, such as a fountain pump jet [11] or thermal counterflow.

Contents

1. Introduction

When helium was first liquefied on July 10th, 1908 by the Dutch physicist Heike Kamerlingh Onnes [12, 13, 14] as the last remaining gas after the liquefaction the other so called permanent gases [15, 16, 17, 18, 19, 20], only few would have guessed that this would mean the emergence of a whole new field of study – low temperature physics. And it proved to be an interesting field of study indeed! Only three years later, superconductivity of mercury was discovered [21] by Kamerlingh Onnes, who was awarded the Nobel prize in 1913 for his low temperature research, and very little was missing to another groundbreaking discovery – superfluidity of ^{4}He below the "lambda-point", T_λ=2.17 K. However, as history shows, the actual discovery of superfluidity had to wait more than another twenty years, and it is nowadays attributed to the Nobel prize laureate of 1978, Pyotr Leonidovich Kapitza [22, 23], as well as to John Frank "Jack" Allan and Don Misener [24, 25, 26]. Apart from the discovery itself, the contributions of Satyendra Nath Bose [27], Albert Einstein [28, 29, 30], Fritz London [31, 32, 33], Laszlo Tisza [34, 35, 36], Lev Davidovich Landau [37, 38, 39, 40, 41, 42], Elefter Luarsabovich Andronikashvili [43, 44, 45], Lars Onsager [46, 47], and Richard Feynmann [48, 49, 50, 51] to the early theories of the superfluid state represent important pieces in the puzzle posed by superfluidity as well, and are certainly deserving of equal merit. Superfluidity in ^{3}He took another four decades to discover due to the fermionic nature of ^{3}He and the much lower critical temperature $T_C \approx 2$ mK, but in 1972 the effort was rewarded with success [52, 53]. Yet another Nobel prize was awarded in the field of low temperature physics 24 years later, this time to David Lee, Douglas Osheroff and Robert Richardson.

This day, over a century after the original liquefaction of helium, superfluidity, and cryogenic fluid dynamics in general, still continue to spark the interest of the scientific community and offer many puzzling and intriguing questions. How do pure superfluids, which flow without friction, dissipate energy? How is this process related to the dynamics of quantized vortices? How can we describe superfluid turbulence, and what exactly happens at its onset? Can studying superfluid turbulence help us to understand classical turbulence as well? These and numerous other open questions are the driving force behind the development of this field of research and behind the continuing attention it receives today from scientists worldwide.

In this Thesis, we have chosen to concentrate on a narrow subset of problems related to cryogenic fluid dynamics, specifically, on periodic oscillatory flows due to submerged bodies. Since the famous Andronikashvili experiment [43], various oscillators in the form of disks, spheres, wires, grids and tuning forks have become the traditional experimental tools for probing cryogenic flows, complementing the works on flows driven on large scales, be it mechanically or thermally, and other available probing techniques, such as ion trapping, second sound attenuation, or in the last few years even direct flow visualization methods.

The advantages of using various oscillators are numerous: (i) it is often possible to make use of the oscillator's resonant properties, greatly enhancing its sensitivity in a low-friction environment, (ii) they are usually small objects that fit easily even into spatially restricted experiments at very low temperatures,

and (iii) there is no need for an external flow source, the oscillator can be used as a flow generator or detector itself, and often it can even fulfill both roles at the same time. On the other hand, one might ask, why should we use helium and low temperatures, when dynamically similar experiments from classical fluid mechanics can be performed at room temperature? The reasons are obvious if we wish to study purely quantum phenomena without classical analogues, but even in classical fluid dynamics, cold helium gas and normal liquid ^{4}He can be used advantageously, as both are fluids with unique and easily tunable properties. Cold ^{4}He can be used very efficiently, for example, in classical turbulent convection studies [54, 55, 56, 57, 58], due to its very low kinematic viscosity, giving us experimental access in standard laboratory experiments to very high Reynolds and Rayleigh numbers, which would require significantly larger facilities if another fluid, such as air, water was to be used. Other working fluids with the best parameters are perhaps the toxic SF_6 gas near its critical point, or various gas mixtures [59, 60, 61, 62]. For turbulence studies, the low kinematic viscosity of liquid helium I and the range in which it can be varied in cold helium gas, are unmatched [1].

In the rest of this Chapter, we will introduce the basic facts about the behaviour of both isotopes of helium in cryogenic conditions, followed by the concepts of superfluidity, the two-fluid model, and quantization of vorticity. Special attention will be devoted to the Andreev reflection process in ^{3}He–B and to the description of a very sensitive detector device – the quartz tuning fork. Finally, we will revisit some of the recent experiments with oscillating bodies in cryogenic helium and summarize their important results.

1.1 Cryogenic Helium – The Two Isotopes

At room temperature and standard pressure, both isotopes of helium, i.e., the naturally abundant ^{4}He and the rare, but stable ^{3}He, behave in almost the same way. Both are monatomic gases that can be described to a good degree of accuracy by the ideal gas model, or more accurately by the van der Waals equation, the only noticeable differences being that ^{3}He is lighter, usually has faster diffusion rates and of course has a large effective cross section for capturing thermal neutrons. However, when we cool them down to temperatures of order several kelvin, quantum phenomena become apparent and much more significant differences between the bosonic ^{4}He and the fermionic ^{3}He arise, as can be seen from their respective phase diagrams in Figs. 1.1 and 1.2.

At 4.2 K (and standard pressure), ^{4}He condenses into a classical liquid, with an extremely low kinematic viscosity, referred to as He I for historical reasons. When cooling further, upon crossing the so-called λ-point at $T_\lambda = 2.17$ K at saturated vapour pressure (SVP), it enters the superfluid state, perhaps best characterised as a quantum liquid, and traditionally called He II. Even at absolute zero, it does not freeze and become solid, unless an external pressure of 25 bar is applied, as otherwise, the energy of the zero point motion of helium atoms is sufficient to preclude the formation of a crystal lattice.

The rare ^{3}He condenses at 3.19 K also to form a classical liquid, which is well described by the Fermi liquid theory [63, 64, 65]. As its viscosity is proportional to T^{-2}, at very low temperatures it becomes much higher than that of He I. A

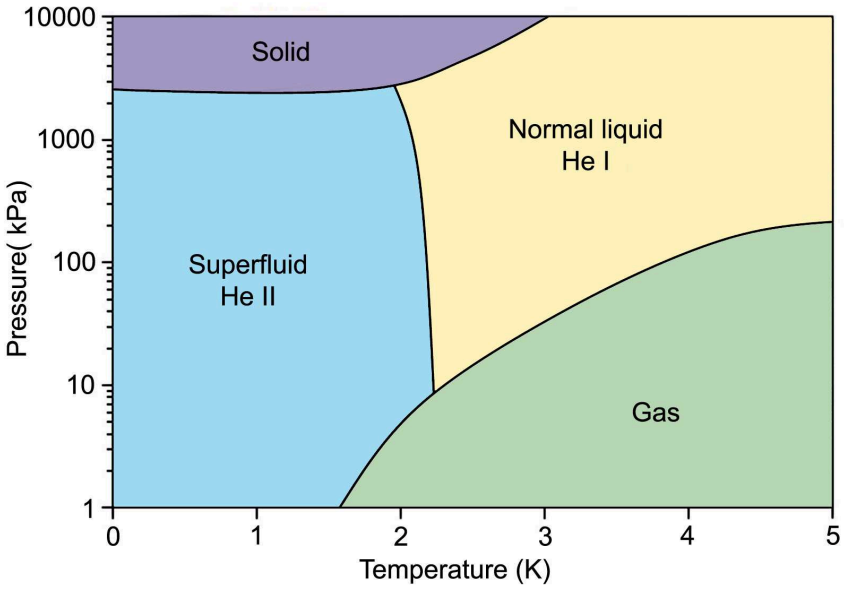

Figure 1.1: Phase diagram of ^{4}He.

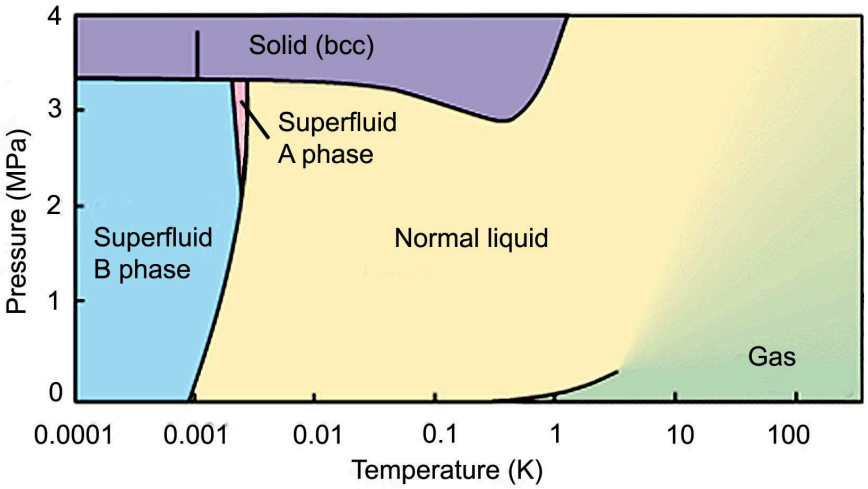

Figure 1.2: Phase diagram of ^{3}He in zero magnetic field.

transition to superfluidity also exists in ^{3}He, but occurs at a much lower temperature, $T_C \approx 2$ mK at SVP and zero magnetic field. In fact, depending on the temperature and the external magnetic field, several different superfluid phases can be obtained: ^{3}He–A, ^{3}He–A$_1$, and ^{3}He–B, see Section 1.2.2 for details. At absolute zero, solid ^{3}He exists again only at elevated pressures above ≈ 34 bar. A distinct feature can be seen on the melting curve of ^{3}He – a prominent minimum exists at about 0.32 K, associated with a crossover in the ratio of the entropies of the liquid and solid phases. As a consequence, below this temperature, the solidification heat is negative and the (adiabatic) crystallization of ^{3}He induced by increasing the external pressure can be used as a method of cooling down to temperatures of order 1 mK. This process has been realized experimentally in 1965 [66], that is roughly 15 years after being first suggested [67], and today is

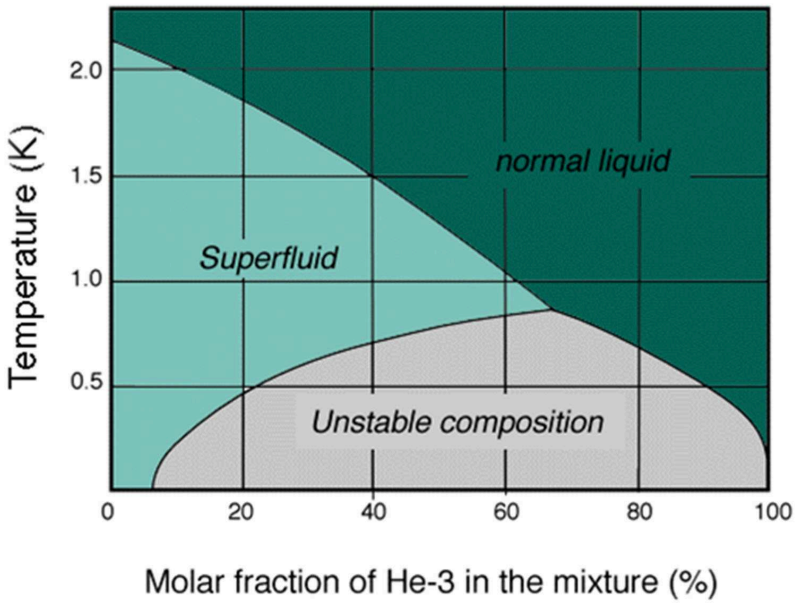

Figure 1.3: Phase diagram of the ^{3}He-^{4}He mixture.

known by the name of its original inventor as Pomeranchuk cooling.

Another cooling method able to reach mK temperatures, which is nowadays preferred, relies on mixing the two isotopes. As the mixture phase diagram in Fig. 1.3 shows, phase separation occurs below 0.8 K, and in a container (mixing chamber) a layer of ^{3}He-rich phase forms above the ^{3}He-dilute phase. Note also the finite solubility of ^{3}He in ^{4}He, even at absolute zero, about 6% of ^{3}He will be present in the dilute phase. Practically, if an underpressure were to be applied on the top ^{3}He-rich layer, a gas consisting mainly of ^{3}He will be pumped away (^{3}He has higher SVP) and the ^{3}He from the dilute phase will cross the phase separation interface to compensate for the ^{3}He pumped away. This process requires energy and draws it from the thermal excitations of the liquid and its surroundings, thus producing a cooling power. Finally, to provide continuous cooling, the ^{3}He gas pumped away from the rich phase is lead in a closed cycle again to the dilute phase, taking care to precool it sufficiently before it re-enters the mixing chamber. This process is called dilution refrigeration and ideally allows reaching temperatures of about 2-10 mK, depending on the specifics of its practical realisation and on the heat load. To reduce the temperature even further, as was the case in the ^{3}He experiments described in Chapter 5, one has to combine dilution refrigeration with more advanced cooling techniques, such as nuclear demagnetization.

1.2 Superfluidity and Quantization of Vorticity

Let us begin with an elementary description of superfluids based on their experimentally observable macroscopic properties. Then, we will proceed with the phenomenological two-fluid model of the superfluids and the basics of their quantum mechanical treatment.

The first thing an observer would notice, when cooling down through the su-

perfluid transition of ^{4}He at 2.17 K at SVP, is that once the transition temperature is reached, the liquid stops boiling and its level forms a smooth surface, disturbed only by the vibrations of the apparatus. Should these vibrations be suppressed sufficiently, then away from the walls of the container, one would in fact see the smoothest and flattest surface Nature can produce, with variations only of order 10^{-10} m (one atomic layer). Upon further investigation, one would find that this is due to an extremely enhanced heat conductivity, at least $3 \cdot 10^6$ times higher compared to the one above the transition. In other words, the whole volume of superfluid ^{4}He cools itself only by evaporation at the interface, there are no local variations of temperature high enough to cause the nucleation of bubbles inside the bulk of the superfluid, unless we insert energy locally on purpose or restrict the flow of the superfluid in a way that limits heat exchange.

When the research of superfluidity was in its beginnings, careful experiments revealed many other unusual and interesting properties of superfluids, such as their ability to flow without measurable friction along pipes under certain conditions [24], to flow easily through the tiniest orifices (Kapitza's experiment [22, 23]), the fountain effect [68] and its counterpart, the mechanocaloric effect [69], which show that temperature gradients inside the superfluid produce pressure gradients and vice versa, or the thin superfluid film that forms on almost any adjoining surface with the known exception of Cesium [70, 71]. The measurements of viscosity available at that time were controversial. A very low value of viscosity (at least 1500 times smaller than in He I) was obtained in capillary flows and in Kapitza's experiment with a volume connected to the outer bath via the extremely thin space between optically smooths discs, but a much higher value resulted from experiments with a torsionally oscillating cylinder [72, 73]. Another key experiment that led to our present understanding of the properties of superfluids was performed by the Georgian (at that time Soviet) physicist Elefter Luarsabovich Andronikashvili [43, 44, 45]. A thinly spaced array of discs immersed in ^{4}He was oscillated torsionally both above and below the transition temperature and the period of oscillation was used to deduce the moment of inertia of the submerged disc stack. From this, the fraction of fluid that was oscillating together with the discs clamped between them by viscosity was determined, and it was found that this fraction is more or less constant in He I, but in the superfluid He II it is a smooth rapidly decreasing function of temperature likely tending towards zero in the limit of zero temperature.

Among other, it was the knowledge of these experimental facts that led Laszlo Tisza [34, 35, 36] and Lev Landau [40, 41, 42] to formulate their own versions of what we now call the two-fluid model. This phenomenological model claims that the superfluid at finite temperature should be described not as a single fluid, but rather as two interpenetrating fluids with independent velocity fields. These two fluids are traditionally called the normal and superfluid components of the superfluid, and are attributed the following properties. The normal component behaves as any classical fluid would, it has a finite viscosity and can transport heat. On the other hand, the superfluid component is thought of as an Eulerian liquid flowing without friction that has no entropy, i.e., cannot transport heat, only absorb it, thus becoming the normal component. It is also postulated that the respective densities of the two components must always add up to the total density of the superfluid and that if their respective velocities differ only little,

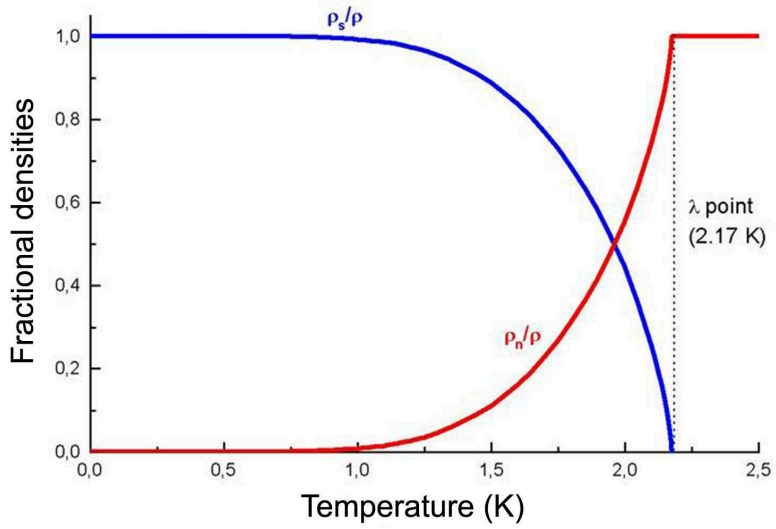

Figure 1.4: Fractional densities of the normal and superfluid component in ^{4}He.

their interaction, known as the mutual friction force, can be neglected. This model resolved the controversy in the viscosity measurements, as in the capillary flow and Kapitza's experiment, only the superfluid component took part in the mass transport, while both components (also likely in non-laminar flow) damped the motion of the oscillating cylinder. In Andronikashvili's experiment, it was believed that the normal component was clamped to the disc stack, increasing its moment of inertia while the superfluid component was unaffected by the oscillations. The reduction of the extra inertia of the disc stack with decreasing temperature was then explained by considering the decreasing fraction of the normal component.

The main differences between Tisza's and Landau's models were the following. Based on the suggestion of Fritz London that superfluidity is related to Bose-Einstein condensation [31, 32, 33], Tisza associated the superfluid component of ^{4}He with the quantum mechanical ground state resulting from the Bose-Einstein condensation theory [27, 28, 29, 30], which will be mentioned in Section 1.2.1. Landau did not make such a claim, in fact, he opposed it strongly, but based on his correct guess at the dispersion relation of the excitations in ^{4}He, with parameters adjusted to fit the known experiments (later confirmed by neutron scattering [74, 75, 76]), he was able to calculate the fractional densities of the normal and superfluid components as functions of temperature, matching the results of Andronikashvili. These fractional densities are plotted versus temperature in Fig. 1.4.

Based on the model assumptions, it is also possible to formulate the equations of motion of the two fluids. The normal component obeys a Navier-Stokes type equation for viscous fluids, while the superfluid component is described by an Euler-type equation for ideal fluids. These are linked only by the mutual friction term and of course, the equation of continuity which governs the mass flow inside the superfluid. If zero dissipation is assumed, we can also write down the conservation of entropy carried by the normal component, neglecting thermody-

namically irreversible processes. Finally, we arrive at a closed set of equations governing the flows inside the superfluid:

$$\rho_n \frac{D\vec{v_n}}{Dt} = -\frac{\rho_n}{\rho}\nabla p - \rho_s S \nabla T + \eta \Delta \vec{v_n} + F_{ns}, \tag{1.1}$$

$$\rho_s \frac{D\vec{v_s}}{Dt} = -\frac{\rho_s}{\rho}\nabla p + \rho_s S \nabla T - F_{ns}, \tag{1.2}$$

$$\frac{\partial \rho}{\partial t} + \nabla\left(\rho_n \vec{v_n} + \rho_s \vec{v_s}\right) = 0, \tag{1.3}$$

$$\frac{\partial\left(\rho S\right)}{\partial t} + \nabla\left(S\rho \vec{v_n}\right) = 0, \tag{1.4}$$

where the operator $D\vec{x}/Dt = \partial\vec{x}/\partial t + \left(\vec{x}\cdot\nabla\right)\vec{x}$ is the convective derivative, η denotes the viscosity of the normal component, S the specific entropy, and the total density is given by $\rho = \rho_n + \rho_s$. The term in Eqs. 1.1 and 1.2, containing ∇T is the thermomechanical coupling term, responsible for the fountain and mechanocaloric effects. The first two equations (1.1 and 1.2) can be added together to get the combined equation of motion:

$$\rho_n \frac{D\vec{v_n}}{Dt} + \rho_s \frac{D\vec{v_s}}{Dt} = -\nabla p + \eta \Delta \vec{v_n}, \tag{1.5}$$

which presents us with a useful description of isothermal flows, where the normal and superfluid components are more likely to flow together with matching velocity fields $\vec{v_n} \simeq \vec{v_s}$, i.e., where they exhibit co-flow. If the velocity fields were matched exactly, $\vec{v_n} = \vec{v_s} \equiv \vec{v}$ this equation would reduce to the classical Navier-Stokes equation, suggesting that some level of similarity with classical fluids can be expected under the given conditions.

The equations 1.1 – 1.4 represent a good description of the motion of the superfluid and are still used today with various corrections or specific forms of the mutual friction term. Even in their original form, they can be used, e.g., to derive the wave phenomena in superfluids such as the existence of first and second sound [39], as well as to explain the fountain [68] and mechanocaloric [69] effects and the low friction flow through tiny orifices [22, 23].

Today we know that Landau was not right in rejecting the importance of Bose-Einstein condensation altogether, because the quantum mechanical ground state description is essential in order to understand another peculiar property of the superfluids – the quantization of vorticity. Fritz London predicted that if liquid ^{4}He is described as an ideal Bose gas, it should start condensing to the ground state at 3.15 K, close enough to the experimentally observed superfluid transition of 2.17 K, especially when we consider that the molecules in any liquid tend to interact rather strongly, unlike the used ideal Bose gas model, which assumes no interactions at all. In ^{3}He, the situation is slightly more complex. Since its atoms are fermions, Bose-Einstein condensation cannot occur directly. Instead, the ^{3}He atoms pair up, similarly to electrons in superconductors forming Cooper pairs [77], which being quasi-bosonic in their nature, then condense into the ground state in macroscopic amounts.

If we now associate the superfluid component with a quantum mechanical ground state[1] as London and Tisza did for ^{4}He, we can describe it with a single macroscopic wave function in the following form (forgetting about the nonzero total spin of ^{3}He for the moment):

$$\psi(\vec{r},t) = \sqrt{\rho_s(\vec{r},t)}\exp(i\varphi(\vec{r},t)), \tag{1.6}$$

where the amplitude of the wavefunction is determined by the superfluid density $\rho_s(\vec{r},t)$, which depends together with the phase $\varphi(\vec{r},t)$ on spatial coordinates and time. If we wish to calculate the superfluid velocity, $\vec{v_s}$, dividing the superfluid mass flux, $\vec{J}(\vec{r},t)$, by the superfluid density, we arrive at:

$$\vec{v_s}(\vec{r},t) = \frac{\vec{J}(\vec{r},t)}{\rho_s(\vec{r},t)} = \frac{-i\hbar}{2m\rho_s(\vec{r},t)}\left[\psi^*(\vec{r},t)\nabla\psi(\vec{r},t) - \psi(\vec{r},t)\nabla\psi^*(\vec{r},t)\right] = \frac{\hbar}{m}\nabla\varphi(\vec{r},t), \tag{1.7}$$

where m is the superfluid particle mass. Note that the superfluid velocity is proportional to the gradient of the quantum mechanical phase. Using a well known identity of vector calculus, it immediately follows that:

$$\nabla\times\vec{v_s}(\vec{r},t) = \frac{\hbar}{m}\nabla\times\nabla\varphi(\vec{r},t) = 0, \tag{1.8}$$

suggesting that the superfluid component should exhibit purely potential flow as its vorticity given by $\nabla\times\vec{v_s}(\vec{r},t)$ is zero. Indeed, if we attempt to calculate the velocity circulation, Γ, around a closed loop C delimiting a singly connected region S, by applying the Stokes theorem, the result is an identical zero:

$$\Gamma = \oint_C \vec{v_s}(\vec{r},t)\cdot\vec{dl} = \int_S \nabla\times\vec{v_s}(\vec{r},t)\,dS = 0. \tag{1.9}$$

This would mean that no vortices could exist in the superfluid component, implying that it cannot participate in rotary motion. This is, however, contrary to observation, as superfluid He II in a rotating cylindrical container mimics the parabolic profile of classical fluids when undergoing "solid body" rotation [81]. Therefore, vortices have to exist in some form, but their cores have to differ from the superfluid bulk, to circumvent the singly connected region requirement of the above calculation. If we now assume a multiply connected region, the Stokes theorem does not apply, and the circulation will be given by:

$$\Gamma = \oint_C \vec{v_s}(\vec{r},t)\cdot\vec{dl} = \frac{\hbar}{m}\oint_C \nabla\varphi(\vec{r},t)\cdot\vec{dl} = \frac{\hbar}{m}\left(\varphi_f - \varphi_i\right), \tag{1.10}$$

where φ_i denotes the initial phase at a given point on the closed loop and φ_f the phase at the same point after traveling around the loop once, when taking the

[1] This assumption is not fully valid, as Bogoliubov proved [78, 79] that for a weakly interacting Bose gas, the fraction of the atoms in the ground state would not be 100%, the condensate would be depleted. It was later verified by neutron diffraction that the condensate fraction indeed differs from the superfluid fractional density, and only between 10% and 20% of the total number of particles condense even in the limit of zero temperature (see Ref. [80] and references therein), while the fractional density of the superfluid component tends towards unity. Nevertheless, making this assumption allows us to easily deduce interesting properties of the superfluids that have already been verified experimentally.

path integral. As the wavefunction $\psi(\vec{r},t)$ must be uniquely defined in space and time, it follows that the difference $\varphi_f - \varphi_i$ must be a multiple of 2π, and hence:

$$\Gamma = \frac{\hbar}{m} 2\pi n = \frac{h}{m} n = n\kappa, \tag{1.11}$$

where n is an integer and $\kappa = h/m$ is the quantum of circulation. This somewhat simplified reasoning yields an important result – it shows that circulation in superfluids can exist in the form of quantized vortices, which have cores that do not correspond to the quantum mechanical ground state of the bulk superfluid, each possessing a given number of circulation quanta (in practice one or two quanta only, see the following Sections 1.2.1 and 1.2.2 for details) and allows us to calculate the quantum of circulation for any given superfluid. Also, because vorticity in superfluids is required to obey the Kelvin theorem [7], which can be interpreted as conservation of vorticity along vortex cores, it is necessary that all vortices either end on container walls or the free surface of the fluid, or form closed rings, in contrast to classical viscous fluids, where vortices may simply end inside the bulk. Keeping these restrictions in mind, we already have the basic understanding of what are the elementary building blocks of any rotary motion in superfluids, and what will eventually also be responsible for the creation of superfluid turbulence.

The dynamics of quantized vortices can be studied by solving the Gross-Pitaevskii equation [82, 83] numerically (see, e.g., Ref. [84]), or within the framework of the so-called vortex filament model, wherein the cores of quantized vortices are represented as one-dimensional lines through space (see, e.g., Ref. [85]). Their motion is governed by the dynamical Equation 1.12 and an analogue of the Biot-Savart law of electrodynamics, because the vortices interact with the flow field composed of all external flows and of the rotational superflow they create themselves. A vortex line segment given by its position $\vec{r}(t)$ and tangential unit vector $\vec{s}(t) = d\vec{r}(t)/dl$, where l refers to the path length along the curved vortex line, and $\vec{s}(t)$ points in the direction of vorticity inside the core, moves with the following velocity $\vec{v}_L$:

$$\vec{v}_L = \frac{d\vec{r}}{dt} = \vec{v}_s + \alpha\vec{s} \times (\vec{v}_n - \vec{v}_s) - \alpha'\vec{s} \times [\vec{s} \times (\vec{v}_n - \vec{v}_s)], \tag{1.12}$$

where, for purposes of brevity, all the quantities are written down without the explicit (t) parameter. Here, α and α' are the dissipative and reactive mutual friction parameters, respectively, which generally depend on temperature and pressure. If the superflow velocity is considered to be caused only by the presence of quantized vortices, then at a given position $\vec{r}$, it can be expressed in analogy with the Biot-Savart law as:

$$\vec{v}_s(\vec{r},t) = \frac{\kappa}{4\pi} \sum_{k=1}^{N} \int \frac{\vec{s_k'}(l,t) \times \left(\vec{r_k'}(l,t) - \vec{r}\right)}{|\vec{r_k'}(l,t) - \vec{r}|^3} dl, \tag{1.13}$$

where the summation is taken over all of the N quantized vortices present, and the integration is taken along the length, l, of their cores whose positions are determined by $\vec{r_k'}(l,t)$.

The above mentioned mutual friction parameters represent the ratio of the energy transferred from the vortices to the normal component (and thus eventu-

ally dissipated) to the energy maintained in the superflow corresponding to the moving quantized vortices. In analogy with classical fluid dynamics, one might thus construct an "effective superfluid Reynolds number"[2] determining how likely quantized vortices are to evolve complicated motion patterns that can result in vortex (self-)reconnections and eventually might lead to the formation of quantum turbulence (chaotic motion resulting from a tangle of many quantized vortices) in the superfluid component:

$$Re_s = \frac{1-\alpha'}{\alpha}. \tag{1.14}$$

Note that Re_s depends only on the mutual friction parameters, i.e., varies only with temperature and pressure, and is *independent* of both normal and superfluid velocities. Therefore, it cannot represent a universal criterion that could be used to determine with what probability laminar and turbulent states are possible, based solely on temperature and pressure. Nevertheless, it does provide useful insight into how difficult it might be to create quantum turbulence under the given conditions by, say, supplying energy to a moving immersed object. As the numerator in Eq. 1.14 varies less rapidly with temperature then the denominator, the behaviour of the quantized vortices is primarily determined by the dissipative parameter α. The temperature dependence of Re_s will be examined separately for the two He isotopes, as it differs in the absolute values significantly. Here, it suffice to say that in He II, Re_s is larger than unity practically at all temperatures, save within tens of mK below the λ – point, meaning that the superfluid component of He II always becomes (quantum-)turbulent readily. In ^{3}He–B, Re_s crosses unity further below the critical temperature, and hence the behaviour of quantized vortices differs greatly at various temperatures as does the likelihood of creating a turbulent burst, when a seed loop is injected [86].

In practice, various complicated arrangements of quantized vortices are usually characterised using the vortex line density L in inverse square meters, which corresponds to the total length of vortex lines per unit volume. It is related to another important parameter, the "mean intervortex distance", ℓ_0, by:

$$\ell_0 = L^{-\frac{1}{2}}. \tag{1.15}$$

While the meaning of ℓ_0 is clear from the above definition, it has the significance of the actual mean intervortex distance only in some special cases, such as an array of straight vortices aligned in a grid, as otherwise, it is in principle even impossible to talk about the distance of two curved lines in 3D space. Nevertheless, it is a useful quantity that gives us a specific length scale, below which we can no longer "average out" the quantized vortices when calculating the flow fields.

After describing the behaviour of the superfluid component and quantized vortices, let us return to the normal component and to what it represents. Within the two fluid model, the heat transport and dissipative capabilities of the superfluid are associated with the normal component alone, and within our simplified

[2] We use the term "effective superfluid Reynolds number" in order to distinguish it from the quantity "superfluid Reynolds number" used in the literature, defined as $Re_{sfl} = UL/\kappa$, i.e., exactly as the classical Reynolds number with the kinematic viscosity replaced by the circulation quantum.

treatment, one might picture it as helium atoms in excited states, in contrast to the ground state filled with the Bose-condensed atoms associated with the superfluid component. However, sometimes, it is favourable to think of helium atoms and thermal excitations separately, taking advantage of the formalism of second quantization, and to describe the excitations as thermal quasiparticles – carriers of heat and entropy – each with its own momentum and energy. At sufficiently high temperatures, not too far below the superfluid transition, the concentration of these quasiparticles will be high and it will be possible do describe them as a continuum (bringing us back to the hydrodynamics of the normal component as given by Eq. 1.1), but at lower temperatures, the quasiparticles will become a rather dilute "gas", necessitating a description in terms of ballistic propagation and related scattering processes. This will strongly affect for example the drag force acting on moving bodies, as in the ballistic regime, momentum and energy would be exchanged more readily with the container walls or free surfaces than with the surrounding layers of fluid.

As will be shown in the following part, the exact form of the superfluid wavefunction (or "order parameter") and the nature of thermal quasiparticles are different in the two helium isotopes and in the different superfluid phases of ^{3}He, but most of the general properties outlined above remain valid although perhaps with modifications, especially regarding the existence of many different types of quantized vortices in the superfluid phases of ^{3}He.

1.2.1 ^{4}He and Bose-Einstein Condensation

Because the nuclei of ^{4}He atoms each consist of two protons and two neutrons, the resulting nuclear spin is zero and ^{4}He behaves as a boson. This means, among other, that ^{4}He obeys Bose-Einstein statistics and that there exists a finite temperature below which macroscopic numbers of ^{4}He atoms will start occupying the ground state and Bose-Einstein condensation will occur [27, 28, 30]. While it is relatively simple to determine this critical temperature for gases of non-interacting atoms, such as realized experimentally in the condensation of nuclei of alkali metals, making a similar prediction for liquid helium is much more difficult, due to the relatively strong interactions between the atoms in the liquid, which complicate the application of the ideal Bose gas model.

Nevertheless, this approach was taken by Fritz London [31, 32, 33], who was able to predict that the critical temperature should be:

$$T_c = \frac{2\pi\hbar^2}{m_4 k_B}\left(\frac{N}{g\,\zeta\,(3/2)}\right) \approx 3.15\ \mathrm{K}, \tag{1.16}$$

where m_4 is the mass of the ^{4}He atom, k_b stands for the Boltzmann constant, N is the number of atoms per unit volume (the number density), g is the quantum degeneracy and ζ denotes the Riemann zeta function. The resulting critical temperature $T = 3.15$ K is remarkably close to the experimentally observed superfluid transition of $T_\lambda = 2.17$ K already hinting at a possible link between superfluidity and Bose-Einstein condensation. From calculating the relative number of atoms in the ground state as a function of temperature, one might determine the expected ratio of the normal and superfluid component. Moreover, it is also possible to derive that in the condensate in equilibrium, all physical properties would be

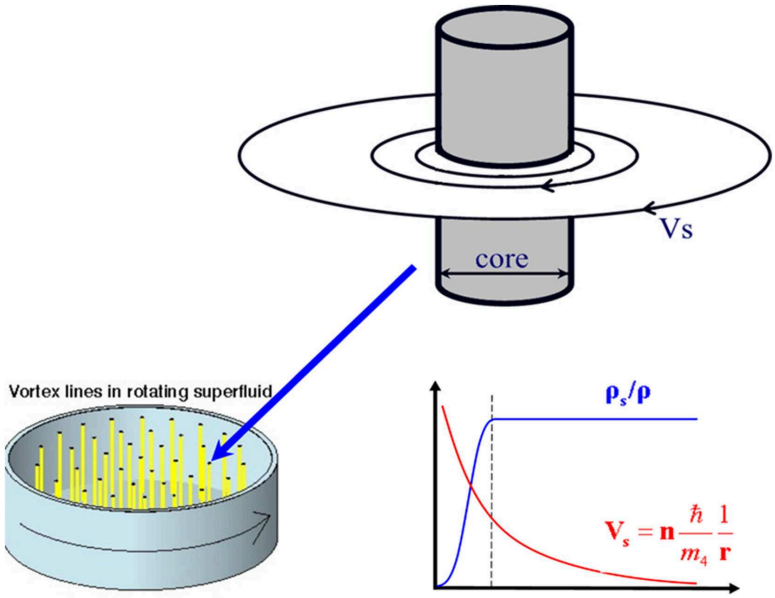

Figure 1.5: A sketch of a quantized vortex in ^{4}He, with the dependences of the superfluid density and velocity on the distance from the core shown in the inset.

determined by specifying a single thermodynamic quantity (e.g., temperature or pressure), which could explain the fountain and mechanocaloric effects, where temperature gradients result in pressure gradients and vice versa. Using the ideal Bose gas model, it is also possible to examine the specific heat of ^{4}He close to the superfluid transition, and doing so confirms that at the transition the specific heat is increased, but the characteristic singularity in the shape of the Greek letter lambda, hinted at by experiments, is not reproduced.

Starting from the condensate macroscopic wavefunction and proceeding as outlined above in Section 1.2, it is also possible to arrive at the quantization of circulation with the circulation quantum $\kappa \approx 10^{-7}$ m^{2}s^{-1}. The existence of quantized vortices in He II was first suggested by Lars Onsager and Richard Feynmann [46, 51], and it was verified experimentally by W. F. Vinen using a vibrating string [87, 88]. The first direct image was produced by Yarmchuk and Packard [89] using photographic imaging of fluorescence induced by ions trapped on the vortices in a rotating container.

The properties of quantized vortices can be further studied by analyzing the Gross-Pitaevskii equation. It is possible to find solutions expected for quantized vortices such that upon approaching the vortex core, only about 1 Å in thickness, the superfluid fractional density drops rather sharply (but in a continuous fashion) to zero. Further from the core, the superfluid velocity scales as $1/r$, where r is the distance from the core, as shown in Fig. 1.5. The energy per unit length of the quantized vortex with n quanta of circulation is mostly given by the kinetic energy of the circulating superfluid (while a smaller contribution comes from the vortex core itself) and thus turns out to be proportional to n^2. For this reason, if a given total circulation Γ_T needs to be distributed among quantized vortices in ^{4}He, it always happens so that each quantized vortex contains only a single circulation quantum, as it is energetically favourable compared to having less vortices with multiple quanta each.

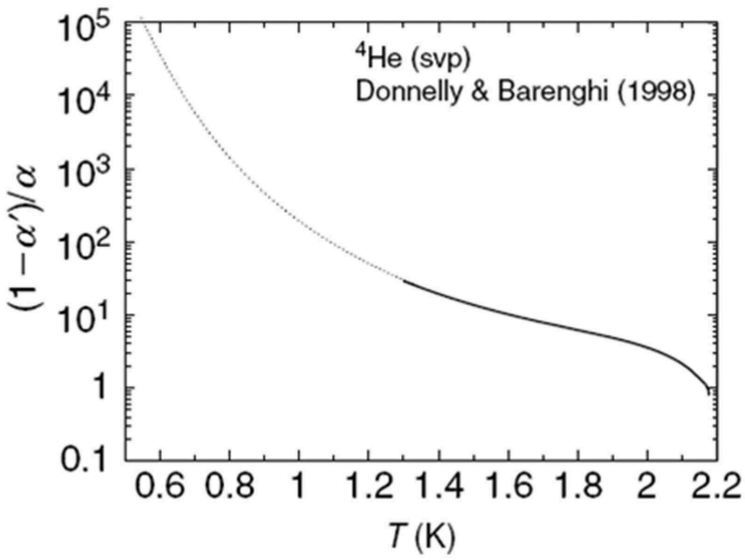

Figure 1.6: The effective superfluid Reynolds number, Re_s, as a function of temperature in ^{4}He [90]. It is evident that everywhere except in the closest vicinity of the superfluid transition, Re_s is greater than unity. This means that, in principle, nothing prevents existing vortices from (self-)reconnecting and forming a turbulent tangle. In practice, a sufficient energy source is needed as well to create the extra vortex line length and to sustain it. This power can be provided, e.g., by moving bodies, or thermally, by driving counterflow. The requirement of having a sufficiently strong external power source means that moving bodies do not generate quantum turbulence in He II automatically at arbitrarily small velocities, but that a certain critical velocity must still be reached, as in classical fluids. As Re_s increases with dropping temperature, it may be expected qualitatively that the observed critical velocities will decrease correspondingly, but we must keep in mind that Re_s only refers to the mechanism of generation of quantum turbulence from quantized vortices in the superfluid component, while in He II under usual experimental conditions, the normal component might be perfectly able to become turbulent on its own, due to its extremely low kinematic viscosity of order 10^{-8} m^{2}s^{-1}. For this reason, it is believed that another dimensionless parameter, such as the "superfluid Reynolds number" defined by $Re_{sfl} = UL/\kappa$ may be necessary to characterise even steady flows in the two-fluid regime.

In ^{4}He, the singly quantized vortices with the properties outlined above represent the building blocks which comprise all rotational motion (including turbulence) in the superfluid component and which are identical in their circulation and differ only by the geometry of their thin cores.

As was mentioned in the first part of Section 1.2, the dynamics of quantized vortices are influenced by the temperature- and pressure-dependent mutual friction parameters α and α', and these can be used to estimate, how likely the quantized vortices are to create quantum turbulence. In Fig 1.6 below, the effective superfluid Reynolds number is plotted versus temperature at saturated vapour pressure.

At this point, it ought to be emphasized once more that an external supply of energy is still needed to create turbulence in He II even though the high

values of Re_s suggest that turbulence should almost be present implicitly, as any quantized vortex could reconnect with itself and generate a complex array of quantized vorticity. However, vortex line length translates more or less directly into energy, and in order to create a large turbulent tangle of quantized vortices, i.e., to increase the vortex line density, L, in a given volume, this energy must be supplied, either mechanically or thermally. Additional energy is later required to maintain the tangle, as will be argued below. Without any energy supply, even a self-reconnecting vortex loop will eventually decay at finite temperature, albeit after producing a few short-lived vortex rings. Even in the zero temperature limit, vortex tangles existing without sufficient energy input will decay as well, only the dissipation due to mutual friction believed to be primarily responsible for the decay of vorticity at higher temperatures, would be replaced by another dissipation mechanism, according to the current understanding possibly phonon emission.

In the now classic case of thermal counterflow (opposite flow of normal and superfluid component along a channel due to a temperature gradient created by a heater at its closed end), the power balance (or vortex line production/decay balance) is described by the Vinen equation [91, 92, 93, 94], which can be written down in the following form, omitting the empirical term accounting for the observed finite critical heat flux:

$$\frac{dL}{dt} = k_1 v_c \frac{\rho_n}{\rho} L^{3/2} - k_2 \kappa L^2, \tag{1.17}$$

where k_1 and k_2 are temperature-dependent parameters of order unity describing the geometry of the flow channel, and of the tangle of quantized vortices (in the case of k_1 also including the effective cross-section of vortex-quasiparticle interaction), $v_c = |\vec{v_n} - \vec{v_s}|$ stands for the counterflow velocity. The two terms on the right hand side are commonly referred to as the production and decay terms, respectively. The significance of the Vinen equation is that in order to sustain a vortex tangle of a given vortex line density L, energy must be supplied externally at a sufficient rate (by driving the counterflow at a given v_c) to compensate the decay term proportional to L^2. Hypothetically, one could easily picture a similar scenario for the case of mechanical generation of turbulence – the decay term would have a similar form, only the generation term would be different, but analogically, it would be a function of the characteristic velocity of the moving body, instead of v_c.

What happens when the driving power is switched off seems to be a more complex question and a subject of current debate, as two different decay laws have been observed experimentally, one in accordance with the Vinen equation 1.17 ($L \propto t^{-1}$) and the other more similar to classical turbulence decay ($L \propto t^{-3/2}$).

To sum up, we know that singly quantized vortices exist in ^{4}He, how they affect the flow field in the superfluid component, how they interact with the normal component via mutual friction, and how their dynamics can be studied. Additionally, we have seen that the conditions in ^{4}He are typically such that the vortices are ready to form a turbulent tangle, if we provide a sufficient power to compensate for its dissipation.

Bearing in mind the results of Bose-Einstein condensation in liquid ^{4}He, let us now start from another vantage point and try to describe the macroscopic

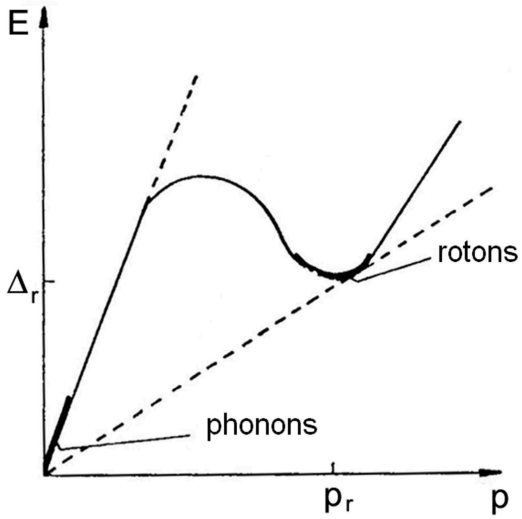

Figure 1.7: The dispersion relation of thermal excitations in ^{4}He. Two types of excitations – phonons and rotons – are distinguished for historical and practical reasons, depending on their position on the curve representing the function $E(p)$ It is currently believed that the roton branch, which is shifted downwards with applied pressure, corresponds to a maximum in the density distribution function of neighbouring atoms and is a hint of the parabolic dispersion relation found in crystalline solids.

hydrodynamics of the superfluid phenomenologically, based on our knowledge of the dispersion relation of thermal excitations, plotted in Fig. 1.7. By Landau's famous argument [40, 41, 42], superfluidity can only exist up to a certain velocity, determined by the minimum of the ratio E/p along the dispersion curve. This ratio is minimal in the roton part of the dispersion relation and corresponds to a velocity of about 60 m/s. In practice, it is hard to verify, because quantized vortices start nucleating from remanent ones already at much lower velocities in ^{4}He and due to their presence, the superfluid component starts acting dissipatively even before reaching Landau's critical velocity. A single measurement by McClintock's group exists [95], where this criterion was tested reliably using electrically driven ions.

Knowing the dispersion relation, it is again possible to calculate the equilibrium concentrations of phonons and rotons as functions of temperature and thus to determine the fractional densities of the normal and superfluid components. Providing also all the assumptions as to what properties the two components should have (inviscid vs. viscous, zero entropy vs. positive entropy), it is possible to arrive at the above mentioned Eqs. 1.1 – 1.4 and all their consequences, such as the fountain and mechanocaloric effects [68, 69] and the existence of multiple wave processes in the superfluid bulk, called first and second sound [39, 40, 41, 42]. On a side note, other sound modes exist and have been observed in thin superfluid films and inside porous media, where the normal component is clamped due to viscous forces. These are called third and fourth sound, respectively, but will not be discussed here any more, as they have little bearing on the topic of this Thesis.

First sound in ^{4}He corresponds to the joint motion of the normal and superfluid component, i.e., to waves of pressure (or density), analogically to the common

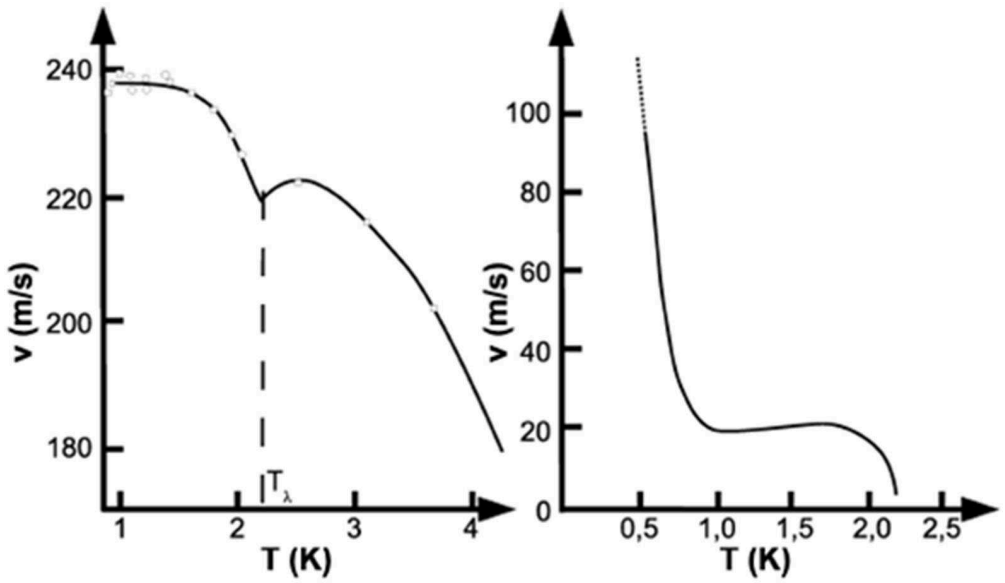

Figure 1.8: Temperature dependence of the velocities of first (left) and second (right) sound in ^{4}He.

sound waves in classical fluids. On the other hand, in second sound waves, the two components oscillate in antiphase, creating an undamped wave of temperature (or entropy) that does not have any direct classical analogy. The velocities of first and second sound, c_1 and c_2, respectively, are given by [39, 40, 41, 42]:

$$c_1^2 = \left[\frac{\partial p}{\partial \rho}\right]_S ; \qquad c_2^2 = S^2 \frac{\rho_n}{\rho_s} \left[\frac{\partial T}{\partial S}\right]_\rho . \tag{1.18}$$

The velocities are also plotted in Fig. 1.8 as functions of temperature. Generally, the temperature range, where it is reasonable to describe second sound as a wave process is given by the temperature dependence of the relative concentrations of the two components. If either of them is too dilute (especially the normal component at low temperatures), second sound as such ceases to be well-defined (the mean free path of thermal excitations becomes comparable to the sound wavelength). For practical purposes, propagation of second sound in ^{4}He is typically considered in the temperature range between the λ–point and 1 K.

Accordingly, it should be emphasized that at temperatures lower than about 0.7 K, the concentration of thermal excitations comprising the normal component drops so low (and their mean free path increases correspondingly) that it may no longer be possible to describe them as a continuous fluid. Of course, 0.7 K is a very rough estimate only, a more precise one would take into account the dimensions of the studied system and compare them to the mean free path of the excitations. Nevertheless, when working at lower temperatures, it is necessary to consider ballistic propagation of thermal quasiparticles instead, as is evidenced, e.g., by the measurement of the laminar drag force acting on an oscillating sphere performed by Niemetz and Schöpe [96, 97], shown in Fig. 1.9.

Finally, it is useful to note that experiments performed in ^{4}He below 0.3 K are commonly referred to as taking place in "pure superfluid", because the density of the normal component is negligibly low compared to that of the superfluid

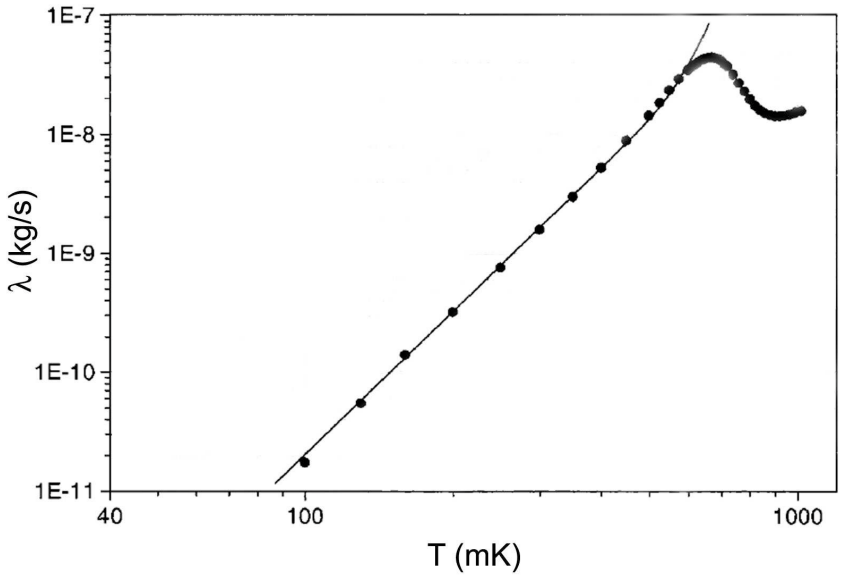

Figure 1.9: Coefficient relating the laminar drag force acting on an oscillating sphere to its velocity in He II above and below 1 K. The minimum at 0.9 K marks a crossover in the ratio of the viscous penetration depth to the diameter of the sphere, while the maximum at 0.7 K represents the transition from the hydrodynamic regime of quasiparticle motion to their ballistic propagation. Of course, the exact temperature at which this happens in a given experiment will depend on the dimensions of the immersed bodies, and of the container.

component. However, it ought to be emphasized that finite and temperature dependent drag forces due to scattering of thermal excitations are still experienced by moving bodies even in this "purely superfluid" environment, just as is shown in Fig. 1.9.

1.2.2 ^{3}He and Cooper Pairing

Unlike the common isotope ^{4}He, the nucleus of the rare ^{3}He consists of an odd number of nucleons – two protons and one neutron. At room temperature, both isotopes behave almost like ideal gases, although they do differ in some aspects. However, it is at low temperatures, corresponding to their liquid phases, that the two isotopes start behaving truly differently. ^{3}He has a nuclear spin of $1/2$, which has two immediate consequences. First of all, ^{3}He is a fermion, therefore follows Fermi-Dirac statistics, cannot form a Bose-Einstein condensate like ^{4}He does, and to describe its properties, one has to use the Fermi liquid theory, as suggested by Landau [63, 98] and later improved by others [64, 65, 99, 100, 101]. It should be stressed that as a consequence, the viscosity of ^{3}He in the normal state is very high at low temperatures (scaling as T^{-2}). The same remains valid for the normal component of its superfluid phases, where, basically, the viscosity is so high that it precludes any kind of turbulent motion in the normal component. Second, the nonzero spin also means a corresponding nuclear magnetic moment, and therefore ^{3}He is a magnetic liquid, in the sense that it is affected by magnetic field and can be probed using techniques such as nuclear magnetic resonance (NMR).

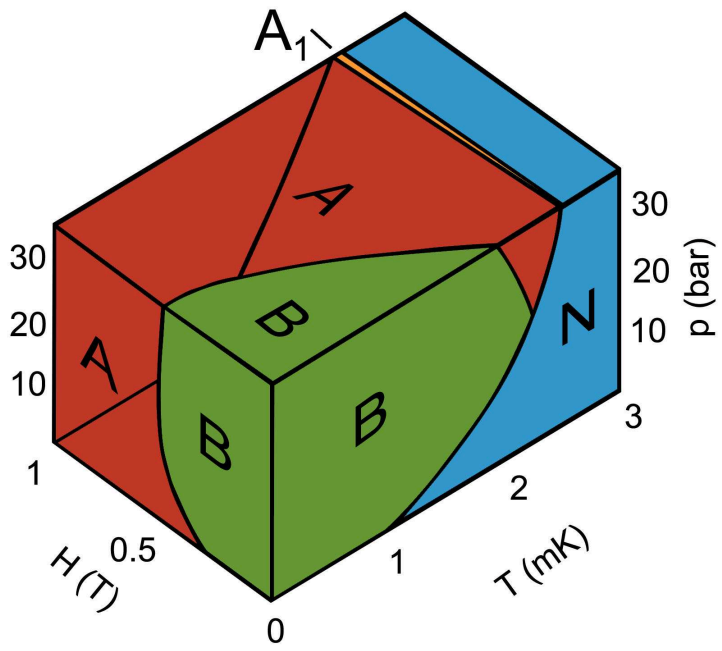

Figure 1.10: The superfluid phases of ^{3}He.

One might ask what is then the mechanism by which ^{3}He becomes superfluid if it cannot happen simply due to Bose-Einstein condensation? It turns out that analogically to superconductors, pairing between atoms is made possible in ^{3}He due to the p-wave interaction, and ^{3}He can become what is known as a BCS-like superfluid [100, 101] at the critical temperature $T_C \approx 2$ mK, three orders of magnitude lower than the λ–point of ^{4}He, through the condensation of the pairs with integer spin, which behave in a quasi-bosonic manner. A notable difference between traditional BCS superconductors and ^{3}He lies in the fact that both the total spin and total orbital momentum of ^{3}He pairs are equal to one, unlike the electron Cooper pairs in s-wave superconductors, which have both their spin and orbital momentum equal to zero.

In fact, several different ^{3}He superfluid phases can be obtained depending on temperature, pressure and external magnetic field, as can be seen in Fig. 1.10. At low temperature, and magnetic field, the ^{3}He–B phase is the preferred state, but near a part of the solidification curve at temperatures close to T_C, the phase ^{3}He–A is stable as well even in zero magnetic field. If an external field is applied, the region of stability of the A–phase can be extended significantly, possibly suppressing the B–phase altogether. In nonzero fields, a third stable phase ^{3}He–A_1 was observed, in a small region between the normal state and ^{3}He–A.

The three phases differ fundamentally in their order parameters and in the shape of their corresponding Fermi surfaces and energy gaps. In ^{3}He–B the pairs can have all available projected spins of $S_z = 0, \pm 1$, and it has an isotropic energy gap in zero magnetic field, while in the phases ^{3}He–A and ^{3}He–A_1, the projected spins are restricted to $S_z = \pm 1$ and $S_z = 1$, respectively, where the z-axis is chosen to be aligned with the magnetic field. The energy gap of the A phases is highly anisotropic, with a maximum in the plane perpendicular to the orbital

momentum vector and with zero gap energy in the parallel direction. The order parameters in matrix form with indices corresponding to the spin states of the ^{3}He atoms constituting the pairs, illustrating the possible spin pairings in the individual phases, are listed symbolically below in Eq. 1.19:

$$\Psi_{\mathrm{B}} = \begin{pmatrix} \Psi_{\uparrow\uparrow} & \Psi_{\uparrow\downarrow} \\ \Psi_{\downarrow\uparrow} & \Psi_{\downarrow\downarrow} \end{pmatrix}, \quad \Psi_{\mathrm{A}} = \begin{pmatrix} \Psi_{\uparrow\uparrow} & 0 \\ 0 & \Psi_{\downarrow\downarrow} \end{pmatrix}, \quad \Psi_{\mathrm{A1}} = \begin{pmatrix} \Psi_{\uparrow\uparrow} & 0 \\ 0 & 0 \end{pmatrix}. \tag{1.19}$$

For practical purposes, however, it is more useful to write down the order parameter as a matrix $A_{\mu j}$, where the indices μ and j correspond to the three degrees of freedom (main axes) in the spin and orbital spaces, respectively. For the sake of completeness, specific forms of the order parameters in the A and B phases are listed below in Eqs. 1.20 and 1.21, while detailed reasoning and explanations are available in the literature [102]. The order parameters are usually written in the following form:

$$^3\text{He–A:} \quad A_{\mu j} = \Delta_{\max} d_\mu \left(m_j + i n_j\right), \tag{1.20}$$

$$^3\text{He–B:} \quad A_{\mu j} = \Delta\, e^{i\varphi} R_{\mu j}\left(\vec{n}, \theta\right), \tag{1.21}$$

where in Eq. 1.20, $\Delta_{\max}$ refers to the maximum of the energy gap, $\vec{d}$ denotes a unit vector in the spin space such that the projection $S_{\vec{d}} = 0$, and $\vec{m}$, $\vec{n}$ are unit vectors in the orbital momentum space, which define another vector $\vec{l} = \vec{m} \times \vec{n}$ that points in the direction of the orbital angular momentum of the pair, i.e., $L_{\vec{l}} = 1$. In Eq. 1.21, Δ is the isotropic gap energy (in zero magnetic field), φ is the phase, and $R_{\mu j}\left(\vec{n}, \theta\right)$ is a rotation matrix that links the orbital and spin coordinates via a rotation around axis $\vec{n}$, by an angle θ. The energy gaps of the ^{3}He–A and ^{3}He–B phases together with the all the functions and fields appearing in the order parameters are schematically plotted in Fig. 1.11.

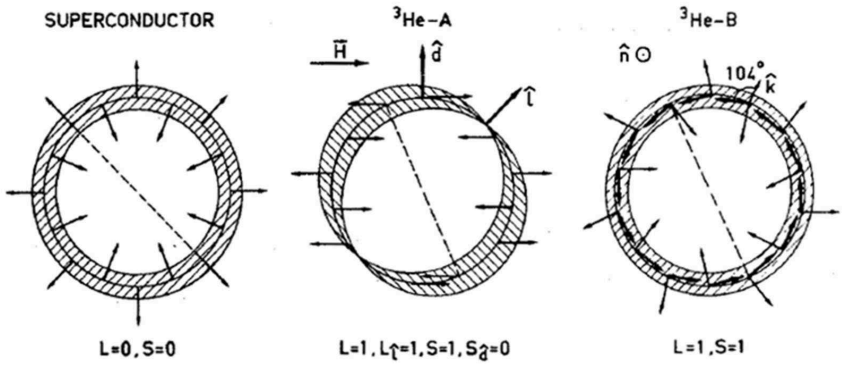

Figure 1.11: Energy gaps of the superfluid phases of ^{3}He compared to that of a superconductor. The easiest case to study is ^{3}He–B with its isotropic energy gap, which can only be weakly perturbed due to magnetic fields or gradients of superfluid velocity. ^{3}He–A is more difficult to describe due to the anisotropy of the energy gap, and many possibilities for complicated textures of the $\vec{d}$ and $\vec{l}$ parameters. The Figure is taken from Ref. [103].

A real sample of ^{3}He–A ought to be described by the textures of the $\vec{d}$ and $\vec{l}$ vectors, which are affected by the magnetic field, by container walls, by counterflow, or by the dipole-dipole interaction of the nuclear spins of the ^{3}He atoms. In ^{3}He–B, textures of the vector $\vec{n}$ are important, as this parameter is also affected by magnetic field (albeit weakly), quantized vortices, and counterflow, while the angle θ has a fixed value of $\theta \approx 104°$ due to the dipole-dipole interaction.

Owing to the complex nature of the order parameters of the ^{3}He superfluids, many different topological defects can exist in them. In ^{3}He–A, three kinds of quantized vortices have been observed using NMR techniques [104, 105], their stability depending on temperature, pressure and magnetic field. The three types of vortices are usually referred to as a continuous unlocked vortex, a locked vortex, and a singular vortex, where the former two have circulation $\Gamma = 2\kappa$, i.e., each contain two circulation quanta, while the last vortex type has only $\Gamma = \kappa$. Moreover, 2D topological defects can be present, such as two types of solitons (domain walls separating regions of parallel and antiparallel $\vec{d}$ and $\vec{l}$), and even vortex sheets can exist, which are a combination of quantized vortices and a soliton. This planar defect then represents a distribution of vorticity along two dimensions. As the topological defects in ^{3}He–A are not the main focus of this work, we will direct the interested readers to Refs. [104, 106, 107, 108, 109] for further information and continue with ^{3}He–B, which was used in the Andreev reflection measurements presented in Chapter 5.

In ^{3}He–B, again more types of quantized vortices exist with their stability depending on temperature and pressure [105, 108, 110]. Leaving aside the special case of the mass-spin vortex, which has a spin current around it as well as flow circulation, two other types of quantized vortices are known, with either axisymmetric or nonaxisymmetric cores. Fortunately, both these types of vortices have a similar form as their counterparts in He II, in the sense that each carries only a single circulation quantum, which is now given as:

$$\kappa = \frac{h}{m} = \frac{h}{2m_3} \approx 6.6 \cdot 10^{-8}\ \mathrm{m^2 s^{-1}}, \tag{1.22}$$

where the mass of the superfluid particle, m, is equal to the mass of the pair of ^{3}He atoms, $2m_3$. There is, however, an important difference between the quantized vortices in ^{3}He–B and He II – in ^{3}He–B, the vortex core has a much larger diameter than in He II, of the order of 100 nm. As a consequence, it is possible to design experiments for ^{3}He–B with sufficiently smooth walls that do not pin vortices easily on surface irregularities, while in He II this is impossible, because even atomic scale roughness could cause vortex pinning.

Fig. 1.12 contains the temperature dependence of the effective superfluid Reynolds number. Unlike He II, Re_s crosses unity at about 0.6 T_C, which means that whether or not quantum turbulence is generated with given experimental methods will strongly depend on temperature. For example, if we attempt to inject energy into the superfluid by means of a spin-up of a sample initially at rest, at high temperatures close to T_C, the energy will be transferred to the normal component (which will be in solid body rotation with the container) and the excess will be dissipated by its high viscosity. No new quantized vortices are created in the superfluid, and if remanent vortices were present, their number is conserved and they will merely slide along the (smooth) walls and extend along the axis of

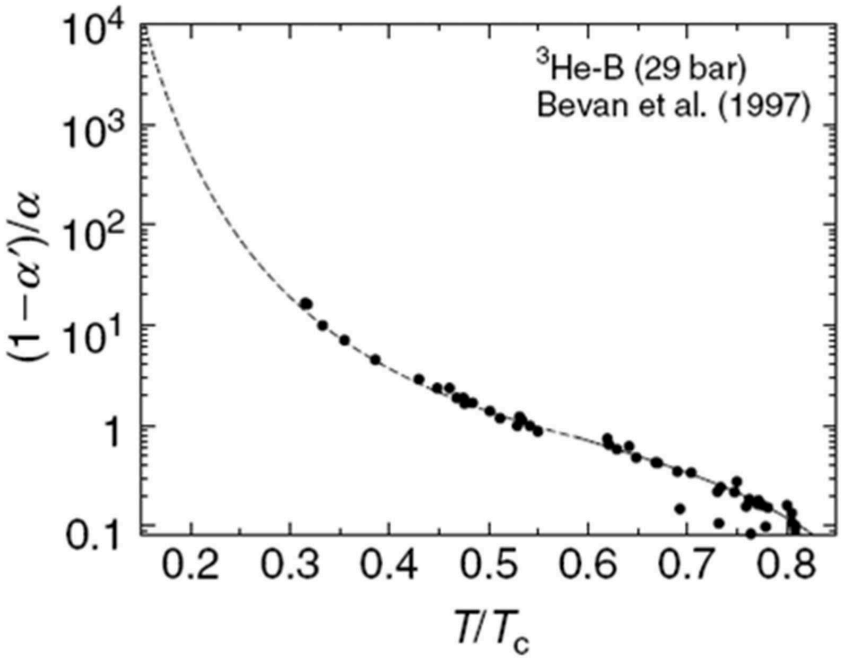

Figure 1.12: The effective superfluid Reynolds number as a function of temperature in ^{3}He–B. A crossover is observed at about 0.6 T_C, where $Re_s = 1$.

rotation to create a lattice of straight vortex lines. If the same amount of energy is supplied at a temperature below approximately 0.6 T_C, where $Re_s > 1$, a turbulent burst will occur, suddenly increasing the number of quantized vortices in the sample and leading to a turbulent spin-up. Of course, at longer timescales, the number of quantized vortices (or the vortex line density) will then relax to its equilibrium value determined by the final angular velocity of rotation. A diagram illustrating at what temperatures the generation of additional quantized vorticity in the form of a turbulent burst is likely and where it most likely cannot happen, is shown in Fig. 1.13, and the scenario of a turbulent spin-up of the superfluid component is provided by Fig. 1.14.

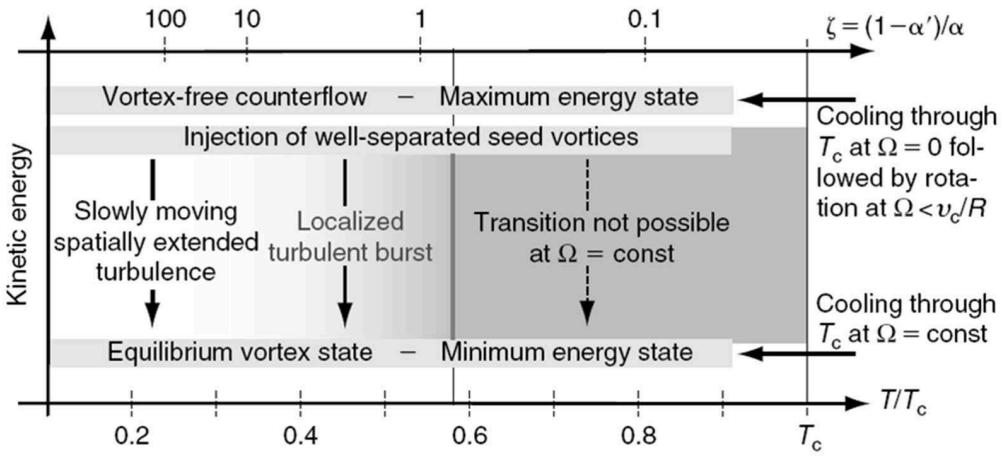

Figure 1.13: A temperature diagram, illustrating the conditions under which quantum turbulence is likely to be formed in ^{3}He–B, taken from Ref. [103].

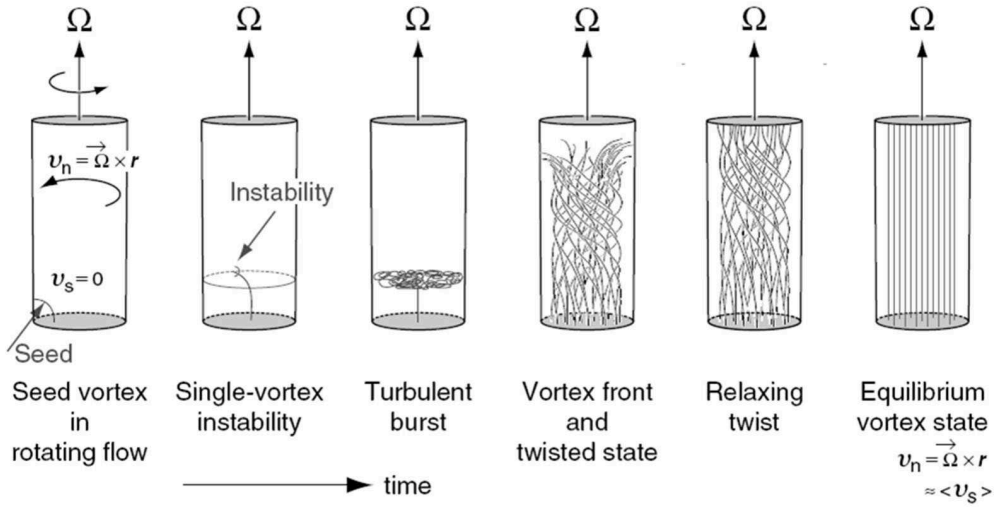

Figure 1.14: A series of panels illustrating how quantum turbulence can be generated from a single seed vortex loop under favourable conditions, taken from Ref. [103].

In ^{3}He–B, a modified BCS theory can be used to calculate the dispersion relation of excitations. It is sketched in Fig. 1.15, together with its most important characteristics – the temperature- and pressure- dependent gap energy, E_g, and the Fermi momentum, p_F. The thermal excitations are defined by their momentum, p, and can be characterised also by their group velocity, $v_g = \frac{dE}{dp}$.

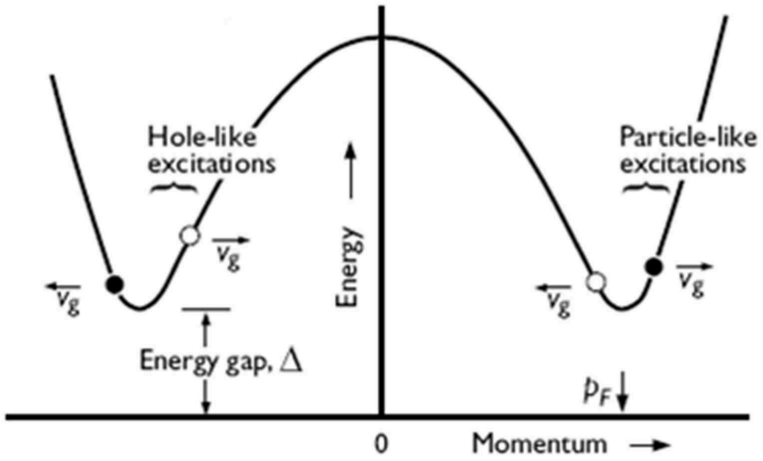

Figure 1.15: BCS-like dispersion relation of thermal excitations in ^{3}He–B. By analogy with solid state physics, excitations with $|p| > p_F$ and with group velocity in the same direction as their momentum are usually referred to as quasiparticles, while excitations with $|p| < p_F$ and group velocity opposite to their momentum are called quasiholes. It should be noted that the above sketch is merely illustrative. In correct scaling, the minima near p_F would appear significantly sharper and therefore a vast majority of thermal excitations present in real ^{3}He–B is concentrated very close to p_F in the momentum space, see, e.g., Ref. [111].

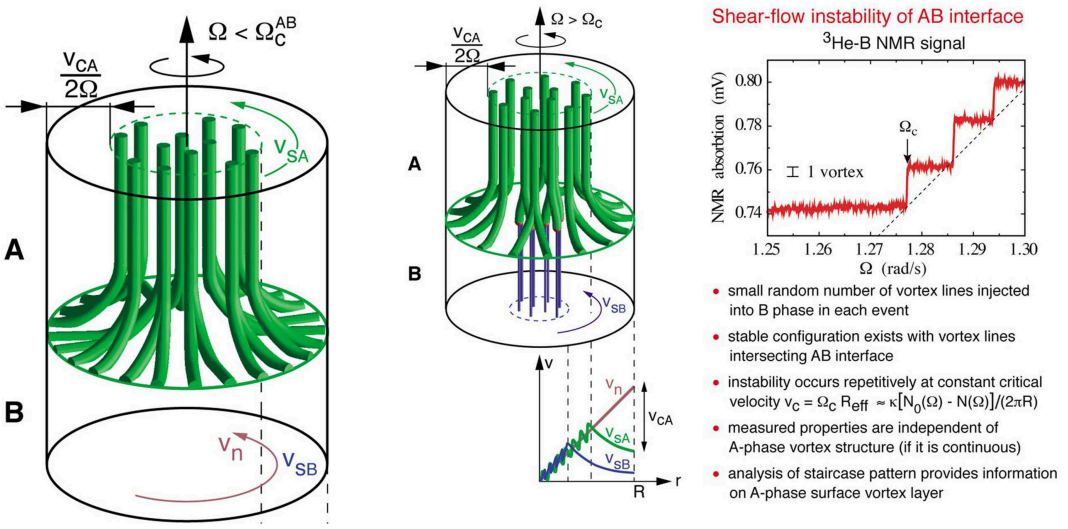

Figure 1.16: Two sketches of quantized vortices at the A–B interface. Left panel: When the rotation angular velocity is sub-critical, the interface of the rotating ^{3}He–A superfluid and the stationary ^{3}He–B superfluid is stable with finite slip velocity, and all the vortices end on container walls. Right panel: When the angular velocity is increased, so is the difference between the velocities of the superfluid component in the two phases, and upon exceeding a critical value, a number of vortices penetrates the interface and extends into the B phase. The profile of the velocities is plotted in the graph below the sketch of the container, and an example of the dependence of the NMR absorption signal in the B phase is shown in the graph to the right. More information on the vortices near the A-B phase boundary can be found in Refs. [109, 112].

Again as in He II, at temperatures sufficiently below T_C (typically 0.3 T_C and lower), the thermal excitations will form a very dilute gas, and to describe it properly, one would have to consider their ballistic propagation and all related scattering processes, which involve normal scattering on solid bodies and walls, as well as the so called Andreev scattering that can also occur on walls, but generally is considered to take place on any gradients of of the energy gap, which may be caused for example by the variations of the order parameter near walls, but especially by the sharp gradient of superfluid velocity near quantized vortices. Section 1.3 introduces this process in more detail and explains how it can be used as an experimental method for detecting vorticity in ^{3}He–B.

Other experimental tools and techniques useful in ^{3}He research often make use of the fluids' magnetic properties. The most important example is perhaps the powerful NMR technique [103, 105], which when applied in continuous wave mode, is sensitive to the texture of the order parameter and thus can be used to detect the presence of quantized vortices or counterflow. The same technique has also been used to identify all the observed topological defects, as each of them leaves a unique signature in the NMR spectrum. Lately, a development has also been made in using NMR to probe domains of homogeneously precessing spins under special conditions, such as inside magnetic traps, which can also be interpreted as the Bose-Einstein condensation of magnons to the lowest state given by the trap potential. Yet other applications of NMR include the search

for special surface states, or states existing inside vortex cores.

Another rather specific but very useful experimental trick attainable using (gradient) magnetic fields is to create and stabilize the interface between the ^{3}He–A and ^{3}He–B phases in one sample. Because quantized vortices nucleate much easier in the A phase, it is then possible to inject them into the B phase in a controlled fashion via the Kelvin-Helmholtz instability [109, 113, 114]. Apart from this direct application of the A–B boundary stabilization, the phenomena occurring at the collapse of two such interfaces are interesting in their own right and can be studied experimentally. To sum up, one could say that while each of the ^{3}He superfluids is by its nature a more complicated system than He II, they offer a wide range of interesting scientific problems and at the same time many available techniques for tackling them, and it seems that ^{3}He research is still likely to bring new and valuable results.

1.3 Andreev Reflection in ^{3}He–B

Andreev reflection was first described in superconductors [115], where electrons or holes can be scattered non-classically with almost no momentum transfer, typically near the surface of the superconducting material or its interfaces with non-superconductors, but more generally on any gradients of the energy gap. Analogically, in ^{3}He–B, Andreev reflection is a non-classical process during which thermal excitations are scattered off gradients of the energy gap, in this case typically caused by the rapid superfluid circulation around quantized vortices, or by the presence of walls. It can be explained if we consider the transformation of the dispersion relation of thermal excitations in case of finite superfluid velocity, as it is plotted in Fig. 1.17.

Because of the transformation of the dispersion relation in regions of finite $\vec{v_s}$, it might happen that upon encountering a gradient of superfluid velocity, a propagating excitation with momentum close to p_F and energy close to Δ would be about to enter a region, where no possible states exist for it, because its branch of the dispersion relation starts to shift towards higher energies, while the energy of the freely propagating excitation remains the same. In ^{3}He–B, this may typically happen when the excitation approaches some topological defect in the superfluid, especially a quantized vortex, around which $\vec{v_s}(\vec{r})$ is given by the Biot-Savart law (Eq. 1.13) and its magnitude decreases with the distance from the core as $1/r$.

In this case, the excitation cannot propagate forward, because it would have no corresponding energy states to occupy. If the gradient of $\vec{v_s}(\vec{r})$ is smooth (as is the case around a quantized vortex), the classical scattering process is prohibited, because it requires a large stepwise exchange of momentum. Therefore, what happens is that the excitation crosses the minimum at its branch and becomes the opposite type of excitation – if it originally were a quasihole, it becomes a quasiparticle, and vice versa. Because, it now has a group velocity opposite to its original one, it can propagate freely away from the gradient of $\vec{v_s}(\vec{r})$ that it has encountered. In fact, since the exchange of momentum is very small, $\delta p/p_F \ll 1$, the excitation retraces its original path almost exactly. This is true even in the 3D case, because the excitation still has virtually the same momentum (all its components), but has changed its "gender" and therefore also swapped the relation

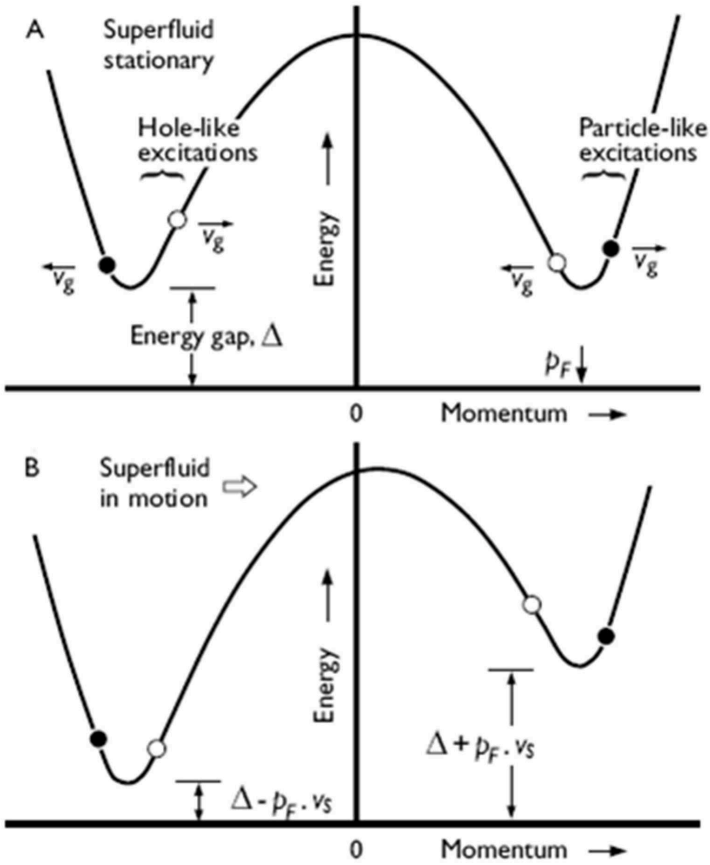

Figure 1.17: Upper panel: One dimensional version of the standard dispersion relation $E(\vec{p})$ of thermal excitations in ^{3}He–B in the frame of reference of the normal component and with $\vec{v_s} = 0$. Lower panel: The same dispersion relation with a finite superfluid velocity in the (positive) direction of the momentum axis. If a finite superfluid velocity exists, the dispersion relation (still in the reference frame of the normal component), becomes tilted according to the Galilean transformation and is given by $E'(\vec{p}) = E(\vec{p}) + \vec{p} \cdot \vec{v_s}$. As a consequence, the two branches are no longer symmetric. Close to the original gap energy, possible states exist only for one sign of the given momentum component, specifically with direction opposite to $\vec{v_s}$

.

between its momentum and group velocity, which point in the same direction of quasiparticles, but in opposite directions for quasiholes. This process is called Andreev reflection (or Andreev scattering) and is illustrated in Fig. 1.18.

In the full 3D case, the description is a little more complicated, nevertheless, at least for a regular array of vortices, whether or not an incoming excitation will be Andreev reflected can be determined based on its trajectory characterised by an impact parameter, b, and an angle between the path of the excitation and the direction of the core of the quantized vortex, θ, according to Fig. 1.19. We can estimate that Andreev reflection will take place if the following condition is satisfied [116]:

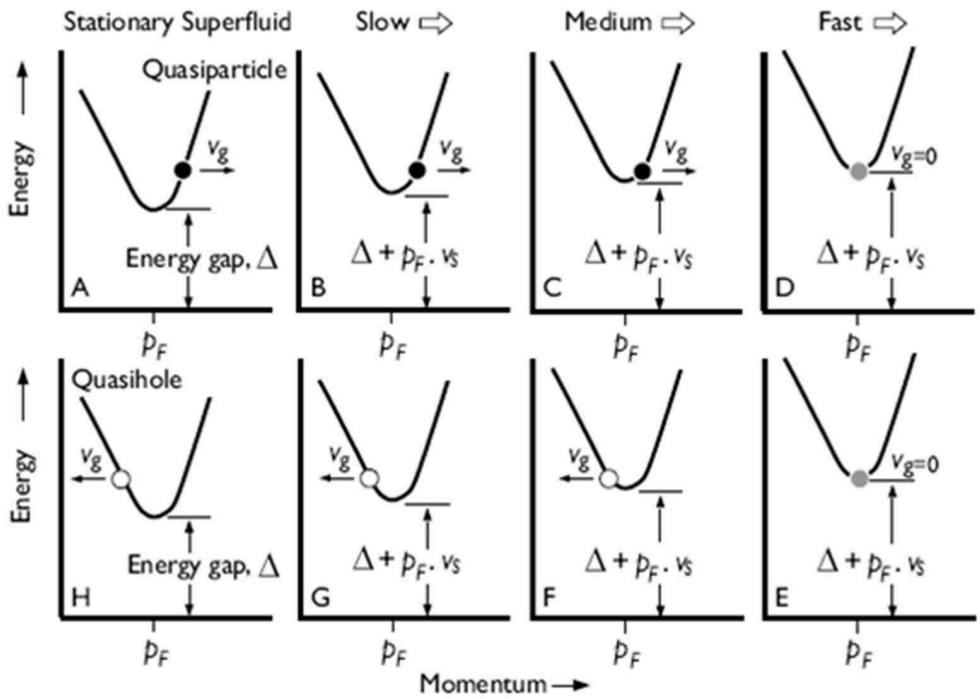

Figure 1.18: A series of panels depicting Andreev reflection on a quantized vortex in ^{3}He–B, taken from Ref. [103]. To understand this figure, it is useful to picture a quantized vortex located at the right side of this page at the level of the lower boundary of the panels, with its core perpendicular to the screen/paper, causing clockwise circulation of the superfluid component. Then starting from the top left panel, a quasiparticle is heading in the direction of this vortex, and gradually enters regions of higher and higher superfluid velocity as indicated above the top series of panels. The dispersion relations become tilted accordingly, as described in Fig. 1.17, and the quasiparticle gradually decelerates, as its group velocity is given by $\vec{v_g} = \nabla_{\vec{p}} E(\vec{p})$. Eventually, the quasiparticle reaches its turning point, where the dispersion relation becomes shifted so much that the energy of the quasiparticle is now equal to the energy of the minimum on its branch, i.e., $E_{\rm qp} = \Delta + p_F v_s$, and its group velocity becomes equal to zero. Since the quasiparticle cannot propagate forward, because no corresponding states would exist in a region of even higher superfluid velocity closer to the quantized vortex, it becomes a quasihole instead, as is indicated in the bottom-right panel. Now following the bottom row of panels from right to left the newly formed quasihole moves in the opposite direction and leaves the proximity of the quantized vortex, having exchanged only very little momentum.

$$b < \frac{p_F}{2m_3}\frac{\hbar}{k_B T}\sin\theta \approx 1\ \mu\text{m for } \theta = \frac{\pi}{4} \text{ and } T = 0.2T_C. \tag{1.23}$$

Finally, it is useful to mention how, due to the process of Andreev scattering of thermal excitations, the quantized vortices may affect heat transport in ^{3}He–B in a suitably chosen experimental configuration. At very low temperatures, where there is only a dilute gas of thermal excitations, the only means of heat exchange in the superfluid is via the ballistic propagation of these excitations and their

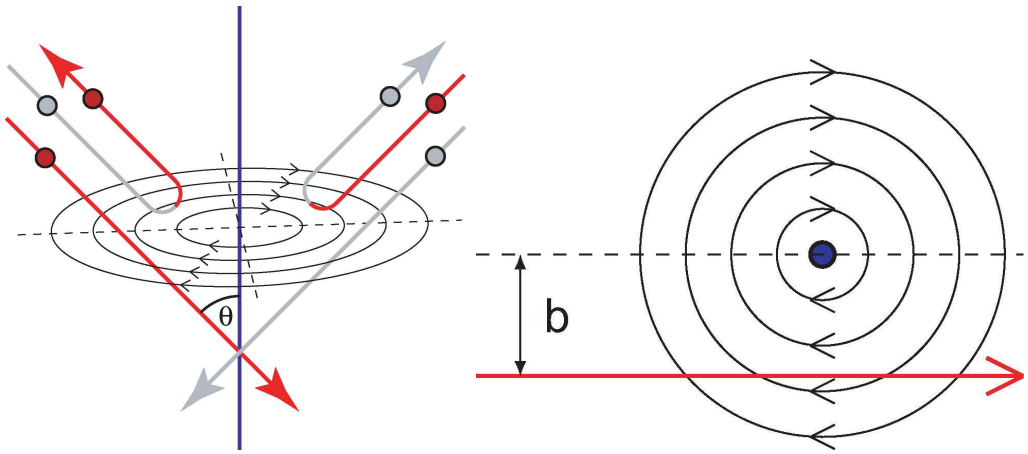

Figure 1.19: Left panel: A sketch illustrating the 3D process of Andreev scattering of excitations off a quantized vortex. The red lines indicate quasiparticles, grey lines quasiholes. Please note that depending on the type of excitation and on the exact way in which it approaches, it may either pass the vortex unimpeded (quasiparticles pass if they enter an area where $\vec{v_s}\cdot\vec{v_g} < 0$, quasiholes if $\vec{v_s}\cdot v_g > 0$), or be Andreev reflected, provided that the condition 1.23 is satisfied. Right panel: A 2D view of the quantized vortex, defining the impact parameter b.

interaction with solid objects, by which energy can be exchanged, leading to the thermalization of the objects. Additionally, the temperature of the superfluid itself is given by nothing else but the concentration of the excitations present in its volume.

If we now imagine two regions of superfluid with different temperatures $T_1 > T_2$ separated by a small orifice, then there is an excess concentration of excitations in the first region compared to the second one. Naturally, to achieve thermodynamic equilibrium, the concentrations will eventually equalize, because more excitations will be traveling through the orifice from the hotter region to the colder one than the other way round. On the other hand, if the temperatures are kept different by a steady heat influx into the hotter region and heat extraction from the colder one, then, if the difference in temperature, $T_1 - T_2$, is at all significant, the excitation flow from the colder region to the hotter one can practically be neglected, because the concentration of quasiparticles depends on temperature exponentially. In this case, the resulting heat flux will be equal only to the power of the excitation beam leaving the hotter region, which can be expressed as [117]:

$$P_{\text{out}} = \frac{\langle N_{\text{ex}} v_g \rangle \langle E_{\text{ex}} \rangle}{4} A_{\text{eff}}, \tag{1.24}$$

where N_{ex}, E_{ex}, v_g are the number density, energy, and group velocity of the thermal excitations, respectively, and A_{eff} is the effective area of the orifice. By substituting for the quantities related to excitations from the theory of their ballistic propagation [117], we obtain:

$$P_{\text{out}} = \frac{4\pi p_F^2}{h^3} k_B^2 T^2 e^{-\delta} (1+\delta) A_{\text{eff}}, \tag{1.25}$$

where $\delta = \Delta / k_B T$ is a convenient shorthand for the reduced temperature.

The time constant of this thermal relaxation process, τ, will depend among other on the area of the orifice. It can be expressed as $\tau = RC$, where R is the thermal resistance associated with the ballistic propagation of excitations through the orifice, and C represents the total heat capacity of the hotter region. These quantities are given by [117, 118]:

$$R^{-1} \equiv \frac{dP_{\text{out}}}{dT} = \frac{8\pi p_F^2}{h^3} k_B^2 T e^{-\delta} \left(1 + \delta + \frac{1}{2}\delta^2\right) A_{\text{eff}}, \tag{1.26}$$

$$C = \sqrt{2\pi} k_B N(E_F) \Delta \, \delta^{\frac{3}{2}} e^{-\delta} \left(1 + \frac{21}{16}\delta^{-1}\right) V, \tag{1.27}$$

where $N(E_F)$ is the number of states at the Fermi energy and V is the volume of the hotter region, assuming that it has a uniform temperature.

However, if quantized vortices are present on the colder side of the orifice, Andreev scattering will take place and as the Andreev-scattered excitations retrace their original trajectories with good accuracy, a part of the incoming excitation beam will be reflected back into the hotter part, without exchanging momentum or energy. Therefore, in this case, the vortices impede heat transport between the two regions leading to an increase of the thermal resistance and hence of the relaxation time constant. This phenomenon may be then described simply by introducing a reflectivity coefficient depending on the density and configuration of vortex lines, or equivalently by considering a reduced effective area of the orifice. This approach has been taken to analyze the experimental data presented in Chapter 5. One of the open questions that remain is, if the combined effect of all the vortices is simply an addition of the contributions of each individual vortex (in other words, whether the "vortex shadow" is just a superposition of the "shadows" of individual vortices) or whether some form of screening occurs, or perhaps more precisely, from what density of vortex lines this effect might become significant.

1.4 Detector Elements – Quartz Tuning Forks

The quartz tuning fork is a mechanical resonator operating usually in the kHz range. Commercially produced tuning forks of the most common type resonate at 2^{15} Hz, i.e., about 32 kHz at room temperature in their evacuated capsules. The tuning forks are often used as frequency standards for semi-precision timing applications, for example, in the circuits of digital watches. Their design (see Fig. 1.20) is such that they have minimal losses due to intrinsic damping (during the motion of the two prongs, which oscillate in anti-phase, the net force on the base is zero), so that only a small amount of energy is lost through dissipation in the quartz crystal or via connections to the base, which damp its low-amplitude flexural motion. As a result, the intrinsic quality factor of the resonator, $Q = f_0/\Delta f$, where f_0 is the fundamental resonance frequency and Δf is the resonant linewidth, i.e., full width at half of the maximum amplitude, is very high. At room temperature it is usually slightly below 10^5, but under cryogenic conditions, it can exceed even 10^6.

Therefore, it is no surprise that the quartz tuning fork found its applications in scientific research. It has been used successfully in atomic force microscopy

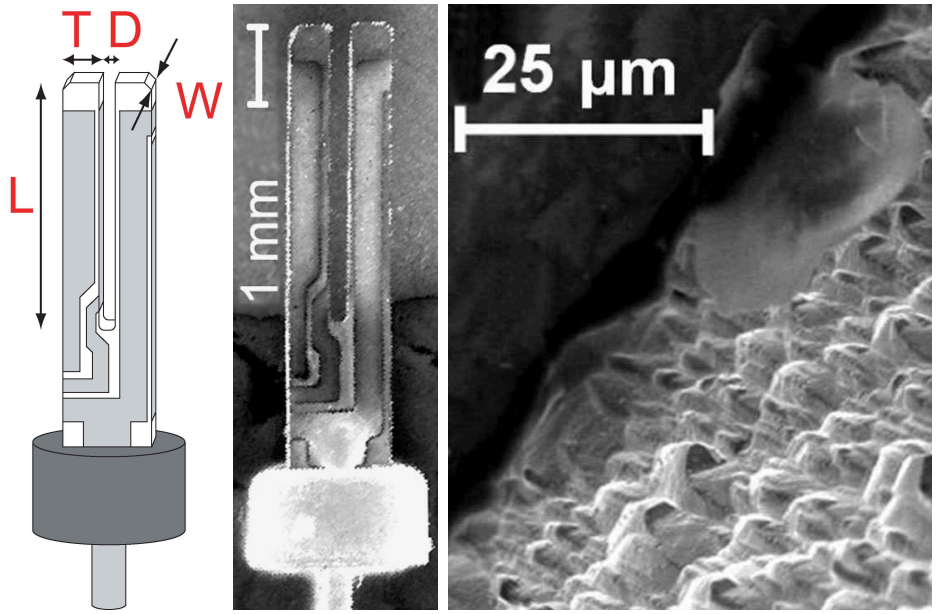

Figure 1.20: From left to right: (i) A sketch of the vibrating tuning fork including specifications of its dimensions. (ii) An electron micrograph of the 32 kHz quartz tuning fork. (iii) A micrograph showing the typical surface roughness of the same commercially available tuning fork.

[119, 120], viscosimetry [121], and in low temperature physics, it became a valuable secondary thermometer in ^{3}He liquids [121]. Specifically in cryogenic fluid dynamics, it is used as a generator and detector of classical and quantum turbulence [1, 2], it can detect cavitation [9, 10], or be used to study acoustic phenomena in pure ^{4}He [4] and in ^{3}He – ^{4}He mixtures [122, 123].

In good approximation, the mechanics of the tuning fork can be described using the Euler-Bernoulli theory of beam motion [124]. A single prong of the tuning fork is characterised as a beam of length L, thickness T, and width W, as defined in Fig. 1.20, while the distance between the two prongs is labeled D. The Euler-Bernoulli equation is in itself an approximation, which neglects shear deformation (although it allows to estimate shear stresses), works only for small amplitudes of oscillation (small deflection angles), and for thin beams, $T, W \ll L$. For an ideal (dissipationless) 1D oscillating beam, it is usually written down in the following form:

$$\mu \frac{\partial^2 w(x,t)}{\partial t^2} + \frac{\partial^2}{\partial x^2}\left(EI\frac{\partial^2 w(x,t)}{\partial x^2}\right) = q(x,t), \tag{1.28}$$

where $w(x,t)$ describes the position of a given section of the oscillating beam determined by x, pointing along the length of the beam, μ and E are the linear density and Young modulus of the beam, respectively, I is the second moment of area of the cross-section of the beam with respect to the neutral axis, and $q(x,t)$ is the distributed load expressed in terms of force per unit length. For a homogeneous beam of rectangular cross-section, such as the prong of the tuning fork, $I = WT^3/12$ and of course $\mu = \rho WT$. The equation must be supplemented by appropriate boundary conditions which depend on the actual situation. For a cantilevered beam, fixed and free ends are considered, and the relevant boundary

conditions are listed below:

$$\begin{aligned}
\text{Fixed end:} \quad & w(x,t)\,|_{x=x_0} &&= 0, \\
& \tfrac{\partial w(x,t)}{\partial x}\,|_{x=x_0} &&= 0, \\
\text{Free end:} \quad & \tfrac{\partial^2 w(x,t)}{\partial x^2}\,|_{x=x_1} &&= 0, \\
& \tfrac{\partial^3 w(x,t)}{\partial x^3}\,|_{x=x_1} &&= 0.
\end{aligned}$$

Assuming harmonic oscillations, the Euler-Bernoulli equation leads to an eigenvalue problem which can be solved for the natural resonances of the beam:

$$\cos(\alpha)\cosh(\alpha) + 1 = 0, \tag{1.29}$$

where α is the product of the wavenumber, a, and the beam length L. The above condition can be solved numerically, obtaining the values α_n belonging to each flexural resonant mode denoted by the integer n. These in turn define the resonant angular frequencies as:

$$\omega_n = \sqrt{\frac{EI}{\mu}}\frac{\alpha_n^2}{L^2} = \sqrt{\frac{EI}{\mu}}a_n^2. \tag{1.30}$$

It is also useful to define the effective mass $m_{\text{eff}}^{(n)}$ and the spring constant k_n of each resonant mode n of the beam. These can be defined based on energetic considerations (Rayleigh method) [124] as:

$$\frac{1}{2}m_{\text{eff}}^{(n)}u_n^2 = \frac{1}{2}\rho WT\int_0^L\left(\frac{\partial w_n(x)}{\partial t}\right)^2 dx, \tag{1.31}$$

$$\frac{1}{2}k_n w_n^2 = \frac{1}{2}EI\int_0^L\left(\frac{\partial^2 w_n(x)}{\partial x^2}\right)^2 dx, \tag{1.32}$$

where w_n and u_n are the displacement and velocity amplitudes of the free end of the cantilever, respectively, and $w_n(x)$ are the displacement amplitudes along the length of the beam for the different modes. Using this definition, it can be derived analytically without any further approximations (albeit the calculation is rather tedious) that *at resonance*, $m_{\text{eff}}^{(n)} \equiv m_{\text{eff}} = 1/4\,\rho TWL$, independently of the resonant mode, while the spring constants k_n increase with n, as expected from the relation $\omega_n^2 = k_n/m_{\text{eff}}$. Hence, using the above expression for m_{eff} and Eq. 1.30, we can express the spring constants as $k_n = \alpha_n^4\,EI/4L^3$. Away from resonance, the effective mass and spring constants should be defined with respect to another quantity then the tip displacement and velocity amplitudes, as when they are defined this way, they will diverge for those *non-resonant* frequencies at which the tip amplitude is zero.

In the literature (see, e.g., Refs. [1, 3, 2, 4, 119, 121]), another approach is often taken, when the spring constant defined with respect to the displacement of the free end under *static deflection*, $k_{\text{stat}} = EWT^3/4L^3$, is used, and the effective mass is calculated from Eq. 1.30. For the fundamental flexural mode, this yields $m_{\text{eff}}^{\text{stat}} = 0.2427\rho WTL$, which is only 3% off compared to the value given by the dynamic theory, and therefore in reasonably good agreement. However,

it is impossible to use the same approach for higher harmonics, as in that case the spring constants defined with respect to the displacement amplitude of the free end differ dramatically from the static one. Of course, for extreme cases of higher harmonics, the Euler-Bernoulli theory itself ceases to be valid, as shear deformation will become more and more important and eventually, one might need to use Timoshenko theory [124, 125, 126] or other modifications of the basic Euler-Bernoulli model.

Having described the basic mechanics of the tuning fork, it is natural to turn to the interaction of the tuning fork with its surroundings. A detailed hydrodynamical model is presented in [121], together with the links between the mechanical and electrical properties of the tuning fork and a procedure enabling its self-calibration utilising its I-V characteristics measured in vacuum. The presented model describes the effects of the medium on the resonant frequency, f_0, and the linewidth, Δf, of the tuning fork in terms of the inertia and viscosity of the surrounding fluid, in the limit where the both the oscillation amplitude and the viscous penetration depth is much lower than the size of the oscillator. The principal results for the resonant frequency and linewidth are listed below:

$$\left(\frac{f_{0\mathrm{vac}}}{f_0}\right)^2 = 1 + \frac{\rho}{\rho_\mathrm{q}}\left(\beta + B\,\frac{S}{V}\sqrt{\frac{\eta}{\pi\rho f_0}}\right), \tag{1.33}$$

$$\Delta f = \Delta f_\mathrm{vac} + \frac{1}{2}\sqrt{\frac{\rho\eta f_0}{\pi}}\,\mathcal{C}\,S\,\frac{(f_0/f_{0\mathrm{vac}})^2}{m_\mathrm{eff}}, \tag{1.34}$$

where the index "vac" signifies values of the quantities as measured in vacuum, ρ and ρ_q are the densities of the surrounding fluid and of quartz, respectively, η is the dynamic viscosity of the fluid, S and V are the surface and volume of a single prong of the tuning fork, and finally β, B, and C are geometry dependent parameters, usually determined by fitting the experimental data with these functions. From these equations it follows that the tuning forks, if calibrated, can be used to measure the density and viscosity of a surrounding *non-conducting* medium, and by extension, to measure temperature or pressure, if the relevant dependencies are known.

Recently, models describing the losses due to sound emission in compressible fluids have also been developed, these can be found in Ref. [4], which is also included in Appendix A as attachment A4. The main result of this analysis was that the power lost due to acoustic emission has a steep frequency dependence, between ω^5 and ω^6, and given the typical dimensions of the commercial tuning forks, it turns out to be important only if they oscillate at frequencies higher than about 50-60 kHz, or if they are placed in a extreme low-friction environment, such as "pure superfluid" below 0.5 K. As the viscous drag in superfluid He II drops rapidly with temperature, while the losses due to acoustic emission tend towards a constant value, it may happen that even the standard tuning forks resonating at 32 kHz will experience a non-negligible "acoustic drag" at very low temperatures, as is discussed in detail in the mentioned Ref. [4] (A4).

1.5 Previous Works with Oscillators in Cryogenic Helium

Here, we will summarize the published knowledge on the behaviour of oscillating bodies immersed in helium liquids starting from the early experiments. More attention will be devoted to ^{4}He than ^{3}He, as it represents the majority of the work related to this Thesis.

It is hardly possible to discuss experiments with oscillators in cryogenic ^{4}He without mentioning at least briefly the investigations of Andronikashvili [44, 45]. He used a stack of thinly spaced discs as a torsional oscillator in order to determine the fraction of the liquid density that would enter rotation together with the discs, as any viscous fluid caught in the spaces between the discs would. By measuring the natural frequency of oscillations both above and below the transition to superfluidity, it was possible to determine experimentally the fractional densities of the two components similarly as they are plotted in Fig. 1.4, assuming that the superfluid component did not enter into motion and contribute to the total inertia. This experiment was key in establishing the two-fluid model, as we use it today.

In the 1950's, Andronikashvili's work was continued by Benson and Hollis Hallett [127, 128] who performed experiments with discs and spheres undergoing decaying torsional oscillations. The amplitude dependence of the logarithmic decrement showed two plateaus, and hence two critical amplitudes were determined. Below the lower one, the flow of the normal component was assumed to be fully laminar, with the superfluid component at rest, and above the higher one, both components were assumed to participate in turbulent flow. For the intermediate regions, explanations were proposed in terms of entrainment of the superfluid component, but its precise meaning remained unclear. Donnelly and Penrose used oscillations of He in a U-tube [129] to determine its viscosity as well as the logarithmic decrements, arriving at similar conclusions. All these experiments were further analysed by Hallett and Donnelly in Ref. [130], where they suggest a dimensionless parameter to characterise the flows of He II.

A pioneering work on quantized vorticity was performed with an oscillating string by W.F. Vinen [87, 88], giving the first proof of the existence of quantized vortices in He II. When the string captured a quantized vortex, its natural resonant mode changed into a circularly polarized one due to the Magnus force, and a shift in the resonance frequency was observed. This measurement provided evidence of single vortex trapping events and led to the experimental confirmation of the value of the circulation quantum $\kappa = h/m_4$.

Another set of experiments investigated the laminar drag due to the helium liquids and its eventual crossover to ballistic drag at low temperatures. Originally, this crossover was investigated by specific heat measurements [131, 132], using electron bubbles and positive ions [133, 134, 135]. Later, macroscopic oscillating bodies were used as well, and the results were confirmed with vibrating wires in ^{4}He [136] and ^{3}He [137]. Recently, a similar measurement was performed by Niemetz and Schöpe using a microsphere [96, 97] in He II. For their results, see also Fig. 1.9, which confirms the expected temperature dependence of the ballistic drag force acting on hard macroscopic bodies, $F_B \propto T^4$.

Classical and quantum cavitation is also often investigated using various os-

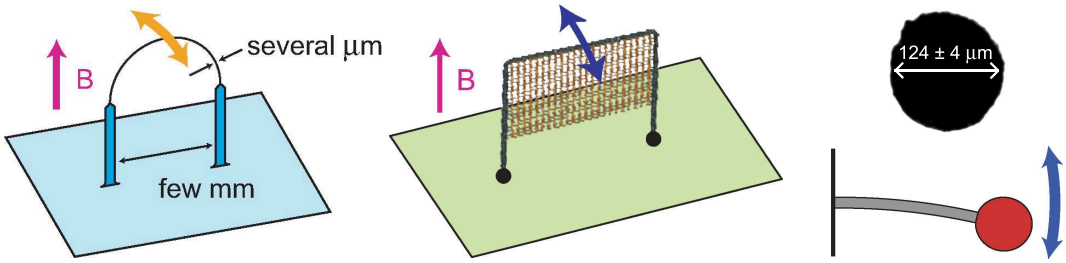

Figure 1.21: From left to right: (i) Sketch of a vibrating wire resonator, (ii) sketch of a vibrating grid, (iii) oscillating spheres – micrograph of the levitated sphere from the work of Niemetz and Schöpe [96, 97] after digital noise suppression, and a sketch of the cantilevered sphere used by Luzuriaga [153].

cillators, be it plane capacitors [138, 139, 140], tubular transducers [141, 142] or hemispherical sound generators [143] that are useful to study homogeneous cavitation in the liquid bulk. For a review, see Ref. [144]. Quartz tuning forks have been used in these studies as well and it was shown [9, 10] that they can create and detect heterogeneous cavitation occurring near their surface.

The most important class of experiments to be mentioned here is, however, related to investigations of classical and quantum turbulence, and perhaps even more specifically, its onset. A large scale of different oscillators have been used: (i) vibrating wire resonators (usually around 1 kHz) [145, 146], (ii) vibrating grids (typically 1 kHz) [147, 148, 149, 150, 151], (iii) oscillating spheres (100 Hz - 1 kHz) [96, 97, 152, 153, 154], and (iv) tuning forks (4 - 100 kHz) [1, 2, 3, 155, 156]. These resonators are sketched in Fig. 1.21. It can be argued that all of them have their own advantages and shortcomings with respect to generation and detection of turbulence in helium liquids.

The vibrating wires are small sensitive detectors, which can provide fine resolution at the transition to turbulence, but they are difficult to prepare and are strongly affected by surface roughness and backflow. Out of the family of oscillators, grids can produce the most homogeneous turbulence, but they usually have a comparatively large intrinsic damping and thus a lower quality factor. With oscillating spheres, the most important advantage is clear, they are (almost) perfectly symmetrical bodies and the flow past a sphere can be described theoretically within classical hydrodynamics with good accuracy. Depending on the size of the sphere, the drawbacks may be related again to surface roughness (microspheres), or to an attached cantilever that provides a restoring force to increase the resonant frequency, but also affects the flow. The tuning forks are, on the one hand, very sensitive, but on the other, it is difficult to give an accurate description of the flow they induce. Their high resonant frequency makes them more practical as it is not necessary to wait so long for each data point (especially in vacuum), but it can also lead to significant sound emission, which acts as a nuisance damping making the use of some tuning forks for the studies of other dissipation mechanisms difficult at very low temperatures. So far, transition to turbulence has been studied successfully using all these types of oscillators, but the one thing that remains to be done is the formulation of a generally valid model or theory that would explain the transition to both classical and quantum turbulence in all these oscillatory flows including the velocity dependence of the

measured drag forces, in the whole range of available temperatures, i.e., from 4.2 K down to tens of millikelvin attainable in a dilution refrigerator.

Lately, new developments in the fields of micro- and nano-fabrication have led to the increasing popularity of tiny oscillators with their typical dimensions in the micrometer range and below. These may include tiny cantilevers [157], or wires in the form of goal-post oscillators [158, 159, 160, 161] and other miniature sensors ranging in resonant frequencies from 10 kHz to and beyond 1 MHz. These may provide unprecedented spatial as well as temporal resolution and an excellent sensitivity to external perturbations, but require extremely sensitive electronics to operate, and the very smallest structures often exhibit intrinsic non-linearities (present even in vacuum), which somewhat complicate the interpretation of the measurements.

A different type of oscillators can be used to generate and detect second sound. If second sound is not driven and detected by a heater/thermometer pair, one might use gold-plated Nuclepore membranes. Their micron-size pores allow the superfluid component to pass almost freely, but normal component cannot do the same due to its viscosity. If such a membrane is made into an electrode of a capacitor, it can either be driven by ac voltage or its motion can be detected by measuring the voltage induced. These are useful for measurements of vortex line density above 1 K in ^{4}He and can be used efficiently to study the transition to turbulence in counterflow or superflow channels [162, 163, 164, 165, 166].

In ^{3}He, oscillators such as wires and tuning forks have been used successfully as secondary thermometers [121, 167], as the drag force acting on them is proportional to the density of thermal excitations, which is an exponential function of temperature. This guarantees a good sensitivity with sub–μK resolution even below 0.2 T_C. In the ballistic regime of propagation of the thermal excitations, these oscillators are then used as probes detecting the intensity of the beam of excitations going out from a region of elevated temperature. This type of measurement can also be used to determine the amount of quantized vortices (usually generated by another oscillator, or simply present due to uniform rotation of the sample) in the path of the beam, as a part of excitations undergoes Andreev scattering upon entering near the vortices, see Chapter 5. It is even planned to create a "screen" composed of multiple tuning forks that would allow performing a low-resolution visualization of a vortex tangle.

With this broad spectrum of available experimental tools and their applications in mind, in the next two Chapters we will concentrate only on a narrow subset of experiments with quartz tuning forks in cold helium gas, normal and superfluid ^{4}He, above 1.3 K, performed in the Laboratory of Superfluidity in Prague with the aim to investigate the transition to turbulence in these cryogenic fluids.

2. Transition to Turbulence in Classical Fluids

Within classical nonrelativistic fluid dynamics, the motion of Newtonian viscous fluids is described by a closed set of equations consisting of the mass conservation law (equation of continuity), entropy evolution law (typically expressed as entropy conservation, neglecting thermodynamically irreversible dissipative phenomena), and the dynamic equation – the general Navier-Stokes equation for compressible fluids. These equations are usually written down as follows [7]:

$$\frac{\partial \rho}{\partial t} + \nabla \cdot (\rho \vec{u}) = 0, \tag{2.1}$$

$$\frac{\partial (\rho s)}{\partial t} + \nabla \cdot (\rho s \vec{u}) = 0, \tag{2.2}$$

$$\rho \left[\frac{\partial \vec{u}}{\partial t} + (\vec{u} \cdot \nabla)\, \vec{u} \right] = -\nabla p + \eta \Delta \vec{u} + (\zeta + \eta/3)\, \nabla \nabla \cdot \vec{u} + \vec{G}, \tag{2.3}$$

where ρ is the fluid density, $\vec{u}$ denotes the fluid velocity, s stands for the specific entropy, p corresponds to the pressure, η, and ζ mark the dynamic viscosity and the second viscosity coefficient, respectively, and finally $\vec{G}$ comprises all volume forces acting on the fluid. Fortunately, the mathematical description is simplified significantly, if the flow in question can be considered isentropic and incompressible. This is typically the case for many viscous flows past a bluff body, including the experiments described further in this Chapter. If we also neglect the effect of other volume forces (including gravity), the above equations reduce to the following form:

$$\rho = const., \tag{2.4}$$

$$s = const., \tag{2.5}$$

$$\nabla \cdot \vec{u} = 0, \tag{2.6}$$

$$\frac{\partial \vec{u}}{\partial t} + (\vec{u} \cdot \nabla)\, \vec{u} + \frac{\nabla p}{\rho} = \nu \Delta \vec{u}, \tag{2.7}$$

where the velocity field is fully determined by the last two equations only, i.e., the equation of continuity and the Navier-Stokes equation for incompressible fluids, in which $\nu = \eta/\rho$ stands for the kinematic viscosity.

It is often convenient to express the Navier-Stokes equation in its dimensionless form. To do so, we define $\vec{u'} = \vec{u}/U$, $\nabla' = L\nabla$, i.e., we rescale all velocities by the magnitude of the main stream velocity U, and all lengths by the characteristic length at which the velocity field may change (typically the size of the body), L. Then, the dimensionless pressure will be given as $p' = p/(\rho U^2)$. This would already be sufficient to formulate a dimensionless equation governing steady flows. However, if oscillatory flows are to be described as well, it is also necessary to rescale the time derivative in the first term independently by a characteristic time in which the flow field changes significantly, e.g., the period of the oscillations, τ.

This gives us $\partial/\partial t' = \tau\,\partial/\partial t$, and the resulting dimensionless dynamic equation can be written as:

$$\frac{L}{\tau U}\frac{\partial \vec{u'}}{\partial t'} + \left(\vec{u'}\cdot\nabla'\right)\vec{u'} + \nabla' p' = \frac{\nu}{UL}\Delta'\vec{u'};\ \text{or} \tag{2.8}$$

$$\frac{1}{St}\frac{\partial \vec{u'}}{\partial t'} + \left(\vec{u'}\cdot\nabla'\right)\vec{u'} + \nabla' p' = \frac{1}{Re}\Delta'\vec{u'}, \tag{2.9}$$

defining the dimensionless Reynolds and Strouhal numbers, $Re = UL/\nu$, and $St = U\tau/L$, respectively. Please note that in oscillatory flows, the meaning of U, changes from the main stream velocity to the mean flow velocity amplitude.

The dimensionless parameters Re and St determine the ratios of the (red) viscous dissipation term and the (green) non-stationary term to the (blue) inertial terms. Given this mathematical description of the flow, a principle of *dynamical similarity* can be formulated, stating that two oscillatory flows past bodies of identical shape (but differing in size), are *dynamically similar*, i.e., governed by the same dynamic equation, if the two corresponding sets of dimensionless parameters (Reynolds and Strouhal numbers) are the same, see also Ref. [7]. Whether a given flow will be laminar or turbulent then depends on the combination of these two numbers. Leaving aside possible flow hysteresis or history dependence, the stability criteria of laminar flows past various bodies can be expressed as curves in the Re–St plane.

In the available literature on classical oscillatory flows past cylinders [168, 169, 170, 171, 172], it is customary to employ a different, but equivalent, description, and to characterise the flows using another set of two dimensionless numbers – the Keulegan-Carpenter number, K_C, and the Stokes number, β. Their definitions are given below:

$$K_C = \frac{2\pi x_0}{D}, \tag{2.10}$$

$$\beta = \frac{\omega D^2}{2\pi\nu} = \frac{1}{\pi}\frac{D^2}{\delta^2}, \tag{2.11}$$

where x_0 is the amplitude of oscillations, D is the characteristic dimension of the body, ω stands for the angular frequency of oscillations, and $\delta = \sqrt{2\nu/\omega}$ is the penetration depth of viscous oscillatory flow (or thickness of the viscous boundary layer near the oscillating body). For a given value of the Stokes number, the transition to turbulence then occurs at some critical value of the Keulegan-Carpenter (K-C) number, and the curve separating the stable laminar and the turbulent flows (not necessarily stable immediately above the critical amplitude of oscillation) can be then expressed as a function $K_C^{\text{crit}}(\beta)$.

In the cryogenic experiments with tuning forks, the measured quantity which we used to characterise the flow is the drag force acting on the prongs of the tuning fork. In laminar oscillatory viscous flow, the amplitude of the drag force, F_0, acting on the prongs is given by a modification of the Stokes solution for a sphere (see, e.g., Ref. [7]), where the limit $\delta \ll D$ is taken, i.e., the viscous penetration depth is considered to be much smaller than the dimensions of the oscillating body (corresponding to $St \gg 1$, which is well satisfied for quartz

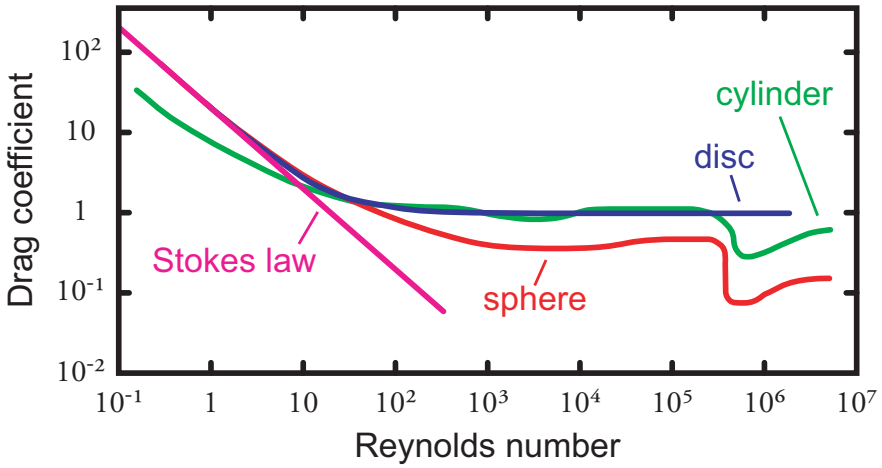

Figure 2.1: Drag coefficient of a sphere, cylinder and flat disc in steady flow plotted versus the Reynolds number and compared to the Stokes law for viscous flow around a sphere. The laminar part is clearly identified by the dependence $C_D \propto Re^{-1}$, while in turbulence $C_D \approx const.$, until the drag crisis at $Re \approx 4 \cdot 10^5$ occurs. The cause of the drag crisis is not yet fully understood, but it is usually attributed to the boundary layer becoming turbulent, which results in a shift of the separation point and consequently a narrower turbulent wake behind the bluff body.

tuning forks). Under these assumptions, the laminar drag force can be written down as:

$$F_0^{\mathrm{lam}} = \alpha S \sqrt{\rho \eta \omega}\, u_0, \tag{2.12}$$

where u_0, is the velocity amplitude, S stands for the surface of the body, and α is a constant of order unity depending on the exact geometry of the oscillator. In analogy to steady flows, The drag force amplitude in turbulent oscillatory flows is typically expressed as:

$$F_0^{\mathrm{turb}} = \frac{1}{2} C_D A \rho\, u_0^2, \tag{2.13}$$

where A is the cross section of the body normal to the flow (to the direction of oscillation), and C_D is the drag coefficient determined by the geometry of the body, again of order unity in turbulent flows (unless the drag crisis is reached at very high flow velocities). For purposes of comparison, the drag coefficient C_D is sometimes evaluated in laminar flows as well, by substituting F_0^{lam} for F_0^{turb} in the above Eq. 2.13. In that case, it is found to be inversely proportional to the laminar flow velocity amplitude:

$$C_D = 2\alpha \frac{S}{A} \sqrt{\nu \omega}\, u_0^{-1}. \tag{2.14}$$

Typical dependences of the drag coefficient on the Reynolds number in steady flows are shown in Fig. 2.1. Using a similar plot, the transition to turbulence may be determined in several different ways. For example, one might simply try to find an intersection of straight lines corresponding to laminar and turbulent flow, which would be equivalent to claiming that at the transition, the two drag

forces must be equal. While this approach is rather straightforward, it need not always yield the most relevant results, as in this way, the critical velocity (or Reynolds number, or K-C number) is found to lie near the middle of the transition region. Therefore, it corresponds to a flow, where strong deviations from the laminar case are already present. In a more careful approach, one might consider a given threshold for the deviation from the laminar drag (e.g., 5% deviation), which would result in the determined critical velocities (or other flow parameters) corresponding more closely to the actual onset of turbulence, specifically to the first instabilities appearing. In analysing the experimental data presented below, both of these methods were used, and their results were compared.

Finally, it is useful to provide at least rough estimates of the critical flow parameters for the transition to turbulence in oscillatory flows. Using the rough approach of equating the drag forces, as outlined above, one may find the two (equivalent) analytical expressions for the critical velocity and the critical K-C number:

$$u_0^{\mathrm{crit}} = 2 f_g \sqrt{\nu\,\omega}, \tag{2.15}$$

$$K_C^{\mathrm{crit}} = \sqrt{8\pi} f_g\, \beta^{-1/2}, \tag{2.16}$$

where $f_g = \alpha S/(C_D A)$ is generally a geometry-dependent factor, in which C_D refers to the constant value of the drag coefficient corresponding to developed turbulent flow, not the one extended to laminar flows by Eq. 2.14.

It should, however, be kept in mind that while these estimates may be useful, e.g., to determine the parameters of an experiment aiming to study the transition to turbulence, they are by no means a precise determination of the flow (in-)stability. They merely mark the approximate region of flow velocities, at which the crossover from laminar to turbulent flow can be expected to occur, and certainly, a more detailed and precise treatment would be necessary to derive any conclusions about the stability of the laminar flow. On the other hand, it is, of course, possible to take these as a starting point and try to verify experimentally, whether the estimated critical parameters are at least roughly correct, or to see whether the expected scaling of the critical velocity with frequency and kinematic viscosity indeed holds.

As an alternative hypothesis for comparison, we suggest considering the Honji instability of the boundary layer around oscillating *circular* cylinders [168, 169, 170]. In this case, it is predicted in Ref. [169] that in the limit of high Stokes numbers, the critical K-C number will scale as $K_C^{\mathrm{crit}} \propto \beta^{-1/4}$, which was verified experimentally in Ref. [170].

2.1 Drag Force Measurements with Tuning Forks

To verify the expected scaling of the critical velocities in the largest possible range of the parameter $\sqrt{\nu\,\omega}$, we used not only liquid He I as a working fluid, but also pressurized cold helium gas at LN_2 temperature (77 K). Additionally, tuning forks resonating at three different frequencies were used, in this case 4 kHz, 8 kHz and 32 kHz. The tuning forks were placed inside a pressure cell, which was indium-sealed and then filled with the desired working fluid. One of the

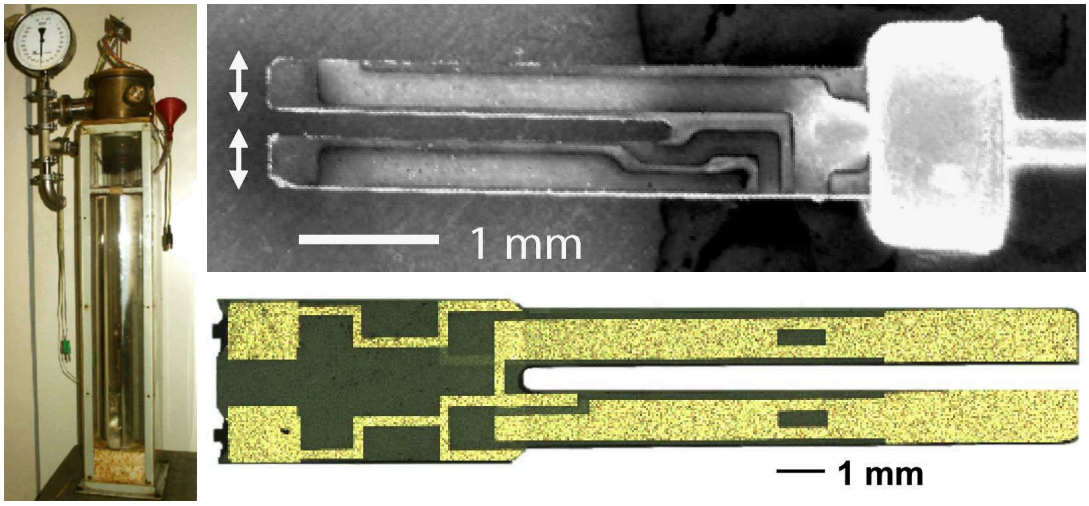

Figure 2.2: Photo of the glass cryostat used (left), micrograph of the 32 kHz tuning fork (top) and photo of the 4 kHz tuning fork (bottom).

advantages of using cryogenic helium (apart from its extremely low kinematic viscosity) is that the experimental conditions can be easily changed *in situ*. For example, it is easy to begin with measurements in pressurized He gas at 77 K (the cell was designed for safe operation up to 35 bar), gradually reduce the pressure, then cool down to LHe temperature and continue the measurements in He I liquid, or in cold He vapour, and finally, to pump the cell to measure the vacuum response of the tuning forks, which is required for calibration. These experiments and their results are also summarized in Refs. [1, 2], included in Appendix A as attachments A1 and A2.

In practice, the measurements in He gas at 77 K and the measurements at and below 4.2 K were usually split between different runs, and special care was taken to ensure that during any given run, the amount of He inside the cell was reduced when changing the pressure/temperature, and never increased, as that might result in impurities being introduced from the room temperature part of the pressurizing system. The experimental protocol was to measure the full resonance curves of the tuning forks, and using the calibration procedure described in Ref. [121], to convert the driving voltage and the resonant current amplitude into the driving force and tip velocity amplitudes, respectively. An impedance-adapted step-up transformer and an attenuator were employed to increase the dynamic range of the drive provided by the Agilent Waveform Generator, resulting in 7 orders of magnitude of the driving force available. For detection, an SR-830 lock-in amplifier was used in voltage mode – the signal from the tuning forks was fed through a current divider and the voltage was measured across a 1 kΩ resistor. Temperature was determined either taking advantage of the boiling points of cryogenic liquids (He, N_2), or from saturated vapour pressure of LHe inside the used glass cryostat, which was determined by high-precision analogue or digital pressure-meters and converted to temperature using either Ref. [90] or the HEPAK software [173, 174]. The cryostat and two of the tuning forks are shown in Fig. 2.2.

The measured force-velocity dependence of several tuning forks is plotted in Fig. 2.3. Linear and approximately quadratic regions of the drag force can be

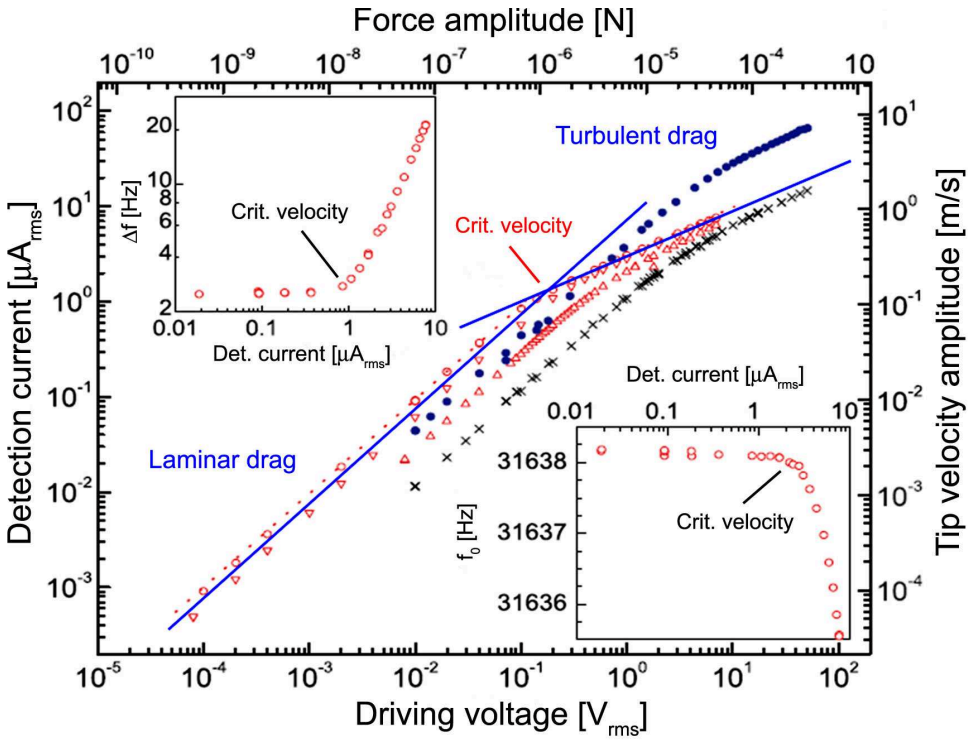

Figure 2.3: Response current vs. driving voltage dependence (left and bottom axes), obtained with a tuning fork at different temperatures and pressures in He, calibrated to velocity vs. force amplitudes (top and right axes). In the main panel, spanning 6 orders of magnitude of the driving force and 5 orders of magnitude of the tip velocity, the transition between linear (laminar) and quadratic (turbulent) drag force is evident. The insets show the observed behaviour of the resonant frequency (bottom-right) and linewidth (top-left) at the transition to turbulence. The method of extracting the critical velocity by equating the drag forces is equivalent to finding the intersection of the two straight lines as indicated.

identified reliably, suggesting that transition to turbulence is indeed observed (as was later confirmed by room temperature visualization of dynamically similar flows, see Section 2.2. The middle region, however, shows that the transition happens to be rather smooth and that the extraction of a definite value of the critical velocity might not be straightforward. The same conclusion can be made from the drag coefficient plots presented in Fig. 2.4.

Therefore, two independent methods of determining the critical velocities have been used. First, the critical velocity was determined from equating the laminar and turbulent drag forces, which corresponds to finding an intersection of the two straight lines in Fig. 2.3 or analogically in Fig. 2.4. The results are plotted in Fig. 2.5 in both linear and logarithmic axes. When the critical velocity is determined in this manner, it is perhaps of little surprise that the expected scaling $u_0^{\mathrm{crit}} \propto \sqrt{\nu\,\omega}$ is confirmed in the entire experimental range, spanning three orders of magnitude of $\sqrt{\nu\,\omega}$, with the kinematic viscosity alone varying by a factor in excess of 100. While this result perhaps bears little significance for general theories of turbulence, as the said scaling law can be found from trivial manipulations of the basic equations for the drag forces, the true meaning of the presented evidence lies in the fact that the mentioned scaling was indeed verified

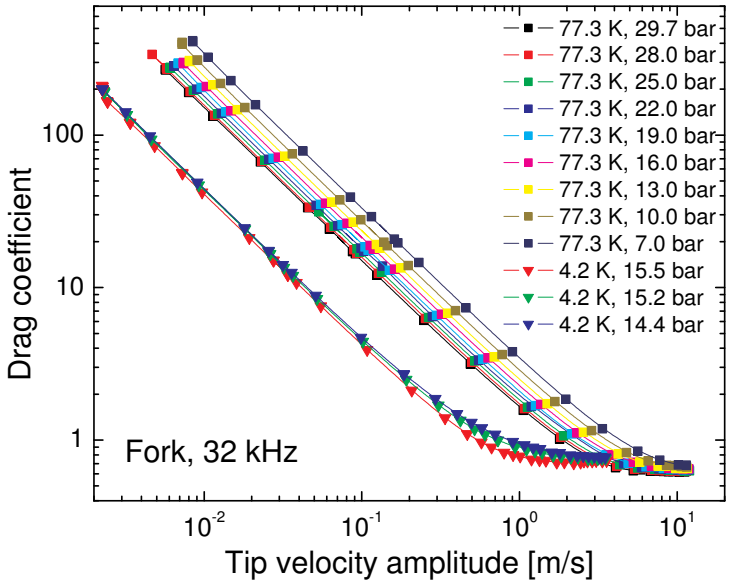

Figure 2.4: Velocity dependence of the drag coefficient obtained in a series of measurements with a single 32 kHz tuning fork in He at the listed temperatures and pressures. The laminar and turbulent regions corresponding to $C_D \propto u_0^{-1}$, and $C_D \approx const.$, respectively, can be identified clearly (although the data do not extend far into the turbulent regime). In this case, the rather smooth transition occurs at about 1 m/s in He I at 4.2 K, while in He gas (or supercritical He, if the reader prefers) at 77.3 K, the critical velocity is about 6 m/s and is found to be weakly pressure dependent, due to the change of kinematic viscosity with density (and thus with pressure). On a side note, at 4.2 K, only results from considerably pressurized liquid are shown for a good reason, other than mere suppression of boiling in helium. Unless a considerable overpressure was applied, the tuning forks vibrating with tip velocities of several metres per second caused cavitation [9, 10] inside the liquid contained in the pressure cell.

experimentally and found to be correct in a very wide range of flow parameters (hardly attainable using air, water or other common fluids), at the same time demonstrating the vast potential of cryogenic systems in classical fluid dynamics research.

Nevertheless, in terms of physics, it is perhaps more interesting to look at the critical parameters corresponding more closely to the first instabilities in the flow. To estimate the critical values of the flow parameters, we established a criterion of 5% deviation from the laminar drag. This criterion is illustrated and compared to the original simpler method of determining the critical parameters in Fig. 2.6, plotting the drag coefficient C_D versus the K-C number (proportional to the amplitude of oscillation, and therefore, to the velocity). The critical value determined by equating the drag forces is labeled K_C^{crit}, while $K_C^{\mathrm{crit}}(0.05)$ denotes the one obtained using the 5% deviation criterion.

It is evident that the critical K-C number determined this way is highly sensitive to the scatter of the data in the laminar range and at the transition, which are rarely obtained as smooth as in the case shown in Fig. 2.6 for illustration. In practice, the critical K-C numbers could be determined in this way with a

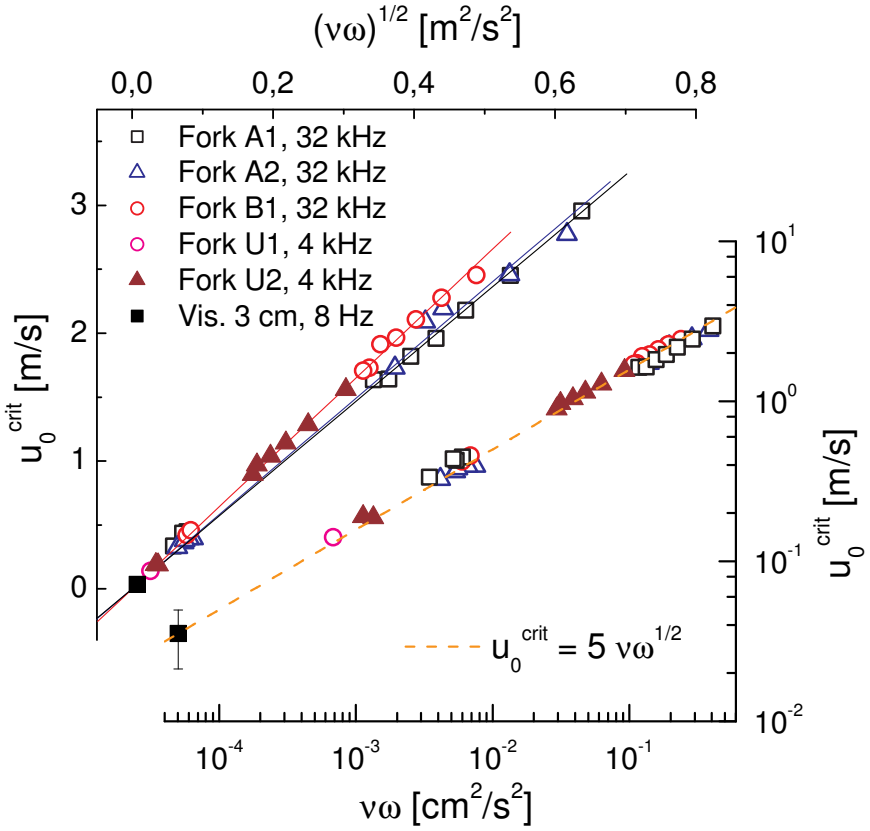

Figure 2.5: Critical velocity determined by equating the drag forces, as measured under varied conditions using multiple tuning forks, including the 32 kHz variety (A, B forks) as well as two 4 kHz forks labeled U1 and U2. A single point from room temperature visualization (see below in Section 2.2) is added for comparison. The upper-left part of the graph illustrates the confirmed scaling law in linear axes, the ordinate being $\sqrt{\nu\,\omega}$. Slightly differing slopes are obtained for different tuning forks, indicating that the exact geometry of the oscillator may have some, albeit limited, significance. In the lower-right part, the same set of data is plotted in logarithmic axes (the ordinate is now $\nu\,\omega$ only) to confirm the power law exponent. By fitting a straight line through the experimental data, one obtains 0.48 ± 0.04, which is in very good agreement with the expected slope of $1/2$.

reasonable degree of accuracy in the whole range of velocities only for two of the tuning forks used. These data are shown in Fig. 2.7 and compared to the critical K-C number obtained using the first discussed method. For other tuning forks, $K_C^{\mathrm{crit}}(0.05)$ could be determined as well, but the resulting uncertainty was too large for the exact values to represent any significant improvement on the results obtained with the first method.

It is found that this critical K-C number, $K_C^{\mathrm{crit}}(0.05)$ is about three times lower than the one obtained by equating the forces, but it is still in accord with the derived scaling. This can be interpreted in the following manner. Based on the results in Figs. 2.5 and 2.7, we may say with a reasonable degree of reliability that the likelihood of instabilities occurring in the (originally laminar) flow is determined to a large extent by the same control parameter $\sqrt{\nu\,\omega}$, which is important for determining the region where the laminar and turbulent drag forces

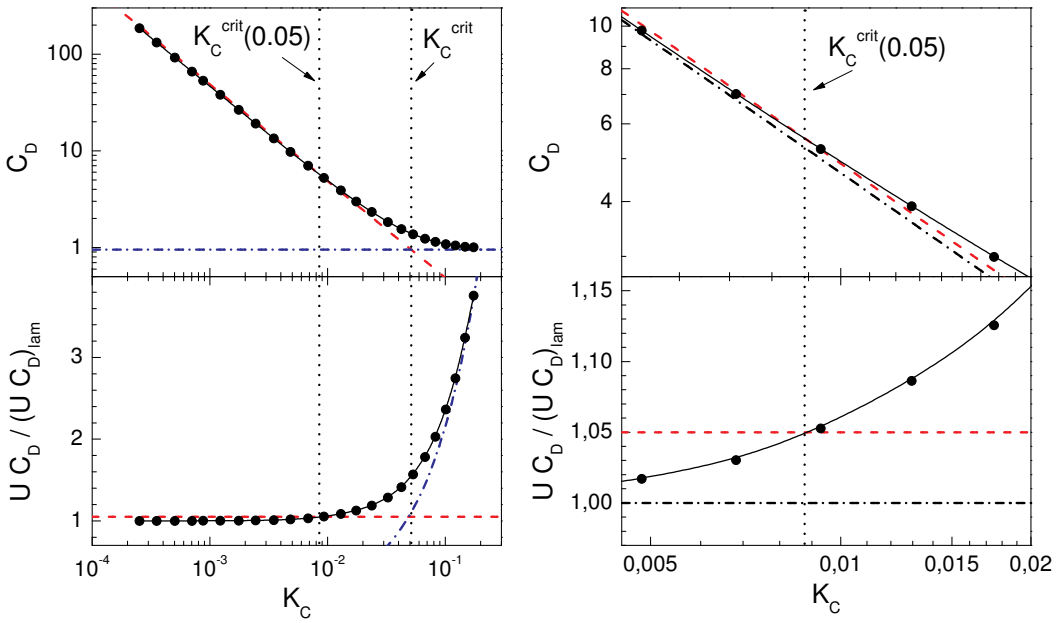

Figure 2.6: An illustration of the two criteria of determining the critical flow parameters (the K-C number, in this case). The upper panels show the plot of the drag coefficient, C_D, versus the K-C number, K_C. In the lower panels, the drag coefficient was multiplied by the tip velocity of the prong and normalized by the value of this quantity in laminar flow. In the left panels, a larger dynamic range is plotted, while the right panels depict the details near the critical K-C number defined using the 5% deviation criterion, $K_C^{\mathrm{crit}}(0.05)$. As one would expect, $K_C^{\mathrm{crit}}(0.05)$ is found to be significantly lower than K_C^{crit}, here they differ by a factor exceeding 5.

are equal. This suggests that in the case of tuning forks, a different instability triggers the turbulent flow than for the mentioned circular cylinders. It might be suspected that the instability is associated with flow past sharp corners/edges of the tuning fork.

However, the exact influence of the geometry and dimensions of the oscillating body on the occurrence of the first instabilities remains unknown. The data plotted in Fig. 2.7 for two different tuning forks seem to be displaced vertically by a factor of 2, but no solid grounds for the explanation of this displacement can be found. However, it turns out that when the critical velocity is determined by equating the drag forces, as in Fig. 2.5, all the data collapse more or less to a single line, suggesting that the geometrical factor f_g in Eqs. 2.15 and 2.16 varies only very little between the tuning forks used, which is indeed the case. It is tempting to say that for these critical velocities, the exact geometry of the oscillator need not be as important as expected, but such a claim cannot be fully justified by the provided data, as it would require a more detailed study where the factor f_g would be known with sufficient precision and the ratio S/A varied, if possible, at least within the better part of an order of magnitude.

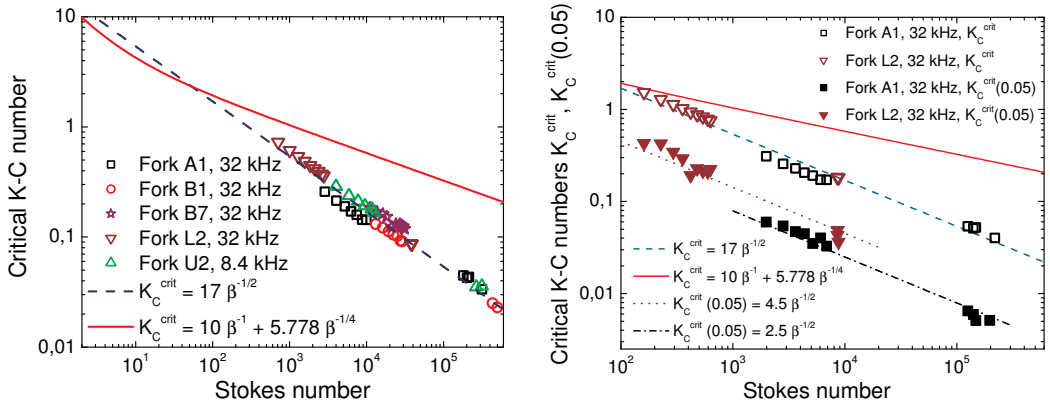

Figure 2.7: Left: Critical K-C number determined by equating the drag forces for a series of different tuning forks. The expected scaling $K_C^{\mathrm{crit}} \propto \beta^{-1/2}$ is reproduced with very good accuracy. Compare with the expected boundary layer instability in Ref. [169] derived a circular cylinder, given as $K_C^{\mathrm{crit}} = 10\beta^{-1} + 5.778\beta^{-1/4}$ and observed in Ref. [170]. Right: Comparison of the frequency dependences of the critical values of the K-C number determined by the two different methods for two selected tuning forks. While $K_C^{\mathrm{crit}}(0.05)$ can be even almost a decade below K_C^{crit} depending probably on the exact geometry of the tuning fork used, the predicted scaling as $\beta^{-1/2}$ is still found to hold, at least for each tuning fork separately.

2.2 Room Temperature Visualization

To gain a better understanding how the measured drag force crossover relates to the instabilities in the flow, and what it may mean for the determined critical velocities, room temperature experiments with oscillating metallic cylinders of square cross-section (shown in Fig. 2.8) were performed under approximately dynamically similar conditions to the cryogenic quartz tuning fork measurements. By "approximate dynamical similarity", we understand that there may be a difference between two prongs in close vicinity undergoing flexural vibrations, and a single solid cylinder oscillating around a fixed point at its base without undergoing any significant deformation.

On the other hand, it could be argued that the presence of two prongs need not be too important for the formation of flow instabilities, because these are most likely restricted to the viscous boundary layer of thickness $\delta \approx 1$ μm around the tuning fork, which is much thinner than the separation of the prongs of about 200 μm. Similarly, one could say that the most important region of the prongs for the generation of the instabilities would be their tips, oscillating at the highest velocity and exhibiting characteristics of 3D flow. In other words, the full information given in the velocity profile along the prong length need not be too important either. If these two claims were correct, the model of the single oscillating cylinder would indeed be a good hydrodynamic equivalent of the tuning fork for the purposes of investigating the first instabilities of the flow, but the final judgment of the degree of veracity of these claims is left to the reader.

Two different visualization methods were employed – first, the oscillating cylinders were studied using the Baker technique [175], and subsequently, the Kalliroscope solution [176] was used for comparison. In both cases, the viscosity

Figure 2.8: The set of cylinders of square cross-section used in room temperature visualization experiments. The sizes of the side of the base used are (from bottom to top) 1 cm, 2 cm, 2 cm (rounded edges), 3 cm, 5 cm. The 3 cm cylinder originally had sharp edges, but later they were trimmed as can be seen here. After the picture had been taken, the sharp-edged 2 cm cylinder had copper filings soldered to it, simulating surface roughness, see Fig. 2.9 for details.

of the (rather dilute) solution was assumed to be equal to that of water. A sketch of the experimental setup is provided in Fig. 2.10. The oscillations of the cylinder were driven by a rod connected to a large bass loudspeaker, to which an amplified signal from a waveform generator was fed, allowing us to change the frequency and amplitude of oscillation easily. Each cylinder had a central rod attached to it, which was used to transmit the drive as well as to record its immediate position using a standard commercial video recorder and a ruler positioned behind the rod. The principal results of the visualization experiments and a comparison with the drag force data obtained using the tuning forks can be found in Ref. [2], included here in Appendix A as attachment A2.

There were several practical limits to these experiments. First, the transition was only observable in a given range of frequencies due to the fact that the critical velocity was found to increase with the square root of frequency as expected. Above a certain frequency (still of order Hz or 10 Hz) the drive was no longer powerful enough to provide the necessary amplitude/velocity of oscillation, which resulted in a limitation of the exploitable frequency range. Higher frequencies were also limited due to the connection of the cylinder via the thin metal rod. Above 10 Hz, the rod no longer acted as a solid body, but started displaying its own resonant flexural modes. Yet another factor limiting higher frequencies is the 25 Hz framerate of the camera, although it can be, and was, improved to double its value by deinterlacing the recorded video frames – splitting them into even and odd lines and evaluating separately. This is possible, because for technical reasons, the two sets of lines in the frame are recorded with a relative time shift

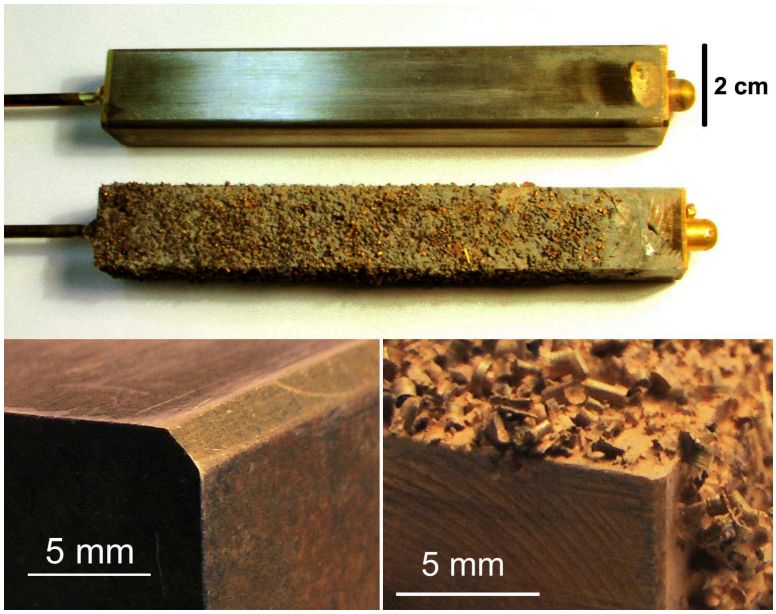

Figure 2.9: Bottom left: Photograph of the trimmed edge of the 3 cm cylinder after the second trimming, referred to as r=2.2 mm in Fig. 2.12. The edge is not replaced by an exact circular arc, instead it is flattened at an angle of 45° and ground smooth. The given value of the radius was determined only approximately. Bottom right: Detail of the rough surface simulated by soldering copper filings to the original 2 cm cylinder. Top: Comparison of the rough and smooth 2 cm cylinders.

corresponding to half the time between two consecutive frames.

The experimental protocol was as follows. The cylinder was oscillated at a given frequency starting from very low amplitudes. At each fixed amplitude, the cylinder was first set into motion, then after some time for stabilization, DC voltage was applied on the surface of the cylinder respective to the electrodes placed at the sides of the tank. This started the reaction crucial for the Baker technique, resulting in a dark blue "ink" being generated in the vicinity of the cylinder. It was then determined subjectively by the observer, whether the ink follows a laminar flow pattern or whether instabilities are present. When using Kalliroscope, of course, no voltage was necessary, and the observations were made based on the motion and orientation of the tiny flat particles suspended in the solution. Finally, the drive of the cylinder was switched off (as well as the DC voltage bias for the Baker technique) and a waiting time of order 1 minute was imposed to let the fluid motion relax, before continuing with a higher amplitude of oscillation. In the measurements of the data presented below, the observer was always the same person, namely our student, Veronika Pilcová, to reduce the ambiguity resulting from subjective observation as much as possible. The instabilities were observed occurring first near the tip of the cylinder, within 0.5–1 cm from its top almost all the time, and later extending downwards. They usually had the form of thin irregular vortices stretching away from the cylinder, see Fig. 2.11.

Once the critical value of the driving voltage for the formation of instabilities was found at a given frequency, the cylinder was oscillated at this amplitude

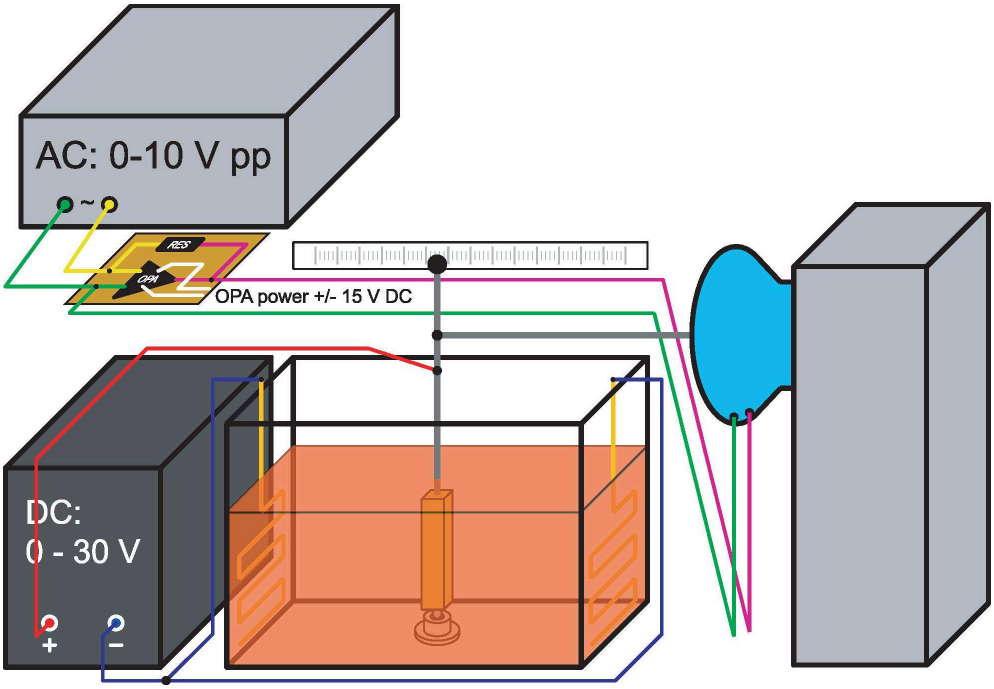

Figure 2.10: The setup used for room temperature visualization experiments employing the Baker technique [175]. The oscillating cylinder was fixed at its bottom end by a spherical knob fitting into a teflon holder, while its upper base was connected via thin metallic rods to the large bass loudspeaker providing the mechanical drive. The signal from a standard Agilent Waveform Generator at frequencies between 1 and 12 Hz was amplified and fed to the speaker, which converted it to mechanical oscillations with a maximum amplitude of about 1 cm. The upper end of the central rod of the cylinder was also used for recording the position with a digital video camera (not shown). A DC bias voltage of 10-15 V was applied on the cylinder respective to the electrodes located at the sides of the tank filled with the Baker solution (consisting of demineralized water, HCl, NaOH, and thymol blue pH indicator) to start the desired electrochemical reaction. When the voltage was switched on, the surroundings of the cylinders became locally slightly more alkaline due to the attracted negative ions, resulting in the pH indicator changing its color locally from orange-red to deep blue. This blue "ink" then followed the local flow patterns and based on observations with the naked eye, it was determined subjectively in each case, whether the flow seems to be predominantly laminar, or whether instabilities are present. For Kalliroscope measurements, the same setup was used, except for the electrodes at the side of the tank and the DC voltage source, which were not needed.

while its position was being recorded by the video camera. The recording was then split into individual frames, deinterlaced, and processed by self-made software, determining the position of the rod in each instant with a sampling rate of 50 Hz. These positions were calibrated against the ruler placed behind the rod, taking into account the angle of observation and the finite distance between the ruler and the rod. The resulting time dependence of the position was fitted with a sine function. Its amplitude then used for the calculation of the critical Keulegan-Carpenter number as defined by Eq. 2.10. It was found during the

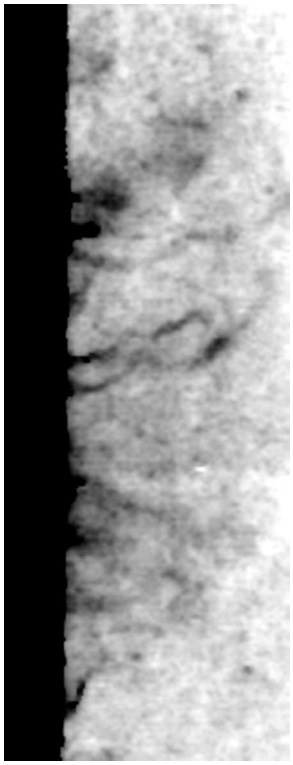

Figure 2.11: Vortex structure observed in turbulent flow around the 3 cm oscillating cylinder. This picture does not correspond to the critical K-C number for that particular situation, it was taken in a turbulent flow that notably exceeds the critical parameters. The vortices marked by the dark colour extend away from the cylinder, forming an irregular structure near its side.

data processing that it is necessary to introduce corrections for the bending of the central rods attached to the cylinders, to determine the amplitude of the top of the cylinder correctly from the amplitude of the top of the rod. This was important especially at higher frequencies (above 10 Hz), as the rods approached their flexural resonance. To arrive at a usable correction procedure, the cylinders were recorded several times in an empty tank (without the solution clouding the image), and a comparison was made between the amplitudes of the rod and the cylinder. This led to an empirically derived power law (in frequency) describing the flexural amplitude of the rod, which was then used to correct the measured amplitudes of the cylinders.

The obtained corrected results are plotted separately in Fig. 2.12 and compared to the results obtained with the quartz tuning forks in cryogenic helium in Fig. 2.13. It is clearly demonstrated that the expected frequency scaling still holds for the oscillating cylinders, moreover, that the values of the critical Keulegan-Carpenter number determined in visualization and for the tuning forks are in good agreement, as the visualization values fall between the critical values determined with the two different criteria from the tuning fork measurements. This allows us to conclude (within the validity of the premises outlined above) that what we measured with the tuning forks as a crossover in the drag force is indeed related to the emergence of turbulent flow patterns, and that the original instabilities occur at critical velocities which scale as $u_0^{\mathrm{crit}} \propto \sqrt{\nu\,\omega}$ within the large available range

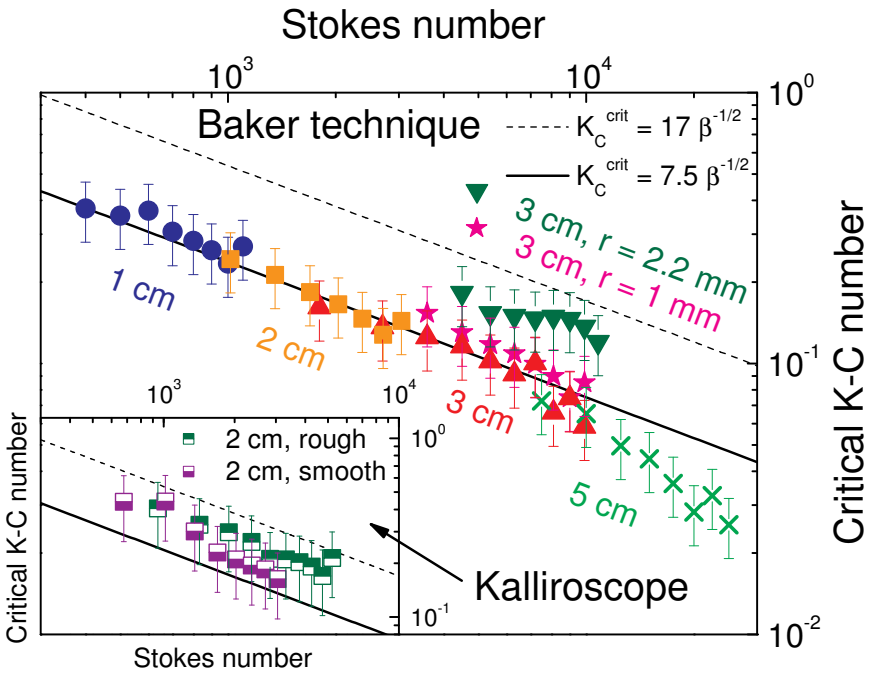

Figure 2.12: Critical Keulegan-Carpenter numbers obtained for the cylinders of square cross-section of the indicated dimensions using the Baker technique [175] and Kalliroscope [176]. In the main panel, the results from the Baker technique are shown, while the inset plots Kalliroscope data for the 2 cm cylinder. The effect of trimming the edges is evident from the data measured with the 3 cm cylinder, more rounded edges (roughly of the indicated radius) result in higher critical K-C number, i.e., higher critical velocity, perhaps gradually approaching the expected dependence for the instability of oscillatory flow past a circular cylinder marked with the red solid line. This corresponds well to our previous guess that the initial instability occurs near the sharp edges, where the flow velocity is significantly enhanced. The influence of surface roughness was tested in Kalliroscope, as the corrosive Baker solution did not permit using even gold plated metallic surfaces (remember, the surface has to be conducting). This was caused by the fact that a mixture of a small amount of nitric acid and hydrochloric acid was used for preparing the solution, after the limited laboratory reserves of concentrated HCl were depleted. Unfortunately, this mixture used consists of the same components as the notorious *aqua regia*, hence even gold-plated surfaces would not last (the metallic cylinders were, of course, damaged by the small amounts of acid as well, but compared to the rough 2 cm cylinder, this process was much slower). The measurements in Kalliroscope were somewhat more difficult to interpret due to the significantly lower contrast of the regions of flow with respect to the rest of the solution. Nevertheless, the obtained results agree with those from the Baker technique within a factor of 2, but no significant influence of surface roughness could be determined due to the large scatter.

of flow parameters. Additionally, in the visualization experiments, the influence of sharp edges and surface roughness on the critical parameters for the transition to turbulence was examined qualitatively as well. The cylinders used are shown in Fig. 2.9 and the results are described in the caption to Fig. 2.12.

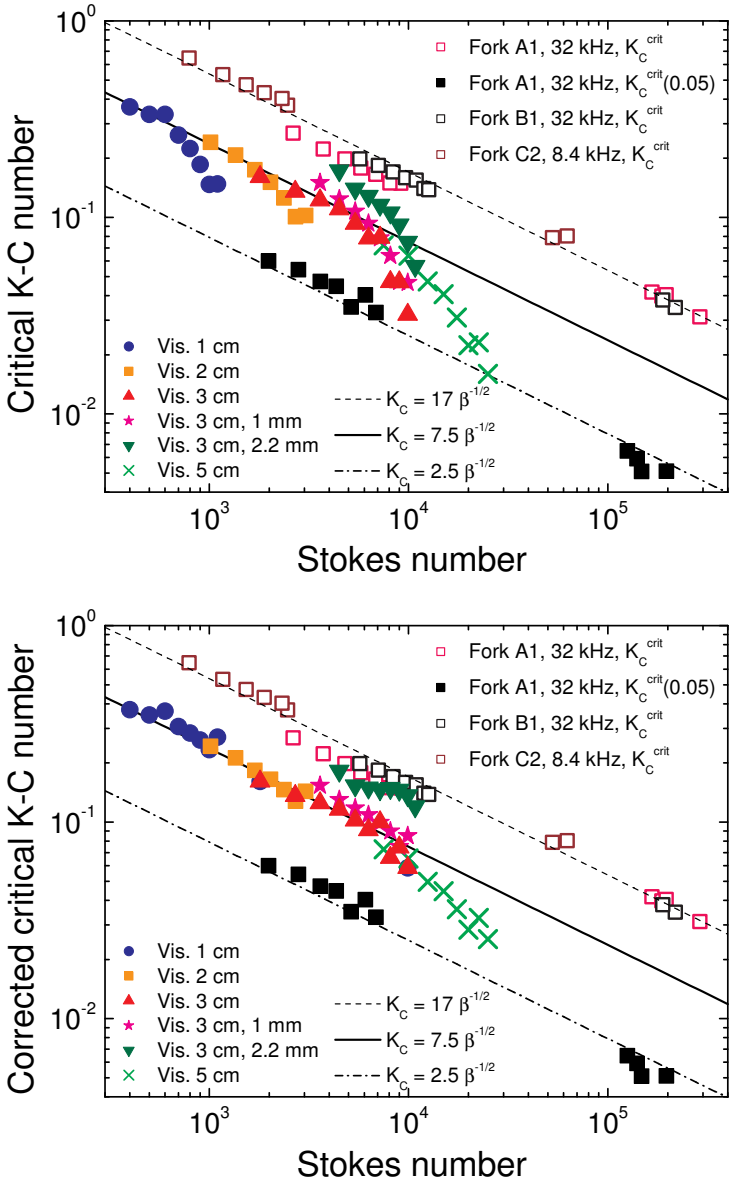

Figure 2.13: Comparison of the critical K-C numbers obtained with Baker technique to those from the measurements of the drag force acting on the tuning forks, determined both by equating the drag forces and using the 5% criterion. The upper panel shows visualization results uncorrected for the flexure of the rod, while the corrected data are plotted in the lower panel. Note that even after the correction, the 5 cm still deviates from the dependence closely followed by the thinner cylinders. Considering the height the cylinders (≈ 14 cm), we attribute this to the flow starting to exhibit 3D behaviour. All visualization observations lie between the critical values of K_C determined for the forks by the two methods, suggesting that a slight discrepancy may exist due to different experimental conditions, or perhaps that the observer cannot register the very smallest initial instabily in the visualization experiments, and notices only an already partly developed structure of vortices. Nevertheless, considering the different scales involved, and the subjective nature of observation in visualization, the resulting agreement is still very good and can be taken as a confirmation that the drag force transition detected with the tuning forks indeed relates to the onset of turbulent flow.

3. Transition to Turbulence in Superfluid ^{4}He

Compared to the case of classical fluids, where the onset of turbulence is caused by an initial instability of laminar viscous flow, the situation in He II may be generally a little more complicated. It is necessary to distinguish two limiting cases depending on temperature – the two-fluid hydrodynamics range between T_λ and roughly 1 K, and the "pure superfluid" range below approximately 0.5 K, where the action of the normal component is reduced to momentum and energy exchange with balistically propagating quasiparticles. In the former case, based on the discussion in the Introduction, in Section 1.2, similarities with classical turbulence may be expected provided that three conditions are satisfied: (i) no notable temperature gradients are present (eliminating counterflow), (ii) the two components can be thought of as having coupled velocity fields, which usually happens only due to the mutual friction force acting on them via quantized vortices, and (iii) only length scales larger than the mean intervortex distance are considered. In the latter case of "purely superfluid" turbulence, any observed similarities to its classical counterpart must simply result from general statistical properties of turbulent flows, the means of energy transfer between different length scales and its eventual dissipation. In this case, the transition to turbulence is no longer caused by an instability of laminar viscous flow, instead, if hydrodynamical language is to be used at all, we might say that it is linked to an instability in the potential flow of an inviscid liquid flowing past the body. However, perhaps the most precise description employs the quantum mechanical treatment of He II, pointing at the instability related to the nucleation of quantized vortices.

In He II, turbulence has traditionally been generated and probed using many different techniques. Apart from the numerous oscillators already described in Section 1.5, other methods include most notably towed grids [177, 178], ion jets producing charged vortex rings or tangles [179, 180, 181, 182], spin-ups/spin-downs [183, 184], and thermal counterflow or superflow [162, 163, 164, 165, 185, 186, 187]. In the following, we will focus mainly on experiments performed using quartz tuning forks, but other oscillating structures are represented as well. As the Prague experiments were restricted to the temperature range from T_λ down to 1.3 K, i.e., to the two-fluid hydrodynamics regime, the results will be complemented by and compared to the data of other groups, extending the available temperature range down to 350 mK, deep in the ballistic regime.

Similarities with classical turbulence can then be expected in the Prague data, more specifically in situations where the number of quantized vortices is sufficiently high to provide strong coupling between the normal and superfluid components. However, this need not be true at the very onset of turbulence, because in the case of laminar/potential flow of the normal/superfluid components, the velocity fields of the two components are expected to be different in the close vicinity of the vibrating tuning fork, as different boundary conditions (full slip/no slip) are imposed on them. The tuning forks used, as well as other important aspects of the performed experiments together with the main results are fully described in Ref. [3], included in Appendix A as attachment A3.

3.1 Quartz Tuning Fork Measurements and the Coupling Model

For the studies of superfluid turbulence, the same setup, and the same procedures were used, as described in the previous Chapter 2, including a similar set of tuning forks. Full resonant curves of the tuning forks were measured, and the drag force was evaluated from the detected linewidth, while the tip velocity was determined from the amplitude of the passing electric current, detected as voltage across a resistor in a current divider. Again, a crossover between linear and quadratic drag regimes was found, but this time with an unexpected temperature-dependent feature in the drag coefficient, as is shown in Fig. 3.1.

Before proceeding to the tentative explanation of the observed drag-velocity dependence, it is prudent to compare our results to the measurements of other groups using other oscillating bodies. Such a comparison can be made between Figs. 3.1 and 3.2, where the latter contains data obtained with an oscillating grid [148, 149, 188], and an oscillating sphere [97], at temperatures both above and below 1 K. It can be seen that the plotted velocity dependences of the drag coefficient show some features specific to the given oscillators. For example, the small sphere could detect intermittent switching between laminar and turbulent states, while the grid and the tuning forks displayed no such phenomenon. Nevertheless, the form of the drag coefficient is very similar in all cases, showing a temperature-dependent minimum. The eventual relaxation towards a temperature-independent constant value is observed with the forks and the grid, while the data for the oscillating sphere do not extend to sufficiently high velocities.

Naturally, we sought a model describing our mid-temperature observations, while retaining some degree of validity/applicability even for the measurements obtained at very low temperatures below 1 K. After numerous consultations with W. F. Vinen, the following scenario, reflected in the phenomenological model presented in Ref. [3] (A3), was proposed.

At low velocities, the normal component (assumed to be present in a significant fraction) forms a laminar flow around the oscillator, contributing to the drag force accordingly, while the zero-viscosity superfluid component exhibits potential flow with no associated drag. Upon reaching a certain critical velocity, u_0^{cS}, quantized vortices start to be generated by the oscillator in significant amounts (depending on the applied drive) and start to couple the two components via the mutual friction force. The coupled components are described as a *single quasiclassical fluid* with a finite effective viscosity, determined by the experimental conditions and the empirical degree of coupling. With increasing drive, the density of the vortices produced will grow, and the two components will become gradually more and more coupled. Eventually, the coupling will lock the motion of the components together, with almost identical velocity fields (of course, only on length scales exceeding the mean intervortex distance). At the same time, this quasiclassical fluid (the coupled components) will become more and more turbulent, until the region is reached, where the drag coefficient assumes its constant value characteristic of stable developed turbulence.

At very low temperatures, there is, of course, only a small fraction of the normal component present, possibly only in the form of ballistic quasiparticles.

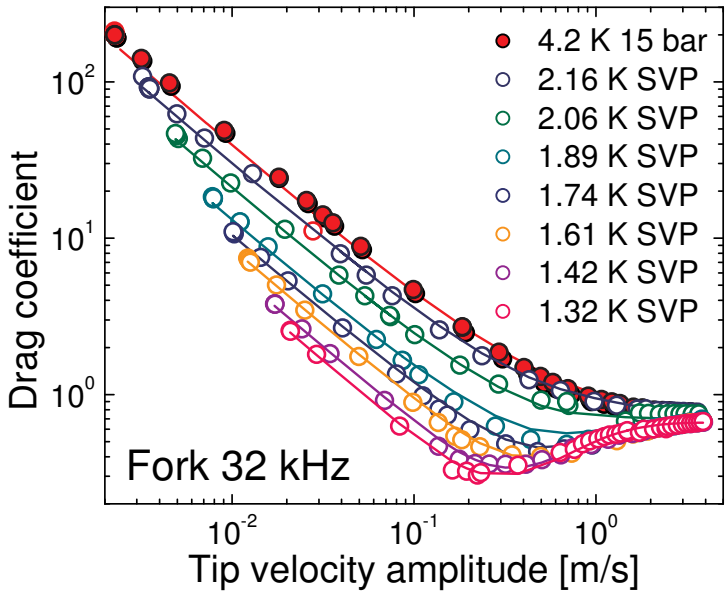

Figure 3.1: Drag coefficient measured with a 32 kHz tuning fork in He II plotted versus tip velocity amplitude for different temperatures along the saturated vapour line. A single measurement in pressurized He I at 4.2 K is added for comparison with classical liquids. It is evident that with decreasing temperature, the laminar drag falls as well, owing to the dropping ratio of the normal component. In the laminar case, the superfluid component exhibits potential inviscid flow around the tuning fork (maybe except for a few pinned vortices), and does not contribute to the drag at all (d'Alembert's paradox). In developed turbulence, in the limit of high velocities, temperature seems to have little effect on the exerted drag force, suggesting that both components are contributing, and that they are likely to be coupled due to the mutual friction force acting via the turbulent vortex tangle. In the transition region, an interesting feature is observed, unknown from the investigations in classical fluids (see the data at 4.2 K or Fig. 2.4 in Chapter 2 for comparison). As the velocity is increased, the drag coefficient appears to reach a minimum, before returning to its constant value of order unity in turbulent flow. This feature is systematically more prominent at lower temperatures, leading us to conjecture that it is related to the mutual coupling of the two components, or in other words, to the superfluid component gradually starting to contribute to the measured drag force. The solid lines are fits obtained using the coupling model discussed further in the text.

Therefore, the coupling model as outlined above need not necessarily provide a physically correct description in terms of the action of the normal component and the coupling process. However, it can still be assumed that the "pure superfluid" can mimic a classical fluid of a given effective viscosity, if an efficient dissipation mechanism is provided. It is one of the current quests of superfluid hydrodynamics research to determine the exact nature of the dissipation mechanism that causes the decay of turbulent vortex tangles in the $T \to 0$ limit, but it is already well-established that such a mechanism exists. Presently, it is generally accepted that the the energy is dissipated in the following manner. The energy stored in the

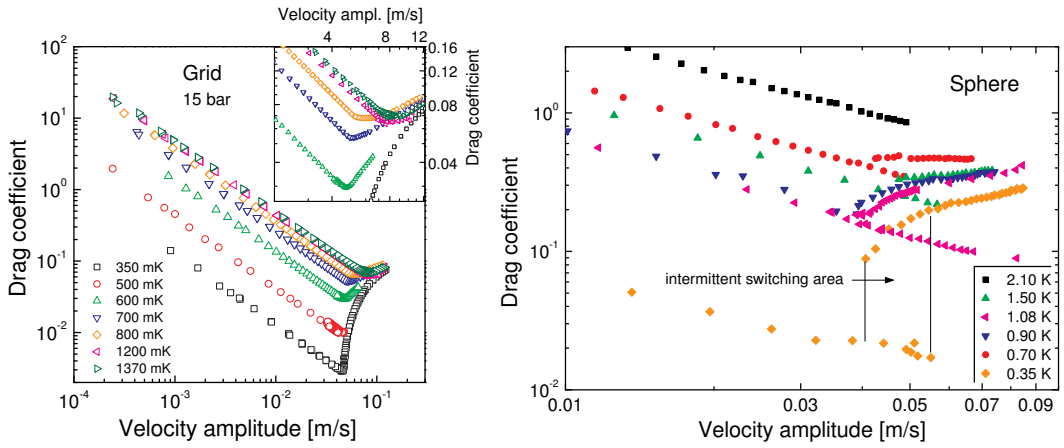

Figure 3.2: Drag coefficient evaluated for an oscillating grid [148, 149, 188] (left, detail in inset) and an oscillating sphere [97] (right) immersed in He II. While the exact form of the drag coefficient may differ slightly between the oscillators (for example, the sphere clearly shows hysteresis, as do vibrating wires [145, 146], while the forks and the grid do not), the general form remains the same as presented in Fig. 3.1. The laminar drag is strongly temperature dependent, and the minimum is more prominent and shaper at lower temperatures (note the difference between scales of the x-axes in the two panels). On the other hand, if we look at more developed turbulence (higher velocities), the available data for the oscillating grid indicate that in this limit, the resulting drag force becomes more or less temperature independent, in agreement with our observations. This remains true even for measurements in the ballistic regime of quasiparticle propagation below 700 mK.

very existence of quantized vortices, their interactions and their motion is believed to be channeled by a cascade of Kelvin waves excited on the quantized vortices to higher and higher wavenumbers (which is possible due to nonlinear Kelvin wave interactions, and likely aided by vortex reconnections), ultimately resulting in uncorrelated phonon emission, i.e., production of heat.

Now, that we have a dissipation mechanism that is efficient only at high wavenumbers and dependent on vortex line density, the analogy with classical fluid dynamics and viscosity becomes more apparent. Therefore, we believe that while the proposed model may provide incorrect physical reasoning when applied to very low temperature measurements, the same mathematical expressions valid in the mid-temperature range can be used to describe the observed low temperature data as well, as is demonstrated in Fig. 3.3. That notwithstanding, to avoid ambiguities, we will limit our further discussion only to the application of this model to the data obtained in the hydrodynamic regime above 1 K, as in Fig. 3.1, where the underlying physical reasoning is fully valid.

Mathematically, the proposed model is described by the following set of equations linking the degree of coupling, the effective kinematic viscosity and the resulting drag coefficient:

$$C_D = 2\alpha \frac{S}{A} \left(\omega x_e \nu_e\right)^{1/2} \frac{1}{u_0} + x_e \gamma, \tag{3.1}$$

where x_e and ν_e are defined as the effective fractional density of the single quasi-

classical fluid (representing the coupled components), and its effective kinematic viscosity, respectively, and γ stands for the constant value of the drag coefficient in developed turbulent flow.

The effective viscosity and fractional density are in turn given by:

$$x_e = x + (1-x)\,\theta(u_0 - u_0^{\mathrm{cS}})\,\frac{(u_0 - u_0^{\mathrm{cS}})^2}{\varepsilon + (u_0 - u_0^{\mathrm{cS}})^2}, \tag{3.2}$$

$$\nu_e = \nu + (\nu_c - \nu)\,\theta(u_0 - u_0^{\mathrm{cS}})\,\frac{(u_0 - u_0^{\mathrm{cS}})^2}{\varepsilon + (u_0 - u_0^{\mathrm{cS}})^2}, \tag{3.3}$$

where x and ν denote the fractional density of the normal component and its kinematic viscosity, respectively, and ν_c is the effective kinematic viscosity of the fully coupled components. The symbol θ refers to the Heaviside step function, and the fraction $(u_0 - u_0^{\mathrm{cS}})^2 \Big/ \left(\varepsilon + (u_0 - u_0^{\mathrm{cS}})^2\right)$ represents the degree of coupling, which is expressed as a sigmoidal function of the velocity amplitude u_0 with a finite step width ε. It should be noted that there is no particular reason for choosing this exact functional form for the degree of coupling, in fact, several different forms of sigmoidal functions have been tested, this one is relatively simple and seems to yield the best agreement with the data. In the analysis, α, γ, ν_c, u_0^{cS}, and ε were determined by fitting the drag coefficient as given by Eqs. 3.1–3.3 to the experimental data. The physical ideas encompassed in the mathematical formulation of the model are also described in more detail in Ref. [3] (A3).

The success of this model is perhaps best judged from the above Fig. 3.1. The overall agreement is rather good, and the model does explain, both qualitatively and quantitatively, what happens at the transition to turbulence. Studying Fig. 3.1 in more detail, a careful viewer will notice that some data series are fitted considerably better than other. This is probably caused by the fitting procedure itself, which is not very straightforward. Given the mathematical expressions above, including the Heaviside step functions, it is not possible to use standard fitting algorithms, and a more "manual" approach is needed, which is described in the following paragraph.

There is little difficulty in determining the parameters α and γ, as this can be done separately with sufficiently good accuracy from the laminar and turbulent parts, respectively. The true complications arise when attempting to determine the exact values of the critical velocity u_0^{cS} and the step width ε, the two quantities which affect the coupling. Here, one is simply forced to resort to a trial and error method, aided only by educated guesses, estimates, and the computing power of tabletop PCs. For example, one useful criterion considered was that the resulting critical velocity must always be lower than or at most equal to the value corresponding to the minimum of the drag coefficient (if present), where the equality was reserved only for sharp minima, such as when attempting to re-analyse the results of other groups from very low temperatures (Fig. 3.3). The final value of the effective kinematic viscosity of the coupled fluids, ν_c, was most notably influenced by the shape of the dependence following the maximum of the drag coefficient (if present) just before it relaxes to its final constant value. Once the critical velocity was established reasonably well, corresponding as closely as possible to the first significant deviations from the laminar drag of the normal

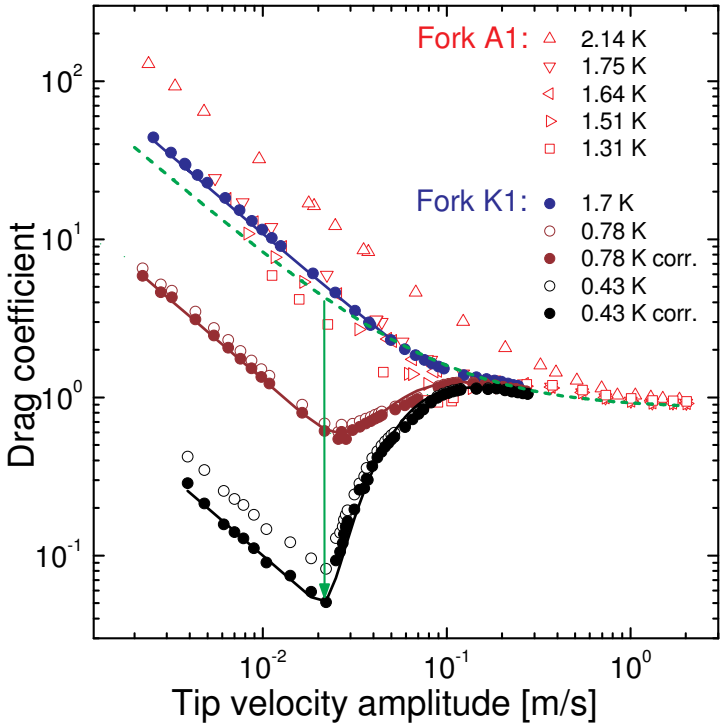

Figure 3.3: Plots of the observed drag coefficient at several low temperatures and at the saturated vapor pressure for the Kharkov tuning fork K1. Results for our fork A1 are included for comparison. Note that at low temperatures, a maximum also appears following the first minimum in the drag coefficient. The lines are fits using the coupling model described in the text. The data for K1 do not extend to high enough velocities to allow an accurate determination of the parameter γ, therefore it is taken to have the same value as that for A1. The uncorrected data for K1 are shown as open circles; data corrected for the internal (vacuum) damping of the fork are shown as filled circles. The broken green line is derived from Eq. 3.1 assuming full coupling in the whole region of flow velocities, i.e., the effective kinematic viscosity is taken as ν_c and effective fractional density is set to 1, thus depicting a classical transition to turbulence in a fluid with kinematic viscosity equal to ν_c.

component, and the effective kinematic viscosity was determined, the ε parameter was adjusted to provide a good optical fit to the data (it influences mainly the region between the minimum and the maximum (if present), and the close vicinity of these two extremes), without much regard to its possible physical significance. As a result of this method, the final values of ε tend to differ significantly between the different oscillators used (see again Ref. [3] or attachment A3 for details), but this is perhaps of little importance to the other aspects of the analysis. In other words, both in the formulation of the model and in the data analysis, our approach is purely phenomenological, but we believe that the obtained results presented in Figs. 3.1 and 3.3 speak for themselves.

The obtained values of the critical velocity, u_0^{cS}, and its dimensionless counterpart (scaled by $\sqrt{\kappa\omega}$) are plotted in Fig. 3.4 and compared to the results of other He II experiments. It turns out to be rather difficult to explain the

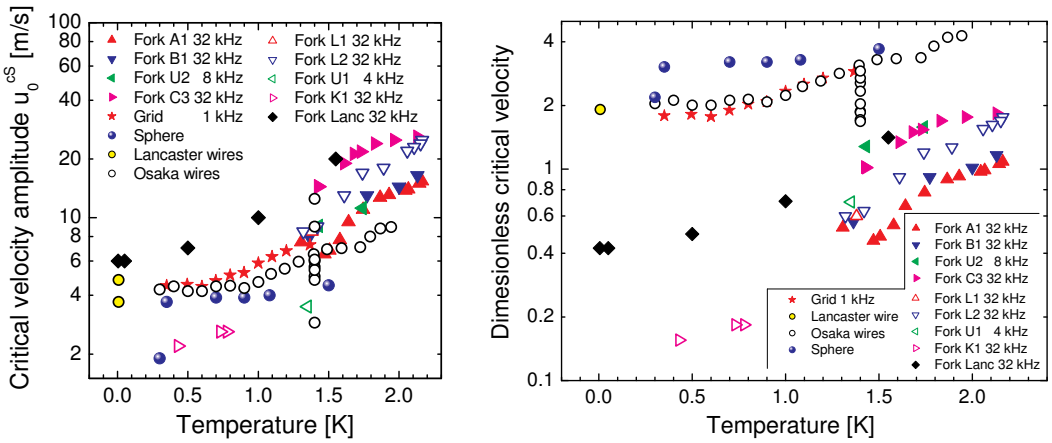

Figure 3.4: Left: Critical velocities for the transition to superfluid turbulence obtained using various oscillators. Significant differences are found between different oscillating bodies, but the general trend is that lower critical velocities are observed at lower temperatures, and a plateau is observed in the $T \to 0$ limit. Right: The same critical velocities plotted in dimensionless form, after scaling by $\sqrt{\kappa\omega}$, where ω has different values for different resonators, and κ is the quantum of circulation in ^{4}He. The dimensionless critical velocities are not found to collapse to a single curve, in fact, the scatter is significantly larger in the dimensionless case than in absolute velocities. This suggests the possibility of some other effects, such as geometry or surface roughness, influencing the transition. The data in both panels were taken from these sources: Lancaster wire [146], Osaka wire [189, 190], sphere [97], grid [148, 149, 188], Lancaster tuning fork [155].

observed variance of the critical velocities between the experiments without assuming some effects due to the different geometries of the oscillators or their surface roughness, which is also related to the configuration of pinned remanent vortices at sub-critical velocities. However, the obtained data are insufficient to quantify such an influence and in this respect further studies, both experimental and theoretical, would be useful.

The effective kinematic viscosities of the coupled fluids, ν_c determined from the fitting procedure are not understood perfectly at this point and leave some room for doubt. For this reason, they are not discussed here in detail and the reader is kindly asked to consult Fig. 6 of Ref. [3] (A3) for their temperature dependence. On a brief note, the fitted effective viscosities do seem to follow a systematic temperature dependence, but differ significantly between the individual experiments, even using the same type of oscillator. This is likely caused by fact that this parameter is rather poorly conditioned in the outlined fitting procedure and the resulting values may be little more than estimates. Physical reasons for the large variations are not excluded either – as ν_c relates to the two fluids coupled via quantized vortices, it might be dependent on the spatial extent, density and polarization of the resulting stable turbulent vortex tangle, which is likely to be different for different oscillators used.

Summarily, the proposed model does describe the observations in the mid-temperature range with good accuracy, and does seem to allow extension to lower

temperatures as well, albeit necessitating different underlying physics. It would be very interesting to compare these results and the predictions of the coupling model with data obtained on other oscillating structures or even in steady flow, provided that the experimental parameters cover a sufficiently large range of velocities. In further experiments, it would also be of great value to control and analyse the surface roughness of the oscillators used, as well as to vary the size of the oscillators and extend the available range of frequencies, optimally all the way from DC flows to units of MHz.

4. Acoustic Emission by Quartz Tuning Forks

Remembering the musical counterparts of our quartz tuning forks, it is perhaps of little surprise that these high frequency oscillators should emit (ultra)sound. For a long time, it was, however, considered that sound emission can be neglected as a mechanism of dissipation of the kinetic energy of the oscillator. Not entirely without reason – under the usual circumstances and using the standard forks, even in low-viscosity fluids, such as He I and He II, viscous drag indeed is the dominating dissipation mechanism (above ≈ 1 K). Additionally, for purposes of simplification, we often resort to incompressible hydrodynamics when describing the studied flows, whereby all acoustic phenomena are *a priori* ruled out.

Nevertheless, the drag due to acoustic emission is measurable with the tuning forks, if the circumstances are favourable. This can happen in two main cases: (i) high frequency tuning forks are used, which exhibit much stronger acoustic emission, or (ii) the temperature is reduced sufficiently below 1 K, leading to a significant fall of the drag force due to viscosity/ballistic excitations so that the acoustic drag, independent of temperature in the $T \to 0$ limit, takes over and becomes the most important dissipation mechanism. The latter case is especially important, since acoustics can become a hindrance in the studies of purely superfluid turbulence at the very lowest temperatures, completely screening the laminar drag due to thermal excitations (after correction for the vacuum response) or introducing unexpected variations of resonant linewidth due to small variations in pressure (and hence in the speed of sound, causing already more significant fluctiations of the emission power). Additionally, acoustic emission may also prove to be essential in analysing the interactions of multiple oscillating objects placed in the same volume of fluid.

It is therefore important to understand this dissipation mechanism and to be able to predict its magnitude in different situations, at least within the correct order of magnitude. In this Chapter, the results obtained on acoustic emission due to quartz tuning forks in normal and superfluid ^{4}He are reviewed together with three models describing approximatively the acoustic fields created by tuning fork oscillators. The full account can be found in Ref. [4], included in Appendix A as attachment A4 .

Two important aspects ought to be pointed out before we begin: (i) only dissipative phenomena related to acoustic emission are considered here, i.e, dispersive action of sound waves on the oscillator is not described in any way, and (ii) when speaking about energy dissipation due to acoustic emission, we do not understand dissipation in its strictly defined meaning, which is "a thermodynamically irreversible loss", but rather an *energy transfer* from the oscillating body to the sound waves in the fluid.

Considering the energy balance for the oscillator, there is little conceptual difference between this energy dissipation and energy transfer *if an infinite volume of fluid is considered*, as the energy of the outward propagating sound waves is ultimately carried off to infinity and lost anyway. However, if walls of finite reflectivity are present, then in the stationary case, our "energy dissipation", or

more precisely, the rate at which the oscillator supplies energy to the sound waves, will only correspond to the energy of the sound waves that happen to be transmitted by the walls outside the volume of the oscillator. The energy of the reflected waves is in first approximation conserved within the experimental volume and can be even partly transferred back to the elastic oscillator via sound absorption.

True dissipation of the energy of the adiabatically propagating sound waves due to finite viscosity and heat conductivity of the fluid and other phenomena associated with the presence of walls are not considered here. In small enclosed volumes comparable to the wavelength (which is the case of the Prague experiments) they can be neglected in He I and He II without any significant effect on accuracy.

4.1 Acoustic Emission in Classical Fluids and Superfluids

It is well-known that any object undergoing accelerated motion in a fluid of finite compressibility emits sound waves [7, 191]. If we constrain ourselves to low velocities of the object (or better said to low Mach numbers) so that no frequency shifts or shock phenomena have to be considered, we can then decompose the flow field around the moving object into the incompressible flow past the body, and into the periodic oscillations of velocity and pressure corresponding to the emitted sound waves.

For practical purposes, within the standard theory of acoustics, various moving and/or oscillating bodies are often represented as acoustic multipoles, i.e., as a spatial arrangement of point sources (perhaps with the exception of a narrow class of bodies for which exact calculations can be carried out analytically). For example a uniformly isotropically pulsating sphere could be represented as a single point source – an acoustic monopole. A body of arbitrary shape undergoing simple translational oscillations without changing its volume is often represented as a dipole, while bodies exhibiting more complex forms of motion are usually described as a combination of several monopoles and dipoles, or, if symmetry permits, as higher order multipoles. Such is the case of the tuning fork, with its two prongs oscillating with (approximately) equal velocities in anti-phase, for which the ideal representation seems to be the longitudinal acoustic quadrupole.

Having thus established the multipole representation of the given body, calculating the acoustic emission power in classical fluid is a rather straightforward (albeit potentially very tedious) procedure of solving the velocity and pressure fields around the given set of point sources. In a superfluid, the situation can be potentially much more complicated, as more than just one bulk sound mode exists. In principle, any accelerating body will thus emit both first and second sound, where the emission of second sound is caused by the different boundary conditions imposed on the normal and superfluid components. Additionally, if finite viscosity is present, an oscillating body will also heat up periodically by the viscous drag force, thus emitting extra second sound at double the frequency of oscillations superimposed on a DC counterflow providing a time-averaged cooling. However, it can be shown at least estimatively [7, 4] that a moving body will

produce first sound much more efficiently then second sound, and therefore unless a resonance of second sound within the constrained geometry of the experiment is encountered, for the purposes of estimating the emission power, second sound can be neglected. A more quantitative argument for this statement regarding the experiments performed in Prague is given in Ref. [4] (A4).

4.2 Models of Acoustic Emission by Tuning Forks

Three models allowing us to calculate the emission power of the tuning fork oscillator have been suggested and tested in Ref. [4] (A4), and here we will summarize their features. First, a full 3D model based on the work of Sillitto [5] was formulated, in which the tuning fork was represented as a longitudinal quadrupole. In the next model, the tuning fork was described as two infinite parallel cylinders performing transverse oscillations in anti-phase, as suggested already by Clubb [6]. This model describes sound emission in 2D only, as all quantities are independent of the dimension along the axes of the cylinders. Finally, to distinguish the effect of describing the prongs of the fork as cylinders from the change in dimensionality, a 2D quadrupole model was formulated as well.

All three models eventually led to their respective emission powers, which were expressed for each model in two forms. First, as an analytical solution involving an infinite series of Bessel functions, and second, in the "long wavelength limit", referring to the comparison of the sound wavelength to the thickness of tuning fork prongs, T, their spacing D, or the radius of the two cylinders, R, and half the distance between their centers, F. All the details can be found in Ref. [4] (A4), here it is sufficient to say that in the simplified limiting form, the formula for the emission power, P, reduces to a simple expression involving different powers of the frequency of oscillations, ω, and the speed of sound, c, varying depending on the dimensionality of the problem. For the 3D case, one obtains $P \propto \omega^6/c^5$, while for the 2D models the result is $P \propto \omega^5/c^4$. From here, it is already easily understood why sound emission is much more important for high frequency tuning forks. Compared to the dependence of the viscous drag on frequency ($\propto \omega^{1/2}$), the acoustic drag rises with increasing frequency much more steeply.

Finally, as many of the experiments were performed with the tuning forks inside their original capsules, a method of taking the solid walls into account at least approximatively had to be developed as well. Based on standard acoustics, two important parameters were evaluated, first, the energy transmittance for plane waves under near-normal incidence, and second, the critical incidence angle for total *external* reflection of the longitudinal sound waves. It turned out that both parameters depend on the temperature and pressure of helium significantly, as any changes in the speed of sound and density are reflected in the acoustic impedance of helium $Z_{\mathrm{He}} = c_1\rho_{\mathrm{He}}$, while the acoustic impedance of the walls is considered constant in the experimental range of temperatures and pressures (T = 1.3 – 2.4 K, p = 0 – 25 bar). It was then postulated that the total ratio of energy transmitted will be proportional to the integral of the transmittance from zero angle of incidence to the rather small critical angle ($\approx 3°$), and the resulting function of temperature and pressure was used to scale the emission powers given by the individual models when attempting to fit the experimental data, see Ref. [4] (A4) for details.

4.3 Experimental Evidence of Acoustic Emission

The first evidence of acoustic emission by tuning forks was observed in the B. Verkin Institute in Kharkov, Ukraine. The resonant linewidth of forks oscillating at frequencies ranging from 32 kHz to 100 kHz was measured at 1.5 K and 350 mK. Originally, this data was intended to be used for turbulence studies, but it was soon found that the observed frequency dependence of the linear drag force does not correspond to $\omega^{1/2}$ expected for viscous drag, even when the slightly differing sizes of the tuning forks used are taken into account. The resonant linewidths, after subtraction of the linewidths due to intrinsic damping of the forks, as measured at low temperature in vacuum, are plotted in Fig. 4.1.

A more systematic study was later performed in Lancaster (yet unpublished), where a custom-made array of tuning forks resonating at varied frequencies was submerged into He II at 4.2 K and 1.5 K. Taking advantage not only of the fundamental flexural mode of the tuning forks, but also of the first harmonic at $\omega_1 \approx 6.2\omega_0$, the available frequency range was extended significantly, which

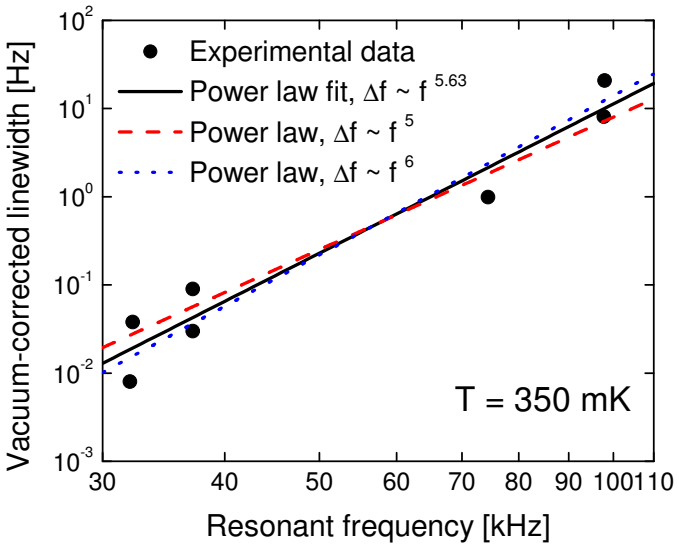

Figure 4.1: Vacuum-corrected resonant linewidths of tuning forks oscillating at various frequencies from 32 kHz to 100 kHz at 350 mK. The power law fitted through data corresponds to an exponent of 5.63, which is clearly different from the expectations for the ballistic drag force, and indicates the likely importance of acoustic emission as a mechanism by which the high frequency oscillators lose most of their energy. From this graph alone, the same cannot be said about the lower frequency tuning forks (32 kHz, 37 kHz) with absolute certainty, as there is no definite guarantee that the fitted power law still extends below these frequencies. Generally speaking, one would expect to find a frequency of order 10 kHz, where the magnitudes of the ballistic and acoustic drag forces would be comparable. Nevertheless, as is discussed in Ref. [4] (A4), the indication seems to be that at this low temperature, acoustic emission is a significant dissipation mechanism for all the used tuning forks.

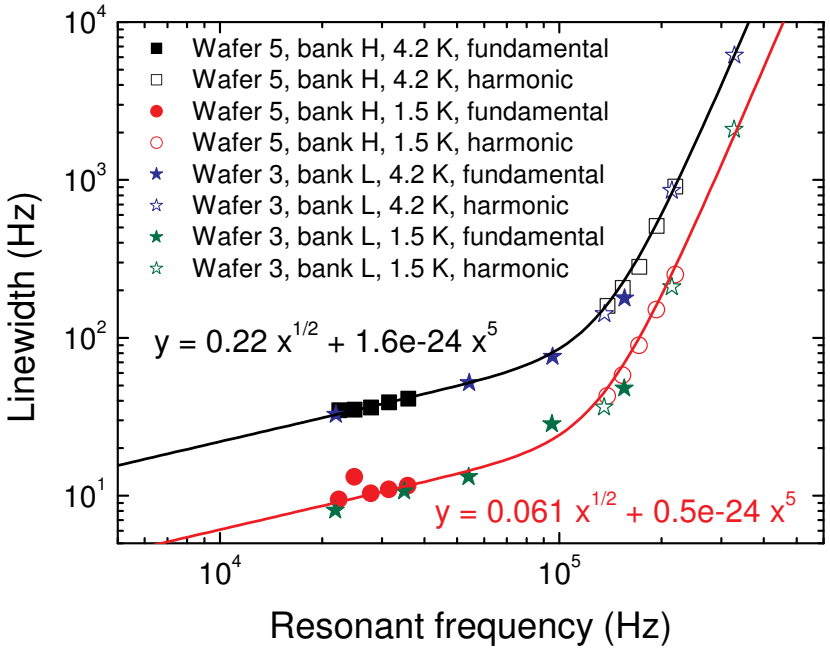

Figure 4.2: Resonant linewidths of various tuning forks in their fundamental and first harmonic flexural modes measured at 4.2 K and 1.5 K. The relative importance of viscosity and acoustic emission is clearly indicated by the gradual departure from the $\omega^{1/2}$ dependence towards a much steeper one, close to ω^5, which is expected from the 2D models of acoustic emission. Arguably, ω^6, corresponding to the 3D acoustic emission model could be used as well, but the reasons for the choice between ω^5 and ω^6 would already depend on fine exact details of the geometries of the tuning forks used. A clear indication of the importance of acoustic emission for high frequency resonators is given in the graph. The region of this crossover in the frequency domain depends of course on the dimensions of the oscillators and on the experimental conditions. For these rather small tuning forks (bank L: $W = 75$ μm, $T = 90$ μm, $L = 700 - 1900$ μm; bank H: W, T are the same, $L \approx 1480 - 1880$ μm) it occurs above 100 kHz both at 4.2 K and 1.5 K, but as was shown in the Kharkov data (Fig. 4.1), for larger forks and at lower temperatures, the same crossover can be expected at much lower frequencies. This is not surprising, as the viscous/ballistic drag falls rapidly below 1 K, and the emission power also strongly depends on the dimensions of the moving body, specifically on the square of the "effective emitting area", hence on the fourth power of a linear dimension [4] (A4).

allowed demonstrating clearly the crossover between the dominance of laminar drag and acoustic emission, as is shown in Fig. 4.2. Another piece of evidence of acoustic phenomena can be seen in the observed level crossings, when upon variation of a control parameter (typically pressure), the resonance of the tuning fork matches briefly an acoustic resonance determined by the geometry of the experimental cell. These phenomena are again described in more detail in Ref. [4] (A4).

Now, it remains to examine the quantitative predictions given by the three models of acoustic emission by tuning forks and compare them to the experiment.

As the models themselves are valid only in a boundless volume of fluid, the correction for the presence of reflecting walls mentioned above has to be taken into account, when attempting to describe the series of Prague experiments, the results of which are presented in Fig. 4.3. In these experiments, the 77 kHz tuning fork was kept inside its original capsule, into which a tiny hole was drilled, to allow liquid He inside. According to the specifications of the manufacturer, the capsules were made of aluminium, and hence act strongly reflectively indeed, as the acoustic impedance mismatch between the liquid helium ($Z_{\mathrm{He}} \approx 3 \cdot 10^4$ kg m^{-2} s^{-1}) and the solid metal ($Z_{\mathrm{Al}} \approx 2 \cdot 10^7$ kg m^{-2} s^{-1}) is enormous. To compare the experimental data to the predictions of the models, the resulting emission powers were used to calculate the corresponding drag force and using the effective mass of a prong as defined in Section 1.4 also the linewidth contribution. For the relation between the linewidth and the magnitude of the drag force, see Ref. [121]. A single degree of freedom was allowed for the fitting, as expressed by a multiplicative parameter assigned to each model of acoustic emission by tuning forks. The same values of these parameters were used to fit all of the three data sets shown.

The mentioned fitting parameters and the method of fitting are described in Ref. [4] (A4). The two cylinders model seems to offer the best description of the experimental data, as its fitting parameter was found to be equal to 1.06, i.e., very little adjustment of the resulting emission power was needed. This might be, however, purely a numerical coincidence, as many assumptions have been made, for example, in estimating the effects of the walls. Nevertheless, from the good agreement with the experimental data taken under dramatically differing conditions (in normal fluid He I and superfluid He II down to 1.3 K, under pressures between 1 and 24 bar, corresponding to sound velocities in the range 180 – 360 m/s), it can be said that the models compare to the observations very successfully, and in this case, the 2D models seem to be more accurate.

Finally, other oscillating structures often used in cryogenic fluid dynamics were examined for the possibility of acoustic emission playing and important part in their damping. These include vibrating wires [189, 190, 192, 145, 146], spheres [153, 154, 97], grids [148, 188, 149], micromachined resonators [160, 161], and the standard tuning forks assumed to operated under different conditions. apart from the tuning forks, these oscillators behave as acoustic dipoles and therefore an independent prediction of the emission power had to be made [4] (A4).

As most of these sensors resonate at significantly lower frequencies then our 77 kHz tuning fork, it was found that for most of them the dissipation due to acoustic emission can be neglected. While the micromachined devices resonate at even higher frequencies, their emission power is suppressed due to small dimensions (it depends roughly on the fourth power of a linear dimension, whereas viscous/ballistic drag force depends on the area, i.e., the linear dimension squared). The exceptions to the rule of neglecting acoustic emission are the standard 32 kHz tuning fork, if operated at sufficiently low temperature, and perhaps also the discussed vibrating grid, as in this case the comparison was made with its intrinsic damping rather than with the actual viscous/ballistic drag force due to its surroundings [4] (A4).

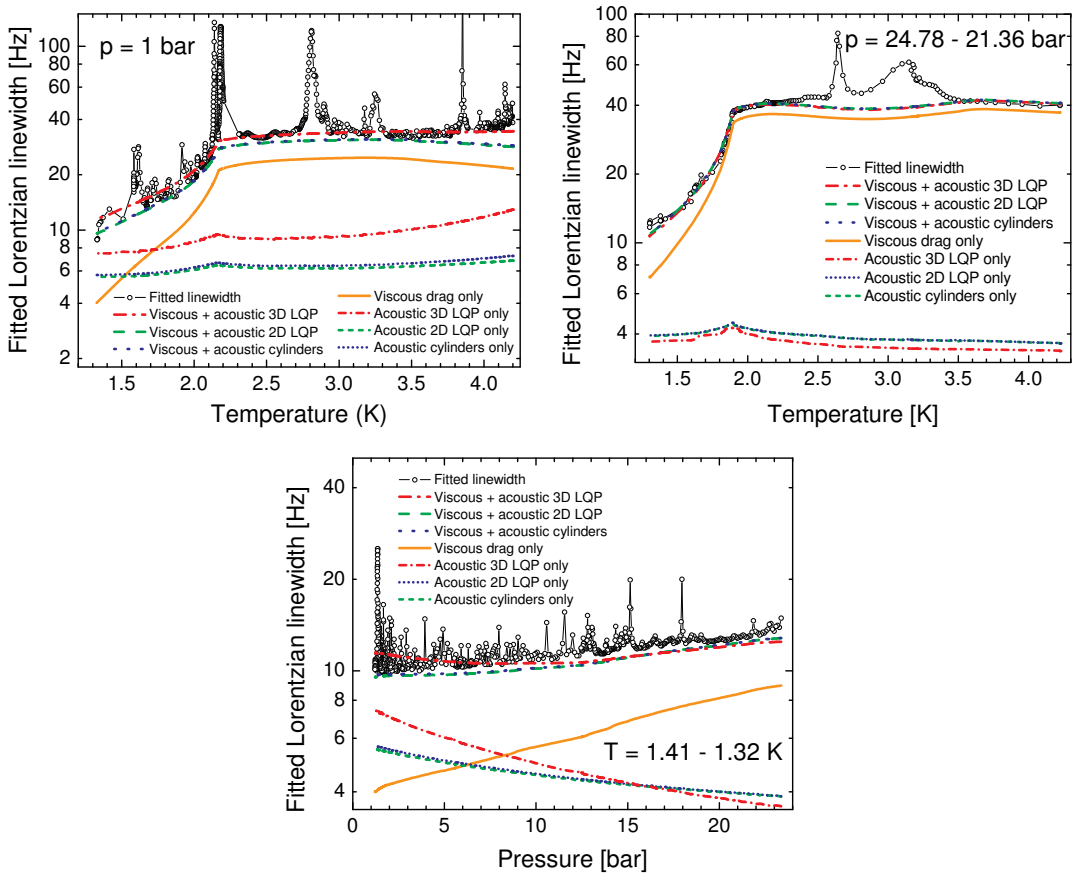

Figure 4.3: Two temperature dependences (top) and one pressure dependence (bottom) of the resonant linewidth of the 77 kHz tuning fork inside its original capsule filled with liquid helium. The linewidth was obtained by measuring the full resonance curves and fitting the result with a Lorentzian absorption function. Therefore, the peaks in the experimental data in all the graphs correspond to various sound resonances inside the capsule of diameter 3 mm, possibly also affected by the enclosing cylindrical pressure cell made of brass, 20 mm in diameter, 20 mm in height. At an acoustic resonance, the rate of energy transfer from the fork to the sound modes is highest. This corresponds to the fact that the amplitude of the sound waves inside the capsule is highest, and therefore the amount of sound wave energy transmitted through the walls per unit time is highest as well. As is indicated in the graphs, the plotted functions correspond to the contribution of the viscous drag force (solid orange line), and to the acoustic contribution as determined by the three models, corrected for the presence of walls, and scaled by a single fitting parameter (green short dashed, blue short dotted, and red short dash-dotted lines). The resulting sum of the contributions is also plotted for each of the three models (green dashed, blue dotted, and red dash-dotted lines). To evaluate the accuracy of the models, these three curves should be compared to the floor of the experimental data, i.e., disregarding the resonances of the experimental volumes. In two of these three experiments, the crossover between the dominance of the viscous drag and of acoustic emission is clearly seen.

5. Andreev Reflection on a Rectilinear Array of Quantized Vortices in ^{3}He–B

In this Chapter, we will describe a series of experiments performed with quartz tuning forks in ^{3}He–B, during the Author's two consecutive visits of a total duration of five months, in the Low Temperature Laboratory of Aalto Univerisity, School of Science and Technology based in Espoo, Finland (called still Helsinki Univeristy of Technology during the first visit in 2009). As the title suggests, the aim of these investigations was to study Andreev reflection of thermal excitations on quantized vortices, which has been a known and widely used phenomenon in ^{3}He and superconductor research for some time. Nevertheless, to the best of the Author's knowledge, this is the first experiment in ^{3}He–B, where Andreev reflection has been studied systematically on a well-known configuration of quantized vortices, both in terms of their density and arrangement. The series of performed experiments and a computer simulation of the propagation of thermal excitations is described in Ref. [8], included in Appendix A as attachment A5.

To attain a well-defined configuration of quantized vortices in ^{3}He–B, one can take advantage of the fact that under uniform rotation, vortices tend to relax to a lattice of straight vortex lines, and their equilibrium number is determined by the angular velocity of rotation, Ω, as:

$$N = \frac{2\Omega}{\kappa}, \tag{5.1}$$

where $\kappa = h/2m_3$ is the circulation quantum in ^{3}He, which also corresponds to the total circulation of the hard-core vortex in ^{3}He–B. If quantized vortices are prepared in this way at sufficiently low temperatures (below 0.3 T_C), one might then use two volumes, separated by a thermal resistance (such as a tiny orifice) and by the vortex lattice, to study heat transport between the two volumes due to balistically propagating excitations and determine how it is affected by the presence and density of vortex lines. The exact experimental realisation of this situation as discussed in the next Section 5.1 differs in details of the arrangement, but the same principle applies – the measured quantity is the effect of quantized vortices on heat transport due to ballistic excitations in ^{3}He–B.

5.1 Experimental Setup

The very nature of this measurement requires sophisticated low temperature experimentation equipment unavailable in the Prague Laboratory of Superfluidity, in this case a rotating dilution refrigerator with a nuclear demagnetization stage. The one constructed and operated by the ROTA group in the Low Temperature Laboratory in Helsinki (Fig. 5.1) can reach temperatures of about 0.2 T_C while rotating at a maximum angular velocity of 3 rad/s. All the technical parameters of the cryostat are discussed in detail in [109, 193], and here, we will only describe its basic features.

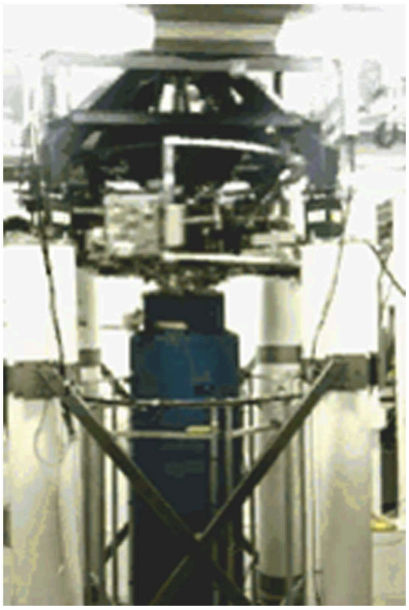

Figure 5.1: The rotating dilution refrigerator ROTA with a nuclear demagnetization stage in the Low Temperature Laboratory at Aalto University, Finland. For a brief description of its features, see the text, full specifications can be found in [109, 193].

The cryostat and its lower rotating platform are suspended on pressurized gas bearings that connect to four concrete pillars. These are also held in position by a set of cross-beams to provide vibration damping. The lower rotating platform contains instrumentation such as room temperature pre-amplifiers and RLC bridges, for which the distance from the site of measurement is critical if low-level signals are to be measured with sufficient sensitivity. Additional weights are added to compensate for the moment of inertia of the instruments and to provide as smooth rotation as possible, without extra forces due to an unbalanced mass with respect to the rotation axis. The upper platform, which contains additional instruments and detectors, is suspended separately, but it is driven by a motor to rotate at the same angular velocity as the cryostat. The signals from the instruments are fed to the computers via optical fibres with connections allowing for mutual rotation. Finally, outside the cryostat, a large coil is placed, which can optionally be used to suppress the Earth's magnetic field.

The dilution refrigerator inside the cryostat is constructed according to a slight modification of the standard design. It is precooled by a volume of ^{4}He, and contains the so-called "1 K pot" to provide precooling for its lower parts at lower temperatures. The mentioned modifications include a cryopump which can be used to operate the dilution refrigerator in single cycle mode while the entire setup is in rotation. Inside the mixing chamber, the temperature can be reduced to below 10 mK. Once the base temperature is attained, the copper nuclear demagnetization part (already under high magnetic field due to a superconducting magnet) is disconnected thermally from the mixing chamber and further cooling by reducing the magnetic field can begin. Temperature of the mixing chamber is usually measured using melting curve thermometry [194, 195], which is also available on the heat exchanger on the nuclear stage, but the lowest temperatures

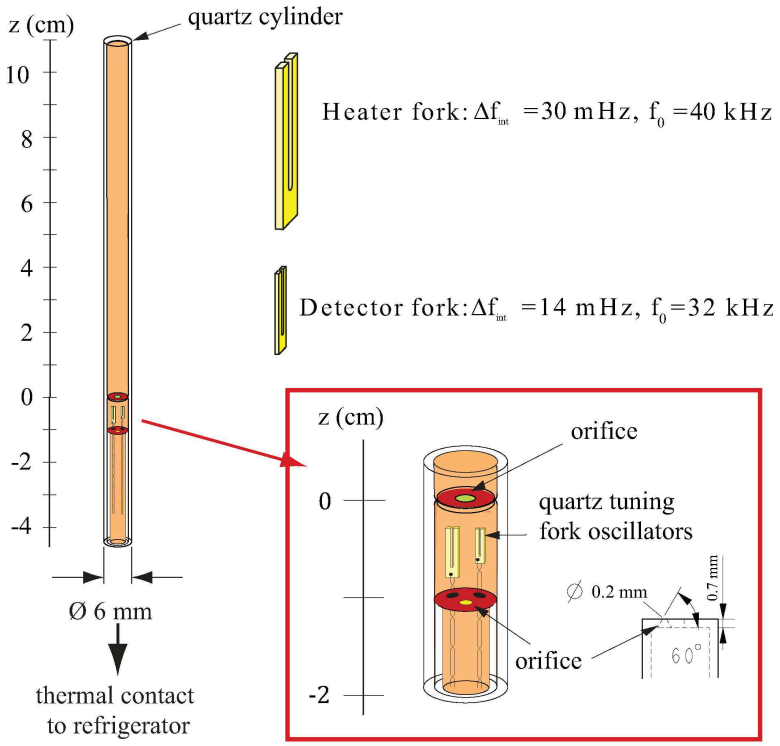

Figure 5.2: A sketch of the experimental cell used in the measurement of Andreev reflection. Two dividers with submillimeter orifices split the cell into three separate volumes. The lowest volume, in direct contact with the surroundings of the cell, and via helium also with the heat exchanger of the nuclear stage, will be further referred to as "sinter volume", the short middle portion containing the tuning forks as "fork volume", and the long upper part as "NMR volume". The diameter of the orifice in the lower divider is $d_1 \approx 0.3$ mm, the upper divider has a larger orifice of diameter $d_2 \approx 0.7$ mm. In the middle section between the dividers, two tuning fork oscillators are installed, one resonating at 32 kHz, acting as a thermometer, and the other, resonating at 40 kHz, acting as a local heater when driven at higher amplitudes. The resonant linewidths of the tuning forks in vacuum at low temperatures are of the order of 0.01 Hz, as is indicated in the figure.

in the sample volume are resolved sensitively by NMR techniques [196, 197] and by a tuning fork thermometer [121].

In our experiment, the cell placed in the sample volume is shown in Fig. 5.2. The walls are made of quartz glass (fused quartz) and have been processed by hydrofluoric (HF) acid on the inside to make them sufficiently smooth for quantized vortices in ^{3}He–B in order to prevent vortex pinning. Remanent vortices are, however, present in the sinter volume, where they stay attached due to the surface roughness of the sintered heat exchanger and the surrounding walls.

When the cryostat is set into uniform rotation at a velocity above 0.1 rad/s, extrinsic nucleation of quantized vortices occurs in the sinter volume, but the cell stays in the vortex-free Landau state. In the actual experiment, the angular velocity was usually set to a higher value than the final intended one, to make sure that vortices can indeed nucleate and relax into their equilibrium lattice. After

stabilization at the given angular velocity, heat transport was studied between the fork volume at about 0.2 T_C and the sinter volume at approximately 0.15 T_C. The temperature of the cell is higher due to a finite heat leak through its suspension (an indium seal between the cell and its holder). During the evaluation of the data, this heat leak could be quantified and turned out to be approximately 10-15 pW, depending on the angular velocity of rotation.

Once the sample was stable at a given rotation velocity, the power input into the heater fork was switched on and changed several times, including both increases and decreases, and finally switched off again, while the amplitude of the thermometer fork was being recorded. When the heater power is switched on, extra thermal excitations are generated in the fork volume, resulting in a local increase of temperature. A net flux of excitations into the NMR and sinter volumes is observed, as is determined by the thermal resistances of the two orifices. For calculations of the energy fluxes and thermal resistances, see the theoretical introduction in Section 1.3. Additionally, the thermal resistance of the lower orifice is affected by the presence of quantized vortices in the sinter volume, which Andreev-reflect a fraction of the incident excitations back through the orifice into the fork volume, as the Andreev-reflected excitations tend to retrace their original trajectories with good accuracy. This effect is expected to be linear with the number of vortices (unless vortex screening is significant), and therefore also linear in Ω.

5.2 Measurements of Andreev Reflection

In the measurement, the AC current signal from the detector tuning fork was fed to a purpose-made I/V converter [198], pre-amplified and then detected by a lock-in amplifier to provide maximum sensitivity and accuracy, while the signal of the heater fork was detected directly in current mode to facilitate the calculation of the exact power dissipated inside the fork volume. The thermometer tuning fork was calibrated against the melting curve thermometers on the heat exchanger on the nuclear stage at 0.3 T_C.

A sample response of the two forks after switching on the power of the heater fork is shown in Fig. 5.3. After the transient period, steady state values can be obtained and used to calculate the dissipated power and the temperature. It is worth to note that the resolution of the thermometer fork at the temperature of 0.2 T_C, i.e., below 500 μK is of the order of 0.1 μK. Therefore, the thermometer fork can easily detect the change in the steady-state temperature of order 10 μK that is typically induced by manipulating the power of the heater fork.

Three series of such steady state data with each point corresponding to a different heater power are plotted in Fig. 5.4 for three different values of Ω. Recalling Equation 1.25, we see that when the measured linewidth of the thermometer tuning fork is used to calculate the quantity corresponding to the abscissa of the graph in Fig. 5.4, it is then rather straightforward to determine the effective area of the orifice (affected by the presence of vortices) as the inverse slope of the fitted straight line, while the parasitic heat leak into the cell is evidently given by the negative intercept with the power (x-)axis.

The most important result is shown in Fig. 5.5. The reflectivity coefficient defined as $R = 1 - A_{\mathrm{eff}}(\Omega)/A_{\mathrm{eff}}(0)$ is plotted versus the angular velocity of rotation,

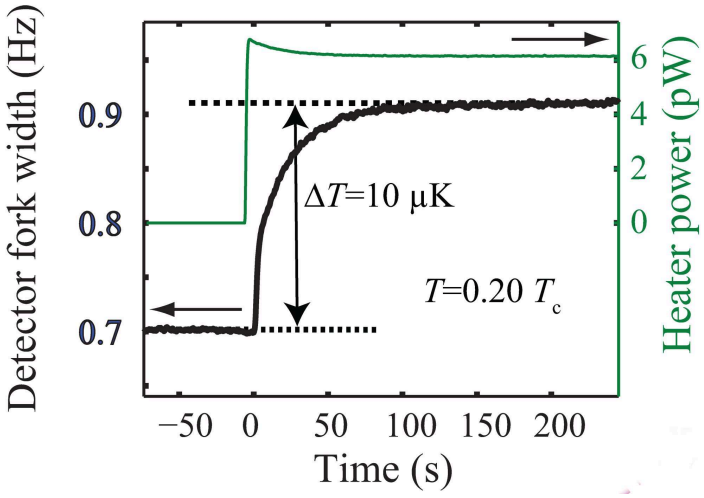

Figure 5.3: Typical responses of the heater and thermometer tuning forks after switching the heater fork on. Please note that the response of the heater fork is plotted in terms of dissipated power. A transient period of about 100 s is observed with both forks, where the temperature in their volume is not stabilized. Heat exchange with the sinter volume is the dominant relaxation process in this time, apart from the first few seconds, which are characterised by faster heat exchange with the NMR volume, see also Fig. 5.6. The overshoot in the heater power happens because until the overall temperature is increased, the heater fork does not experience the full ballistic drag due to the newly created excitations.

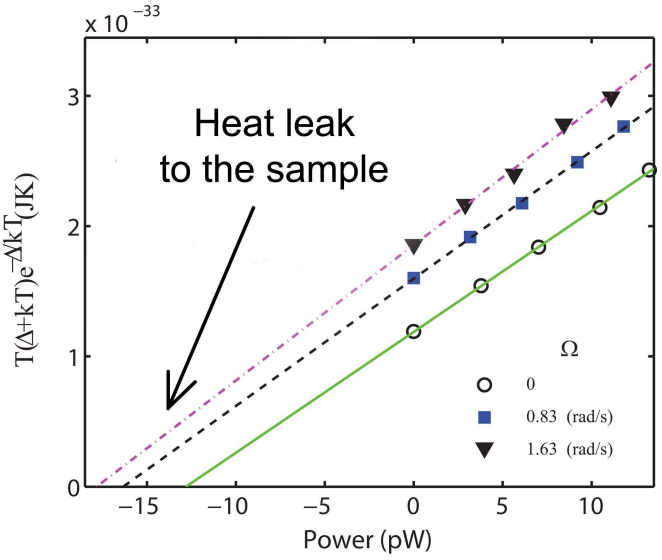

Figure 5.4: A graph illustrating the procedure used to obtain the effective area, A_{eff}, and the parasitic heat leak from the steady state measurements of temperature inside the fork volume. The quantity plotted on the y-axis (chosen based on Eq. 1.25) can be calculated from the linewidth of the thermometer fork [8] (A5), and the dissipated power on the x-axis is given by the amplitude of the heater fork. The effective area can then be determined as the inverse slope of the fitted lines, while the parasitic heat leak to the cell is given by the negative intercept with the x-axis.

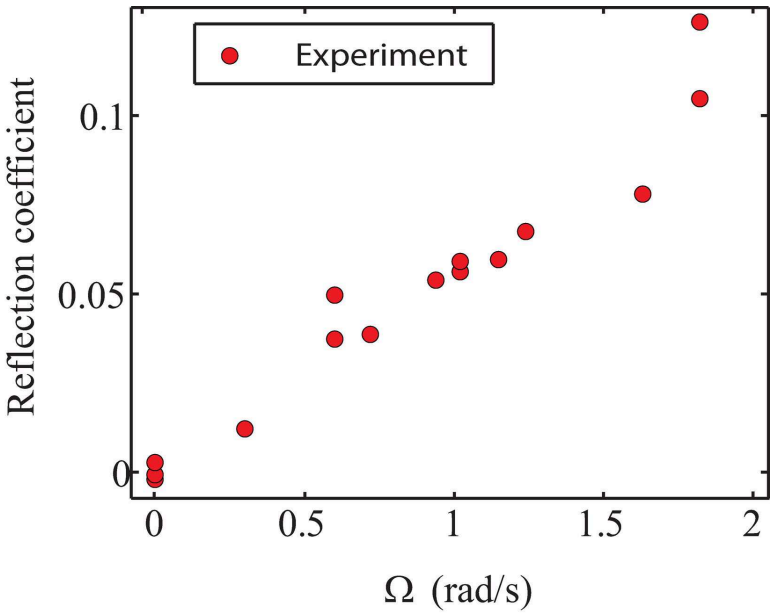

Figure 5.5: Angular velocity dependence of the reflectivity coefficient as defined in the text. While the experimental data show significant scatter at high angular velocities, they seem to be linear with Ω to a good degree of accuracy. The obvious linear fit through zero is not shown here to avoid *a priori* bias, cf. Fig. 5.7 showing these experimental results and the results of a numerical simulation.

and within the experimental error, the expected linear scaling is reproduced. This figure then represents an assertion that the current understanding of the process of Andreev reflection on quantized vortices is more or less correct and provides justification for the use of Andreev reflection in other studies of quantized vorticity and quantum turbulence in ^{3}He–B.

Now, let us go back to the typical response of the thermometer fork to a change in the heater power as shown in Fig. 5.3 and focus on the transient period before the steady state is reached. It is very instructive to analyze these dynamic relaxations and to try to determine the relaxation time constant, assuming an exponential relaxation process. If our interpretation of the measurements is correct, this time constant should correspond to the heat capacity of the helium inside the cell and the thermal resistance determined from the steady state data.

A typical relaxation of the thermometer response is shown in Fig. 5.6. First, the individual regions of the relaxation process are identified, where the initial fast process corresponds to the mutual thermalization of the NMR and fork volumes via the larger orifice in the upper divider, and the later slower decay corresponds to the relaxation of these two volumes to their equilibrium temperatures determined by the parasitic heat leak. Please note that in the experiment, most of the parasitic heat leak to the cell is absorbed in the NMR volume, and therefore the resulting temperatures of the NMR and fork volumes will differ slightly due to the finite thermal resistance associated with the upper divider/orifice. As a consequence, the word "equilibrium" is used somewhat loosely here to refer to a situation which is not, and in principle cannot be, perfect thermodynamical equilibrium, but represents a steady and stable temperature distribution inside the cell, nonetheless. Physically, this approach is justified by the fact that the

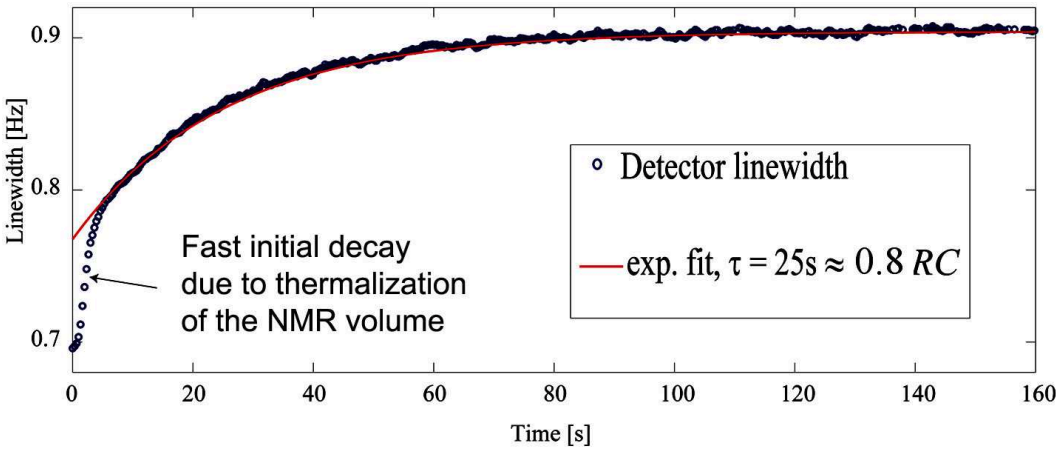

Figure 5.6: Relaxation of the thermometer linewidth after the heater is switched on at zero angular velocity. During the first few seconds (about 5 s), rapid heat exchange between the fork and NMR volumes occurs, through the larger upper orifice of about 0.7 mm diameter. This is followed by the joint thermalization of these two volumes to the sinter volume through the small lower orifice of diameter about 0.3 mm, which corresponds to the long region of approximately exponential decay with a time constant of about 25 s. Due to the finite heat leak to the cell, the final temperature of the cell is not equal to that of the sinter volume, see the text for details. Nevertheless, the heat transport properties can be analysed from these data, as to a good degree of approximation, they depend only on the known absolute temperature of the fork volume and the effective area of the orifice, and not on the temperature difference between the fork and sinter volumes. Upon closer inspection, it is found that the long decay region is not strictly exponential. If the time constant is determined for each point separately from the (smoothed) derivative of this decay, it is found that there is an overall increasing tendency, and that the time constant may vary by tenths of percent of its value in the region, where it can still be derived from the measured data reliably.

thermal resistance of the upper orifice is at least an order of magnitude lower than the thermal resistance of the lower orifice, which we are interested in, and therefore the associated steady state temperature gradients will also scale accordingly. This means that the temperature drop between the NMR and fork volumes will be at least an order of magnitude lower than the temperature difference between the fork and sinter volumes. Therefore, the exact temperature of the NMR volume is of little consequence to the interpretation of the data, except for the initial part of the relaxation.

The relaxation time constant is then determined using a linear fit of the relevant part of the decay plotted in a log-linear graph, with the final value of the linewidth subtracted. As it is difficult to determine this final value, or baseline, from the data with sufficient precision, the points too close to the baseline are excluded from the fitting as well as the initial region, in order to minimize the error in the determined time constant. It turns out that the resulting time constant does not match the one obtained from the steady state thermal resistance and the heat capacity (given by Eqs. 1.26 and 1.27) exactly, but typically is about 20

percent lower. Nevertheless, bearing in mind the simplifications we have made and also the observed fact that the relaxation process is not strictly exponential (although the deviations are rather small), this value can be considered to be in good agreement with the steady state data and taken as a confirmation that, with this degree of accuracy, the heat transport through the orifice by means of ballistic thermal excitations can be described by the equations presented in Section 1.3.

5.3 Computer Simulations of Quasiparticle Motion

To verify the experimental results, a computer simulation was performed by Jere Mäkinen with the idea to track excitation paths and determine whether a given excitation will be reflected or not, depending on its initial position, momentum, and the configuration of vortices. The reflectivity coefficient, i.e., the probability that a random excitation will be Andreev-reflected, is calculated by an integral over the equilibrium ensemble of excitations that may possibly travel through the orifice. A detailed description of the utilised Monte-Carlo integration is again given in Ref. [8] (A5).

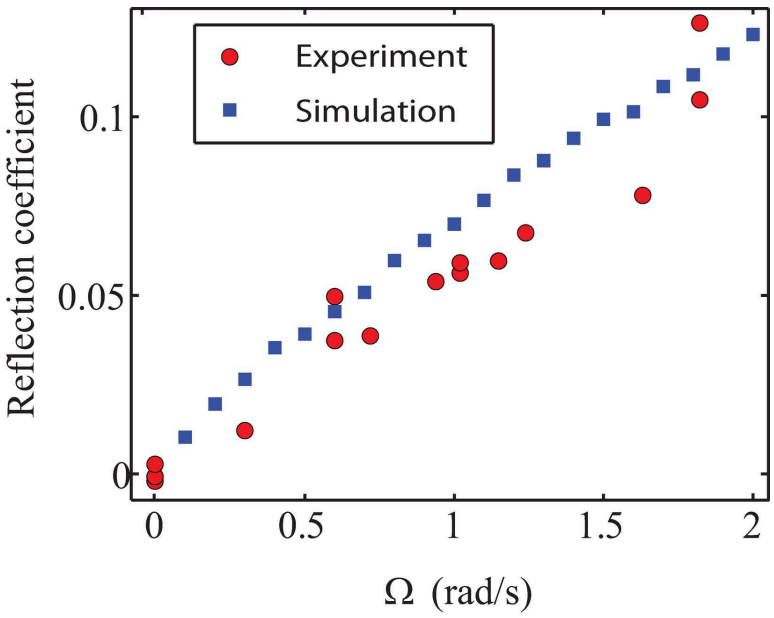

Figure 5.7: Numerical simulation of the reflectivity coefficient at angular velocities from 0 to 2 rad/s. The results are in good agreement with the experimental data and show an approximately linear dependence on Ω with only small deviations towards lower reflectivity at high Ω. However, it is probably not possible to determine any significant influence of vortex screening from these data, as the deviations from linearity are minimal and comparable to the scatter. Moreover, the lack of significant vortex screening is actually in accord with the parameters of the experiment (and the simulation), as the typical intervortex distance of order 0.1 mm is significantly larger than the scattering radius, which can be found from Eq. 1.23 as approximately 1 μm.

One open question before performing this calculation was whether to assume specular scattering on the container walls (used in the exact experimental geometry), or whether to add some degree of diffusion. It was found that purely specular scattering gave unrealistic results, namely that all excitations found their way back through the orifice into the fork volume. This might be caused by the fact that the aspect ratio of the cell is expressed only with finite precision in the simulation, or by a similar property of the performed calculations.

Better results were obtained with fully diffusive scattering, as is shown in Fig. 5.7. The reflectivity from the numerical simulation is found to be in good agreement with the experimental data, and also confirms that it is approximately linear with Ω, although some small deviations can be seen. This simulation strongly supports the claim that the experimental data indeed represent the Andreev reflection of thermal excitations on a rectilinear array of quantized vortices, and that the presented description of this phenomenon is correct to a good degree of accuracy.

6. Conclusions

The aim of this Thesis was to summarize selected areas of the work in which the Author took part during the four years of his PhD. studies, concentrating on experiments with oscillating structures in cryogenic helium fluids. Within this work, the most prominent representative of the various oscillators is the quartz tuning fork, which became the traditional tool for cryogenic fluid dynamics both in the Prague Laboratory of Superfluidity and abroad.

In Chapter 2, the transition to turbulence in classical helium fluids was examined by measuring the drag force acting on various tuning fork resonators, and the expected scaling law of the critical velocity with the square root of the product of frequency and viscosity was confirmed quantitatively over a wide range of experimental parameters. Moreover, the cryogenic measurements of the drag force were compared to the results of room temperature visualization experiments in water using cylinders of square cross-section as models of the prong of a tuning fork under dynamically similar conditions. Two methods of visualization were employed, the Baker technique and the Kalliroscope solution, providing direct visual evidence that the observed crossover in the drag force is indeed related to the emergence of turbulent flow.

The following Chapter 3, extends the drag force measurements to superfluid He II, where the transition to turbulence was found to be characterised by a non-classical feature in the measured drag coefficients. A phenomenological model was formulated, based on gradual coupling of the normal and superfluid components due to the mutual friction force acting through the presence of quantized vortices, and its results were compared to the observations, yielding a good agreement. While the scope of the validity of the model is generally restricted to the hydrodynamic regime of the normal component of He II (above 1 K), extensions of its mathematical formulation to lower temperatures seem possible, although based on different physics.

When analysing the damping forces acting on the tuning fork resonators, it was found that another dissipation mechanism apart from the laminar viscous force or turbulent drag is important – acoustic emission. Using high frequency tuning forks, the dissipation due to acoustic emission was studied systematically and three models of acoustic emission by tuning forks were formulated, incorporating the influence of reflecting boundaries as well. The experimental observations were reproduced to a good degree of accuracy and the models were also used to provide estimates of the relative importance of acoustic emission and viscosity for other types of oscillators resonating at different frequencies. The experimental observations and the proposed models are summarized in Chapter 4.

In Chapter 5 we described a separate investigation performed in the Low Temperature Laboratory of the Aalto University in Espoo, Finland. The aim was to study Andreev reflection of thermal excitations on a well-known configuration of quantized vortices in rotating ^{3}He–B, a measurement which is essential, if Andreev reflection is to be used reliably as a means of detection of quantized vorticity in ^{3}He superfluids. Steady heat flux from a black body radiator was analysed and the thermal resistance due to the tiny orifice in the radiator was found to be affected by the presence of quantized vortices, as expected from

the theory describing Andreev reflection of balistically propagating excitations. The results were double-checked by analysing the thermal relaxation of the same volume and by a numerical simulation of the excitation trajectories, and in both cases, sufficiently good agreement was found.

Altogether, this Thesis mostly represents a summary of the recent experiments performed in Prague on oscillatory flows in classical and superfluid cryogenic ^{4}He liquids, centered around the studies of the transition to turbulence and energy dissipation due to acoustic emission by quartz tuning forks. These experiments are complementary to the work of other groups active in cryogenic fluid dynamics and were often consulted with them, and compared to their results in hope to provide grounds for conclusions of more general validity and to contribute a small piece to the development of our understanding of superfluidity and quantum turbulence.

As is proven by the very fact that the Author could take part in the Andreev reflection measurements in an extent warranting a devoted Chapter in this Thesis, we can say with confidence that in today's cryogenic fluid dynamics community, the relations between the individual groups and their mutual cooperation indeed often extend beyond mere discussions of scientific results and principles. Therefore, if, at the end, one personal wish may be expressed, it is for this friendly and cooperative spirit to last, so that future students and young scientists can benefit from the same opportunities that were, during his studies, presented to the Author of this Thesis.

Bibliography

[1] M. Blažková, D. Schmoranzer, and L. Skrbek. Transition from laminar to turbulent drag in flow due to a vibrating quartz fork. *Phys. Rev. E*, 75(2, Part 2), 2007.

[2] D. Schmoranzer, M. Kráľová, V. Pilcová, W. F. Vinen, and L. Skrbek. Experiments relating to the flow induced by a vibrating quartz tuning fork and similar structures in a classical fluid. *Phys. Rev. E*, 81(6, Part 2), 2010.

[3] M. Blažková, D. Schmoranzer, L. Skrbek, and W. F. Vinen. Generation of turbulence by vibrating forks and other structures in superfluid He-4. *Phys. Rev. B*, 79(5), 2009.

[4] D. Schmoranzer, M. La Mantia, G. Sheshin, I. Gritsenko, A. Zadorozhko, M. Rotter, and L. Skrbek. Acoustic Emission by Quartz Tuning Forks and Other Oscillating Structures in Cryogenic He-4 Fluids. *J. Low Temp. Phys.*, 163(5-6):317–344, 2011.

[5] R. M. Sillitto. Angular Distribution of the Acoustic Radiation from a Tuning Fork. *American J. Phys.*, 34(8):639–644, 1966.

[6] D. O. Clubb, O. V. L. Buu, R. M. Bowley, R. Nyman, and J. R. Owers-Bradley. Quartz tuning fork viscometers for helium liquids. *J. Low Temp. Phys.*, 136(1-2):1–13, 2004.

[7] L. D. Landau and E. M. Lifshitz. *Hydrodynamics*. 2nd ed. edition.

[8] J. J. Hosio, V. B. Eltsov, R. de Graaf, M. Krusius, J. Mäkinen, and D. Schmoranzer. Angular Distribution of the Acoustic Radiation from a Tuning Fork. arXiv:1103.2633v1 [cond-mat.other].

[9] M. Blažková, T. V. Chagovets, M. Rotter, D. Schmoranzer, and L. Skrbek. Cavitation in liquid helium observed in a flow due to a vibrating quartz fork. *J. Low Temp. Phys.*, 150(3-4):194–199, 2008. International Symposium on Quantum Fluids and Solids (QFS-2007), Kazan, Russia, Aug 01-06, 2007.

[10] M. Blažková, D. Schmoranzer, and L. Skrbek. On cavitation in liquid helium in a flow due to a vibrating quartz fork. *Low Temp. Phys.*, 34(4-5):298–307, 2008.

[11] D. Schmoranzer and L. Skrbek. The Use of Vibrating Quartz Forks in Cryogenic Helium Research - On Their Ability to Detect an Externally Applied Flow in Superfluid He-4. In Kes, P. and Jochemsen, R., editor, *25th International Conference on Low Temperature Physics (LT25), part 1 - Cryogenic Technologies and Applications* , volume 150 of *Journal of Physics Conference Series*, 2009.

[12] H. K. Onnes. The liquefaction of helium. *Proc. Koninklijke Akademie van Wetenschappen te Amsterdam*, 11(Part 1):168–185, 1908.

[13] H. K. Onnes. The condensation of helium. *Nature*, 77:559, 1908.

[14] H. K. Onnes. The condensation of helium. *Nature*, 77:581, 1908.

[15] M. Faraday and T. Northmore. *The liquefaction of gases*. Edinburgh, W. F. Clay; London, Simpkin, Marshall, Hamilton, Kent, & co., ltd, 1896.

[16] L. P. Cailletet. The Liquefaction of Oxygen. *Science*, ns-6(128):51–52, 1885.

[17] R. Pictet. *Mémoire sur la liquéfaction de l'oxygène, la liquéfaction et la solidification de l'hydrogène, et sur les théories des changements des corps*. J. Sandoz (Genève), 1878.

[18] Z. F. Wroblewski and K. Olszewski. *Comptes Rendus Acad. Sciences*, 96:1140–1142, 1225–1226, 1883.

[19] K. Olszewski. *Nature*, 51:355, 1895.

[20] J. Dewar. Preliminary Note on the Liquefaction of Hydrogen and Helium. *Proc. Royal Soc. London*, 63:256–258, 1898.

[21] H. K. Onnes. Further experiments with liquid helium D - On the change of the electrical resistance of pure metals at very low temperatures, etc V, The disappearance of the resistance of mercury. *Proc. Koninklijke Akademie van Wetenschappen te Amsterdam*, 14(Part 1):113–115, 1911.

[22] P. Kapitza. Viscosity of liquid helium below the gimel-point. *Nature*, 141:74, 1938.

[23] P. Kapitza. Viscosity of liquid helium below the lambda-point. *Comptes Rendus Acad. Sciences de l'URSS*, 18:21–23, 1938.

[24] J. F. Allen and A. D. Misener. Flow of liquid helium II. *Nature*, 141:75, 1938.

[25] J. F. Allen and A. D. Misener. Flow phenomena in liquid helium II. *Nature*, 142:643–644, 1938.

[26] J. F. Allen and A. D. Misener. The properties of flow of liquid HeII. *Proc. Royal Soc. London Series A-Math. Phys. Sciences*, 172(A951):0467–0491, 1939.

[27] S. N. Bose. Thermal equilibrium of the radiation field in the presence of matter. *Zeitschrift fur Physik*, 27:384–392, 1924.

[28] A. Einstein. Quantum theory of monatomic ideal gases. *Sitzungsberichte Preuss. Akademie Wissenschaften Phys.-Math. Klasse*, pages 261–267, 1924.

[29] A. Einstein. Quantum theory of mono-atomic ideal gas. Second paper. *Sitzungsberichte Preuss. Akademie Wissenschaften Phys.-Math. Klasse*, pages 3–14, 1925.

[30] A. Einstein. Quantum theory of the ideal gas. *Sitzungsberichte Preuss. Akademie Wissenschaften Phys.-Math. Klasse*, pages 18–25, 1925.

[31] F. London. The lambda-phenomenon of liquid helium and the Bose-Einstein degeneracy. *Nature*, 141:643–644, 1938.

[32] F. London. On the Bose-Einstein condensation. *Physical Review*, 54(11):947–954, 1938.

[33] F. London. The state of liquid helium near absolute zero. *J. Phys. Chem.*, 43(1):49–69, 1939.

[34] L. Tisza. Transport phenomena in helium II. *Nature*, 141:913, 1938.

[35] L. Tisza. On the thermal supraconductibility of liquid helium II and the Bose-Einstein statistics. *Comptes Rendus Acad. Sciences*, 207:1035–1037, 1938.

[36] L. Tisza. The viscosity of liquid helium and the Bose-Einstein statistic. *Comptes Rendus Acad. Sciences*, 207:1186–1189, 1938.

[37] L. D. Landau. Theory of the superfluidity of helium II. *Physical Review*, 60(4):356–358, 1941.

[38] L. D. Landau. The theory of superfluidity of helium II. *J. Phys.-USSR*, 5(1-6):71–90, 1941.

[39] L. D. Landau. On the hydrodynamics of helium II. *J. Phys.-USSR*, 8(1-6):1–3, 1944.

[40] L. D. Landau. *J. Phys.-USSR*, 11:91, 1947.

[41] L. D. Landau. K Teorii Sverkhtekuchesti. *Doklady Akademii Nauk SSSR*, 61(2):253–256, 1948.

[42] L. D. Landau. On the Theory of Superfluidity. *Physical Review*, 75(5):884–885, 1949.

[43] E. L. Andronikashvili. *Journal of Physics (Moscow)*, 10:201, 1946.

[44] E. L. Andronikashvili. *Temperaturnaya Zavisimost Normalnoi Plotnosti Geliya-II. *Zhur. Eksper. i Teor. Fiziki*, 18(5):424–428, 1948.

[45] E. L. Andronikashvili. *Issledovanie Vyazkosti Normalnoi Komponenty Geliya-II. *Zhur. Eksper. i Teor. Fiziki*, 18(5):429–433, 1948.

[46] L. Onsager. . *Nuovo Cimento*, 6(Suppl. 2):249, 1949.

[47] O. Penrose and L. Onsager. Bose-Einstein Condensation and Liquid Helium. *Physical Review*, 104(3):576–584, 1956.

[48] R. P. Feynman. Atomic Theory of Liquid Helium Near Absolute Zero. *Physical Review*, 91(6):1301–1308, 1953.

[49] R. P. Feynman. Atomic Theory of the lambda-transition in Helium. *Physical Review*, 91(6):1291–1301, 1953.

[50] R. P. Feynman. Atomic Theory of the 2-fluid Model of Liquid Helium. *Physical Review*, 94(2):262–277, 1954.

[51] R. P. Feynman. Chapter ii application of quantum mechanics to liquid helium. volume 1 of *Progress in Low Temperature Physics*, pages 17 – 53. Elsevier, 1955.

[52] D. D. Osheroff, R. C. Richardson, and D. M. Lee. Evidence for a New Phase of Solid He-3. *Phys. Rev. Lett*, 28(14):885, 1972.

[53] D. D. Osheroff, W. J. Gully, R. C. Richardson, and D. M. Lee. New Magnetic Phenomena in Liquid He-3 Below 3 mK. *Phys. Rev. Lett.*, 29(4):920, 1972.

[54] J. J. Niemela, L. Skrbek, K. R. Sreenivasan, and R. J. Donnelly. Turbulent convection at very high Rayleigh numbers. *Nature*, 404(6780):837–840, 2000.

[55] J. J. Niemela, L. Skrbek, K. R. Sreenivasan, and R. J. Donnelly. The wind in confined thermal convection. *Journal of Fluid Mechanics*, 449:169–178, 2001.

[56] P. E. Roche, B. Castaing, B. Chabaud, and B. Hebral. Observation of the 1/2 power law in Rayleigh-Benard convection. *Phys. Rev. E*, 63(4, Part 2):art. no.–045303, 2001.

[57] P. E. Roche, B. Castaing, B. Chabaud, and B. Hebral. Prandtl and Rayleigh numbers dependences in Rayleigh-Benard convection. *Europhys. Lett.*, 58(5):693–698, 2002.

[58] J. J. Niemela, S. Babuin, and K. R. Sreenivasan. Turbulent rotating convection at high Rayleigh and Taylor numbers. *Journal of Fluid Mechanics*, 649:509–522, 2010.

[59] M. Assenheimer and V. Steinberg. Rayleigh-Benard Convection Near the Gas-Liquid Critical-Point. *Phys. Rev. Lett.*, 70(25):3888–3891, 1993.

[60] J. Liu and G. Ahlers. Rayleigh-Benard convection in binary-gas mixtures: Thermophysical properties and the onset of convection. *Phys. Rev. E*, 55(6, Part A):6950–6968, 1997.

[61] S. Ashkenazi and V. Steinberg. Spectra and statistics of velocity and temperature fluctuations in turbulent convection. *Phys. Rev. Lett.*, 83(23):4760–4763, 1999.

[62] S. Ashkenazi and V. Steinberg. High Rayleigh number turbulent convection in a gas near the gas-liquid critical point. *Phys. Rev. Lett.*, 83(18):3641–3644, 1999.

[63] L. D. Landau. The Theory of a Fermi Liquid. *Soviet Physics JETP-USSR*, 3(6):920–925, 1957.

[64] A. A. Abrikosov and I. M. Khalatnikov. Theory of the Fermi Liquid. *Usp. Fiz. Nauk*, 66(2):177–212, 1958.

[65] E. M. Lifschitz and L. P. Pitaevski. In *Statistical Physics part 2*, Landau and Lifschitz course of Theoretical physics. Pergamon Press, Oxford, UK, 1980.

[66] Y. D. Anufriyev. Use of Pomeranchuk Effect to Obtain Low Temperatures. *JETP Lett.-USSR*, 1(6):155, 1965.

[67] I. Pomeranchuk. . *Zh. Exp. i Teor. Fiziki*, 20:919, 1950.

[68] J. F. Allen and A. D. Misener. Flow of liquid helium II. *Nature*, 141:75, 1938.

[69] J. G. Daunt and K. Mendelssohn. Surface transport in liquid helium II. *Nature*, 143:719–720, 1939.

[70] E. Cheng, M. W. Cole, W. F. Saam, and J. Treiner. Helium Prewetting and Nonwetting on Weak-Binding Substrates. *Phys. Rev. Lett.*, 67(8):1007–1010, 1991.

[71] P. J. Nacher and J. Dupontroc. Experimental Evidence for Nonwetting with Superfluid Helium. *Phys. Rev. Lett.*, 67(21):2966–2969, 1991.

[72] E. F. Burton. Viscosity of helium I and helium II. *NATURE*, 135:265, 1935.

[73] J. O. Wilhelm, A. D. Misener, and A. R. Clark. The viscosity of liquid helium. *Proc. Royal Soc. London Series A-Math. Phys. Sci.*, 151(A873):0342–0347, 1935.
[74] H. Palevsky, K. Otnes, and K. E. Larsson. Excitations of Rotons in Helium-II by Cold Neutrons. *Physical Review*, 112(1):11–18, 1958.
[75] J. L. Yarnell, G. P. Arnold, P. J. Bendt, and E. C. Kerr. Excitations in Liquid Helium - Neutron Scattering Measurements. *Physical Review*, 113(6):1379–1386, 1959.
[76] D. G. Henshaw and A. D. B. Woods. Modes of Atomic Motions in Liquid Helium by Inelastic Scattering of Neutrons. *Physical Review*, 121(5):1266, 1961.
[77] J. Bardeen, L. N. Cooper, and J. R. Schrieffer. . *Physical Review*, 108:1175, 1957.
[78] N. N. Bogoliubov. K Teorii Sverkhtekuchesti. *Izv. Akademii Nauk USSR*, 11(1):77, 1947.
[79] N. N. Bogoliubov. On the Theory of Superfluidity. *Journal of Physics*, 11(1):23–32, 1947.
[80] V. F. Sears, E. C. Svensson, P. Martel, and A. D. B. Woods. Neutron-scattering determination of the momentum distribution and the condensate fraction in liquid 4he. *Phys. Rev. Lett.*, 49(4):279–282, 1982.
[81] D. V. Osborne. The Rotation of Liquid Helium-II. *Proc. Royal Soc. London Series A-Math. Phys. Sciences*, 63(368):909–912, 1950.
[82] E. Gross. Structure of a quantized vortex in boson systems. *Il Nuovo Cimento (1955-1965)*, 20:454–477, 1961.
[83] L. P. Pitaevski. Vortex lines in an imperfect bose gas. *Soviet Physics JETP-USSR*, 13(2), 1961.
[84] Makoto Tsubota, Kenichi Kasamatsu, and Masahito Ueda. Vortex lattice formation in a rotating bose-einstein condensate. *Phys. Rev. A*, 65(2):023603, 2002.
[85] T. Araki, M. Tsubota, and S. K. Nemirovskii. Energy spectrum of superfluid turbulence with no normal-fluid component. *Phys. Rev. Lett.*, 89(14):145301, 2002.
[86] A. P. Finne, T. Araki, R. Blaauwgeers, V. B. Eltsov, N. B. Kopnin, M. Krusius, L. Skrbek, M. Tsubota, and G. E. Volovik. An intrinsic velocity-independent criterion for superfluid turbulence. *Nature*, 424(6952):1022–1025, 2003.
[87] W. F. Vinen. Detection of Single Quanta of Circulation in Rotating Helium-II. *Nature*, 181(4622):1524–1525, 1958.
[88] W. F. Vinen. Detection of Single Quanta of Circulation in Liquid Helium-II. *Proc. Royal Soc. London Series A-Math. Phys. Sciences*, 260(130):218, 1961.
[89] E. J. Yarmchuk and R. E. Packard. Photographic Studies of Quantized Vortex Lines. *J. Low Temp. Phys.*, 46(5-6):479–515, 1982.
[90] R. J. Donnelly and C. F. Barenghi. The observed properties of liquid helium at the saturated vapor pressure. *J. Phys. Chem. Reference Data*, 27(6):1217–1274, 1998.
[91] W. F. Vinen. Mutual Friction in a Heat Current in Liquid Helium-II .1. Experiments on Steady Heat Currents. *Proc. Royal Soc. London Series A-Math. Phys. Sciences*, 240(1220):114–127, 1957.
[92] W. F. Vinen. Mutual Friction in a Heat Current in Liquid Helium-II .2. Experiments on Transient Effects. *Proc. Royal Soc. London Series A-Math. Phys. Sciences*, 240(1220):128, 1957.
[93] W. F. Vinen. Mutual Friction in a Heat Current in Liquid Helium-II .3. Theory of the Mutual Friction. *Proc. Royal Soc. London Series A-Math. Phys. Sciences*, 242(1231):493–515, 1957.
[94] W. F. Vinen. Mutual Friction in a Heat Current in Liquid Helium-II .4. Critical Heat Currents in Wide Channels. *Proc. Royal Soc. London Series A-Math. Phys.*

Sciences, 243(1234):400–413, 1958.

[95] P. V. E. McClintock and R. M. Bowley. volume 1 of *Progress in Low Temperature Physics*, page 3. Elsevier, 1995.

[96] J. Jager, B. Schuderer, and W. Schoepe. Turbulent and Laminar Drag of Superfluid Helium on an Oscillating Microsphere. *Phys. Rev. Lett.*, 74(4):566–569, 1995.

[97] M. Niemetz and W. Schoepe. Stability of Laminar and turbulent flow of superfluid He-4 at mK temperatures around an oscillating microsphere. *J. Low Temp. Phys.*, 135(5-6):447–469, 2004.

[98] L. D. Landau. On the Theory of a Fermi Liquid. *Soviet Physics JETP-USSR*, 8(1):70–74, 1959.

[99] A. A. Abrikosov and I. M. Khalatnikov. The Theory of a Fermi Liquid - (The Properties of Liquid He-3 at Low Temperatures). *Reports on Progress in Physics*, 22:329–367, 1959.

[100] A. J. Leggett. Theory of a Superfluid Fermi Liquid. I. General Formalism and Static Properties. *Physical Review*, 140(6A):1869–&, 1965.

[101] A. J. Leggett. Theory of a Superfluid Fermi Liquid. 2. Collective Oscillations. *Physical Review*, 147(1):119–&, 1966.

[102] D. VollHardt and P. Wölfle. *The Superfluid Phases of Helium 3.* Taylor & Francis, London, UK, 1990.

[103] V. B. Eltsov, R. de Graaf, R. Hanninen, M. Krusius, R. F. Solntsev, V. S. L`vov, A. I. Golov, and P. M. Walmsley. volume 16 of *Progress in Low Temperature Physics*. Elsevier B.V., Amsterdam, 2009. arXiv:0803.3225.

[104] P. J. Hakonen, O. T. Ikkala, S. T. Islander, O. V. Lounasmaa, T. K. Markkula, P. Roubeau, K. M. Saloheimo, G. E. Volovik, E. L. Andronikashvili, D. I. Garibashvili, and J. S. Tsakadze. NMR Experiments on Rotating Superfluid 3He-A - Evidence for Vorticity. *Phys. Rev. Lett.*, 48(26):1838–1841, 1982.

[105] P. J. Hakonen, O. T. Ikkala, S. T. Islander, O. V. Lounasmaa, and G. E. Volovik. NMR Experiments on Rotating Superfluid 3He-A and 3He-B and Their Theoretical Interpretation. *J. Low Temp. Phys.*, 53(3-4):425–476, 1983.

[106] H. K. Seppälä and G. E. Volovik. . *J. Low Temp. Phys.*, 3/4:278, 1983.

[107] J. Karimäki and E. V. Thuneberg. . *Phys. Rev. B*, 60, 1999.

[108] Ville Ruutu. *NMR Experiments on Topological Defects in 3He Superfluids.* PhD thesis, Helsinki Univeristy of Technology, Finland.

[109] Rob Blaauwgeers. *Unconventional Quantized Vortices-A study on 3He and UPt3.* PhD thesis, Universiteit Leiden, Netherlands and Helsinki University of Technology, Finland.

[110] J. P. Pekola, J. T. Simola, P. J. Hakonen, M. Krusius, O. V. Lounasmaa, K. K. Nummila, G. Mamnishvili, R. E. Packard, and G. E. Volovik. Phase-Diagram of the 1st-order Vortex-Core Transition in Superfluid 3He-B. *Phys. Rev. Lett.*, 53(6):584–587, 1984.

[111] M. P. Enrico, S. N. Fisher, A. M. Guénault, G. R. Pickett, and K. Torizuka. Direct Observation of the Andreev Reflection of a Beam of Excitations in Superfluid 3He-B. *Phys. Rev. Lett.*, 70(12):1846–1849, 1993.

[112] Ü. Parts, Y. Kondo, J. S. Korhonen, M. Krusius, and E. V. Thuneberg. Vortex Layer on the Interface Between the A-phase and B-phase in Superfluid He-3. *Phys. Rev. Lett.*, 71(18):2951–2954, 1993.

[113] Lord Kelvin (Sir William Thomson). Hydrodynamics and general dynamics. In *Mathematical and Physical Papers Vol. 4*. Cambridge University Press, Cambridge, England, 1910.

[114] R. Blaauwgeers, V. B. Eltsov, G. Eska, A. P. Finne, R. P. Haley, M. Krusius,

J. J. Ruohio, L. Skrbek, and G. E. Volovik. Shear flow and Kelvin-Helmholtz instability in superfluids. *Phys. Rev. Lett.*, 89(15), 2002.

[115] A. F. Andreev. The Thermal Conductivity of the Intermediate State in Superconductors. *Soviet Physics JETP-USSR*, 19(5):1228–1231, 1964.

[116] C. F. Barenghi, Y. A. Sergeev, and N. Suramlishvili. Ballistic propagation of thermal excitations near a vortex in superfluid He-3-B. *Phys. Rev.B.*, 77(10), 2008.

[117] A. M. Guénault and G. R. Picket. Liquid-He-3 at Ultralow Temperatures - The Long Mean Free-Path Limit. *Physica B & C*, 126(1-3):260–266, 1984.

[118] C. Bauerle, Y. M. Bunkov, S. N. Fisher, and H. Godfrin. Temperature scale and heat capacity of superfluid He-3-B in the 100 mu K range. *Phys. Rev. B*, 57(22):14381–14386, 1998.

[119] K. Karrai and R. D. Grober. Tip-sample distance control for near-field scanning optical microscopes. In M. A. Paesler and P. T. Moyer, editors, *Near-Field Optics*, volume 2535 of *Proc. SPIE*, pages 69–81, 1995.

[120] R.D. Grober, J. Acimovic, J. Schuck, D. Hessman, P. J. Kindlemann, J. Hespanha, S. Morse, K. Karrai, I. Tiemann, and S. Manus. . *Rev. Sci. Instrum.*, 71:2776, 2000.

[121] R. Blaauwgeers, M. Blažková, M. Človečko, V. B. Eltsov, R. de Graaf, J. Hosio, M. Krusius, D. Schmoranzer, W. Schoepe, L. Skrbek, P. Skyba, R. E. Solntsev, and D. E. Zmeev. Quartz tuning fork: Thermometer, pressure- and viscometer for helium liquids. *J. Low Temp. Phys.*, 146(5-6):537–562, 2007.

[122] E. M. Pentti, J. T. Tuoriniemi, A. J. Salmela, and A. P. Sebedash. Quartz Tuning Fork in Helium. *J. Low Temp. Phys.*, 150(3-4):555–560, 2008.

[123] E. M. Pentti, J. T. Tuoriniemi, A. J. Salmela, and A. P. Sebedash. Solubility of He-3 in He-4 at millikelvin Temperatures up to the Melting Pressure Measured by a Quartz Tuning Fork. *Phys. Rev. B*, 78(6), 2008.

[124] J. M. Gere and S. P. Timoshenko. *Mechanics of Materials*. Third Edition edition.

[125] S. P. Timoshenko. On the correction for shear of the differential equation for transverse vibrations of prismatic bars. *Philosophical Magazine*, 41(245, Sp. Iss. 6th Series):744–746, 1921.

[126] S. P. Timoshenko. On the transverse vibrations of bars of uniform cross-section. *Philosophical Magazine*, 43(253, Sp. Iss. 6th Series):125–131, 1922.

[127] A. C. Hollis Hallett. . *Proc. Royal Soc.*, A210:404, 1952.

[128] C. B. Benson and A. C. Hollis Hallett. . *Can. J. Phys.*, 34:668, 1956.

[129] R. J. Donnelly and O Penrose. Oscillations of Liquid Helium in a U-tube. *Physical Review*, 103(5):1137–1144, 1956.

[130] R. J. Donnelly and A. C. Hollis Hallett. Periodic Boundary Layer Experiments in Liquid Helium. *Annals of Physics*, 3(3):320–345, 1958.

[131] H. C. Kramers, J. D. Wasscher, and C. J. Gorter. The specific heat of liouid helium between 0.25 and 1.9Â°k. *Physica*, 18(5):329 – 338, 1952.

[132] J. Wiebes, C. G. NielsHakkenberg, and H. C. Kramers. New experiments on the specific heat of liquid 4he below 0.7Â°k. *Physica*, 23(6-10):625 – 632, 1957.

[133] K. W. Schwarz and R. W. Stark. Phonon-limited drift of the electron bubble in superlfuid helium. *Phys. Rev. Lett.*, 21(14):967–969, 1968.

[134] G. Baym, R. G. Barrera, and C. J. Pethick. Mobility of the electron bubble in superlfuid helium. *Phys. Rev. Lett.*, 22(1):20–23, 1969.

[135] K. W. Schwarz and R. W. Stark. Scattering of positive ions by elementary excitations in superfluid helium. *Phys. Rev. Lett.*, 22(24):1278–1280, 1969.

[136] M. Morishita, T. Kuroda, A. Sawada, and T. Satoh. Mean Free Path Effects in Superfluid 4He. *J. Low Temp. Phys.*, 76(5-6), 1989.

[137] A. M. Guénault, V. Keith, C. J. Kennedy, S. G. Mussett, and G. R. Picket. The Mechanical Behavior of a Vibrating Wire in Superfluid 3He-B in the Ballistic Limit. *J. Low Temp. Phys.*, 62(5-6):511–523, 1986.

[138] R.D. Finch, R. Kagiwada, M. Barmatz, and I. Rudnick. . *Physical Review*, 134:A 1425, 1964.

[139] R.D. Finch and T. G. J. Wang. . *J. Acoust. Soc. Am.*, 39:511, 1966.

[140] R.D. Finch, T. G. J. Wang, R. Kagiwada, M. Barmatz, and I. Rudnick. . *J. Acoust. Soc. Am.*, 40:211, 1966.

[141] P. D. Jarman and K. J. Taylor. . *J. Low Temp. Phys.*, 2:389, 1970.

[142] P. L. Marston. . *J. Low Temp. Phys.*, 25:383, 1976.

[143] H.J. Maris, S. Balibar, and M.S. Petersen. . *J. Low Temp. Phys.*, 93:1069, 1993.

[144] S. Balibar. . *J. Low Temp. Phys.*, 129:363, 2002.

[145] H. Yano, T. Ogawa, A. Mori, Y. Miura, Y. Nago, K. Obara, O. Ishikawa, and T. Hata. Transition to Quantum Turbulence Generated by Thin Vibrating Wires in Superfluid He-4. *J. Low Temp. Phys.*, 156(3-6):132–144, 2009.

[146] D. I. Bradley, S. N. Fisher, A. M. Guenault, R. P. Haley, V. Tsepelin, G. R. Pickett, and K. L. Zaki. The Transition to Turbulent Drag for a Cylinder Oscillating in Superfluid He-4: A Comparison of Quantum and Classical Behavior. *J. Low Temp. Phys.*, 154(3-4):97–116, 2009.

[147] W. F. Vinen, L. Skrbek, and H. A. Nichol. The nucleation of superfluid turbulence at very low temperatures by flow through a grid. *J. Low Temp. Phys.*, 135(5-6):423–445, 2004.

[148] H. A. Nichol, L. Skrbek, P. C. Hendry, and P. V. E. McClintock. Experimental investigation of the macroscopic flow of HeII due to an oscillating grid in the zero temperature limit. *Phys. Rev. E*, 70(5, Part 2), 2004.

[149] D. Charalambous, L. Skrbek, P. C. Hendry, P. V. E. McClintock, and W. F. Vinen. Experimental investigation of the dynamics of a vibrating grid in superfluid He-4 over a range of temperatures and pressures. *Phys. Rev. E*, 74(3, Part 2), 2006.

[150] D. I. Bradley, D. O. Clubb, S. N. Fisher, A. M. Guenault, R. P. Haley, C. J. Matthews, G. R. Pickett, V. Tsepelin, and K. Zaki. Decay of pure quantum turbulence in superfluid He-3-B. *Phys. Rev. Lett.*, 96(3), 2006.

[151] V. B. Efimov, Deepak Garg, M. Giltrow, P. V. E. McClintock, L. Skrbek, and W. F. Vinen. Experiments on a High Quality Grid Oscillating in Superfluid He-4 at Very Low Temperatures. *J. Low Temp. Phys.*, 158(3-4):462–467, 2010.

[152] W. Schoepe. Fluctuations and stability of superfluid turbulence at mK temperatures. *Phys. Rev. Lett.*, 92(9), 2004.

[153] J Luzuriaga. Measurements in the laminar and turbulent regime of superfluid He-4 by means of an oscillating sphere. *J. Low Temp. Phys.*, 108(3-4):267–277, 1997.

[154] A. M. Hemmati, S. Fuzier, E. Bosque, and S. W. Van Sciver. Drag Measurement on an Oscillating Sphere in Helium II. *J. Low Temp. Phys.*, 156(3-6):71–83, 2009.

[155] D. I. Bradley, M. J. Fear, S. N. Fisher, A. M. Guenault, R. P. Haley, C. R. Lawson, P. V. E. McClintock, G. R. Pickett, R. Schanen, V. Tsepelin, and L. A. Wheatland. Transition to Turbulence for a Quartz Tuning Fork in Superfluid He-4. *J. Low Temp. Phys.*, 156(3-6):116–131, 2009.

[156] V. Chagovets, I. Gritsenko, E. Rudavskii, G. Sheshin, and A. Zadorozhko. Flow regimes of the superfluid helium caused by oscillating quartz tuning fork. In Kes, P. and Jochemsen, R., editor, *25th International Conference on Low Temperature Physics (LT25), Part 3 - Quantum Gases, Liquids and Solids*, volume 150 of *Journal of Physics Conference Series*, 2009.

[157] J. Salort and P. E. Roche. private communication.

[158] S. Triqueneaux, E. Collin, D. J. Cousins, T. Fournier, C. Bauerle, Y. M. Bunkov, and H. Godfrin. Microfabrication of silicon vibrating wires. *Physica B*, 284(Part 2):2141–2142, 2000. 22nd International Conference on Low Temperature Physics, Helsinki, Finland, Aug 04-11, 1999.

[159] E. Collin, L. Filleau, T. Fournier, Y. M. Bunkov, and H. Godfrin. Silicon vibrating wires at low temperatures. *J. Low Temp. Phys.*, 150(5-6):739–790, 2008.

[160] E. Collin, J. Kofler, J. S. Heron, O. Bourgeois, Y. M. Bunkov, and H. Godfrin. Novel "Vibrating Wire Like" NEMS and MEMS Structures for Low Temperature Physics. *J. Low Temp. Phys.*, 158(3-4):678–684, 2010.

[161] E. Collin, T. Moutonet, J. S. Heron, O. Bourgeois, Y. M. Bunkov, and H. Godfrin. A Tunable Hybrid Electro-magnetomotive NEMS Device for Low Temperature Physics. *J. Low Temp. Phys.*, 162(5-6):653–660, 2011.

[162] AV Gordeev, TV Chagovets, F Soukup, and L Skrbek. Decaying counterflow turbulence in HeII. *J. Low Temp. Phys.*, 138(3-4, Sp. Iss. SI):549–554, 2005. International Symposium on Quantum Fluids and Solids (QFS 2004), Povo, Italy, Jul 05-09, 2004.

[163] C. F. Barenghi, A. V. Gordeev, and L. Skrbek. Depolarization of decaying counterflow turbulence in HeII. *Phys. Rev. E*, 74(2, Part 2), 2006.

[164] T. V. Chagovets and L. Skrbek. Steady and decaying flow of he II in a channel with ends blocked by superleaks. *Phys. Rev. Lett.*, 100(21), 2008.

[165] T. V. Chagovets and L. Skrbek. On Flow of He II in Channels with Ends Blocked by Superleaks. *J. Low Temp. Phys.*, 153(5-6):162–188, 2008. Symposium on Quantum Phenomena and Devices at Low Temperatures, Espoo, Finland, 2008.

[166] Tymofiy V. Chagovets. *Experimental Investigation of Quantum Turbulence in Superfluid 4He*. PhD thesis. Doctoral Thesis, Charles University in Prague, Czech Republic.

[167] C. B. Winkelmann, E. Collin, Y. M. Bunkov, and H. Godfrin. Vibrating wire thermometry in superfluid He-3. *J. Low Temp. Phys.*, 135(1-2):3–14, 2004. Conference on Pushing Physics at Low Temperatures held in Honour of Francisco LaCruz, San Carlos Bariloche, Argentina, Sep 25-26, 2003.

[168] H. Honji. Streaked Flow Around an Oscillating Circular-Cylinder. *J. Fluid Mech.*, 107:509–520, 1981.

[169] P. Hall. On the Stability of the Unsteady Boundary-Layer on a Cylinder Oscillating Transversely in a Viscous Fluid. *J. Fluid Mech.*, 146:347–367, 1984.

[170] T. Sarpkaya. Force on a Circular-Cylinder in Viscous Oscillatory Flow at Low Keulegan-Carpenter Numbers. *J. Fluid Mech.*, 165:61–71, 1986.

[171] E. D. Obasaju, P. W. Bearman, and J. M. R. Graham. A Study of Forces, Circulation and Vortex Patterns Around a Circular-Cylinder in Oscillating Flow. *J. Fluid Mech.*, 196:467–&, 1988.

[172] M. Tatsuno and P. W. Bearman. A Visual Study of the Flow Around an Oscillating Circular-Cylinder at Low Keulegan-Carpenter Numbers and Low Stokes Numbers. *J. Fluid Mech.*, 211:157–182, 1990.

[173] R. D. McCarty. Thermophysical Properties of Helium-4 from 2 to 1500 K with Pressures to 1000 Atmospheres. Technical report, 1972. Technical Note 631, National Bureau of Standards.

[174] V. D. Arp and R. D. McCarty. The properties of critical helium gass. Technical report, 1998. Tech. Rep., U. of Oregon.

[175] D. J. Baker. . *J. Fluid Mech.*, 26(573), 1966.

[176] Kalliroscope. See www.kalliroscope.com/juices/rheoscopic_fluids.htm.

[177] L. Skrbek, J. J. Niemela, and R. J. Donnelly. Four regimes of decaying grid turbulence in a finite channel. *Phys. Rev. Lett.*, 85(14):2973–2976, 2000.

[178] L. Skrbek, J. J. Niemela, and K. R. Sreenivasan. Energy spectrum of grid-generated HeII turbulence. *Phys. Rev. E*, 64(6, Part 2), 2001.

[179] P. M. Walmsley, A. A. Levchenko, S. E. May, and A. I. Golov. Detection of vortices in superfluid He-4 in the T=0 limit using charged vortex rings. *J. Low Temp. Phys.*, 146(5-6):511–523, 2007.

[180] P. M. Walmsley, A. I. Golov, H. E. Hall, A. A. Levchenko, and W. F. Vinen. Dissipation of quantum turbulence in the zero temperature limit. *Phys. Rev. Lett.*, 99(26), 2007.

[181] P. M. Walmsley and A. I. Golov. Quantum and quasiclassical types of superfluid turbulence. *Phys. Rev. Lett.*, 100(24), 2008.

[182] A. I. Golov, P. M. Walmsley, and P. A. Tompsett. Charged Tangles of Quantized Vortices in Superfluid He-4. *J. Low Temp. Phys.*, 161(5-6, Sp. Iss. SI):509–525, 2010.

[183] P. M. Walmsley, A. I. Golov, H. E. Hall, W. F. Vinen, and A. A. Levchenko. Decay of Turbulence Generated by Spin-Down to Rest in Superfluid He-4. *J. Low Temp. Phys.*, 153(5-6):127–139, 2008. Symposium on Quantum Phenomena and Devices at Low Temperatures, Espoo, Finland, 2008.

[184] A. I. Golov and P. M. Walmsley. Homogeneous Turbulence in Superfluid He-4 in the Low-Temperature Limit: Experimental Progress. *J. Low Temp. Phys.*, 156(3-6):51–70, 2009.

[185] R. A. Ashton, L. B. Opatowsky, and J. T. Tough. Turbulence in Pure Superfluid Flow. *Phys. Rev. Lett.*, 46(10):658–661, 1981.

[186] J. T. Tough, R. A. Ashton, and L. B. Opatowsky. Superfluid Turbulence in Counterflow and Pure Superflow. *Physica B & C*, 108(1-3):1127–1128, 1981.

[187] J. T. Tough. volume 8 of *Progress in Low Temperature Physics*. North-Holland Publ. Co., 1982.

[188] H. A. Nichol, L. Skrbek, P. C. Hendry, and P. V. E. McClintock. Flow of HeII due to an oscillating grid in the low-temperature limit. *Phys. Rev. Lett.*, 92(24), 2004.

[189] H. Yano, A. Handa, H. Nakagawa, K. Obara, O. Ishikawa, T. Hata, and M. Nakagawa. Observation of laminar and turbulent flow in superfluid He-4 using a vibrating wire. *J. Low Temp. Phys.*, 138(3-4):561–566, 2005. International Symposium on Quantum Fluids and Solids (QFS 2004), Povo, Italy, Jul 05-09, 2004.

[190] H. Yano, N. Hashimoto, A. Handa, M. Nakagawa, K. Obara, O. Ishikawa, and T. Hata. Motions of quantized vortices attached to a boundary in alternating currents of superfluid He-4. *Phys. Rev. B*, 75(1), 2007.

[191] P. M. Morse and K. U. Ingard. *Theoretical acoustics*. Princeton University Press, 1986.

[192] R. Goto, S. Fujiyama, H. Yano, Y. Nago, N. Hashimoto, K. Obara, O. Ishikawa, M. Tsubota, and T. Hata. Turbulence in boundary flow of superfluid He-4 triggered by free vortex rings. *Phys. Rev. Lett.*, 100(4), 2008.

[193] Robert Jan de Graaf. *Dynamics of Quantized Vortices in Applied Flow in Superfluid 3He-B*. PhD thesis, Aalto Univeristy, Finland.

[194] D. C. Straty and E. D. Adams. . *Rev. Sci. Instr.*, 40:1393, 1969.

[195] D. S. Greywall and P. A. Bush. . *J. Low Temp. Phys.*, 46:451, 1982.

[196] F. Pobell. *Matter and Methods at Low Temperatures*. Springer-Verlag, Berlin, 1992.

[197] K. Gloos, P. Smeibidl, C. Kennedy, A. Singaas, P. Sekowski, R. M. Mueller, and F. Pobell. . *J. Low Temp. Phys.*, 73:101, 1988.

[198] P. Skyba. Notes on Measurement Methods of Mechanical Resonators Used in Low Temperature Physics. *J. Low Temp. Phys.*, 160(5-6):219–239, 2010.

Selected Publications

Table of Contents of the included publications:

PHYSICAL REVIEW E **75**, 025302(R) (2007)

Transition from laminar to turbulent drag in flow due to a vibrating quartz fork

M. Blažková, D. Schmoranzer, and L. Skrbek
Joint Low Temperature Laboratory, Institute of Physics ASCR and Faculty of Mathematics and Physics, Charles University, V Holešovičkách 2, 180 00 Prague, Czech Republic

(Received 5 September 2006; published 9 February 2007)

Flow due to a commercially available vibrating quartz fork is studied in gaseous helium, He I and He II, over a wide range of temperatures and pressures. On increasing the driving force applied to the fork, the drag changes in character from laminar (characterized by a linear drive vs velocity dependence) to turbulent (characterized by a quadratic drive vs velocity dependence). We characterize this transition by a critical Reynolds number $\mathrm{Re}_{\mathrm{cr}}^{\delta}=U_{\mathrm{cr}}\delta/\nu$, where U_{cr} is the critical velocity, ν stands for the kinematic viscosity, $\delta=\sqrt{2\nu/\omega}$ is the viscous penetration depth, and ω is the angular frequency of oscillations. We have experimentally verified that the corresponding scaling $U_{cr}\propto\sqrt{\nu\omega}$ holds in a classical viscous fluid over two decades of ν.

DOI: 10.1103/PhysRevE.75.025302 PACS number(s): 47.27.Cn, 47.27.nb, 67.40.Bz, 67.55.Fa

The vibrating quartz tuning fork (Fig. 1) represents an easy to use, robust, cheap, and widely available tool to generate and probe an important class of flows—oscillating boundary layer flows, especially under cryogenic conditions [1]. Commercially produced piezoelectric forks—frequency standards ($2^{15}=32\,768$ Hz) for watches—are supplied by various producers [2] in a cylindrical vacuum-tight metal can that for fluid dynamical applications has to be entirely or partly removed. In this work, we use them to study one particular feature of an oscillating boundary layer flow—its transition from the laminar to the turbulent drag regime.

The bare fork, its typical surface roughness, and the electrical scheme used for measurements are shown in Fig. 1. The fork is excited with an ac voltage $U_{\mathrm{D}}=U_0\cos(\omega t)$, where ω is the angular frequency of oscillations. The observable quantity is a current owing to the piezoelectric effect $I=aU$ measured by the SR 830 lock-in amplifier, which is proportional to the derivative of the fork deflection, i.e., its velocity U. For calibration, one needs to find the proportionality constant a. We use the vacuum measurements of the linewidth $\Delta\omega$ obtained by slowly sweeping the drive frequency across the resonance at liquid-nitrogen ($\approx$78 K) or liquid-helium ($\approx$4.2 K) temperature, at which the flow is then probed. As explained in detail in Ref. [1], $a^2=2m\Delta\omega/R_{\mathrm{e}}$, where m is the mass of one fork's leg and R_{e} denotes its equivalent electrical resistance. The driving force per one leg of the fork is $F=aU_0/2$.

We have shown [1] that subject to a low drive, within a laminar regime, the resonance frequency f_0 of the fork of density ρ_{f} and full width of the Lorentzian absorption curve Δf at half height (see an example of typical absorption and dispersion curves in the inset of Fig. 2) depend on the fluid density ρ and dynamic viscosity η as

$$\left(\frac{f_{0\mathrm{vac}}}{f_0}\right)^2=1+\frac{\rho}{\rho_{\mathrm{f}}}\left(\beta+B\frac{S}{V}\sqrt{\frac{\eta}{\pi\rho f_0}}\right), \tag{1}$$

$$\Delta f=\frac{1}{2}\sqrt{\frac{\rho\eta f_0}{\pi}}CS\frac{(f_0/f_{0\mathrm{vac}})^2}{\rho_{\mathrm{f}}V}. \tag{2}$$

Here $V=L_3L_2L_1$ is the volume of one fork's leg of length L_1 and rectangular cross section L_3L_2, $S=2(L_3+L_2)L_1$. Equations (1) and (2) ignore the vacuum linewidth (at low temperature typically $\Delta f_{\mathrm{vac}}\approx 0.05\ \mathrm{Hz}\ll\Delta f\approx 1-10$ Hz) and account fairly well for the behavior of the vibrating fork in fluids with known ρ and η if β, B, and C are determined as fitting parameters [3].

The main result which we present here is our experimental observation of the transition from the laminar drag regime [characterized by the driving force $F\propto U$, where U is the peak velocity of the fork; $f_0\cong$const; $\Delta f\cong$const; in accord with Eqs. (1) and (2)] to the turbulent drag regime (characterized by $F\propto U^2$) in an oscillatory boundary layer flow [4].

The vibrating fork is an ideal tool for our investigations in that the same fork can be used in a rich variety of classical and quantum working fluids. Here we use ^{4}He, offering three remarkable fluids of interest, primarily due to their extremely low values of kinematic viscosity, $\nu=\eta/\rho$, lowest of all known substances. Cryogenic helium gas in addition to its very low viscosity also allows an unprecedented flexibility, as its fluid properties can be easily tuned over many orders of magnitude by varying the temperature and/or pressure. Normal liquid helium (He I) is a Navier-Stokes fluid having normal boiling point at 4.2 K and existing (along the saturated vapor line, SVP) down to $T_\lambda\approx 2.17$ K, below which it becomes superfluid and is usually referred to as He II. Properties of ^{4}He are well known [5,6] and are easily tuneable by adjusting temperature and pressure *in situ* in the same pressure cell.

With cryogenic working fluids, such as He I or He II, care must be taken in order to prevent the extremely sensitive fork (typically $Q\approx 10^5-10^6$ in vacuum at low temperature) from gathering solid particles of air or other contaminants. We therefore start measurement cycles with liquid helium under high pressure in the cell, so that for any subsequent measurement the amount of fluid in the pressure cell is either kept constant or decreases.

Our experimental protocol is based on recording families of resonant curves in various working fluids (i.e., in helium at various temperature and pressure) over six orders of magnitude of the drive—for such a wide dynamical range we need an additional attenuator and a step-up transformer. As shown in Fig. 2, on increasing the drive the Lorentzian shape of the absorption becomes distorted and the point of maxi-

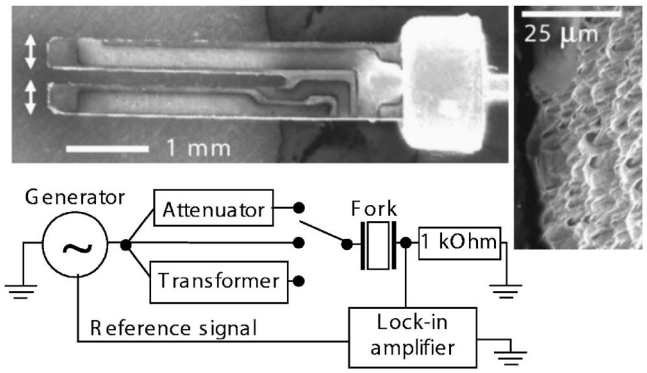

FIG. 1. The micrograph of the quartz tuning fork with the detail of its surface showing the typical surface roughness and the principal electrical circuitry used for measurements.

mum response f_{max} shifts towards lower frequency [7].

In a steady classical flow past a submerged object, transition from laminar to turbulent drag occurs at some critical value of Reynolds number $\mathrm{Re}_{cr}=U_{cr}\ell/\nu$, where U_{cr} denotes the critical flow velocity and ℓ is a characteristic size of the object [8]. In a viscous flow due to an oscillating submerged body of the angular frequency of oscillation $\omega=2\pi f$ a new important length scale $\delta=\sqrt{2\nu/\omega}=\sqrt{2\eta/\rho\omega}$ of the viscous penetration depth emerges. If $\ell \ll \delta$ and, additionally, the Reynolds number $U\ell/\nu$ is small, then the flow at any given instant can be regarded as steady—as if the body were moving uniformly with its instantaneous velocity. If, on the other hand, $\ell \gg \delta$ and the amplitude of motion $U/\omega \ll \ell$, then the Reynolds number need not be small in order to neglect the nonlinear term in the Navier-Stokes equation. In a thin layer near the surface of the body the flow is rotational but in the rest of the fluid it is potential [9].

We suggest that in this case the transition from laminar to turbulent drag ought to be characterized by a critical Reynolds number based on the penetration depth:

$$\mathrm{Re}_{cr}^{\delta}=U_{cr}\delta/\nu. \tag{3}$$

It immediately follows that the critical velocity ought to scale as $U_{cr}\propto\sqrt{\nu\omega}$.

For full description of oscillatory flows, besides the Reynolds number one needs to define an additional dimensionless number such as the Strouhal number $\mathrm{St}=U\tau/\ell$ [9], where $\tau=2\pi/\omega$ is a characteristic time. Note that if one assumes that the characteristic length scale is the penetration depth, Reynolds and Strouhal numbers become equal (except for a numerical constant of π). Consequently, the crossover from the laminar to turbulent drag can be described by the Reynolds number $\mathrm{Re}_{cr}^{\delta}$ alone.

Note that with our quartz tuning fork oscillating at about 32 kHz (despite covering six orders of magnitude of F resulting in five orders of magnitude of U) we always operate in the limit $U/\omega \leq 20\ \mu\mathrm{m} \ll \ell \cong 400\ \mu\mathrm{m} \gg \delta \leq 4.3\ \mu\mathrm{m}$. The velocity when the amplitude of oscillation would reach the thickness of the fork's leg would be $U \simeq 80$ m/s and cannot be reached in practice—the fork mechanically breaks at velocities of order of a few m/s [10].

In most cases, however, the attainable velocity of the fork is high enough to comfortably observe the transition from laminar to turbulent drag regime (see Fig. 3). It is clearly marked as a change in the velocity vs drive slope as well as by the onset of increase in observed Δf or an onset of decrease of f_{max}. Experimentally, we define the critical velocity U_{cr} as a crosspoint of fitted linear and square-root velocity vs

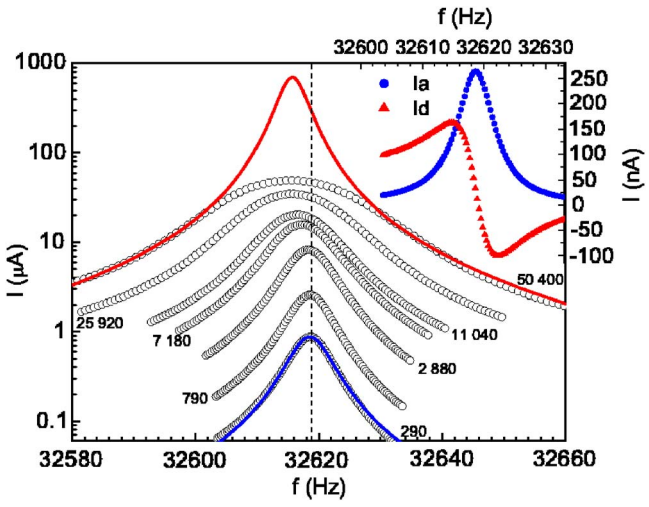

FIG. 2. (Color online) Left: The in-phase resonant response of the driven quartz fork vs applied frequency measured for various drive voltage levels (in $\mathrm{mV_{rms}}$) as indicated. The solid curves are Lorentzian fits to the data. The inset shows both absorption and dispersion curves for the drive level of 290 $\mathrm{mV_{rms}}$.

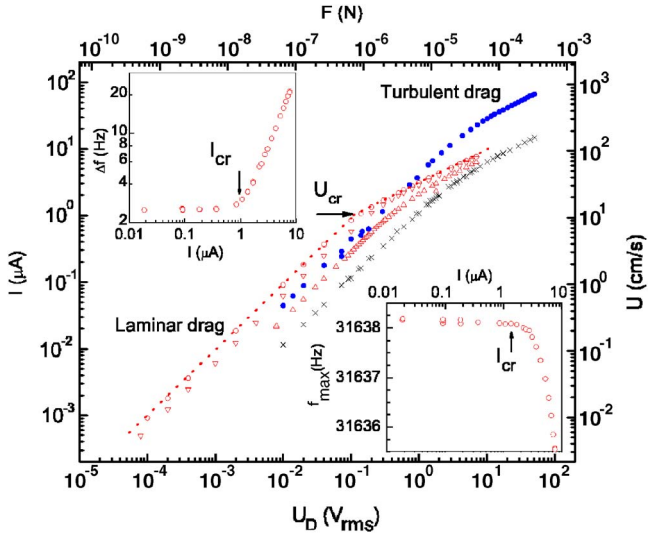

FIG. 3. (Color online) Transition from laminar to turbulent drag regime as detected by the vibrating quartz fork A2 in He I at 4.2 K and 18.6 bars (×), in He II at SVP at 1.37 K(○), 1.61 K (▽), 2.06 K (△), and in gaseous helium at 78 K and 10.05 bars(●). For conversion of measured electrical quantities U_D and I to F and U, see [1]. The insets show the width Δf of the in-phase resonance response (top) and the frequency of maximum response f_{max} (bottom) vs measured current, both being constant in a linear regime. Increase of Δf and decrease of f_{max} indicate an onset of the turbulent drag regime.

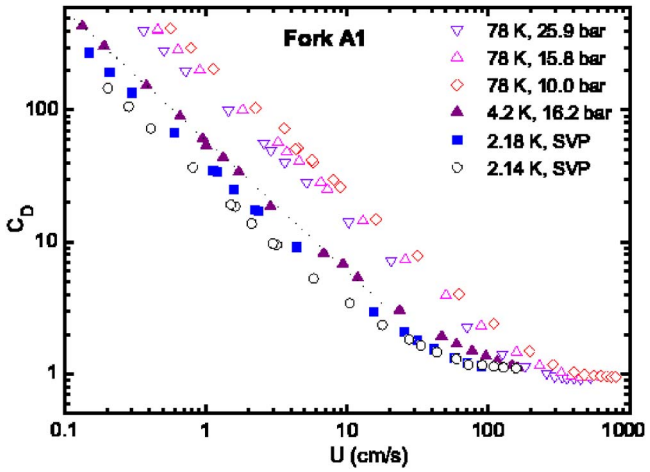

FIG. 4. (Color online) The drag factor C_D plotted vs the peak velocity U of the fork. Measurements in helium gas, in normal liquid He I as well as in superfluid He II close to the transition temperature, are shown at conditions as indicated. The dotted line is included to appreciate an expected $C_D \propto 1/U$ behavior in laminar regime.

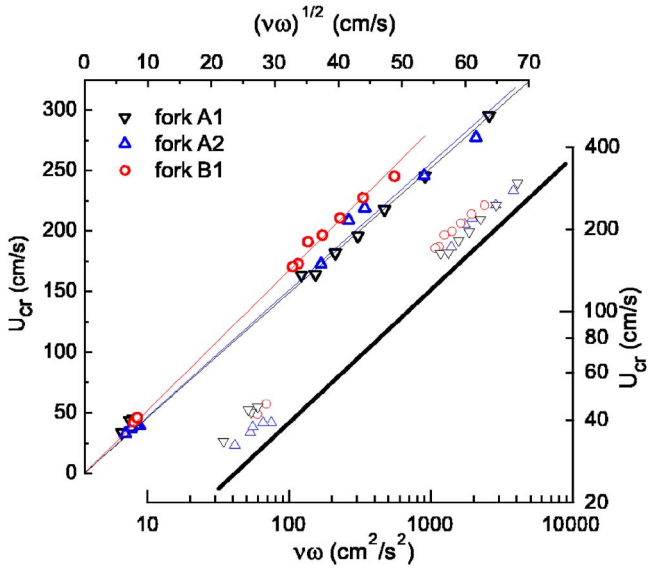

FIG. 5. (Color online) The critical velocity at which transition from laminar to turbulent drag occurs for three different forks A1, A2, and B1 [2] in classical fluids (data points obtained using He I in the temperature range $2.2 < T < 4.2$ K and He gas at 78 K at ambient and elevated pressure up to 30 bars) plotted vs $\sqrt{\nu\omega}$. The solid lines represent the best linear fit that includes the (0,0) point (top). This scaling is confirmed by comparison with the thick solid line in the logarithmic plot (bottom); the fitted power laws for the three forks yield 0.48 ± 0.04.

driving force dependence, neglecting the data points where rounding in the vicinity of U_{cr} takes place.

The universal crossover behavior is even better displayed in a nondimensional way in Fig. 4, where we plot the velocity dependence of the classical drag factor defined as $C_{\mathrm{D}} = 2F/\rho A U^2$, where $A = L_1 L_2$ is the projected area of the fork's leg. As a numerical example, for the fork A1 (see Fig. 4) $C_D = 1 \pm 0.2$ over two decades of ν and more than a decade of ρ, as measured in classical fluids He I and He gas at various applied pressures.

Our data obtained in classical viscous fluids (covering two orders of magnitude of ν and thus demonstrating the usefulness of cryogenic helium for laboratory fluid dynamical research) displayed in Fig. 5 verify the scaling $U_{\mathrm{cr}} \propto \sqrt{\nu\omega}$ in the limit $\ell \gg \delta$ [11]. In order to stress that our results do not depend on the particular fork, we show our results obtained with two nominally identical forks A1 and A2 and with a bigger fork B1 [2]. The critical value of $\mathrm{Re}_{\mathrm{cr}}^{\delta}$ is about 5 [12] and varies slightly from fork to fork (within about 20%), but the scaling for each individual fork holds. Thus for oscillatory flow due to a vibrating object, in the limit $U/\omega \ll \ell \gg \delta$, the characteristic length scale is not the size of the object, but the viscous penetration depth.

To better appreciate our experimental results, it is instructive to consider an analytically tractable example of a viscous flow due to an oscillating hydrodynamically smooth sphere. In a laminar regime, the drag force acting upon a sphere of radius R is given [9], $F_{\mathrm{lam}} = \lambda U = 6\pi\eta R(1 + R/\delta)U$. For the turbulent drag regime we adopt $F_{\mathrm{turb}} = \gamma U^2 = C_D \rho \pi R^2 U^2/2$. Assuming that the transition occurs when these forces become equal in a limit of high frequency ($R \gg \delta$) we arrive at

$$U_{\mathrm{cr}} = \frac{\lambda}{\gamma} \cong \frac{6\sqrt{2}}{C_D}\sqrt{\nu\omega} \simeq 21\sqrt{\nu\omega}. \qquad (4)$$

Here we assumed that for a smooth sphere $C_D \simeq 0.4$. In He I at the saturated vapor curve just above the superfluid transition this would give a critical velocity of about 1.3 m/s, about four times higher than we observe for the oscillating fork. It seems therefore that for submerged oscillating bodies of arbitrary shape (such as, e.g., quartz fork) Eq. (4) generally holds, with appropriate numerical values of λ and γ. Here we assume that $\ell \gg \delta$. The expression for F_{lam} suggests that there ought to be a crossover from a regime where $\ell \ll \delta$ to $\ell \gg \delta$. It is an interesting question if such a crossover is always present in boundary layer flows due to bodies of various forms.

The example of a sphere is certainly too simple to account for any details within the crossover region, such as instability against Taylor-Görtler vortices [13]. We have chosen this simplest example of a sphere having in mind that the flow over the tip of the fork is inherently three dimensional. Taking into account the surface roughness (see Fig. 1) and the fact that the tip of the fork's leg is partly ground off by the manufacturer to adjust the desired room-temperature frequency, it is hardly possible to accurately describe the flow analytically or even numerically. It seems, nevertheless, that the underlying physics of a crossover from laminar to turbulent drag regime is captured and such a comparison is useful.

We have extended our measurements and analysis to a quantum fluid—He II. One might expect a very different behavior here, as it is well known that He II displays the two-fluid phenomena and circulation in its superfluid component is quantized. It is remarkable therefore that in He II we observe similar drive dependencies as in He I and He gas. In particular, no appreciable change in the measured quantities is observed when crossing T_λ (see Figs. 3 and 4). On decreasing the temperature of He II along the saturated vapor

curve further, however, the crossover becomes gradually sharper and across the transition region the drag coefficient displays additional pronounced features. We observe neither irregularities nor any hysteretic phenomena down to about 1.3 K, although we have especially searched for them. Such features have been commonly observed with oscillating wires [14], spheres [15], or grids [16], but in most cases at lower temperatures. Due to space restriction, we postpone a detailed account and analysis of He II measurements to a later publication; here we restrict ourselves to merely stating their main features.

To conclude, we have experimentally confirmed that a critical velocity for the crossover from laminar to turbulent drag regime in a viscous flow due to an oscillating quartz fork in the limit $U/\omega \ll \ell \gg \delta$ scales as $U_{cr} \propto \sqrt{\nu\omega}$ over at least two decades of kinematic viscosity. Taking into account the geometrical shape of the tip of the fork's leg and its surface roughness, this result strongly suggests that for such an oscillatory flow the characteristic length scale is not the size of the object, but the viscous penetration depth $\delta = \sqrt{2\nu/\omega}$.

The authors appreciate the technical help of T. V. Chagovets, L. Doležal, M. Rotter, F. Soukup, and P. Vacek, stimulating discussion with many colleagues, especially D. Charalambous, V. B. Eltsov, R. Hanninen, J. Hosio, M. Krusius, P. V. E. McClintock, J. J. Niemela, W. Schoepe, P. Skyba, K. R. Sreenivasan, W. F. Vinen, H. Yano, and thank J. Pešička for providing the fork micrographs. This research was supported by research plans MS 0021620834, AVOZ 10100520, and by GAČR under 202/05/0218.

[1] R. Blaauwgeers *et al.*, Quartz Tuning Forks—Thermometers, Pressure- and Viscometers for Cryogenic Fluids, J. Low Temp. Phys., Nos. 5/7 (2007), in e-print, cond-mat/0608385.

[2] Forks specified as type DT26 (A1,A2) and DT38 (B1) used in this work have been produced by Fronter Electronics, China, www.chinafronter.com

[3] This approach does not take into account a steady secondary flow through the action of viscosity in the boundary layer (e.g., streaming [8]) and β therefore weakly depends on the geometry of the surrounding container.

[4] This transition in He II was independently observed by J. Hosio, V. B. Eltsov, and M. Krusius in LTL Helsinki; (private communication).

[5] R. D. McCarty, Technical Note 631, National Bureau of Standards, Gaithersburg, Maryland, 1972; V. D. Arp, R. D. McCarty, "The Properties of Critical Helium Gas," Technical Report, University of Oregon, 1998.

[6] R. J. Donnelly and C. F. Barenghi, J. Phys. Chem. Ref. Data **27**, 1217 (1998).

[7] We do not use the term resonant frequency as above the transition the response curve ceases to be of the Lorentzian form, as illustrated in Fig. 2.

[8] H. Schlichting and K. Gersten, *Boundary-Layer Theory* (Springer, New York, 1996).

[9] L. D. Landau and E. M. Lifshitz, *Fluid Mechanics* (Pergamon, New York, 1959).

[10] An additional factor that has to be taken into account is cavitation that often occurs when working in liquid helium at or near the saturated vapor pressure and the fork oscillates at large amplitude. Its signature is an irregular shift of the resonant frequency to values between those of the liquid and gaseous phases. Our measurements of heterogeneous cavitation in He I and He II will be reported and discussed in detail elsewhere.

[11] Note that this scaling differs from that found using the transversally oscillating cylinders, see T. Sarpkaya, J. Fluid Mech. **165**, 61 (1986), and references therein.

[12] Comparison with other oscillating objects is not straightforward, as the flow becomes enhanced while passing the sharp edges of the fork and due to surface roughness.

[13] S. R. Otto, J. Fluid Mech. **239**, 47 (1992).

[14] M. Morishita, T. Kuroda, A. Sawada, and T. Satoh, J. Low Temp. Phys. **76**, 387 (1989); H. Yano *et al.*, *ibid.* **138**, 561 (2005); (private communication).

[15] J. Jäger, B. Schuderer, and W. Schoepe, Phys. Rev. Lett. **74**, 566 (1995).

[16] H. A. Nichol, L. Skrbek, P. C. Hendry, and P. V. E. McClintock, Phys. Rev. Lett. **92**, 244501 (2004); Phys. Rev. E **70**, 056307 (2004); D. Charalambous *et al.*, *ibid.* **74**, 036307 (2006).

Experiments relating to the flow induced by a vibrating quartz tuning fork and similar structures in a classical fluid

D. Schmoranzer,[1] M. Král'ová,[2] V. Pilcová,[1] W. F. Vinen,[3] and L. Skrbek[1]
[1]*Faculty of Mathematics and Physics, Charles University, Ke Karlovu 3, 121 16 Prague, Czech Republic*
[2]*Institute of Physics ASCR, v.v.i., Na Slovance 2, 182 21 Prague, Czech Republic*
[3]*School of Physics and Astronomy, University of Birmingham, Birmingham B15 2TT, United Kingdom*
(Received 12 March 2010; published 28 June 2010)

We report on an experimental study of the behavior of a number of commercially available quartz tuning forks oscillating in a classical cryogenic fluid, in the form of either liquid helium I or gaseous helium, extending our previous studies [M. Blazkova *et al.* Phys. Rev. E **75**, 025302 (2007)]. Measurements of the damping of the oscillations allowed us to deduce the drag on the prong of a fork, as a function of the velocity with which the prong moves, for various sizes of fork and various oscillation frequencies. Transitions to turbulent flow have been identified, and the dependence of the critical velocity, expressed as a dimensionless critical Keulegan-Carpenter number, on the dimensionless Stokes number has been established. These measurements have not allowed us to visualize the flow, so we have carried out visualization experiments with oscillating rods in water, the rod dimensions, and the frequencies of oscillation, being chosen so that the relevant dimensionless parameters are similar to those for the prongs of the forks. Some information about the nature of the instability that leads to turbulence has been obtained in this way, and the results for the critical Keulegan-Carpenter number for the rods in water have been compared with values for the tuning forks in a cryogenic fluid.

DOI: 10.1103/PhysRevE.81.066316 PACS number(s): 47.27.Cn, 47.80.−v, 67.25.B−, 85.50.−n

I. INTRODUCTION

During the past few years a number of papers have reported applications of vibrating piezoelectric quartz tuning forks in the study of cryogenic fluids [1–7]. Such forks are available commercially at little cost since they are made in large numbers as frequency standards for watches. The usual frequency is $2^{15}=32\,768$ Hz, although forks with other frequencies are also available. The forks are normally supplied in cylindrical vacuum-tight metal cans, but removal of this can allows the fork to interact with a surrounding fluid. The piezoelectric properties of the quartz allow both controlled application of a periodic driving force and the measurement of the corresponding response, by purely electrical means. Vibration of a fork at low velocities induces laminar flow in the surrounding fluid, and this allows the fork to be used to monitor the state of the fluid, such as its temperature or pressure, a feature that is particularly valuable in cryogenic applications [2,4]. At higher velocities vibration of the fork can induce turbulent flow, and studies have been reported of the way in which the drag on the prongs of the fork varies with velocity in the transition to fully turbulent flow [3,4,6,7]. This transition has been studied in both gaseous and liquid helium, and in the latter case studies have included both the normal and the superfluid phases. In the case of the superfluid phase we are dealing with quantum turbulence, and the studies have contributed to our understanding of the way in which such turbulence can be generated by a vibrating structure.

Laminar flow induced by vibration of a fork at low velocities seems to be well understood in terms of well-established theory [2,8]. The frequency with which the forks vibrate is such that in either gaseous or liquid helium the viscous penetration depth is small compared with the dimensions of a prong, and there is potential flow outside this penetration depth. The amplitude of the oscillations in drag force, F, per unit length of prong is then related to the velocity amplitude of oscillation, U, through a relation of the form

$$F = \alpha S \rho (\omega \nu)^{1/2} U, \tag{1}$$

where S is the surface area of a prong per unit length; ρ and ν are, respectively, the density and kinematic viscosity of the fluid; ω is the angular frequency of oscillation; and α is a numerical factor, of order unity, which depends on the shape of a prong. The drag force can also be expressed in terms of a drag coefficient C_D,

$$C_D = 2\alpha \frac{S}{A} (\omega \nu)^{1/2} \frac{1}{U}, \tag{2}$$

where A is the projected area of unit length of a prong on a plane normal to its motion and C_D is defined by the equation

$$F = \tfrac{1}{2} \rho A C_D U^2. \tag{3}$$

This paper is concerned with the behavior of a tuning fork in a classical fluid when the velocity is increased through the transition to turbulence. As we shall see, this behavior is interesting in itself, but it is interesting also in connection with the generation of quantum turbulence. A question that arises in the study of quantum turbulence is the extent to which quantum turbulence can mimic classical turbulence. This question has arisen repeatedly in the study of the generation of quantum turbulence by various forms of oscillating structure [9], and it has arisen most recently, and perhaps most vividly, in recent experimental studies of the generation of quantum turbulence by an oscillating tuning fork [6,7]. The pursuit of this question has been hampered, as we shall

see, by the fact that very little seems to be known about the generation of turbulence by a tuning fork, or by similar structures, in a classical fluid.

If we ignore the fact that a tuning fork has two prongs, and that the velocity with which a prong moves varies along its length, we see that the oscillation of such a fork in a fluid must be closely related to the transverse oscillation of a bar of rectangular cross section. Many experimental and theoretical studies have been published relating to the transverse oscillation of a rod of circular cross section in a fluid (for example, [10–15]), with the experiments having included both measurements of the drag coefficient through the transition to turbulence and visual observations of the flow at different stages in this transition. However, to our knowledge no corresponding studies have been made for a bar of rectangular cross section. This paper, which is an extension of our previous studies [3], is a contribution to the filling of this gap in our knowledge. Our measurements include studies of the drag-force–velocity relationship for a range of tuning forks in helium, supplementing the results presented in [3], together with visual observations of the flow induced in water by transverse oscillations of a rectangular bar, for which the dimensionless parameters are chosen to match those relevant to the tuning forks. Our results suggest that there may be significant differences between the behaviors of a rod of circular cross section and that of our rectangular bars, although we cannot be sure of the reason and further experiments are clearly required.

In presenting our experimental results we shall use the dimensionless parameters that are commonly used in the classical literature. The drag will be described by the dimensionless drag coefficient, defined by Eq. (3). At a finite frequency this drag coefficient must be a function of two independent dimensionless parameters, which we take to be the Keulegan-Carpenter number, defined by the equation

$$K_C = \frac{2\pi a}{d}, \tag{4}$$

and the Stokes number, defined by the equation

$$\beta = \frac{\omega d^2}{2\pi\nu}, \tag{5}$$

where a is the amplitude of oscillation of the structure and d is a characteristic dimension. In terms of these dimensionless parameters Eq. (2) becomes

$$C_D = (8\pi)^{1/2}\alpha\frac{S}{A}\beta^{-1/2}K_C^{-1}. \tag{6}$$

At velocities exceeding those at which there is laminar flow the form of Eq. (6) becomes generally more complicated, although it is often the case that in the limit of very large K_C the drag coefficient tends to a constant value of order unity, which we denote by Γ.

II. EXPERIMENTAL RESULTS: DRAG ON THE VIBRATING TUNING FORKS

Details of the quartz forks that we have studied are summarized in Table I, with the dimensions being defined in Fig. 1. The surfaces of the forks are rough on a scale of a few microns, as shown in Fig. 1. The way in which our experimental results have been obtained was described in earlier papers.

TABLE I. Description of quartz forks.

Fork	Frequency (kHz)	L (mm)	T (mm)	W (mm)	D (mm)
A1	32	3.71	0.42	0.35	0.21
B1	32	3.65	0.68	0.46	0.18
C3	32	2.51	0.25	0.10	0.13
U1	4	19.70	2.20	0.80	
U2	8	9.50	0.45	0.90	0.50
L2	32	2.17	0.21	0.10	0.12
L1	32	2.17	0.21	0.10	0.12
K1	32	3.9	0.39	0.28	

A typical plot of observed drag coefficient against Keulegan-Carpenter number, for a fixed value of Stokes number, is shown in Fig. 2. We see that there is a smooth (monotonic) transition between the laminar behavior, described by Eq. (6), and a limiting constant value $C_D=\Gamma$ at high velocity, where the constant Γ is close to unity. We find that this smooth transition can be represented to a good approximation by the equation

$$C_D = (8\pi)^{1/2}\alpha\frac{S}{A}\beta^{-1/2}K_C^{-1} + \Gamma, \tag{7}$$

which describes all solid lines in Fig. 2.

We note that this smooth variation is different from that observed with a circular cylinder, where C_D often varies with K_C in an oscillatory way in the region of the transition to turbulent flow [10]. Furthermore, there is evidence that the limiting value of the drag coefficient for a circular cylinder, although of order unity, does in fact decrease systematically and significantly with increasing β. This suggests that the physical processes occurring in the transition region may be different in character in the two cases, although—as we discuss later—part, at least, of the difference might be due to the fact that the transverse velocity with which a fork vibrates must vary along its length.

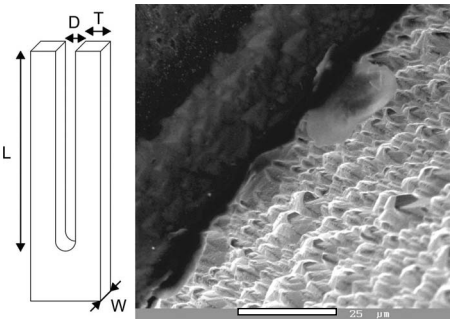

FIG. 1. Schematic sketch of a quartz tuning fork and a micrograph of the surface of tuning fork A1 (the marker is 25 μm long).

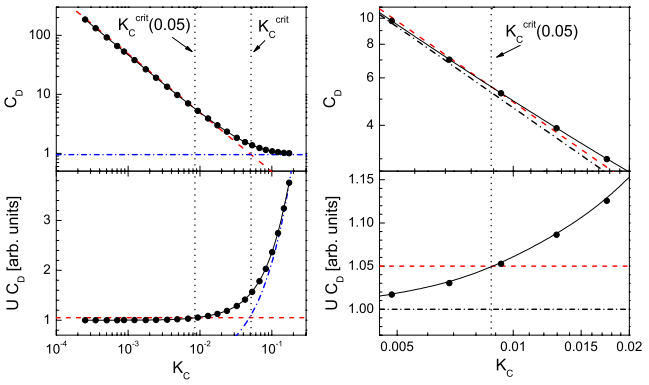

FIG. 2. (Color online) Upper left panel: the observed drag coefficient plotted against Keulegan-Carpenter number for a 32 kHz fork of type B1. Lower left panel: the same drag coefficient multiplied by velocity (normalized to unity)—this quantity indicates a departure from linearity more clearly. The (blue) dashed-dotted line indicates the fully turbulent drag. The right panels show detailed view of the departures from linear regime indicated by the (black) dashed-dotted line. In all panels the 5% departure criterion is marked by the (red) dashed line and the critical Keulegan-Carpenter numbers are marked with vertical black dotted lines.

We shall be interested in defining a critical Keulegan-Carpenter number K_C^{crit} associated with this transition. It is tempting to define this number as that at which the two terms on the right-hand side of Eq. (7) are equal, so that

$$K_C^{(\mathrm{crit})} = (8\pi)^{1/2}\frac{\alpha}{\Gamma}\frac{S}{A}\beta^{-1/2}. \tag{8}$$

We note that this form implies that the corresponding critical velocity scales as $(\omega\nu)^{1/2}$ for a given oscillating structure, a form of scaling that was noted in Ref. [3]. However, this scaling is an automatic consequence of the limiting forms of C_D in the laminar and fully turbulent regimes; it has no special physical significance in the sense that the critical velocity does not correspond to any special change in the character of the flow [6]. Of more significance is the value of K_C at which the first instability appears in the laminar flow. Unfortunately, since the observed variation of C_D is quite smooth, it is not possible to identify this critical condition. The best we can achieve is to identify the value of K_C, $K_C^{\mathrm{crit}}(x)$, at which C_D differs from its laminar value by an arbitrary factor $(1+x)$, where $x \ll 1$.

In Figs. 3 and 4 we show plots of the observed values of K_C^{crit} and $K_C^{\mathrm{crit}}(0.05)$ against Stokes number. We see from Fig. 3 that K_C^{crit} varies with Stokes number as $\beta^{-1/2}$, in accord with Eq. (8). We see from Fig. 4 that $K_C^{\mathrm{crit}}(0.05)$ also varies with Stokes number as $\beta^{-1/2}$, within the (considerable) experimental error. This strongly suggests (but perhaps does not yet conclusively prove) that the critical Keulegan-Carpenter number at which the laminar flow first becomes unstable also varies with Stokes number as $\beta^{-1/2}$. In this respect an oscillating fork seems to behave differently from an oscillating rod of circular cross section, for which the critical Keulegan-Carpenter number at the first onset of instability (the Honji instability [12], discussed below) varies less rapidly with

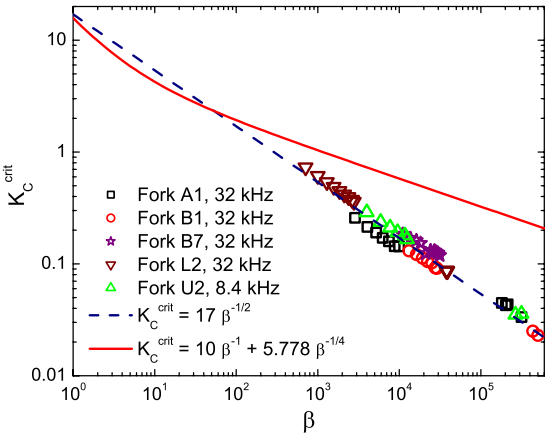

FIG. 3. (Color online) The critical Keulegan-Carpenter number K_C^{crit} plotted against Stokes number β for different forks as indicated, vibrating in normal liquid ^{4}He and in cold pressurized helium gas at liquid-nitrogen temperature. The solid (red) line represents the expected instability for circular cylinders and the (blue) dashed line represents the observed square-root behavior as indicated.

Stokes number (as $\beta^{-1/4}$ for large β [10]). This less rapid variation with β may be related to the fact, noted above, that the value of Γ seems to decrease systematically with increasing β.

III. VISUALIZATION

These experimental results leave unanswered a number of important questions. To what extent is the behavior of a fork influenced by the sharp corners on the prongs and by roughness of the surface of a prong? To what extent is it influenced by the close proximity of two prongs and the nonuniform transverse velocity of a prong? And what is the nature of the first instability as the Keulegan-Carpenter number is increased?

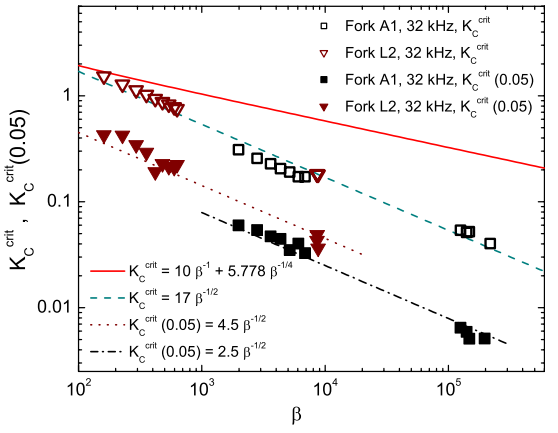

FIG. 4. (Color online) The critical Keulegan-Carpenter numbers, K_C^{crit} and $K_C^{\mathrm{crit}}(0.05)$, plotted against Stokes number for different forks as indicated, vibrating in normal liquid ^{4}He and in cold pressurized helium gas at liquid-nitrogen temperature. The (red) solid line represents the expected instability for circular cylinders; the other lines are the individual observed square-root dependences.

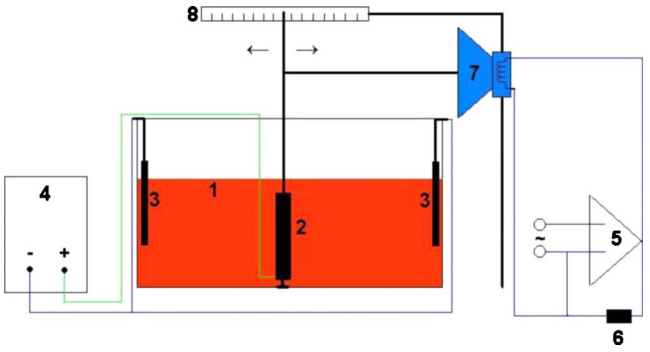

FIG. 5. (Color online) Schematic diagram of the apparatus used to visualize the flow produced by an oscillating bar in water. For a detailed description, see the text.

It is difficult to answer these questions with the forks themselves. They cannot easily be modified to answer the first two questions. Establishing experimentally the nature of the first instability requires a visualization of the flow, for which the required technique does not exist for such a small structure immersed in a cryogenic fluid. We have therefore started to investigate the behavior of large metal rods of rectangular cross sections oscillating in water, aiming by suitable scaling at ranges of values of K_C and β similar to those relevant to the forks. Ideally, we should have measured the drag coefficients for such systems, but as yet we do not have the equipment necessary for such measurements. But we have attempted to visualize the flow, using both the Baker solution technique [16] and a Kalliroscope solution [17].

A. Experimental technique

The apparatus based on the Baker *p*H technique is shown schematically in Fig. 5. Approximately 25 l of Baker solution composed of water, small concentrations of NaOH and HCl, and thymol blue *p*H indicator (labeled 1) were contained in a tank of dimensions $20\times30\times25$ cm^3. The oscillating rod (2) was pivoted at the base of the tank with a spherical knob fitting into a Teflon holder. Oscillation of the rod about the pivot in a vertical plane was driven via two thin rods by a large bass loudspeaker (7), driven by the oscillator (5), over a range of frequencies from 1 to 12 Hz. The loudspeaker was used in its linear mode, so that the amplitude of oscillation was proportional to the applied ac signal. In the experiment, the oscillating rod could move along its sides only and was pivoted at its lower end in order for its motion to be similar to that of a prong of a tuning fork. The surface of the rod was biased by a dc voltage of 10–15 V relative to the brass electrodes (3), in accordance with the recipe given in Ref. [16]. When the dc bias voltage is applied, an electrochemical reaction starts on the surface of the rod, affecting the concentrations of the dissociated ions locally thus increasing the local *p*H, and forcing the *p*H indicator in the vicinity of the rod to change its color from orange-red to dark blue. This "ink" then freely drifts in the liquid, marking its flow pattern accurately at low velocities up to about 5 cm/s. The same tank, without the electrodes, was used for experiments with the Kalliroscope solution, which outlines the flow pattern via small reflective platelets contained in it. Calibration of the displacement and velocity of the rod was carried out with a video camera that recorded the position of the top of the system of thin rods as a function of time relative to the scale (8).

B. Existing observations

Before we present our own observations of the flow of water round our oscillating rods, we shall describe existing observations of flow round an oscillating rod of circular cross section [10,12], together with one previous unpublished observation of the flow round an oscillating rod of square cross section [18]. Comparison between the different observations will prove instructive.

An important and detailed study of the flow of water round a rod of circular cross section oscillating in a direction at right angles to its length was reported by Honji [12]. Similar observations, together with corresponding measurements of the drag coefficient versus Keulegan-Carpenter number, were reported by Sarpkaya [10]. The observed flows can be summarized in a slightly oversimplified way as follows. At a small velocity (or K_C), within the laminar regime, oscillation leads to not only an oscillating boundary layer, but also to a steady streaming flow [19,20]. The streaming flow is two dimensional in the sense that the streaming velocity points in a direction normal to the length of the rod. It arises from a nonlinear effect when flow in the oscillating boundary layer varies with position in the direction in which the flow takes place; for the case of an incompressible fluid the equation of continuity demands that there must then be some flow normal to the plane of oscillation. The relevant theory was given by Schlichting and was discussed by Batchelor [21]. At a higher Keulegan-Carpenter number the flow starts to exhibit a three-dimensional structure involving mushroom-shaped vortices moving away from the surface (see, for example, Ref. [12], Fig. 10). It is now accepted that this flow arises from an instability of the flow in the boundary layer when the rigid boundary has convex curvature, with the instability leading to the generation of Taylor-Görtler vortices [15]. As long as these vortices remain in the thin boundary layer they are hard to see, but the steady streaming flow causes them to be swept away from the cylinder, so that they appear very clearly in the form of the mushroom-shaped vortices to which we have referred. Theory [15] leads to the prediction that the critical Keulegan-Carpenter number at which the Taylor-Görtler vortices are formed (the initial instability) is given in the limit of large β by

$$K_C^{(\mathrm{crit})} = 5.778\beta^{-1/4}. \tag{9}$$

This dependence on β, to which we have already referred, has been verified experimentally [10].

The only study of flow induced by the transverse oscillation of a rod of rectangular cross section of which we are aware has been carried out by Hershberger and Donnelly [18]. They used Kalliroscope to visualize the flow, and their bar oscillated with a velocity amplitude that was uniform along its length. They did not report any observation of steady streaming at low velocities, but they did observe

FIG. 6. (Color online) A photograph of the (brass or stainless steel) rods of square cross section that we have studied. They have cross sections of 5×5, 3×3, 2×2 (with rounded corners), 2×2, and 1×1 cm^2.

mushroomlike vortices formed along the whole length of the bar at higher velocities, with the vortices being arranged in a regular pattern along the length of the bar. They did not carry out a complete study, and the precise location of the mushroom vortices remains unclear.

C. Present observations

Photographs of the rods that we have studied are shown in Figs. 6–8. The 2×2 cm^2 rod with rounded edges showed no transition within the range of velocities available to us. All the others showed a transition in which vortex motion leaves the surface, as shown in the typical photograph reproduced in Fig. 9. These vortices are not arranged in the regular pattern along the rod as observed by Hershberger and Donnelly, and they first appear at the top of the rod (we neglect structures shed by the upper edge). On increasing the amplitude of oscillation further above the critical value, vortices start appearing further away from the top of the rod. These features are consistent with the fact that the transverse velocities with which our rods move are not uniform along their lengths, but increase from zero at the bottom to a maximum value at the top of each rod. We identify a critical velocity as that velocity at the top of a rod at which the first vortices are observed to be produced 0.5–1 cm below the upper edge. The corresponding critical Keulegan-Carpenter numbers are plotted against the Stokes number in Fig. 10.

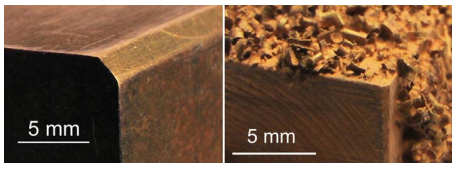

FIG. 7. (Color online) Left: the detail of the trimmed edge (after the second trimming) of the 3×3 cm^2 brass rod. Right: the detail of the roughened gold-plated surface of the 2×2 cm^2 brass rod.

FIG. 8. (Color online) A photograph of two brass cylinders of square cross section 2×2 cm^2. The surface of the lower one was roughened by soldering small brass shavings to it; this surface was then electrochemically cleaned and gold plated.

We see from Fig. 10 that most of the data are consistent with a critical Keulegan-Carpenter number K_C^{crit} that is proportional $\beta^{-1/2}$, as was the case with the tuning forks. The

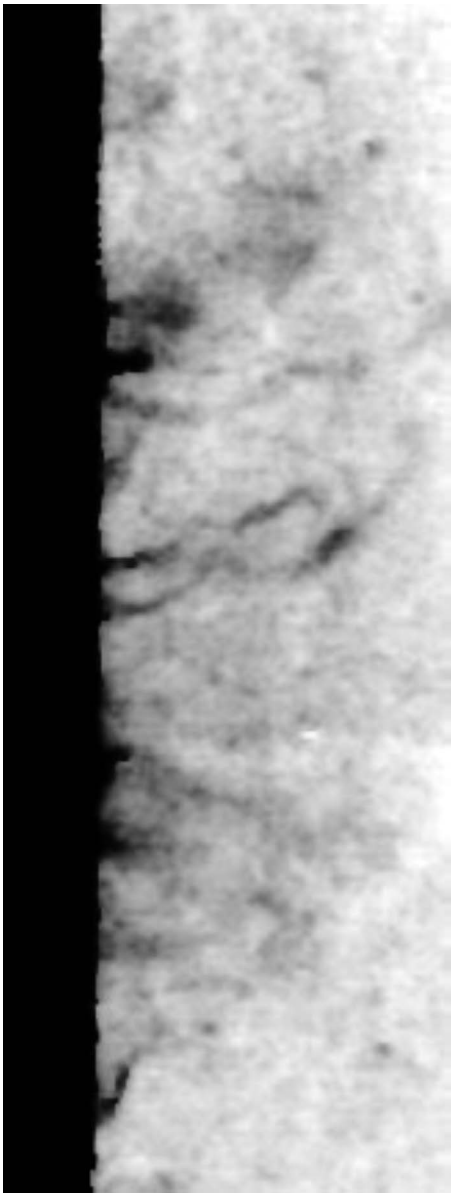

FIG. 9. A photograph showing a typical pattern of vortices produced by an oscillating rod of cross section 3×3 cm^2 at a velocity amplitude well above the transition.

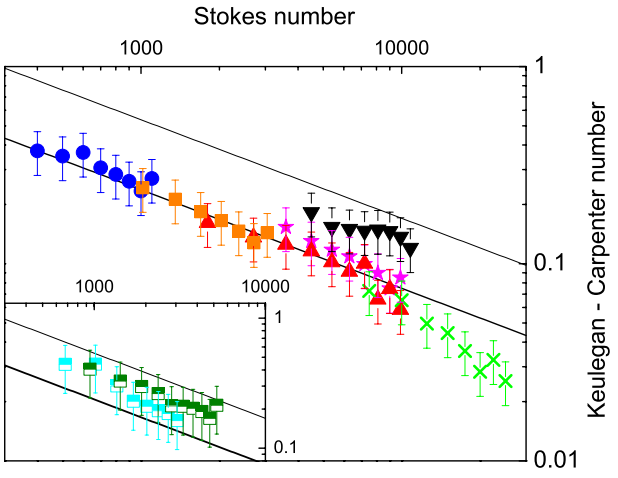

FIG. 10. (Color online) The critical Keulegan-Carpenter number plotted against Stokes number for various rods of square cross section oscillating in water. All the data were obtained by visualization, and relate to the first appearance of vortices being shed by the rod about 0.5 cm below the upper edge. The data in the main graph were obtained with the Baker *p*H technique; those in the inset were obtained by the Kalliroscope technique. In the main graph, filled (blue) circles, filled (orange) squares, filled (red) triangles, and (green) crosses represent the data observed with rods of 1×1, 2×2, 3×3, and 5×5 cm^2 square cross sections, respectively; (magenta) stars and (black) triangles show how the critical Keulegan-Carpenter number changes when the sharp edges of the 3×3 cm^2 rod are trimmed successively. The inset shows the critical Keulegan-Carpenter number for the 2×2 cm^2 rod, obtained with the Kalliroscope technique before [upper (dark green) symbols] and after [lower (cyan) symbols] roughening of the surface. The dotted straight line corresponds to $K_C^{\rm crit}=17\beta^{-1/2}$ (c.f. Fig. 3) and the solid line is $K_C^{\rm crit}=7.5\beta^{-1/2}$.

only exception is the rod with cross section 5×5 cm^2, the anomalous behavior of which may be associated with the fact that its length is not sufficiently large compared with its width to ensure that end effects are not important. We note that the absolute values of $K_C^{\rm crit}$ for our rods, for a given value of β, are closely similar to those of $K_C^{\rm crit}(0.05)$ for the tuning forks, suggesting that our "5% criterion" in the latter case does indeed indicate reasonably accurately the first instability, as observed with the bars in water.

To check the influence of sharpness of the edges on $K_C^{\rm crit}$ experimentally, we have successively trimmed the edges of the 3×3 cm^2 rod. This trimming has been done very accurately using a milling cutter (see Fig. 7), so that the size of the trim was 1 and 2 mm, respectively, after the first and the second trimming. The fact that $K_C^{\rm crit}$ for the rod of cross section 3×3 cm^2 is increased when the sharp corners are trimmed suggests that the onset of the first instability in the laminar flow is associated with these sharp corners. In contrast with a rod of circular cross section, the overall width of the rod may therefore be irrelevant to this instability, and this difference may account for the different dependence of $K_C^{\rm crit}$ on β in the two cases; instead of the overall width, what may be important is either the radius of curvature at the sharp edge or the radius of curvature of the outer surface of the viscous penetration depth, whichever is the larger. The fact that roughening the surface of the rod of cross section 2×2 cm^2 has such a small effect is surprising, in view of the fact that the scale of the roughness is larger than the viscous penetration depth. It does, however, suggest that surface roughness may not be an important factor in the behavior of the tuning forks. Our experiments do not tell us whether the proximity of the two prongs of a tuning fork is important.

IV. CONCLUSIONS

Commercially available quartz tuning forks are being used increasingly in various applications at cryogenic temperatures. We have measured the damping of the oscillations of a range of such forks in classical cryogenic fluids (helium I and helium vapor), and we have observed the transition from laminar to turbulent flow. The critical Keulegan-Carpenter number $K_C^{\rm crit}$ corresponding to the initial departure from laminar behavior, and so to the initial instability of laminar flow, is found probably to be proportional to $\beta^{-1/2}$, where β is the Stokes number. In order to throw more light on the behavior of these forks, we have carried out experiments on rods of square cross section (to mimic a prong of a fork) oscillating in water, with the dimensions and frequency of oscillation being chosen to correspond to values of the relevant dimensionless parameters that are close to those for the forks. Visualization of the flow of the water suggests that, as is known to be the case with rods of circular cross section, the transition to turbulence involves an initial instability within the viscous penetration depth, with the resulting vortex motion being dragged away from the surface by the steady streaming that is known to be associated with oscillatory motion of a curved structure in a classical fluid. Values of $K_C^{\rm crit}$ obtained from the visual observations display the same dependence on β as was observed with the tuning forks. When the sharp corners of a rod were trimmed the value of $K_C^{\rm crit}$ was found to increase significantly. This suggests that the initial instability is associated with the small radius of curvature at these corners. The dependence of $K_C^{\rm crit}$ on β that we observe ($\beta^{-1/2}$) is different from that reported for rods of circular cross section ($\beta^{-1/4}$ at high velocities). We suggest that this difference arises because the relevant radius of curvature is the overall radius in the case of a rod of circular cross section, while it is the radius of curvature associated with the corners of a rod of square cross section, with this latter radius being the actual radius or the radius of curvature of the outer part of the viscous penetration depth, whichever is the larger. In the case of a rod of circular cross section the drag coefficient tends to oscillate in value with increasing β, in the neighborhood of the transition, while the drag coefficient that we observe with our forks varies smoothly. While this difference may reflect a different type of flow, it may also be associated, at least in part, with the fact that the velocity with which a prong of one of our forks moves varies along its length. Roughening the surface of one of our rods was observed, surprisingly, to have little effect on the value of $K_C^{\rm crit}$.

ACKNOWLEDGMENTS

We are grateful to O. Kolosov and B. Studer for providing some of quartz tuning forks used in this work, to R. Hershberger and R. J. Donnelly for showing us the results of their research prior to publishing, and to L. Doležal for skillful manufacturing of the visualization equipment. This research was supported by research plans MS 0021620834 and by GAČR Contract No. 202/08/0276.

[1] D. O. Clubb, O. V. L. Buu, R. M. Bowley, R. Nyman, and J. R. Owers-Bradley, J. Low Temp. Phys. **136**, 1 (2004).
[2] R. Blaauwgeers *et al.*, J. Low Temp. Phys. **146**, 537 (2007).
[3] M. Blažková, D. Schmoranzer, and L. Skrbek, Phys. Rev. E **75**, 025302 (2007).
[4] M. Blažková *et al.*, J. Low Temp. Phys. **148**, 305 (2007); **150**, 525 (2008).
[5] E. M. Pentti, J. T. Tuoriniemi, A. J. Salmela, and A. P. Sebedash, J. Low Temp. Phys. **150**, 555 (2008).
[6] M. Blažková, D. Schmoranzer, L. Skrbek, and W. F. Vinen, Phys. Rev. B **79**, 054522 (2009).
[7] D. I. Bradley *et al.*, J. Low Temp. Phys. **157**, 476 (2009).
[8] L. D. Landau and E. M. Lifshitz, *Fluid Mechanics*, 2nd ed. (Butterworth-Heinemann, Oxford, 1987).
[9] L. Skrbek and W. F. Vinen, in *Progress in Low Temperature Physics*, edited by M. Tsubota and W. P. Halperin (Elsevier, New York, 2009), Vol. XVI, Chap. 4.
[10] T. Sarpkaya, J. Fluid Mech. **165**, 61 (1986).
[11] M. Tatsuno and P. W. Bearman, J. Fluid Mech. **211**, 157 (1990).
[12] H. Honji, J. Fluid Mech. **107**, 509 (1981).
[13] C. H. K. Williamson, J. Fluid Mech. **155**, 141 (1985).
[14] E. D. Obasaju, P. W. Bearman, and J. M. R. Graham, J. Fluid Mech. **196**, 467 (1988).
[15] P. Hall, J. Fluid Mech. **146**, 347 (1984).
[16] D. J. Baker, J. Fluid Mech. **26**, 573 (1966).
[17] www.Kalliroscope.com/juices/rheoscopic_fluids.htm
[18] R. Hershberger and R. J. Donnelly (private communication).
[19] H. Schlichting, Phys. Z. **33**, 327 (1932).
[20] H. Schlichting and K. Gersten, *Boundary-Layer Theory* (Springer, New York, 1996).
[21] G. K. Batchelor, *An Introduction to Fluid Dynamics* (Cambridge University Press, Cambridge, England, 1967).

Generation of turbulence by vibrating forks and other structures in superfluid ^{4}He

M. Blažková,[1] D. Schmoranzer,[2] L. Skrbek,[2] and W. F. Vinen[3]
[1]*Institute of Physics, ASCR, v.v.i., Na Slovance 2, 182 21 Prague, Czech Republic*
[2]*Faculty of Mathematics and Physics, Charles University, Ke Karlovu 3, 121 16 Prague, Czech Republic*
[3]*School of Physics and Astronomy, University of Birmingham, Birmingham B15 2TT, United Kingdom*
(Received 28 October 2008; revised manuscript received 6 January 2009; published 20 February 2009)

A study of the drag on the prongs of a number of quartz forks vibrating in the superfluid phase of ^{4}He is reported, and particular attention is paid to the transitions from laminar to turbulent flow over a wide range of temperature. Behavior in the normal phase is consistent with that for a classical fluid, as has already been reported [Phys. Rev. E **75**, 025302 (2007)]. Behavior in the superfluid phase is compared to that of other structures vibrating in superfluid ^{4}He, and similarities and differences are noted. We focus on the observed behavior of the drag coefficient as a function of velocity, and the problems posed by this behavior are explored. There is evidence for a sharp critical velocity at which significant turbulence starts to be generated in the superfluid component. At high velocities the drag coefficient tends to that observed in a classical fluid, suggesting that the two fluids, strongly coupled by mutual friction, are then behaving like a single classical viscous fluid. Behavior in the intermediate region seems to vary from one case to another. Evidence is presented that in the case of some structures the transition to single-fluid behavior takes place rather abruptly at a velocity that is only slightly greater than the sharp superfluid critical velocity, but that in other structures the transition is more gradual. Observed values of both the superfluid critical velocity and the effective viscosity of the fully coupled fluids are presented and discussed. It is suggested that the critical superfluid velocity is always closely similar to that at which the coupled fluids would be expected to undergo a classical transition between a flow that is strictly laminar and one that displays the first instability, and a possible reason is discussed.

DOI: 10.1103/PhysRevB.79.054522 PACS number(s): 67.25.dk, 67.25.dm, 47.27.Cn, 47.37.+q

I. INTRODUCTION

Recently many studies of the behavior of vibrating wires,[1,2] spheres,[3] and grids[4–6] in the superfluid phases of both ^{4}He and ^{3}He were reported. Attention has been focused especially on the change in damping associated with the transition to turbulent flow. Critical velocities have been reported, together with the dependence of the damping on velocity in the supercritical regime; sometimes this transition is accompanied by hysteresis or switching. Important questions in classical turbulence relate to the forms of turbulence generated by flow past various types of obstacle and to the processes by which these forms are produced. The experiments on vibrating structures in superfluids allow us to address analogous questions relating to quantum turbulence. Turbulence in a superfluid, or quantum turbulence,[7] differs from that in a classical fluid for three reasons: except at the lowest temperatures, the superfluid exhibits two-fluid behavior, a normal-fluid component coexisting with a superfluid component—the two fluids being able to support independent velocity fields; the superfluid component can flow without dissipation; and flow of the superfluid is subject to severe quantum restrictions. These restrictions mean that the only form of rotational motion allowed in the superfluid component is a quantized vortex line, in which there is an irrotational circulation equal to $2\pi\hbar/m$ round a thin vortex core, where m is the mass of a ^{4}He atom or two ^{3}He atoms. Turbulent flow of the superfluid component must therefore take the form of some irregular tangle of vortex line. On length scales greater than the spacing between the vortex lines, flow of the superfluid component can mimic that of a classical fluid. However, on smaller length scales, including typically those at which dissipation occurs, the flow must be very different. At a finite temperature any vortex line moving relative to the normal fluid suffers a drag (mutual friction), which can cause motion in the two fluids to become strongly coupled. The study of quantum turbulence combines the challenges we meet in the study of classical turbulence with those associated with quantum phenomena.

The first aim of this paper is to describe observations made with a number of vibrating forks[8] in superfluid ^{4}He at temperatures above 1 K, where there is a significant fraction of normal fluid. The observations are compared to those reported very recently for vibrating forks in ^{4}He at lower temperatures and with those relating to other forms of oscillating structure in ^{4}He. Experimental results are presented in the form of plots of the drag coefficient against velocity. We demonstrate that all these experimental results exhibit certain common features: a sharp critical velocity, with or without hysteresis or switching, associated with the onset of turbulence in the superfluid component; a tendency for the drag coefficient to approach a constant value, of order unity, at high velocities, similar to the behavior observed with classical fluids; and an intermediate region in which the drag coefficient varies with velocity in a way that differs to some extent from one type of oscillating structure to another. We go on to set out the nature of the problems raised by these observations, emphasizing both the similarities to, and the differences from, those relevant to classical fluids. We argue that the observed behavior at high velocities indicates "quasiclassical behavior," in which, even at high temperatures, there is a single turbulent velocity field (arising from coupled motion of the two fluids) that mimics that occurring in a classical fluid. We consider the intermediate region, arguing

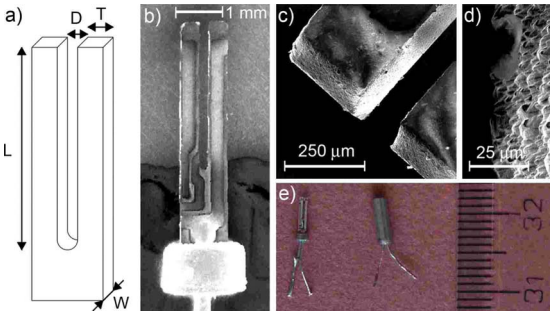

FIG. 1. (Color online) A commercially available quartz tuning fork (Ref. 12). (a) A schematic drawing of the fork; (b) micrograph of the entire fork; (c) micrograph of the ends of its prongs; (d) detail of its surface roughness; (e) fork in its original can and with the can removed.

that for some structures there is a rather sudden transition to quasiclassical behavior, with a more gradual transition for others. We observe that the superfluid critical velocity seems to coincide with the velocity at which flow of the quasiclassical coupled fluids would make a transition between a strictly laminar form and one in which the first instability of that flow is evident, and we suggest a tentative reason. We shall wish to emphasize that the way in which the drag coefficient is observed to vary with velocity, over the whole range of velocities, contains much information about the processes accompanying the vibration of the structure over and above that contained simply in the observed superfluid critical velocity. Our discussion relates only to superfluid ^{4}He; superfluid ^{3}He, even in the *B* phase, appears to behave differently.[9,10]

There are two different theoretical (or computational) approaches to the generation of quantum turbulence by vibrating structures. In the case of very small structures, when only small numbers of vortex lines may be involved, the evolution of the turbulence might well be examined by computer simulation.[11] However, for larger structures, when large numbers of vortex lines are likely to be involved, especially in fully developed turbulence, computer simulations of the type so far available are inadequate since they cannot cope with large vortex densities.[10] In this latter case, we must rely on general physical arguments, essentially statistical in nature, such as those associated with the concept of an eddy viscosity. Discussion of our experimental results in this paper will be based on such general arguments, so that they may not be relevant to the behavior of the smallest structures. We note that the characteristic dimensions of the forks with which this paper is primarily concerned are significantly larger than those of most other vibrating structures that have been studied in superfluid helium.

II. EXPERIMENTAL RESULTS WITH VIBRATING FORKS IN SUPERFLUID ^{4}He

The forks are made of quartz and are available commercially as frequency standards,[12] typically for 2^{15} Hz ($\sim$33 kHz) at room temperature; those we have used in most of our work have the shapes shown in Fig. 1 and their dimensions are given in Table I. The forks are excited at their resonant frequencies, and we measure the amplitude of the resonant response as a function of the drive force F.[13] The way in which the amplitude of the response and the drive force are derived from the electrical measurements is described in Ref. 8. It is illuminating to plot the results in terms of a drag coefficient, C_D, which is defined by the equation

TABLE I. Dimensions of forks.

Fork	Freq. (kHz)	L (mm)	T (mm)	W (mm)	D (mm)
A1	32	3.71	0.42	0.35	0.21
B1	32	3.65	0.68	0.46	0.18
C3	32	2.51	0.25	0.10	0.13
U1	4	19.70	2.20	0.80	
U2	8	9.50	0.45	0.90	0.50
L2	32	2.17	0.21	0.10	0.12
L1	32	2.17	0.21	0.10	0.12
K1	32	3.9	0.39	0.28	

$$F = \frac{1}{2} C_D \rho A U^2, \tag{1}$$

where ρ is the appropriate fluid density, $A=LW$ is the area of a prong projected on a plane normal to the motion, and U is the amplitude of the velocity response at the ends of the prongs of the fork. (Strictly speaking we should take into account the fact that the velocity with which any particular part of a prong moves varies along the length of the prong. However, in the overall damping there is a heavy weighting in favor of the region of a prong near its tip.) Figures 2–4 show typical results for three forks (A1, L2, and U1) in the form of plots of C_D against U for different temperatures.

III. DISCUSSION OF EXPERIMENTAL RESULTS

A. Normal phase

Consider first the drag exerted on the prongs of the fork A1 at a temperature of 2.16 K. The fraction of superfluid is then very small, and we can assume that the observed form of dependence of C_D on U is that for a classical fluid with kinematic viscosity, ν, equal to the viscosity of the normal fluid divided by the total fluid density. (We attempted to take data above the lambda transition, but we found that at the highest velocities they were affected by cavitation.[14]) At the angular frequency, ω, appropriate to the fork, the classical viscous penetration depth, $\delta=(2\nu/\omega)^{1/2}$, is small compared to all dimensions of a prong. We can then expect the drag coefficient at low velocities (laminar flow) to have the form[15]

$$C_D = 2\alpha \frac{S}{A} (\omega\nu)^{1/2} \frac{1}{U}, \tag{2}$$

where $S \approx 2L(T+W)$ is the total surface area of a prong and α is a constant of order unity that depends on the shape of the fork. We ignore streaming effects.[15] In the limit of high

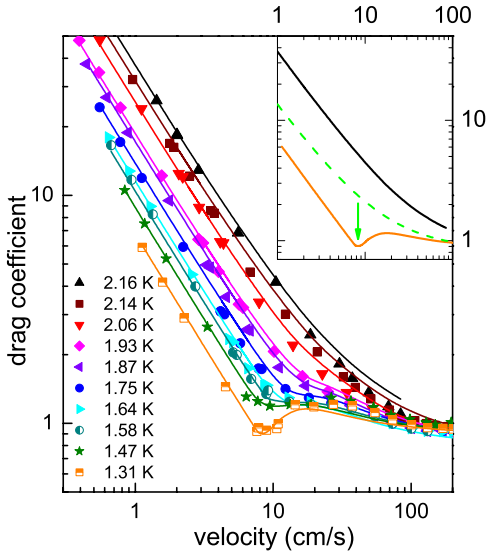

FIG. 2. (Color online) Plots of the observed drag coefficient at various temperatures and at the saturated vapor pressure for vibrating tuning fork A1 (Ref. 12). The lines are fits to a theoretical expression that is described in the text. In the inset we show the experimental curves for temperatures of 1.31 and 2.16 K, together with the broken (green) line, which shows how the drag coefficient would behave for a classical fluid with the kinematic viscosity ν_c evaluated for fork A1 at a temperature of 1.31 K (ν_c is defined in the text).

velocities we expect to have fully developed turbulent flow, for which the drag coefficient is expected to be a constant, β, of order unity. These expectations are consistent with our experimental results at 2.16 K, and they are consistent also with results already published.[16] A drag coefficient given by the simple interpolation formula,

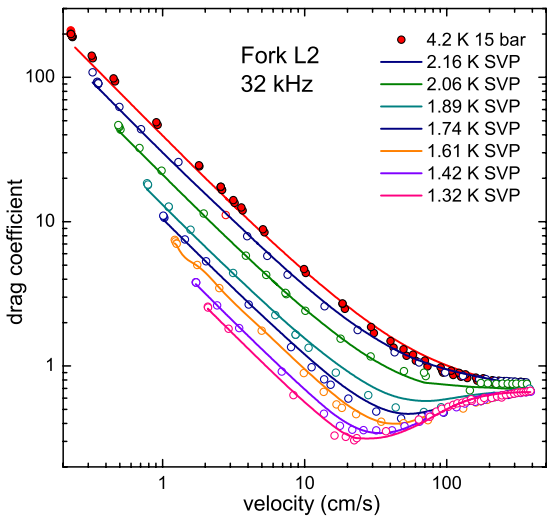

FIG. 3. (Color online) Plots of the observed drag coefficient at various temperatures and at the saturated vapor pressure for vibrating tuning fork L2. Behavior of the fork L1 is very similar. The lines are fits to a theoretical expression that is described in the text.

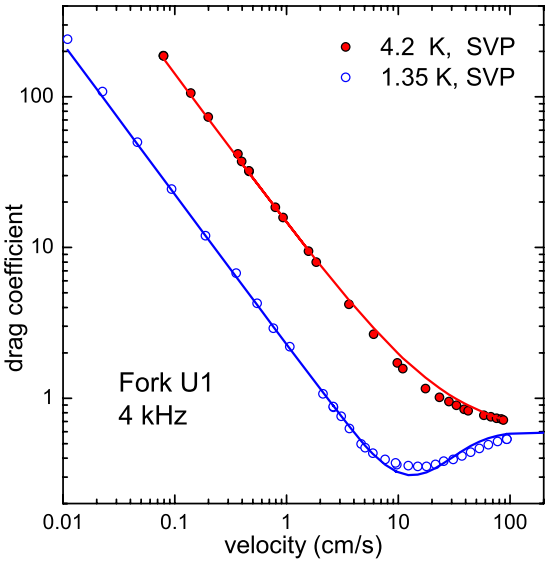

FIG. 4. (Color online) Plots of the observed drag coefficient at two temperatures and at the saturated vapor pressure for vibrating tuning fork U1. The lines are fits to a theoretical expression that is described in the text.

$$C_D = 2\alpha\frac{S}{A}(\omega\nu)^{1/2}\frac{1}{U} + \beta, \tag{3}$$

describes the experimental results rather well over the whole range of velocities. In earlier publications we have defined the critical velocity for the classical transition from laminar to turbulent flow as the velocity at which the two terms on the right-hand side of Eq. (3) are equal, so that

$$U_c = 2\frac{\alpha}{\beta}\frac{S}{A}(\omega\nu)^{1/2}. \tag{4}$$

In fact this definition is misleading because, almost certainly, it does not correspond to any significant change in flow pattern. It is probable that in reality the gradual change in the form of the drag coefficient, from that corresponding to strictly laminar flow to that corresponding to a fully turbulent regime with eddy motion on scales up to width of a prong, reflects a sequence of different flow patterns; the first one displaying the primary instability of the laminar flow. For the case of a vibrating fork the details of this sequence are not known. The details are known for the case of a cylinder with circular cross section, undergoing transverse oscillations in water, with visualization of the flow,[17–20] and in this case the initial instability is a Taylor (Taylor-Görtler) instability in the viscous penetration depth arising from the curvature of the surface of the cylinder.[18,21,22] Attempts to carry out similar experiments with a rod of rectangular cross section in water (i.e., with a suitably scaled version of the prong of a fork) are in progress in our own laboratory in Prague and by Donnelly and Hershberger[23] at the University of Oregon, but they are proving hard to interpret (in setting up these classical experiments we have assumed that the two prongs of a fork do not lead to flows that interfere with each other); it might be expected that the first instability would arise at the corners of

the rod, but, if this is indeed the case, the instability seems to spread rapidly over the whole surface of the rod. In the present context we shall find later that the physically significant classical critical velocity seems to be that at which the first instability occurs, which we identify with the first departure of the drag coefficient from that corresponding to strictly laminar flow and which we denote by U_{c1}. For the purposes of rough quantitative analysis we take U_{c1} as the velocity at which the first term on the right-hand side of Eq. (3) is four times β; i.e., we take

$$U_{c1} = \frac{\alpha}{2\beta}\frac{S}{A}(\omega\nu)^{1/2}. \tag{5}$$

B. Superfluid phase: Forks A1, B1, and C3

Looking at Figs. 2–4, we see that the curves for temperatures well below the lambda transition are quite different in shape from those for the normal phase. Especially at the lowest temperatures, there is a minimum in the drag coefficient; in the case of fork A1 this minimum is rather sharp, although it is less sharp in the case of forks L1/L2 and U1. A sharp minimum suggests the existence of a sharp critical velocity. Since this feature becomes well marked at only the lowest temperatures we make the reasonable assumption that it is associated with the superfluid component; i.e., that it marks the onset of significant vorticity, in the form of a significant density of vortex lines, in the superfluid component. We denote this critical velocity by U_{cs}. We emphasize that no hysteretic behavior is seen; the form of the drag versus velocity is the same for increasing velocities as it is for decreasing velocities.

Let us now focus our attention on the results obtained with fork A1; those obtained with forks B1 and C3 are similar. We see that, at velocities greater than that which we identify as the superfluid critical velocity, the drag coefficient passes through a broad maximum and then follows a curve that is very similar to that for a classical fluid, tending to a constant value of order unity at the highest velocity. Thus there appears to be a critical velocity analogous to that given by Eq. (4) in addition to the critical velocity U_{cs}. At first sight we were tempted to associate this second transition with the normal fluid,[24] but in fact this is not reasonable because of the strong coupling between the two fluids that must result from the vortex lines produced by the transition in the superfluid component. Instead we start by suggesting the following tentative scenario. The transition in the superfluid component leads to the formation of a random tangle of vortex line in the neighborhood of the fork. The resulting mutual friction couples the two fluids together, so that they behave as a single quasiclassical fluid. We assume that this single coupled fluid can be characterized by an effective kinematic viscosity, ν_e, which describes the combined effect of the viscosity of the normal fluid and an eddy viscosity characterizing small-scale momentum transfer in the superfluid due to small-scale vortex motion in the random tangle. The length scale associated with this small-scale motion is the vortex spacing, ℓ, and the velocity scale is of order κ/ℓ, where κ is the quantum of circulation. The eddy kinematic viscosity must therefore be of order κ, which has the same order of magnitude as the kinematic viscosity, η_n/ρ, of the normal fluid (ρ is the total density of the helium). Thus the effective kinematic viscosity of the coupled fluids is likely to be of order η_n/ρ; the precise value may be either larger or smaller by a factor of order unity. It is natural now to assume that, provided that the vortex tangle extends far enough from the surface of the fork, this coupled fluid system can undergo a gradual transition to large-scale turbulence (turbulent eddies on a scale of order the width of the prongs of the fork), in a way similar to that occurring in a classical fluid. Thus we might assume tentatively that there are two transitions: the first establishes a more or less random tangle in the superfluid component, allowing that component to undergo rotational motion and to couple its motion to the normal component; the second being a quasiclassical transition to large-scale turbulence in the coupled components. At velocities greater than the superfluid critical velocity but less than that associated with the coupled fluids, the "random" vortex tangle in the superfluid component might allow that component to flow in a quasiclassical laminar mode, matching the laminar flow in the normal fluid; the vortex tangle is then not strictly random to the extent that it allows the superfluid to flow with the large-scale vorticity field characteristic of laminar viscous flow. We remark that in this laminar viscous flow the parallel component of the velocity field, relative to the velocity of the oscillating fork, would need to vanish at the boundaries of the fork; this would be achieved by partial pinning of the vortices on the rough surface of the fork. We emphasize that these are tentative ideas. We shall find later, following a more detailed consideration of the experimental results, that they need some modifications; in particular coupled laminar viscous flow does not seem to be observed, the transition in the superfluid at the velocity U_{cs} leading immediately to turbulent flow of the coupled fluids.

Our ideas can be expressed in terms of a model, according to which the total drag coefficient can be represented mathematically by the following equations:

$$C_D = 2\alpha\frac{S}{A}(\omega x_e \nu_e)^{1/2}\frac{1}{U} + x_e\beta, \tag{6}$$

where

$$x_e = x + (1-x)\Phi(U-U_{cs})\frac{(U-U_{cs})^2}{\varepsilon + (U-U_{cs})^2}, \tag{7}$$

$$\nu_e = \nu + (\nu_c - \nu)\Phi(U-U_{cs})\frac{(U-U_{cs})^2}{\varepsilon + (U-U_{cs})^2}, \tag{8}$$

where U is the velocity amplitude of a fork, x is the normal-fluid fraction, ρ_n/ρ, $\nu = \eta_n/\rho$ is the kinematic viscosity of the normal fluid referred to the total fluid density, $\Phi(y)$ is the Heaviside step function, U_{cs} is the critical velocity of the superfluid component, ν_c is the effective kinematic viscosity of the fully coupled fluids, and α, β, and ε are constants. Equation (6) has the form that applies to a classical fluid with an effective density $x_e\rho$ and effective kinematic viscosity ν_e [(cf. Eq. (3)]. We see that, according to these equations, the effective normal-fluid fraction starts to rise from x to unity

TABLE II. Values of the adjustable parameters α, β, and ϵ.

Fork	α	β	ϵ
A1	0.72	0.85	0.015
B1	0.65	0.43	0.045
C3	0.36	0.42	0.075
U1	0.26	0.52	0.14
U2	0.27	0.5	
L2	0.4	0.63	0.85
L1	0.38	0.63	0.95
K1	0.55	0.85	0.003

when the superfluid velocity exceeds the critical velocity U_{cs}, the change taking place over range of velocity determined by the parameter ε, and that the effective kinematic viscosity changes (increases or decreases) from ν to ν_c in a similar way. The precise description of the transition region of width ϵ implied by these equations should not be taken too seriously. The equations are intended to provide simply an interpolation between the regime in which the two fluids are uncoupled, for $U < U_{cs}$, and that in which the fluids are fully coupled, for $U \gg U_{cs}$. (It can be added, however, that other simple forms of interpolation seem less successful when attempting to fit all available experimental data. Better agreement between the fits and the experimental data might be achieved with additional free fitting parameters, but it is hardly justified in view of the limited experimental accuracy.)

The solid lines in Fig. 2 are obtained with these fitting functions, α, U_{cs}, β, ν_e, and ε being adjustable parameters (normal-fluid parameters are taken from Donnelly and Barenghi[25]). We see that the fits are rather good, providing evidence in favor of our model. We note in particular that the model reproduces the maximum in C_D at a velocity of order 200 mm s^{-1}. As expected, the fitting parameters α, β, and ε are independent of temperature, and they are displayed in Table II. Values of the superfluid critical velocity, U_{cs}, and the effective kinematic viscosity, ν_c, will be discussed later. As expected, the parameters α and β are of order unity, while ν_c is not very different from ν. The parameter ε is small, showing that the initial transition that generates a vortex tangle in the superfluid leads to a sharp rise in the coupling between the two fluids.

C. Superfluid phase: Forks L1/L2 and U1

Looking at Figs. 3 and 4 we see what appears to be a rather different behavior: the minimum that we associate with the superfluid critical velocity is less sharp and at velocities greater than the superfluid critical velocity there is no maximum before the drag coefficient levels off at a constant value. Nevertheless, as we see from Figs. 3 and 4, our trial functions 6, 7, and 8 can still be fitted, but only with a value of ϵ that is significantly increased. This difference implies that vortex line starts to be produced at velocities above the superfluid critical value at a rate that is significantly smaller, so that full coupling between the two fluids sets in more gradually. The reason for this difference is not known. The difference does not seem to be associated with a different size or frequency of fork. A possible reason is that forks L1/L2 and U1 have prongs with surfaces that are smoother than is the case with forks A1, B1, and C3.

We remark at this point that not only does ϵ vary from one fork to another, but also α and β, although the variation of these latter parameters is much smaller. The variation of α reflects an expected dependence of the laminar drag on the exact shape of the fork. The variation of β reflects some not-unexpected dependence of the limiting value of the drag coefficient at large velocity on the detailed geometry. We can add, however, that the values of β set out in Table II agree within experimental error ($\sim$20%) in cases where we have measured them with those obtained when the fork oscillates in a classical fluid (either gaseous helium at 77 K or the normal phase of liquid helium at an elevated pressure, the elevated pressure ensuring that the cavitation observed at the vapor pressure in the normal phase is suppressed[14]); this observation is consistent with our assertion that at high velocities the superfluid in the neighborhood of the fork is behaving like a classical fluid.

D. Comparison to vibrating forks at very low temperatures

The experimental results that we have been presenting relate to vibrating forks in superfluid ^{4}He at temperatures above 1 K, where there is a significant fraction of normal fluid. Very recently measurements at lower temperatures were performed in Kharkov[26] and we now compare them to our own.

Details of the fork (K1) used in Kharkov are included in Table I. For reasons connected with the way the experiments were carried out, the response of the fork and the driving force could not be calibrated in absolute units. Absolute values have therefore been obtained by direct comparison to the measurements on our fork A1, which displays almost identical behavior in an overlapping range of temperature. Typical results so obtained for the fork K1 are shown in Fig. 5, along with those for our fork A1 for comparison. We see a very similar behavior, except that the drag on fork K1 at subcritical velocities is much smaller. There is no hysteresis.

Various forks suffer some damping due to internal friction even *in vacuo* (the Q factor *in vacuo* is typically 5×10^5). At temperatures above 1 K this damping can be neglected at all velocities in comparison to that due to the helium. In the case of the Kharkov results, however, relating to temperatures below 1 K, the damping cannot be neglected. It leads to an apparently temperature-independent contribution to the drag at low velocities, a contribution that is dominant at the lowest temperatures. Subtraction of this contribution leads to a linear drag that is proportional to T^4 at the lowest temperatures, which is to be expected from the scattering of ballistic phonons. In Fig. 5 we show both the uncorrected and the corrected values of the drag.

If our ideas were correct, we can expect that our Eqs. (6)–(8) will still describe the corrected results, provided that we modify our model to take account of this ballistic scattering, which replaces laminar drag from the normal fluid.

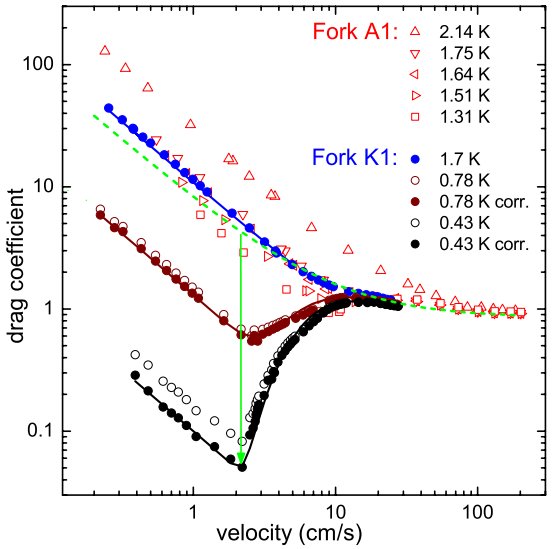

FIG. 5. (Color online) Plots of the observed drag coefficient at several low temperatures and at the saturated vapor pressure for the vibrating tuning fork K1. Results for our fork A1 are included for comparison. The lines are fits to a theoretical expression that is described in the text. The data for K1 do not extend to high enough velocities to allow an accurate determination of the parameter β and therefore β is taken to have the same value as that for A1. The uncorrected data for K1 are shown as open circles; data corrected for the internal damping of the fork (see text) are shown as filled circles. The broken (green) line is derived from Eq. (3) for a classical fluid of kinematic viscosity ν_c.

The phonons form what is in effect a fluid with high viscosity, which cannot become turbulent. We shall suppose that the drag due to the phonons is unaffected by the transition to turbulence in the superfluid component. This may not be strictly correct because the ballistic scattering may be affected by interaction between the phonons and the vortex lines, but the drag due to the phonons is small in comparison to that due to the superfluid turbulence, so that corrections to it are unlikely to be important. We can therefore modify Eqs. (6)–(8) by putting $x=0$ and adding to Eq. (6) a term $\gamma(T)/U$ to represent the effect of the ballistic scattering. The fits seen in Fig. 5 are obtained by taking $\gamma(0.78\ \mathrm{K})=0.013\ \mathrm{ms}^{-1}$ and $\gamma(0.43\ \mathrm{K})=0.001\ \mathrm{ms}^{-1}$. The good quality of these fits provides evidence in favor of our model. Values of the other adjustable parameters are given in Table II. Judging from the value of ε we see that the transition to turbulence in the superfluid is such that the vortex line is produced at a rate that increases rather sharply with increasing velocity, as was seen with forks A1, B1, and C3, but not with the other forks.

E. Values of the effective kinematic viscosity

Values of the effective kinematic viscosity ν_c deduced by fitting Eqs. (6)–(8) (modified in the case of K1) to the experimental data for the various forks are shown in Fig. 6. Although the values have the expected orders of magnitude, they fall into two distinct groups: those with $\nu_c \sim 10^{-8}\ \mathrm{m}^2\ \mathrm{s}^{-1}$ and those with $\nu_c \sim 2\times 10^{-9}\ \mathrm{m}^2\ \mathrm{s}^{-1}$. There is no obvious explanation of this fact; the forks belonging to one group do not seem to have any obvious characteristic that is different from those in the other group.

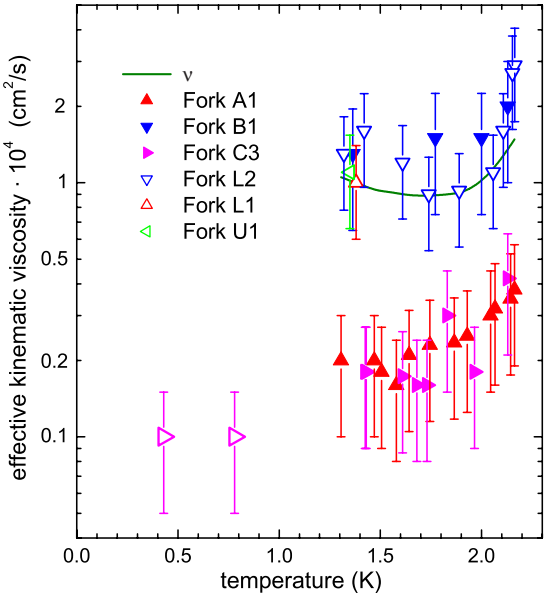

FIG. 6. (Color online) Plots of the effective kinematic ν_c against temperature for the various forks as indicated. The solid (green) line is a plot of kinematic viscosity of the normal fluid (referred to the total fluid density; i.e., η_n/ρ), based on values tabulated by Donnelly and Barenghi (Ref. 25).

IV. COMPARISON TO OTHER VIBRATING STRUCTURES

In Figs. 7 and 8 we show plots of the drag coefficient versus velocity for an oscillating grid[4,5] and an oscillating sphere.[3] The results for the grid, which show little or no hysteresis, have a form very similar to that for the forks. However, the data do not extend to sufficiently large velocities for us to determine the limiting value of the drag coefficient (i.e., the value of β). The sphere exhibits hysteretic

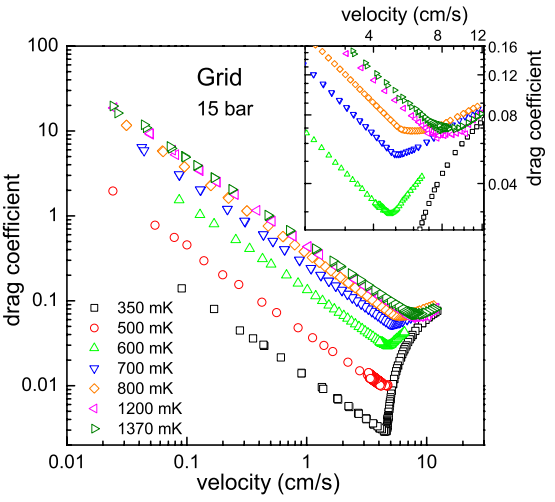

FIG. 7. (Color online) Plots of the observed drag coefficient at various temperatures and at the saturated vapor pressure for a vibrating grid.

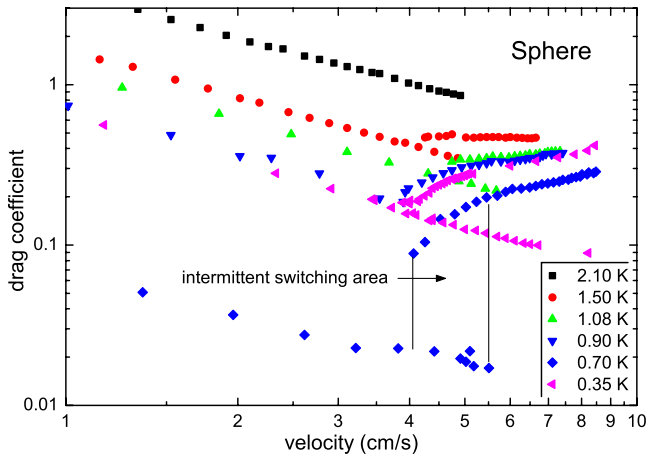

FIG. 8. (Color online) Plots of the observed drag coefficient at various temperatures and at the saturated vapor pressure for vibrating sphere.

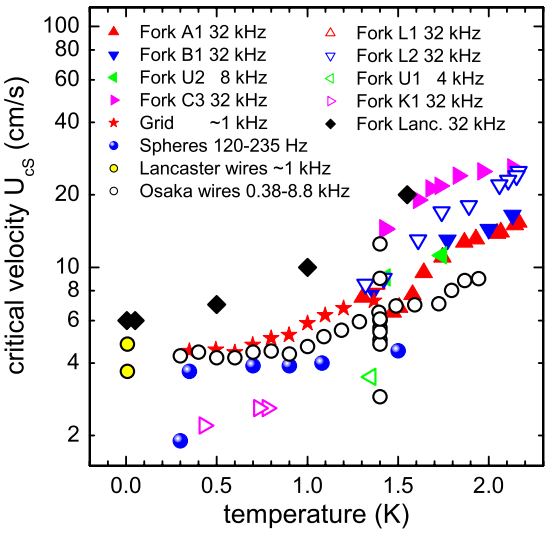

FIG. 9. (Color online) Values of the critical superfluid velocity, U_{cs}, observed for various oscillating structures, plotted against temperature. The different structures oscillate at different frequencies as shown.

and switching effects,[3] which we shall discuss later, but again the data seem not to extend to high enough velocities (the apparent rise in drag coefficient at high velocities suggests that the data might then be affected by heating). We do not show data for vibrating wires:[1,2] again they do not extend to large enough velocities and, more seriously, it seems difficult from the available data to correct for significant nonlinear internal damping. Furthermore, the wires have very small diameters, so that our type of analysis may not be applicable. We conclude that the available data for oscillating grids, spheres, and wires are not sufficiently extensive to permit the type of detailed analysis that underlies our Eqs. (6)–(8) and that they can be used only to extract values of the superfluid critical velocity. Further experiments are clearly required.

Values of the observed critical velocities for the various oscillating structures are displayed in Fig. 9 (the data labeled "Fork Lanc" were provided by Haley[27]). In cases where there is hysteresis we have taken the critical velocity that is observed on reducing the velocity. We see that there is a clear indication that the critical velocities increase with increasing temperature. Structures of different size seem to have critical velocities that are very similar in magnitude, but not exactly the same. The suggestion has been made (see Sec. V) that the critical velocities increase with increasing angular frequency, ω, as $\omega^{1/2}$. To test this suggestion we have plotted in Fig. 10 the dimensionless ratio $U_{cs}/(\omega\kappa)^{1/2}$ against temperature. There is little evidence that the data then collapse onto a single line, as would be required by this suggestion. We return to this question in Sec. V.

V. ORIGIN OF THE CRITICAL SUPERFLUID VELOCITY

It is generally accepted that when the superfluid critical velocity is exceeded a tangle of vortex lines forms in the superfluid component in the neighborhood of the oscillating structure. We argued in earlier sections that at high temperatures this leads to a strong coupling between the two fluids, and that the coupled fluids, behaving like a single fluid with a kinematic viscosity determined by a combination of the viscosity of the normal fluid and the eddy viscosity of the superfluid, undergoes a gradual transition to a fully turbulent state in a way closely similar to that observed when the structure oscillates in a classical fluid. At very low temperatures, when the normal fluid is effectively absent, there is a similar gradual transition, but one in which the superfluid component acts alone as a single quasiclassical fluid with a kinematic viscosity equal to the eddy viscosity associated with a tangle of vortex lines. These pictures leave us with an important open question: can we understand the value of the velocity at which the superfluid makes the initial transition to a tangled vortex state?

The first point that must be made is that the nucleation of vortex line at the critical velocity must be "extrinsic"; i.e., it must arise from the multiplication or stretching of existing remanent vortex line. Intrinsic nucleation of vortex line is

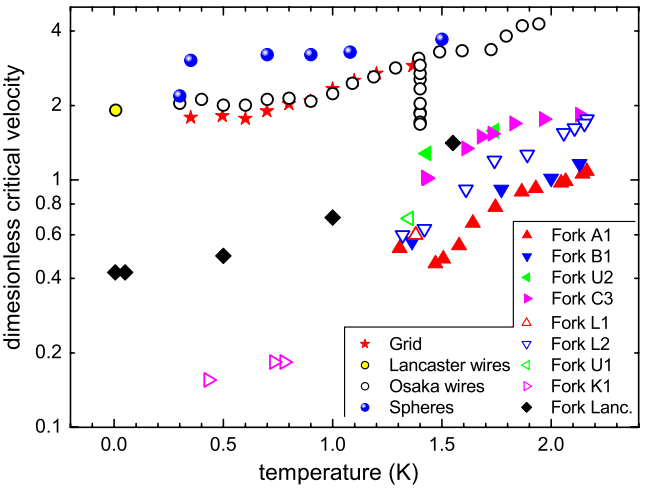

FIG. 10. (Color online) Values of the dimensionless ratio $U_{cs}/(\omega\kappa)^{1/2}$ plotted against temperature.

possible in superfluid ^{4}He only at velocities that are much larger than those encountered here. Very strong experimental evidence comes from the recent work of the Osaka group with vibrating wires.[1]

As we have already mentioned, the superfluid critical velocity seems not to depend very strongly on the size of the oscillating structure. If it were accurately independent of size and shape and if it were then to depend on only the angular frequency, ω, and the quantum of circulation, κ, a dimensional argument leads to

$$U_{cs} = \text{const}(\omega\kappa)^{1/2}. \tag{9}$$

This is the predicted dependence on frequency that we mentioned earlier. However, as we also mentioned earlier, there is as yet little convincing experimental evidence for this dependence. The wide scatter on the experimental points in Figs. 9 and 10 leads us to believe that the critical velocity depends to a significant extent on the detailed geometry of the structure and perhaps also on the state of roughness of the surface. Moreover, it may depend also on the form of the remanent vortex or vortices.

We shall now focus largely on the behavior of the forks because, as we have explained, it is for this case that we have the most complete sets of experimental data. We recall from Sec. III A that the transition to turbulence in a classical fluid is rather gradual and described by Eq. (3). Let us look especially at the superfluid data in Fig. 2 and consider the way in which the drag coefficient varies as the velocity is reduced from a large value. The drag coefficient is observed to rise with decreasing velocity, just as it does in a classical fluid. As it approaches proportionality to $1/U$, the drag coefficient drops rather suddenly to the value appropriate to the normal fluid acting alone. In other words, the superfluid critical velocity appears at a velocity closely equal to that at which flow of a classical fluid with density equal to the total helium density and kinematic viscosity equal to the parameter ν_c makes a transition to laminar flow; i.e., at a velocity analogous to the classical critical velocity U_{c1} introduced in Sec. III A (see especially the broken green lines in Figs. 2 and 5). Although data for other forks are less clear cut, owing to a larger value of the smoothing parameter, ϵ, they nevertheless show very similar behavior. Furthermore, this behavior seems to be common to all oscillating structures, although more detailed experimental data will be needed to provide really convincing evidence. Evidence that the superfluid critical velocity is generally very similar to the classical critical velocity U_{c1} was discussed in more detail in a recent review by Skrbek and Vinen.[9]

Of course this similarity may result from a numerical accident. The classical critical velocity [Eq. (4)] is of the order $(\omega\nu)^{1/2}$. The effective kinematic viscosity of the fully coupled fluids is of the order 0.1κ and therefore the critical velocity given by Eq. (9) is similar in order of magnitude to that given by Eq. (5). But the observations suggest that the two critical velocities are not merely similar in order of magnitude but are actually closely equal.

At first sight this equality seems very strange. The two transitions are apparently quite different in character: the classical transition is from a state of laminar *viscous* flow with zero slip at a solid boundary; the quantum transition is from a state of laminar *potential* flow with complete slip at a solid boundary. However, this picture of the quantum transition is not quite correct because of the need for one or more nucleating vortices. Superfluid transitions arise from the multiplication and stretching of these nucleating vortices. The way in which this multiplication and stretching occurs is not generally known. Appropriate simulations would be helpful, but only those of Hänninen *et al.*[10] are available and they relate to an oscillating structure (a sphere) the surface of which is smooth, so that the nucleating vortices are not pinned to particular points on the sphere. However, the results of these simulations ought to be considered. The temperature is assumed to be zero. The nucleating vortex is in the form of a vortex stretching across the helium, to which the sphere is attached. Oscillation of the sphere at angular frequency ω leads to the generation of Kelvin waves on the nucleating vortex with wave number equal to approximately $k=(\omega/\kappa)^{1/2}$, and as the amplitude of these waves increases to values of order k^{-1} self-reconnections result in the production of vortex rings with radius of order k^{-1}. These rings are produced even at quite low velocities. However, above a certain critical velocity, which we denote by U_{cH}, the density of these rings in the neighborhood of the sphere suddenly increases and leads to the formation of what appears to be a random vortex tangle, which is usually localized in the form of a wake that oscillates from one side of the sphere to the other as the sphere itself oscillates. It should be noted that the critical velocity obtained in the simulations is significantly larger than the observed value of U_{cs} for a sphere.

The formation of this tangle would undoubtedly be modified if the oscillating structure were rough, but let us suppose that something similar still occurs, only at a lower velocity. We suppose then that when the critical velocity U_{cs} is exceeded a dense tangle of vortex line envelopes the oscillating structure. At very low temperatures this tangle causes the superfluid in the region of the tangle to behave like a classical viscous fluid, with viscosity equal to the eddy viscosity associated with a random tangle of vortex line; at a higher temperature, mutual friction gives rise to a strong coupling between the two fluids, so that they behave as a single fluid with an effective viscosity, ν_c, that depends on both the normal-fluid viscosity and the superfluid eddy viscosity. This is of course the idea that we used in developing the model on which Eqs. (6)–(8) are based. We assumed also that the enveloping tangle of vortex line extends away from the oscillating structure to a distance of order that at which flow is induced by the oscillation of the structure concerned.

However, this quasiclassical behavior requires presumably that the density of vortex line be sufficiently large. In other words the line spacing, ℓ, must be small compared with some characteristic lengths in the quasiclassical flow. One obvious characteristic length in the quasiclassical flow is the classical viscous penetration depth, given by

$$\delta = \left(\frac{2\nu_c}{\omega}\right)^{1/2}. \tag{10}$$

This penetration depth is clearly relevant to quasiclassical *laminar* flow; such laminar flow is possible only if $\ell < \delta$. The

characteristic length that is relevant to flow at velocities greater than those for which laminar flow is stable is less obvious. We can, however, assert with fair certainty that the *initial* instability occurs on a scale that is equal to the viscous penetration depth (this is known to be true for an oscillating cylinder of circular cross section[21,22]). As long as there is no hysteresis, which is the case with our tuning forks, the scale of the turbulent motion at velocities close to critical must also be confined to a region of size comparable with the viscous penetration depth, even when the velocity has been reduced from a large value. Thus we conclude that turbulent motion also requires that $\ell < \delta$, at least at velocities close to critical.

We return to the way in which the drag coefficient changes as the velocity is reduced from a large value. Experiment tells us that, as the velocity is reduced toward a value at which quasiclassical turbulence might be expected to give way to quasiclassical purely laminar flow (the analog of U_{c1}), the vortex density must decrease rather suddenly to a value that is too small to maintain quasiclassical behavior; i.e., to a density such that $\ell > \delta$. A sensible conclusion is that the high density of vortex lines at velocities where there is quasiclassical turbulence is being maintained by the quasiclassical turbulence itself.

This view is not unreasonable. The large-scale quasiclassical turbulence is maintained by the large-scale flow round the structure (combined with the no-slip boundary condition). There is an injection of energy into the large-scale turbulent motion in much the same way as occurs in flow through a grid (the large superfluid eddies being associated with a partial polarization of the underlying vortex tangle). The energy in the large eddies tends to flow through nonlinear coupling into smaller-scale turbulence until it reaches a scale of order the vortex spacing, where it serves to generate extra length of vortex line. The rate of decay of the large eddies is governed by their lifetimes, which are equal to their turnover times. Thus an important contribution to the generation of vortex line could come from the large-scale turbulence, so that failure to maintain this turbulence, for quasiclassical reasons, could result in a rather sudden reduction in the vortex line density. The observed link between the critical velocity U_{cs} and the velocity at which quasiclassical turbulence is extinguished then becomes natural. Similarly, during an increase in velocity, the vortex line density cannot increase to a value large enough to produce an observable drag until there is a development of large-scale turbulence. This situation implies an instability, so that the development of large-scale turbulence linked to the generation of a large vortex density may take place in practice only at a velocity larger than that at which the large-scale turbulence disappears on reducing the velocity. As we have noted, such hysteresis is indeed observed with some, but not all, structures, especially at lower temperatures.

We have noted that a critical velocity, U_{cH}, is observed in the simulations of Hänninen *et al.*,[10] although its magnitude is larger than the observed U_{cs}. This critical velocity seems to be unrelated to any quasiclassical critical velocity. There are various possibilities: the existence of U_{cH} may be peculiar to a structure with a smooth surface; U_{cH} may always be larger than U_{cs} and therefore unobservable; or the line density produced in a steady state above U_{cH} may remain quite small and too small to allow a quasiclassical transition to turbulent flow.

It is instructive to estimate the rate of production of vortex line resulting from the decay of large-scale turbulence. In the case of homogeneous isotropic turbulence the largest eddies, characterized by a velocity U and size D, decay on a timescale D/U, so that they lead to a flux of energy to smaller scales equal to roughly U^3/D per unit mass of helium. If we suppose that this decay rate applies also to eddies of size of order W in a volume of order $WTL/2$ around each prong of a tuning fork (W, L, and T are the fork dimensions shown in Fig. 1), then the rate of production of vortex line must be given in order of magnitude by

$$\rho_s \kappa^2 \frac{d\mathcal{L}}{dt} = \frac{U_s^3}{W} \rho \frac{WTL}{2}, \tag{11}$$

where $\mathcal{L}$ is the total length of vortex line, U_s is the superfluid velocity relative to a prong of the fork, and where we have taken the energy per unit length of vortex line, in a random tangle, to be $\rho_s \kappa^2$. For typical values of the various parameters, we find that $d\mathcal{L}/dt \sim 7 \times 10^6$ ms^{-1}. This is much larger than the values found in the simulations of Ref. 10, tending therefore to confirm that vortex production by decay of large-scale eddy motion is more effective than by direct stretching of remanent vortices (although the proviso must be added that the simulations of Ref. 10 were not extended to very large times).

Our model of the physics underlying the critical velocity U_{cs} implies that there is a small density of vortex lines in the neighborhood of the oscillating structure at velocities less than U_{cs}. The model does not tell us the magnitude of this small density. Experiments reported so far indicate a density that is too small to have an observable effect on the drag, although we note that the drag is likely to be determined not only by the density but also by the configuration of vortex line. Experiments at lower temperatures than have so far been studied, where the drag due to the normal fluid has become very small, ought to throw light on this question.

We return to the actual value of the critical superfluid velocity U_{cs}. We have suggested that it is equal to U_{c1}, evaluated for a classical fluid with kinematic viscosity equal to the effective kinematic viscosity ν_c; i.e.,

$$U_{cs} = \frac{\alpha}{2\beta} \frac{S}{A} (\omega \nu_c)^{1/2}. \tag{12}$$

Thus we predict that U_{cs} is proportional to the square root of the frequency only if the parameters α, β, S/A, and ν_c are constant. This prediction is consistent with our earlier suggestion that the critical velocity seems to depend to a significant extent on the detailed geometry of the structure.

The views that we have been expressing are of course speculative. Significant features of the experimental results, especially the variation of both the parameter ϵ and the effective kinematic viscosity ν_c from one structure to another, remain puzzling. But we hope that our views will serve to stimulate further work, both in the acquisition of more extensive experimental data and in the development of the

theory. If confirmed, a link between a superfluid critical velocity and an instability of quasiclassical flow would be an interesting feature of quantum turbulence.

We have noted that we have as yet little detailed knowledge or understanding of the transition to turbulence in the flow round our oscillating forks in a classical fluid. We emphasize, however, that this fact does not seriously affect our argument. In essence we have based this argument on the idea that quasiclassical flow of the superfluid around our forks mimics the purely classical flow, whatever that classical flow might be. This is not to say that a detailed knowledge of this classical flow would not lead ultimately to a better understanding of the quantum case.

VI. SUMMARY AND CONCLUSIONS

We have reported the results of experiments in which we have measured the drag on the prongs of a number of small tuning forks oscillating in superfluid ^{4}He, over a range of temperatures above 1 K, and we have compared our results to those obtained with forks at lower temperatures and with other forms of oscillating structure. We have presented our results in the form of plots of the drag coefficient against velocity; we have argued that the detailed form of these plots contains valuable information that extends beyond a knowledge of a critical superfuid velocity above which there is an increased drag; and we have noted similarities with the behavior of oscillating structures in classical fluids. In the light of this information we have discussed the nature of the critical superfluid velocity. We have observed that the velocity seems often to be associated with a transition to turbulence that is essentially classical in its characteristics, and we have tentatively suggested that this quasiclassical behavior has its origin in an instability in which the generation of vortex line at the rate required to produce large-scale turbulence is a by-product of the large-scale turbulence itself.

ACKNOWLEDGMENTS

We are grateful to many colleagues for stimulating discussions, especially R. Hänninen, M. Krusius, M. Tsubota, W. Schoepe, P. Skyba, and H. Yano. We thank O. Kolosov for supplying some of the quartz forks. This research is supported by research Plans No. MS 0021620834, No. AVOZ 10100520, No. GAUK 7953/2007, and No. GAČR 202/08/0276.

[1] H. Yano, A. Handa, H. Nakagawa, K. Obara, O. Ishikawa, T. Hata, and M. Nakagawa, J. Low Temp. Phys. **138**, 561 (2005); H. Yano, A. Handa, H. Nakagawa, M. Nakagawa, K. Obara, O. Ishikawa, and T. Hata, J. Phys. Chem. Solids **66**, 1501 (2005); H. Yano, N. Hashimoto, A. Handa, M. Nakagawa, K. Obara, O. Ishikawa, and T. Hata, Phys. Rev. B **75**, 012502 (2007); N. Hashimoto, R. Goto, H. Yano, K. Obara, O. Ishikawa, and T. Hata, *ibid.* **76**, 020504(R) (2007).

[2] D. I. Bradley, D. O. Clubb, S. N. Fisher, A. M. Guenault, R. P. Haley, C. J. Matthews, G. R. Pickett, and K. Zaki, J. Low Temp. Phys. **138**, 493 (2005); D. I. Bradley, Phys. Rev. Lett. **84**, 1252 (2000); D. I. Bradley, S. N. Fisher, A. M. Guenault, M. R. Lowe, G. R. Pickett, A. Rahm, and R. C. V. Whitehead, *ibid.* **93**, 235302 (2004).

[3] J. Jäger, B. Schuderer, and W. Schoepe, Phys. Rev. Lett. **74**, 566 (1995); J. Jäger, B. Schuderer, and W. Schoepe, Physica B **210**, 201 (1995); J. Luzuriaga, J. Low Temp. Phys. **108**, 561 (1997); M. Niemetz, H. Kerscher, and W. Schoepe, *ibid.* **126**, 287 (2002).

[4] H. A. Nichol, L. Skrbek, P. C. Hendry, and P. V. E. McClintock, Phys. Rev. Lett. **92**, 244501 (2004); Phys. Rev. E **70**, 056307 (2004).

[5] D. Charalambous, L. Skrbek, P. C. Hendry, P. V. E. McClintock, and W. F. Vinen, Phys. Rev. E **74**, 036307 (2006).

[6] D. I. Bradley, D. O. Clubb, S. N. Fisher, A. M. Guenault, C. J. Matthews, and G. R. Pickett, J. Low Temp. Phys. **134**, 381 (2004); D. I. Bradley, D. O. Clubb, S. N. Fisher, A. M. Guenault, R. P. Haley, C. J. Matthews, G. R. Pickett, V. Tsepelin, and K. Zaki, Phys. Rev. Lett. **95**, 035302 (2005).

[7] W. F. Vinen and J. J. Niemela, J. Low Temp. Phys. **128**, 167 (2002).

[8] R. Blaauwgeers, M. Blazkova, M. Clovecko, V. B. Eltsov, R. de Graaf, J. Hosio, M. Krusius, D. Schmoranzer, W. Schoepe, L. Skrbek, P. Skyba, R. E. Solntsev, and D. E. Zmeev, J. Low Temp. Phys. **146**, 537 (2007).

[9] L. Skrbek and W. F. Vinen, *Progress in Low Temperature Physics* (Elsevier, Amsterdam, 2009), Vol. XVI, Chap. 4.

[10] R. Hänninen, M. Tsubota, and W. F. Vinen, Phys. Rev. B **75**, 064502 (2007).

[11] R. Goto, S. Fujiyama, H. Yano, Y. Nago, N. Hashimoto, K. Obara, O. Ishikawa, M. Tsubota, and T. Hata, Phys. Rev. Lett. **100**, 045301 (2008).

[12] Forks specified as type DT26 (A1) and DT38 (B1) used in this work have been produced by Fronter Electronics, China, www.chinafronter.com. Forks C, U1, U2, L1, and L2 were provided by O. Kolosov, Lancaster University.

[13] The measurements have been performed in a brass pressure cell, which was filled by helium through a thin capillary via a nitrogen trap and copper sinter inside the cell to prevent the deposit of frozen air or water on the fork. To keep the highest possible Q value, forks A and B have only the tops of their original metal cans removed. The small surrounding volume of liquid helium of extremely low viscosity also results in a shorter characteristic time required to obtain steady-state flow.

[14] M. Blažková, T. V. Chagovets, M. Rotter, D. Schmoranzer, and L. Skrbek, J. Low Temp. Phys. **150**, 194 (2008); M. Blažková, D. Schmoranzer, and L. Skrbek, Low Temp. Phys. **34**, 298 (2008).

[15] G. K. Batchelor, *An Introduction to Fluid Dynamics* (Cambridge University Press, Cambridge, 1967).

[16] M. Blažková, D. Schmoranzer, and L. Skrbek, Phys. Rev. E **75**, 025302(R), (2007).

[17] C. H. K. Williamson, J. Fluid Mech. **155**, 141 (1985).

[18] T. Sarpkaya, J. Fluid Mech. **165**, 61 (1986).

[19] E. D. Obasaju, P. W. Bearman, and J. M. R. Graham, J. Fluid Mech. **196**, 467 (1988).
[20] M. Tatsuno and P. W. Bearman, J. Fluid Mech. **211**, 157 (1990).
[21] H. Honji, J. Fluid Mech. **107**, 509 (1981).
[22] P. Hall, J. Fluid Mech. **146**, 347 (1984).
[23] R. J. Donnelly and R. Hershberger (private communication).
[24] M. Blažková, M. Človečko, V. B. Eltsov, E. Gažo, R. de Graaf, J. J. Hosio, M. Krusius, D. Schmoranzer, W. Schoepe, L. Skrbek, P. Skyba, R. E. Solntsev, and W. F. Vinen, J. Low Temp. Phys. **150**, 525 (2008).
[25] R. J. Donnelly and C. F. Barenghi, J. Phys. Chem. Ref. Data **27**, 1217 (1998).
[26] G. A. Sheshin, A. A. Zadorozhko, E. Y. Rudavskii, V. K. Chagovets, L. Skrbek, and M. Blazkova, Low Temp. Phys. **34**, 875 (2008).
[27] R. P. Haley (private communication).

J Low Temp Phys (2011) 163: 317–344
DOI 10.1007/s10909-011-0353-1

Acoustic Emission by Quartz Tuning Forks and Other Oscillating Structures in Cryogenic ^{4}He Fluids

D. Schmoranzer · M. La Mantia · G. Sheshin · I. Gritsenko · A. Zadorozhko · M. Rotter · L. Skrbek

Received: 7 December 2010 / Accepted: 17 February 2011 / Published online: 4 March 2011

Abstract We report on experimental investigations of acoustic emission by quartz tuning forks resonating at frequencies 32 kHz, 38 kHz, 77 kHz and 100 kHz immersed in cold gaseous ^{4}He and its normal and superfluid liquid phases. Frequency dependence of the observed low-drive-linewidth at 350 mK together with the temperature and pressure dependences ($1.3\ \mathrm{K} < T < 4.2\ \mathrm{K}$, $0 < p < 25$ bar) of the observed damping of the high frequency (77 and 100 kHz) resonators measured in normal liquid ^{4}He and its superfluid phase provide strong and direct evidence of the importance of sound emission by these tuning forks. Three analytical models of acoustic emission by vibrating tuning forks are developed and compared with the experimental results. We also discuss the importance of sound emission for experiments with the commonly used 32 kHz tuning forks as well as other oscillating structures—spheres, wires, grids and various micromachined sensors. We compare the relative importance of dissipative losses due to laminar viscous/ballistic drag and acoustic emission in liquid and superfluid ^{4}He.

Keywords Quartz tuning fork · Cryogenic helium · Acoustic emission

1 Introduction

Quartz tuning forks, mass produced as frequency standards for digital watches with a large number of other applications [1, 2], have recently become popular research

D. Schmoranzer (✉) · M. La Mantia · M. Rotter · L. Skrbek
Faculty of Mathematics and Physics, Charles University, V Holesovickach 2, 180 00, Prague, Czech Republic
e-mail: david.schmoranzer@mff.cuni.cz

G. Sheshin · I. Gritsenko · A. Zadorozhko
B. Verkin Institute for Low Temperature Physics and Engineering, 47 Lenin Ave., 61103, Kharkov, Ukraine

tools in cryogenic fluid dynamics [3]. They are relatively easy to use, allow self-calibration of the proportionality coefficient relating their electrical and mechanical properties [4], and if their resonant response is measured correctly [5], their high sensitivity enables their use as thermo-, pressure- and viscometers in all the helium fluids [4]. They have been used to study the temperature dependences of density of normal ^{3}He liquid and of liquid and gaseous ^{4}He [6]; cavitation in cryogenic ^{4}He liquids [7, 8] or solubility of ^{3}He in ^{4}He at millikelvin temperature [9]. Moreover, they are also being employed (mostly in cryogenic environments) as generators and detectors of both classical [10–12] and quantum turbulence [12–18].

One of the most important characteristics of these resonators is the amount of damping they experience due to interactions with the surrounding fluid, as this can be used, e.g., to determine the transition from laminar to turbulent drag regime or to infer the fluid properties. Therefore, understanding all the damping forces is essential in order to interpret correctly the results from the numerous experiments already performed in cryogenic helium.

Dissipation due to laminar viscous drag [10, 12] or due to ballistic drag at low temperatures in ^{4}He [13, 15], as well as the dissipation due to the scattering of thermal excitations in ^{3}He [16, 17] are already largely understood and their dependences on most of the important physical quantities are known. In this report we try to illuminate the dissipation due to acoustic emission in ^{4}He fluids, extending the works of Clubb et al. [19] and Pentti et al. [6]. In most other studies, acoustic emission by tuning forks was considered to be negligible in comparison with other losses.

We believe, however, that this assumption is valid only under certain conditions, and that acoustic emission or the interaction through sound waves might be at least partly responsible for some of the phenomena observed by us as well as by others that still remain unexplained (such as anomalously broad and time-dependent low-drive-linewidth of "standard" 32 kHz forks and their mutual interactions in pure ^{4}He at very low temperature [20]). We do not intend to put forward a full comprehensive and detailed description of all the acoustics related to tuning forks. Our hope is to provide sufficiently good insight into the dissipative phenomena related to sound emission and to offer approximative estimates of the magnitude of acoustic emission in various situations. Dispersive effects of acoustic emission are beyond the scope of this paper and are not discussed here with the exception of an observed level crossing.

The paper is organized as follows—after this brief Introduction, in Sect. 2 we describe various aspects of the phenomenon of acoustic emission due to a tuning fork oscillating in a compressible fluid (mentioning special physical properties of quantum fluids) and in Sect. 3 three workable theoretical models are developed. We present our experimental data in Sect. 4 and compare them with the model predictions, while the predictions for other common oscillating structures are given in Sect. 5. Conclusions are drawn in Sect. 6.

2 Acoustic Emission by a Tuning Fork

Let us begin by a brief qualitative description of this rather complex phenomenon. It is known that any body oscillating in a classical viscous fluid with finite compressibility emits sound waves [21]. If we assume for simplicity that the oscillations are

harmonic, then the acoustic velocity field (superimposed on the velocity field due to laminar[1] flow past the body) will depend on several factors. The most important ones are the geometry of the oscillating body, the spatial extent and properties of the surrounding fluid as well as the geometry and material properties of its boundaries. More specifically, relevant physical properties include fluid density, speed of sound and frequency of oscillations, or alternatively, wavelength of the emitted sound waves. A more detailed consideration also ought to take into account the dissipation of the emitted sound waves, affected by fluid viscosity and thermal diffusivity (responsible for damping of adiabatically propagating sound waves), and also the reflectivity and absorptivity of the boundaries, in turn depending on their acoustic impedances, heat conductivity and the Kapitza thermal resistance between the fluid and the walls.

It is readily seen that a full description of all the above mentioned processes is next to impossible, perhaps with the exception of highly advanced and sophisticated numerical simulations of special cases. For a review of computational acoustics, see Ref. [22]. Several examples of acoustic emission models can be found in Refs. [23, 24]. Therefore, we seek simplified analytically tractable working models that would give us a meaningful approximative description of the dissipation rate due to acoustic emission rather than a full account of all the relevant physical processes.

2.1 Acoustic Field in an Unbounded Classical Fluid

The simplest case of acoustic emission is perhaps to consider an infinitely large unbounded volume of a classical fluid with negligible damping of the propagating sound waves. In this case, all the energy content of the emitted waves is carried away from the source and it is more or less straightforward to find an analytical expression for the emission power of an oscillator, assuming certain simplifications regarding the geometry of the oscillator and neglecting the dissipation of sound waves traveling in the fluid. The general procedure is to write down the velocity potential for outward propagating spherical or cylindrical waves from a suitably chosen set of point sources representing a simplified description of such an oscillator and use it to derive the velocity and pressure fields, and from these to calculate the energy flux. As we are limited neither by geometrical considerations nor by dissipation of energy in the sound waves, we can then use approximations for the values of these fields at large distances from the oscillating body. Then, by integrating over an enclosing surface, we shall find the total emitted power.

It should be noted that, even in this textbook case, several important simplifications are already assumed. The strongest one is the representation of the oscillating body (a tuning fork) as a set of several point sources with given acoustic strengths (usually four sources [25], in a form of either lateral or longitudinal/linear quadrupole [26], see later). In reality, the oscillating prongs of the tuning fork do not act only as sources of sound waves, they also reflect and absorb them. This can be especially important if the wavelength is comparable to the dimensions of the tuning fork. Moreover, the prongs have a velocity profile along their length, which can be approximated by solving the oscillations of an ideal cantilever. Therefore, in the direction of its axis each prong

[1] We do not consider acoustic emission generated by turbulent flows or acoustic streaming.

should ideally be represented by an infinite number of acoustic sources with varying strengths from the base to the tip, rather than just as an acoustic dipole (thus making the entire tuning fork a longitudinal quadrupole). This simplification will become even more important if we choose to consider only the close vicinity of the tuning fork with distances from the tines comparable to the tine length, which we should keep in mind later, when describing a tuning fork placed inside its original can.

2.2 Effect of Solid Boundaries

If solid boundaries are present, the situation starts to look even more complicated. Strictly speaking, for calculating the acoustic fields, one should use proper solutions of the wave equation, which would be standing waves in the case of perfectly solid (and fully reflecting) walls. Note that this also means the appearance of acoustic resonances determined purely by the geometry of the container and the sound wavelength.

However, standing waves do not transport energy. A real experimental situation corresponds better to a superposition—linear combination—of propagating and standing waves, as the waves reflected off the walls will be of a lower amplitude than the incident ones, due to several factors. First, no wall is infinitely rigid and even metallic walls posses non-unity reflectivity and non-zero transmission. In other words, acoustic energy will be partly channeled into refracted waves and lost within or outside the walls. Second, additional damping of sound waves occurs at solid boundaries due to viscosity of the fluid and finite heat conductivity of the wall. The importance of these two effects depends, among other factors, on the angle of incidence of the waves. Moreover, in a real fluid, a traveling sound wave (which is adiabatic and thus includes both pressure and temperature variations) is damped due to viscous forces and thermal diffusivity and its amplitude decreases as it propagates though the fluid.

To sum up, we need to describe a situation where the velocity and pressure fields are described by a superposition of standing and outward propagating waves and depend on a number of the above mentioned parameters, but mainly on the intrinsic acoustic resonances of the closed volume under consideration, which can couple to the oscillations of the tuning fork.

2.3 Acoustic Emission in Superfluid ^{4}He

Several potentially important differences arise when sound emission in a superfluid is considered, the main one being the existence of a new type of wave motion of the fluid—second sound—that can be thought of as waves of temperature, in which the normal and superfluid components move in anti-phase. As other nonclassical sound modes are not considered here, we therefore have mutually independent approximately *isothermal* first sound (pressure waves) and approximately *isobaric* second sound (temperature waves). The acoustic fields produced in He II by any moving body will always be a combination of these two sound modes. The emission of first sound is more or less analogical to the adiabatic sound waves in classical fluids, including similar magnitudes of sound velocity in He I and He II.

Second sound will be emitted by the tuning fork for two reasons. First, as the body moves, boundary conditions change differently for the normal (viscous liquid) and

superfluid (Euler-like inviscid liquid) components, resulting in their relative motion at the frequency of oscillations, i.e., second sound. Second, if finite viscous (or ballistic at very low temperature of He II) drag forces are still present, the surface of the moving body and the surrounding layer of fluid will be heated periodically, due to these dissipative forces. Therefore, an additional second sound field will be present, due to the temperature gradient in the liquid (superimposed on a steady counterflow cooling the oscillator), but this time at double the frequency of oscillations.

It is known that an oscillating body radiates first sound much more efficiently than second sound. For a plane oscillating in a direction perpendicular to itself, the ratio of the amplitudes of the two sound waves is given by: $\beta^2 T u_2^3/c u_1$, where β is the heat expansion coefficient, T denotes the temperature, u_1 and u_2 are the speeds of first and second sound, respectively, and c is the specific heat, which is very similar for both adiabatic and isothermal processes in He II except close to the λ-point [21, 27]. As $\beta \ll 1$, $u_2 < u_1$, and in our case $T \approx 1.5$ K and $c > 500\ \mathrm{J\,kg^{-1}\,K^{-1}}$ for all temperatures above 1.3 K, we see that the ratio of amplitudes will be indeed much lower than unity. We can therefore say that the second sound emission power due to the oscillations of the tuning fork will be negligible compared to that of first sound unless enhanced by another effect, such a resonance inside the experimental cell.

Of course, both first and second sound waves travel with their own group velocities and will again have their own standing wave resonances determined by the geometry of the experimental cell. Such second sound resonances have been observed in both ^{3}He–^{4}He mixtures and in pure ^{4}He and are reported in Refs. [6, 9]. Based on the above considerations, we believe that unless a second sound resonance within the cell is encountered, the power lost due to emission of second sound will be much lower than the power lost because of the emission of first sound. Therefore in the following models, second sound emission is not considered quantitatively as the sharp increases in linewidth due to resonances inside the experimental cell (i.e., the only occasions at which second sound may be important) are filtered out during data processing anyway. In other words, for the purposes of calculating the emission power when away from sound resonances (and for these purposes only), we describe superfluid ^{4}He as a classical compressible fluid.

3 Models of Acoustic Emission by Tuning Forks in a Classical Fluid

In this section, we discuss three different analytical models of acoustic emission by a tuning fork, together with their advantages and shortcomings. All these models deal with sound emission in an infinite volume of a classical fluid, but a few simple modifications will be introduced to account, at least qualitatively, for the presence of walls. The models described below are (i) 3D longitudinal quadrupole emission, (ii) emission by two infinite translationally oscillating cylinders, and (iii) 2D longitudinal quadrupole emission. The first two models are based on the works of Clubb et al. [19] and Sillitto [25], and the third one will be developed here. All these models assume potential compressible flow, so the viscous damping of sound waves is neglected. The application of these models on the quartz tuning fork is not meant to provide a rigorously accurate description of its behavior, our aim is more to illustrate

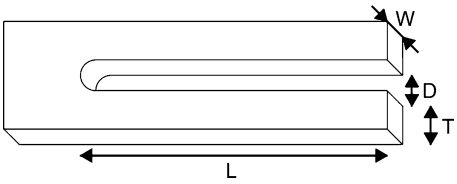

Fig. 1 A schematic sketch of a quartz tuning fork marking its dimensions

Table 1 Dimensions of the 38 kHz, 77 kHz and 100 kHz tuning forks used in this work (labeled F38, F77 and F100, respectively) as well as of typical 32 kHz tuning fork oscillators (F32, F38 and F100 type forks are supplied in a 3 mm diameter case 8 mm long, F32s and F77 type forks are smaller, supplied in a 2 mm diameter case 6 mm long). The dimensions have been measured using either optical (0.01 mm precision) or electron (0.001 mm precision) microscopy. For each tuning fork, the proportionality factor between the electric current and tip velocity, a, is listed, together with its quality factor, Q_{vac}, measured in vacuum at 4.2 K

Fork type	f_0 kHz	L mm	T mm	W mm	D mm	a C m^{-1}	Q_{vac}
F32	32	3.79	0.589	0.300	0.308	2.3×10^{-5}	6.3×10^5
F32s	32	2.53	0.249	0.100	0.127	3.4×10^{-6}	1.0×10^6
F38	38	3.41	0.599	0.330	0.306	1.6×10^{-5}	6.5×10^5
F77	77.5	1.93	0.402	0.340	0.206	1.3×10^{-5}	7.0×10^5
F100	100	1.98	0.585	0.335	0.302	2.1×10^{-5}	6.2×10^5

the basic features of acoustic emission by tuning forks, providing estimates of the emitted acoustic power that are correct at least in their orders of magnitude. In due course we shall also test these models against our experimental data.

Throughout the rest of this paper, the fork dimensions T, L, W, D will be used as introduced in Fig. 1; see Table 1 for their numerical values. Also the following set of symbols will be used: i as the imaginary unit, ρ as the fluid density, c as the sound velocity, ω as the angular frequency of oscillation, k as the wavenumber related to the sound waves, U as the velocity amplitude of the tip of the prongs and $L_e = 0.3915L$ as an *effective emitting length* of a prong, taking into account at least roughly the varying velocity profile along the length of the prong. The numerical coefficient corresponds to the ratio of the average velocity along the prong to the tip velocity, as follows from the Euler beam equation [28]. This value remains the same for all dimensions of the tuning forks if the fundamental bending mode is considered and as long as the assumptions of Euler beam theory for a thin dissipationless cantilever remain at least approximately valid.[2]

3.1 Description of Acoustic Emission Within Existing Models and Their Extension

A brief description of the two known models is presented below and we restate the resulting acoustic emission powers in two forms—first, using a more general expression (in practice an infinite sum of Bessel functions) and second, after taking the long

[2]The effective emitting length approximation can also be justified only if the entire problem of acoustic emission is understood as linear.

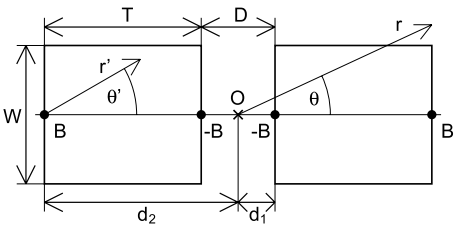

Fig. 2 The tuning fork (view of the tips of the prongs) represented as a longitudinal quadrupole. The variables r, θ belong to the universal coordinate system of the entire quadrupole with origin at O, while the primed variables belong to individual acoustic monopoles

wavelength limit, i.e., "wavelength $\gg$ relevant oscillator dimensions", which means mathematically that the arguments of all relevant Bessel functions must be much smaller than unity.

We begin with looking at the most commonly used model of acoustic emission by tuning forks , which describes the tuning fork as a longitudinal quadrupole oscillating in a 3D fluid. A full and detailed derivation of the pressure and velocity fields as well as the predicted emission power can be found in Ref. [25], here we only outline its main ideas. We begin by writing the velocity potential for an outward propagating wave due to an acoustic monopole in 3D (a pulsating sphere reduced to a point source):

$$\Phi_{3D,1}(r',t) = \frac{Be^{i(kr'-\omega t)}}{4\pi r'}, \tag{1}$$

where r' is the distance from the monopole and B is the acoustic source strength, defined as the product of emitting area times the (normal) velocity amplitude, in our case $B = WL_eU$. The longitudinal quadrupole used to model the tuning fork then consists of two point sources with strength B and two with strength $-B$ arranged according to Fig. 2. Using identities for displaced spherical harmonics [29], we arrive at the velocity potential of the entire quadrupole in the coordinate system with its origin in the center of mass of the quadrupole (r, θ):

$$\Phi_{3D}(r,\theta,t) = \frac{iBke^{-i\omega t}}{2\pi} \sum_{\substack{m=0 \\ even}}^{\infty} (2m+1) P_m(\cos\theta) h_m(kr)[j_m(kd_2) - j_m(kd_1)], \tag{2}$$

where $P_m(\cos\theta)$ are Legendre polynomials, $h_m(kr)$ are spherical Hankel functions, $j_m(kd_i)$ are spherical Bessel functions, and $d_1 = D/2$, $d_2 = D/2+T$. The potential is independent of the azimuthal angle, φ, due to axial symmetry around the quadrupole axis (which is, of course, not valid for the actual tuning fork). The emission power using the notation of tuning fork dimensions results as follows:

$$P_{3D} = \frac{\rho\omega k W^2 L_e^2 U^2}{2\pi} \sum_{\substack{m=0 \\ even}}^{\infty} (2m+1)\left[j_m(kd_2) - j_m(kd_1)\right]^2 ; \tag{3a}$$

$$P'_{3D} = \frac{\rho\omega k^5 W^2 T^2 (T+D)^2 L_e^2}{40\pi} U^2 = \frac{\rho\omega^6 W^2 T^2 (T+D)^2 L_e^2}{40\pi c^5} U^2, \tag{3b}$$

where (3b) is the simplification of (3a) in the long wavelength limit.

The main advantage of this model, i.e., the fact that it gives a full 3D description of the acoustic field, is unfortunately also related to its most severe drawback. By considering the tuning fork as a set of collinear point sources in 3D space, an assumption is already implied that its length and width are much shorter than the wavelength, $L, W \ll \lambda$. Note that this is true even before taking the "long wavelength" limit, which applies to other dimensions, namely T and D. By estimating the wavelength for a typical 32 kHz tuning fork at 4.2 K we get $\lambda \approx 5.6$ mm, which increases to about 7.5 mm at lower temperatures. This is still larger than the length of a prong of a typical 32 kHz tuning fork, but of the same order of magnitude and definitely comparable. The ratio of the wavelength to prong length is even worse for the 77 kHz and 100 kHz tuning forks discussed in Sect. 4, the consequence being that this model tends to underpredict the emission power.

This was pointed out already by Clubb et al. [19] for a simplified version of the same model, with the dependence on tuning fork geometry limited only to considering W and using slightly different approximations than Ref. [25]. Clubb et al. suggested to use a different model instead—two infinite cylinders performing transverse translational oscillations in antiphase.

Again, we begin by the velocity potential around a single infinite transversely oscillating cylinder, which can be derived based on the calculations in Ref. [21]:

$$\Phi_{C,1}(r', \varphi, t) = \frac{\pi R^2}{2i} k U H_1(kr') \cos\varphi \, e^{-i\omega t}, \tag{4}$$

where R is the radius of the cylinder and $H_1(kr)$ is the first order cylindrical Hankel function. The potential around the second cylinder has to be taken with a minus sign, as they oscillate in antiphase. This time we express $\cos\varphi$ as a sum of complex exponentials and use the identities for displaced cylindrical harmonics, arriving at:

$$\Phi_C(r, \varphi, t) = \frac{\pi R^2 k U e^{-i\omega t}}{2i} \sum_{\substack{m=-\infty \\ odd}}^{\infty} J_m(kF)\left[H_{m+1}(kr)e^{i(m+1)\varphi} - H_{m-1}(kr)e^{i(m-1)\varphi}\right] \tag{5}$$

for both cylinders, where $J_m(kF)$, $H_m(kr)$ are cylindrical Bessel and Hankel functions, respectively, and $F = (T+D)/2$ is the distance of the center of mass of one cylinder from the origin placed exactly between the cylinders. This potential yields the following emission power:

$$P_C = \rho\omega\pi^2 R^4 k^2 L_e U^2 \sum_{\substack{m=-\infty \\ odd}}^{\infty} J_m(kF)\left[J_m(kF) - J_{m-2}(kF)\right]; \tag{6a}$$

$$P'_C = \frac{3}{16}\rho\omega k^4 W^2 T^2 (T+D)^2 L_e U^2 = \frac{3}{16}\frac{\rho\omega^5 W^2 T^2 (T+D)^2 L_e}{c^4} U^2, \tag{6b}$$

where in (6b) we took the long wavelength limit and replaced the cross-section of the cylinder, πR^2, by the cross-section of a prong, WT. Dimensionally, this result is in agreement with Ref. [19], however, different prefactors were obtained. The difference in the prefactors arises from our usage of velocity amplitude, U, instead of mean square velocity, $\langle u^2 \rangle$, used in Ref. [19] and from a different method of replacing the cylinder diameter with tuning fork dimensions.[3]

This 2D model in its full form (6a) takes the relationship between the tuning fork dimensions and the wavelength to the opposite extreme—the length of the cylinders is assumed to be infinite, while other dimensions are represented more or less correctly, although cylindrical symmetry of each prong is forced artificially. This means that we are now operating in the $L \gg \lambda$ limit and the emission power might be overpredicted, although this effect would probably be smaller than the underprediction of the first model, especially for our 77 kHz and 100 kHz tuning forks.

Comparing these two models, we might say that they can be treated as opposing limiting cases and that the actual emission power of the tuning fork should lie somewhere between the respective predicted values. Please note that in the experimental part of this paper, all the emission powers are scaled by fitting parameters and therefore appear comparable in the presented figures. See Sect. 4 for the values of these parameters and comparison of the individual predicted emission powers.

3.2 2D Longitudinal Quadrupole Emission

In this section, we present the derivation of the last model of acoustic emission by tuning forks—2D longitudinal quadrupole emission. The aim in developing this model is to overcome the difficulties with the previous models, that is, to avoid the wavelength vs. prong length issue of the 3D quadrupole model, but at the same time to avoid introducing cylindrical symmetry of both prongs artificially, and also to provide a reasonable basis for comparison, lying between the "extreme" cases represented by the two above mentioned models.

Although we do not expect the result of this new 2D model to be largely different from the infinite cylinders model (also 2D), we hope that it might provide a more accurate description of acoustic emission, especially for the 77 kHz and 100 kHz tuning forks used in our experiment. The derivation of this model is given in greater detail, since we are not aware of any literature that contains the same in its entirety and also to illustrate the methodology, which was also used in a very similar manner to derive the emission powers from the first two models.

Again, we begin by considering the velocity potential of an outward propagating wave due to a 2D acoustic monopole (a pulsating cylinder reduced to a point source), which can be derived based on the textbook examples in Ref. [21]:

$$\Phi_{2D,1}(r', t) = \frac{B}{4i} H_0(kr') e^{-i\omega t}, \tag{7}$$

where B is again the acoustic source strength, equal to the (normal) velocity amplitude multiplied by the emitting line length, which is the 2D equivalent of the emitting

[3]We also believe there was an accidental misprint in the denominator of (5) in Ref. [19].

area in 3D; in this case $B = WU$. Similarly to the 3D quadrupole model, we now assume four acoustic sources arranged as in Fig. 2, two with strength B and two with $-B$. Combining their potentials using identities for displaced cylindrical harmonics [29], we arrive at:

$$\Phi_{2D}(r,\varphi,t) = \frac{B}{2i}e^{-i\omega t}\sum_{\substack{m=-\infty\\ even}}^{\infty} H_m(kr)e^{im\varphi}\left[J_m(kd_1) - J_m\left(kd_2\right)\right]. \tag{8}$$

The next step is to calculate the velocity and pressure fields according to:

$$\mathbf{v}(r,\varphi,t) = \nabla\Phi(r,\varphi,t); \qquad p(r,\varphi,t) = -\rho\frac{\partial\Phi(r,\varphi,t)}{\partial t}. \tag{9}$$

Eventually, we will also need to calculate the mean sound intensity, $\mathbf{I}$, and the emission power, P, according to:

$$\mathbf{I}(r,\varphi) = \frac{1}{2}\mathrm{Re}\{p(r,\varphi,t)\ \mathbf{v}^*(r,\varphi,t)\}; \tag{10}$$

$$P = L_e\oint \mathbf{I}(r,\varphi)\cdot\mathbf{dl} = r\ L_e\int_0^{2\pi} I_r(r,\varphi)\,\mathrm{d}\varphi, \tag{11}$$

where the path integral is taken over a closed circular loop and $\mathbf{dl}$ is an outward pointing vector normal to the path segment and its magnitude is equal to the length of the same segment. It follows that we will only be interested in the radial component of the mean sound intensity (and of the velocity field) and, more specifically, only in those terms that do not vanish upon integration over the full range of the polar angle.

The potential in (8) yields the following radial velocity and pressure fields:

$$v_r(r,\varphi,t) = \frac{Be^{-i\omega t}}{2ir}\sum_{\substack{m=-\infty\\ even}}^{\infty}[mH_m(kr) - kr\ H_{m+1}(kr)][J_m(kd_1) - J_m(kd_2)]e^{im\varphi}; \tag{12}$$

$$p(r,\varphi,t) = -\frac{1}{2}\rho\omega Be^{-i\omega t}\sum_{\substack{m=-\infty\\ even}}^{\infty} H_m(kr)e^{im\varphi}[J_m(kd_1) - J_m(kd_2)]. \tag{13}$$

The radial component of the mean sound intensity is then:

$$I_r(r,\varphi) = -\frac{\rho\omega B^2}{8r}\mathrm{Im}\left\{\sum_{\substack{m=-\infty\\ even}}^{\infty}\sum_{\substack{n=-\infty\\ even}}^{\infty} H_n(kr)[mH_m^*(kr) - kr\ H_{m+1}^*(kr)]\right.$$
$$\left.\times\,[J_n(kd_1) - J_n(kd_2)][J_m(kd_1) - J_m(kd_2)]e^{i(n-m)\varphi}\right\}. \tag{14}$$

To eliminate the double sum, we remember that the angular parts of cylindrical harmonics, which is the only φ-dependent term in (14), are orthogonal on the interval $[0, 2\pi]$:

$$\int_0^{2\pi} e^{in\varphi} e^{-im\varphi}\, \mathrm{d}\varphi = 2\pi\,\delta_{m,n}. \tag{15}$$

It therefore follows (as the Bessel functions have real values here, and the product of H_m and H_m^* is also real) that the emission power can be expressed from (11) as:

$$P = \frac{\pi\rho\omega k r B^2 L_\mathrm{e}}{4} \sum_{\substack{m=-\infty \\ even}}^{\infty} [J_m(kd_1) - J_m(kd_2)]^2 \mathrm{Im}\{H_m(kr) H_{m+1}^*(kr)\}. \tag{16}$$

From the law of conservation of energy it follows that the radiation power (if dissipation is neglected) cannot depend on r. For the purposes of this calculation, we can therefore replace the Hankel functions by their asymptotics for $r \to \infty$:

$$H_m\,(kr)\, H_{m+1}^*\,(kr) \approx \sqrt{\frac{2}{\pi kr}}\; e^{\,i\left(kr - \frac{m\pi}{2} - \frac{\pi}{4}\right)} \sqrt{\frac{2}{\pi kr}}\; e^{\,-i\left(kr - \frac{(m+1)\pi}{2} - \frac{\pi}{4}\right)} = i\,\frac{2}{\pi kr}. \tag{17}$$

Using (17) and substituting $B = WU$, we finally arrive at the emission power:

$$P_{2\mathrm{D}} = \frac{\rho\omega W^2 L_\mathrm{e} U^2}{2} \sum_{\substack{m=-\infty \\ even}}^{\infty} [J_m\,(kd_1) - J_m\,(kd_2)]^2\,. \tag{18a}$$

In the long wavelength limit (we take the lowest order term of the Taylor expansion of the Bessel functions), and substituting $d_1 = D/2$ and $d_2 = D/2 + T$, this reduces to:

$$P'_{2\mathrm{D}} = \frac{3}{64}\rho\omega k^4 W^2 T^2 (T+D)^2 L_\mathrm{e} U^2 = \frac{3\,\rho\omega^5 W^2 T^2 (T+D)^2 L_\mathrm{e}}{64 c^4}\, U^2. \tag{18b}$$

It is apparent that in the long wavelength limit, the emission power given by the 2D quadrupole model is always exactly four times smaller than the one predicted by the cylinders model. However, without taking this limit, the relation between these two models is not so straightforward as they scale slightly differently with the wave vector, and therefore also with the sound velocity and frequency of oscillations.

3.3 Application of Acoustic Emission Models

There are several important issues that should be kept in mind when applying the above mentioned models to interpret various cryogenic experiments with quartz tuning forks. First of all, the models are derived for an infinite volume of dissipationless fluid, and we have to modify them to take into account the fact that tuning forks vibrate in a closed volume of helium.

When the resonant frequency of the tuning fork matches some acoustic resonance of the cell (acting as a 3D sound resonator), the signal is suppressed, as the same amount of supplied power is now divided among several damped modes of coupled oscillatory motion, which can be seen in the tuning fork's spectra as multiple resonance peaks, provided they are strong enough, see Figs. 3 and 4 in Sect. 4 for a practical example. Such data would generally show "increased linewidths" (also Figs. 7, 8, 9 in Sect. 4), especially due to the fact that commonly used processing software usually attempts to fit these complicated spectra with a single Lorentzian function. As the best Lorentzian fit does not have any physical meaning in these situations, we merely use this kind of data as an indication of an acoustic resonance present inside the cell (be it first or second sound resonance), but we do not take the numerical values of the linewidth into account in any quantitative way.

Having thus identified and separated the acoustic resonances of the cell, we focus only on the rest of the data (the "floor" in Figs. 7, 8, 9 in Sect. 4). Then we find that we also need to introduce a parameter that describes the energy balance at the boundaries. We have therefore considered the power transmission coefficient, $T(\theta)$, for plane waves propagating in liquid helium incident on a planar surface of a wall (the tuning fork capsule used is made of aluminium) at an angle θ. The power transmission coefficient is determined [30] as:

$$T(\theta) = \frac{4\rho_{\mathrm{He}}\rho_{\mathrm{Al}}c_{\mathrm{Al}}\cos\theta\sqrt{c_{\mathrm{He}}^2 - c_{\mathrm{Al}}^2\sin^2\theta}}{\left(\rho_{\mathrm{Al}}c_{\mathrm{Al}}\cos\theta + \rho_{\mathrm{He}}\sqrt{c_{\mathrm{He}}^2 - c_{\mathrm{Al}}^2\sin^2\theta}\right)^2}. \tag{19}$$

In the simplest case of normal incidence, it can be expressed in terms of the specific acoustic impedances of helium and the wall material (aluminium), Z_{He} and Z_{Al}, respectively:

$$T(0) = \frac{4Z_{\mathrm{Al}}Z_{\mathrm{He}}}{(Z_{\mathrm{Al}} + Z_{\mathrm{He}})^2}, \tag{20}$$

where the individual specific acoustic impedances are defined as the products of the speed of sound and the density of the given media. The values we use for aluminium are $\rho_{\mathrm{Al}} = 2700\ \mathrm{kg\,m^{-3}}$, $c_{\mathrm{Al}} = 6420\ \mathrm{m\,s^{-1}}$.[4] These depend mainly on the exact composition of the aluminium alloy used and on the method of preparation of the material, and can be considered pressure and temperature independent in our experimental range between 0 and 25 bar, and 1.3 and 4.2 K, respectively. On the other hand, the relevant helium properties vary considerably with temperature and pressure and are therefore calculated accurately for each individual data point using the HEPAK software package [31, 32].

Even though the exact geometry of the experiment is rather complicated, we still believe that the actual ratio of the transmitted energy will be roughly proportional to the integral of the power transmission coefficient from zero angle of incidence to the

[4] The exact values of aluminium density and speed of sound depend significantly on the method of preparation. We use the values provided at www.signal-processing.com for rolled aluminium.

rather small (≈3 degrees) critical angle for total internal reflection, θ_C, which is given by:

$$\theta_C = \arcsin\left(\frac{c_{He}}{c_{Al}}\right), \tag{21}$$

as it is easy to imagine that acoustic waves will arrive at the walls at angles differing by much more than just $\theta_C \approx 3$ degrees. The mentioned integral is found to depend on temperature and pressure in a nontrivial manner due to the changing acoustic properties of liquid helium. In this approach, we have to assume that the angular distribution of the incident waves (when decomposed to plane wave components) is roughly constant between 0 and θ_C, or at least, even if it does exhibit some angular dependence in this small range of available angles, that the character of the dependence does not change dramatically with temperature or pressure in the explored experimental range.

Due to the enormous acoustic impedance mismatch between liquid helium and aluminium, $Z_{Al} \gg Z_{He}$, and the small value of the critical angle ($\sin\theta \approx \theta$, $\cos\theta \approx 1$ for $\theta < \theta_C$) or, in other words, due to the large Kapitza resistance [33] of the boundary, $T(\theta)$ can be approximated by an elliptical function:

$$T(\theta) = 4\frac{\rho_{He}}{\rho_{Al}}\sqrt{\left(\frac{c_{He}}{c_{Al}}\right)^2 - \theta^2}. \tag{22}$$

The above mentioned integral can then be expressed as the area under the quarter-ellipse, $(\pi/4)\,T(0)\theta_C$. The emission power given by the respective models is then multiplied by this value, taking into account at least approximately the effects of the boundaries. Note that the obtained emission power is still fully determined only by the experimental conditions.

When this approach is subjected to a careful analysis, one would find that it only considers a singular transmission/reflection on the solid boundary and therefore neglects the influence of multiple reflections. In reality, what happens will be similar to the following scenario. First, a wave of some undetermined 3D profile is emitted by the tuning fork. It propagates toward the solid boundary (experiencing low damping in He), where it is partly transmitted, partly reflected, and partly dissipated. The reflected wave then returns to the tuning fork, where it is partly absorbed, partly scattered, and partly dissipated again. The scattered wave will eventually reach the outer boundary again and the whole process will be repeated until all the energy in the wave is re-absorbed by the tuning fork, transmitted through the solid boundary or dissipated into heat. A full treatment of these phenomena (even neglecting dissipation) seems unfeasible to us at the moment even in terms of a cylindrically symmetrical 2D model, because of the complicated geometry of the actual experiment as the dimensions of the tuning fork are comparable both with the diameter of its capsule and with the wavelength of the acoustic radiation.

It is, however, instructive to estimate the importance of multiple reflections by considering a simplified 1D model with an acoustic source located at one end of a resonator and a partly transmitting boundary at the other. Complementing it with the proper boundary conditions (velocity matches that of the source at its surface, and the ratio of the amplitudes of the incident and reflected waves on the boundary is given by

the finite amplitude reflectivity coefficient) one can arrive (i) at the actual resonance frequencies of such a system, and (ii) at the energy flow through the solid boundary. It follows that the transmitted energy depends on tuning/detuning of the source to/from the resonance of the system, as can be expected. For example, one finds that in resonance, the transmitted energy is enhanced by a large factor inversely proportional to the (rather small) power transmission coefficient of the boundary, compared to the case exactly between resonances. This is qualitatively in agreement with the experiment—the dissipation was observed to increase significantly when a resonance of the experimental volume was encountered. Another important result follows from this simplified 1D model—by considering the case exactly between resonances, one may find that the transmitted power differs from the one determined by the above mentioned single-reflection approach only by a constant factor of two. While the magnitude of this constant factor may generally change with the dimensionality of the model problem, it will still remain a constant value for any selected number of dimensions in which the model is formulated, independent of any experimental conditions, such as the speed of sound (and by extension temperature and pressure), as long as we stay far away from all resonances (analogically to being exactly between them in the simplified 1D case).

Therefore, as the complex geometry of the experiment complicates its exact description, we take the resulting emission power according to the suggested single-reflection approach for each of the three models and multiply it by an arbitrary constant, which we consider as the only fitting parameter for each model. The values of this multiplicative constant then differ among the three models, but are not changed for different experiments interpreted using the same model. The final value of the emission power is then used to calculate the corresponding drag force and using the effective mass of the tuning fork prong as defined in [4] also to arrive at the corresponding increase in linewidth of the tuning fork due to acoustic emission, which is then added to the linewidth due to viscous drag (also containing a multiplicative constant as a fitting parameter) and compared to the experimental data.

Another issue relates to the ratio of tuning fork dimensions and the wavelength, especially to the choice of the final formula used to calculate the emission power within each model. While for the common 32 kHz forks, the simplified (long wavelength limit) version is quite sufficient, giving roughly 5% relative errors when compared to the full formula, it fails badly for our higher frequency (77 kHz and especially 100 kHz) forks, where it may result in errors as large as 50%. In this work, we therefore use the full form of all the models for calculating the emission powers. A numerical calculation shows that it is usually sufficient to take into account only a few terms around $m = 0$ in the infinite series to reduce the error below 1% (two or three terms in both directions of $m = 0$ are usually sufficient).

4 Experimental Results and Discussion

All the results presented here were obtained using tuning forks placed inside a pressure cell of 20 mm diameter located inside a glass cryostat. The cell was connected via a capillary to a pressurizing system utilizing a carbon cold trap. Both the cell

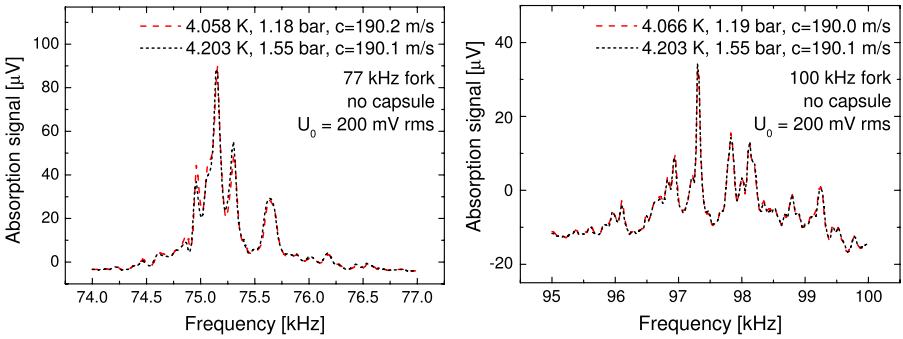

Fig. 3 (Color online) Sample spectra obtained with open tuning forks in our cylindrical pressure cell of 20 mm diameter. Under stable temperature and pressure, the spectra were also stable and very reproducible; within the resolution of this figure they appear identical. Here, they reproduce very closely even though the two temperatures listed in the graphs differ, as the speed of sound and therefore wavelength does not change much between them, due to an according change in pressure, which was achieved simply by keeping the pressure cell volume closed during cooldown. The fact that the spectra seem to reproduce under different experimental conditions linked only by very close sound velocities serves as evidence that the extra peaks indeed result from acoustic phenomena. In contrast, resonances measured in vacuum at 4.2 K (not shown here) display only a single peak that can be fitted by a Lorentzian function with very good accuracy. For comparison, at 4.2 K, the 77 kHz tuning fork used here has a vacuum linewidth as low as 58 mHz ($Q > 10^6$; measured using an excitation voltage of 20 mV rms attenuated by 40 dB)

and the cold trap could be shut off using manually operated high pressure valves. The pressure inside the cell was measured using an MKS Baratron with a 5000 Torr range, while bath temperature was calculated based on saturated vapor pressure which was measured by a more sensitive Baratron model with a range of 1000 Torr. The electrical part of the setup consisted of an Agilent waveform generator that provided the driving voltage, a SR-830 lock-in amplifier operated in voltage mode that was used to detect the electrical signal, and an I/V converter made in Lancaster and described in Ref. [5] with a gain setting of 1000 V/A. The exact magnitude of the driving voltage was also monitored using a Keithley digital multimeter.

The first hint of acoustic emission and coupling to resonant sound modes can already be seen when recording a single spectrum of a high frequency tuning fork oscillating in liquid helium, such as the illustrative examples in Fig. 3, which were obtained with "open" tuning forks, i.e., with their original capsules removed, or in Fig. 4, with the forks inside their capsules. We stress that if the experimental conditions, i.e., temperature and pressure in the cell, are controlled and kept constant, the spectra are perfectly reproducible within experimental accuracy when the frequency of the drive is swept many times in either direction. Also, the complicated pattern in these spectra seems to depend only on the sound velocity that can be calculated for the relevant experimental conditions (temperature and pressure).

Although it is hard to make practical use of the shape of such a complicated spectrum, it can provide us with general information on the qualitative level, in that sound waves within the surrounding medium indeed do affect the behavior of the tuning forks. The number of the peaks observed can also be used as an estimate of the number of resonant sound modes coupling to the resonance of the tuning fork, although it should be kept in mind that even in spectra showing only a single Lorentzian peak

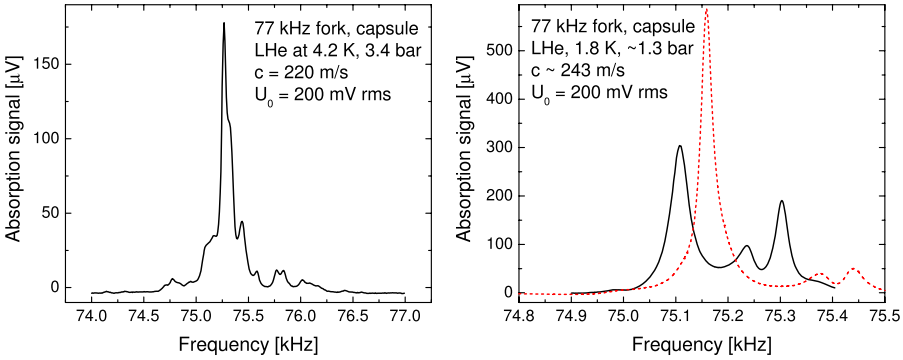

Fig. 4 (Color online) Spectra obtained with tuning forks inside their original capsules. These already exhibit a much simpler structure, as less acoustic modes fit inside the small 2 mm capsule than into the 20 mm pressure cell. The *right panel* shows two spectra obtained under similar conditions differing only by a small change in pressure (21 mbar). However, this small difference is sufficient to shift the frequencies of acoustic resonances as is shown in the graph. The (*red*) *dashed line* represents the situation where the acoustic resonances are still far from the tuning fork resonance, while the (*black*) *solid line* shows the acoustic modes already very close to the resonance of the tuning fork itself (refer to Fig. 6 for more details on interaction of the tuning fork resonance with acoustic ones). In the latter case, the response of the tuning fork itself appears suppressed compared to the previous case, as the supplied power is now distributed more evenly among the different types of damped motion. It is also worthwhile to notice that an attempt to fit the latter spectrum with a single Lorentzian function would also result in a higher fitted value of linewidth, which would, however, under the given circumstances, have no direct physical meaning

at the first sight, small hidden features due to acoustic resonances may be present as well. We believe that the complicated form of these spectra relates to the complicated geometry of the tuning forks and their surroundings. For example, in the case of Fig. 3, the tuning forks were placed inside a cylindrical pressure cell with a diameter of 20 mm, and the sound wavelengths were about 3.5 mm and 2.5 mm for the 77 kHz and 100 kHz tuning forks, respectively, while in Fig. 4, the 77 kHz tuning fork inside its original capsule of about 2 mm diameter exhibits much simpler spectra. The figures also suggest that the acoustic fields inside the cell form a complicated pattern due to the nonsymmetric positions of the tuning forks and multiple reflections of the emitted sound waves. Let us add for completeness that these forks driven at room (RT) or low temperature in vacuum display the usual narrow (linewidth of order 1 Hz at RT, and about 100 mHz at 4.2 K, typical for most of commercially produced forks) Lorentzian response, so the complicated spectra obtained in cryogenic helium indeed seem to be a consequence of the interaction with the surrounding media by the emission of sound.

It should be stressed that the spectra become simpler if the tuning forks are kept inside their much smaller original cans (diameter of about 3 mm or smaller), or if the speed of sound (and therefore the sound wavelength) is increased, by changing the temperature and/or pressure. This was the case of the spectra measured in a cell attached to the mixing chamber of a dilution refrigerator in Kharkov, Ukraine [13], which already had the form of single peaks only (or at least approached it with reasonable accuracy) and therefore could be fitted by a single Lorentzian function. The resulting damping (expressed in terms of the resonant linewidth) is plotted in Fig. 5

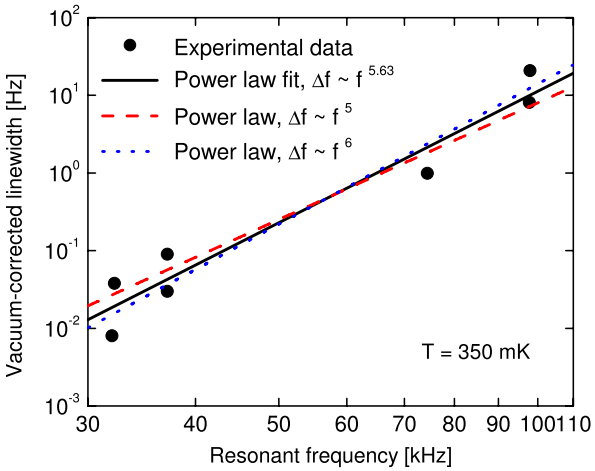

Fig. 5 (Color online) Linewidth (with its low temperature vacuum value subtracted) plotted versus the resonant frequency of different tuning fork oscillators at very low temperature. The high exponent in the power law fit is a clear indication of acoustic emission. The (*black*) *solid line* is a full power law fit, the (*red*) *dashed line* is a fit with the exponent fixed at 5 and the (*blue*) *dotted line* is the same with the exponent fixed at 6. Note that at 350 mK, ballistic drag due to phonon scattering is negligible with respect to the acoustic drag force for the high frequency forks. For the 32 kHz and 38 kHz forks, we estimate these to be comparable in orders of magnitude, see Sect. 6

for tuning forks oscillating at their respective resonant frequencies of 32, 38, 77 and 100 kHz. This very steep frequency dependence serves as direct proof of acoustic emission playing an important part at low temperatures in ^{4}He. The power law fit yields an exponent of about 5.6, which is between 5 and 6 as predicted from the above discussed 2D and 3D models, respectively, and largely differs from the value of $1/2$ expected due to the viscous drag force [12]. As the ordinate variable in Fig. 5 is the vacuum-corrected linewidth, it follows that the frequency dependence of the amount of damping is not normalized for the slightly different geometries and the exact sizes of the individual tuning forks, although generally, dependences on tuning fork dimensions are to be expected from the models described in Sect. 3. This is because it would be very difficult to take into account at the same time also the differing geometry of the surroundings of the tuning forks in two successive experiments, which comprise the data shown in Fig. 5. We therefore use the data corrected only for the vacuum linewidth as presented in Fig. 5 as they are perhaps more reliable than the data normalized for tuning fork geometries would be.[5]

Next, we examine in greater detail what happens when the resonance of the tuning fork is crossed by an acoustic resonance determined by its surroundings (primarily by the geometry of the experimental cell). Both these resonances move in the frequency domain due to changing experimental conditions. For this purpose, a measurement taken in cryogenic He gas at 4.2 K (enabling an easy control of pressure) serves very

[5]An attempt to take into account the slightly differing dimensions of the tuning forks as per the models actually resulted in an exponent even higher than 6, allowing us to conclude once again that the importance of acoustic emission is indeed firmly established.

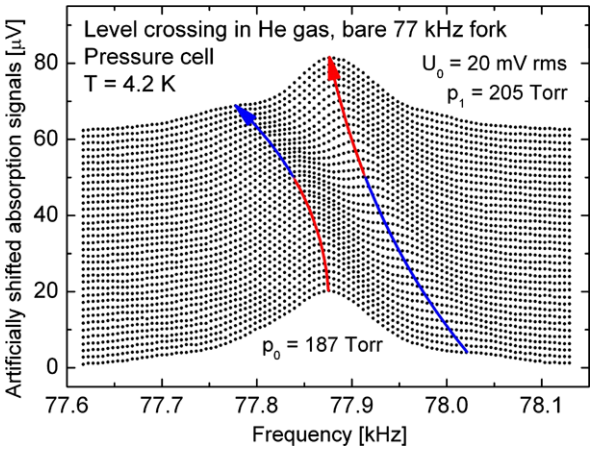

Fig. 6 (Color online) The gradual appearance and disappearance of a level crossing event is shown for an experiment in He gas at 4.2 K. Similar events were observed in both normal liquid and superfluid helium, but in He gas it is much easier to control the experimental conditions, and therefore the studied level crossing is seen more clearly. During this event, the resonance of the tuning fork becomes gradually coupled to and decoupled from an acoustic resonance of the pressure cell. Strictly speaking, one cannot say which peak belongs to the resonance of the tuning fork and which to the acoustic mode during this process, as both resonances are the result of coupling between these two types of oscillatory motion. However, for the sake of clarity, we can tentatively describe the scenario as follows. At the beginning, while the acoustic peak (*blue arrow*) moves in from the right, the resonance of the tuning fork (*red arrow*) stays almost constant. As they approach each other, the level splitting due to coupling will become more apparent, manifesting as a "repulsion" between the peaks. Eventually, the peaks will become equal in amplitude, at which point, each peak represents both types of motion (tuning fork oscillation and acoustic waves) equally. A literal crossing is avoided, as at this point the peaks exchange their roles. Afterwards, the left one belongs predominantly to the acoustic mode and continues to drift to the left, while the right one can be associated more readily with the resonance of the tuning fork and stays more or less at a constant frequency, only slowly returning to its original position

well, although a similar effect was also observed in He liquids while slowly varying pressure and/or temperature. However, since the spectrum of the high frequency tuning forks is usually much more complicated in He liquids unless special care is taken, such data are less illustrative. The results from He gas at 4.2 K are plotted in Fig. 6, showing an acoustic peak moving past the tuning fork resonance, as the pressure is increased from 187 to 205 Torr. The amplitude of such peaks at each instant is affected by the resonance of the tuning fork itself—when they are far away from the resonance they are small, as they approach the tuning fork's maximum amplitude, they grow significantly and again gradually disappear as they move away.

During these measurements, the relative change of the resonant frequency of the tuning fork can be expected to be about 6×10^{-5} (about 4.7 Hz), see Ref. [4] for its dependence on the fluid density, while the relative change in the frequency of the acoustic resonances should be 3.4×10^{-3} (about 260 Hz), as this corresponds to the relative change of the speed of sound between the initial and final pressures. This fact supports the interpretation that a coupled acoustic resonance peak is indeed observed passing by the (suppressed) tuning fork resonance. Therefore, during experiments with imperfect thermodynamical stability (variations of temperature, pressure, or any

other quantity affecting the sound wavelength or the acoustic boundary conditions), similar level crossings may be observed. Their occurrence will depend on the total magnitude of the change of the acoustic fields inside the experimental volume regardless of the rate of these variations, even if all the properties of the tuning fork itself are assumed perfectly constant.

For example, if small hidden peaks present in the signal are moving across the resonance of the tuning fork, the linewidth as obtained from a Lorentzian fit would be seen to increase when the two resonances start to overlap and decrease again when they move apart. At the same time the fitted resonant frequency would first move in one direction from its real value, then cross this value again, moving to its other side (as the extra acoustic peak moves across the resonance of the tuning fork), before relaxing again to its original value as the acoustic peak moves further away and decouples gradually. It is an open question if temporal changes in observed low-drive-linewidth of the tuning fork at very low temperature under apparently very stable experimental conditions such as observed by the Lancaster group [20] could be explained due to the slow drift of remnant quantized vortices in the cell, as the associated superflow may slightly alter the acoustic resonant conditions, leading in turn to time-dependent losses due to acoustic emission.

It should be noted though that reproducibility of level crossings was not ascertained in this particular experiment as even very small changes in the bath temperature may lead to significant drifting of acoustic resonance peaks. The drifting would be observable very clearly on the scale of Fig. 6, unless compensated by proper adjustments of pressure to achieve the same sound velocity. We hope the reader understands that, in this case, achieving a level of reproducibility of the frequency spectra as presented above in Fig. 3, would be a highly nontrivial task requiring a series of delicate adjustments of both temperature and gas pressure inside the cell. Attempting this in a glass cryostat with a rather simple manually controlled pressurizing system could prove quite unpractical, as any sudden pressure change inside the cell also upsets the temperature therein and thermal relaxation usually takes about 10–20 minutes. Nevertheless, a hint on reproducibility could perhaps be gleaned from the above mentioned Fig. 3.

Although it is important to describe all the observed acoustic phenomena such as the resonances inside the experimental cell qualitatively, for the purposes of quantitative description and comparison with the models, we shall concentrate on the measurements that are most likely unaffected by these extra resonances. In Figs. 7, 8, 9 which show the linewidth of the 77 kHz tuning fork in its can versus temperature and pressure, these data correspond to the (quasi-continuous) floor of the graph, as it is plausible that the peaks in the linewidth correspond to level crossing events. These figures show the comparison of the experimental data with the predictions of the individual models. The small variations of pressure in the temperature dependences (Figs. 7, 8) have been fully taken into account, as well as the small variation of temperature in the pressure dependence data (Fig. 9).

As all the models of acoustic emission contain one constant (denoted C_{3D}, C_{2D}, or C_C) as a fitting parameter and one more constant, α, (depending on the geometry of the tuning fork in an unknown way) is also included in the viscous drag force, the following procedure was introduced to determine the values of these four constants that would describe all the experiments performed with the same 77 kHz fork

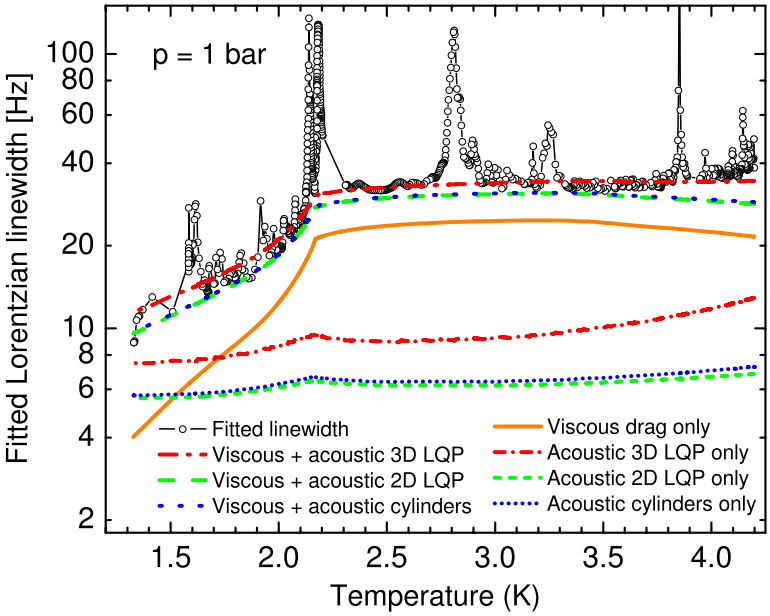

Fig. 7 (Color online) Temperature dependence of the 77 kHz tuning fork linewidth measured at a fixed pressure of 1 bar—(*black*) *open circles*—is compared to the results of the three models of acoustic emission. For this purpose, the linewidth due to the viscous drag force calculated according to [12] is also added to the dissipation due to acoustic emission as well as displayed separately. The (*red*) *dash-dotted lines* represent the results of the 3D longitudinal quadrupole model, the (*green*) *dashed lines* the 2D quadrupole model, the (*blue*) *dotted lines* the 2D cylinders model each with (*long dots* and *dashes*) and without (*short dots* and *dashes*) the viscous drag added to them. Finally the (*orange*) *solid line* represents the magnitude of the viscous drag alone. It is clearly seen here that at about 1.5 K, the viscous drag is comparable to the losses due to acoustic emission and at lower temperatures, sound emission becomes the dominant dissipative process. Note also the sound resonances/level-crossing events seen as sharp peaks in the experimental data

(i.e., temperature dependence at 1 bar—Fig. 7, temperature dependence at high pressure (24.78–21.36 bar)—Fig. 8, and pressure dependence at about 1.35 K—Fig. 9) as accurately as possible. First, the viscous drag constant, α, was estimated from the temperature dependence at high pressure as there the speed of sound reaches its maximum [31, 32] and therefore the acoustic emission power its minimum. Having thus estimated the viscous dissipation, the temperature dependence at 1 bar, and the pressure dependence were then both used to estimate the constants pertaining to the individual models of acoustic emission, C_{3D}, C_{2D}, C_C for the 3D longitudinal quadrupole, 2D longitudinal quadrupole and 2D cylinders models, respectively. The obtained values of acoustic emission power were then used to refine the viscous dissipation constant by comparison to the high pressure data, and two more iterations like this were performed until the fine details have been settled within the limits of accuracy. The values of the fitting parameters obtained this way follow: $\alpha = 0.59$, $C_{3D} = 15$, $C_{2D} = 4.55$ and $C_C = 1.06$. We see that the 3D model, which was expected to underpredict the emission power requires the highest correction factor to match the experimental data. On the other hand, the cylinders model, which was ex-

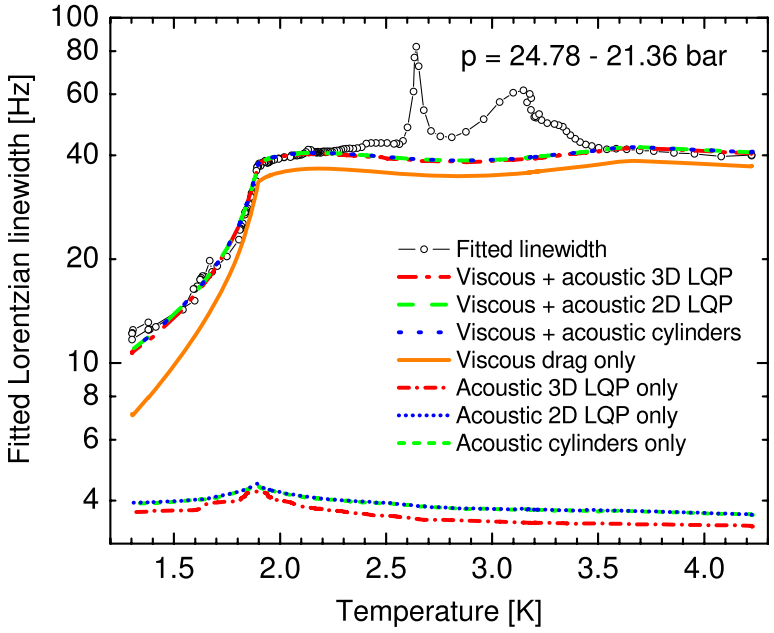

Fig. 8 (Color online) Temperature dependence of the 77 kHz tuning fork linewidth measured at slightly varying high pressures is compared to the results of the three models of acoustic emission. The symbols, line styles and colors are the same as in Fig. 7. In this case, the drag force is completely dominated by viscosity except for the lowest temperatures. The data are described very well in the whole range except for the vicinity of the cell resonances. Please note the minimum in the expected viscous drag force in the same region—it is present here, because, as was mentioned in the text, we take into account the pressure falling slowly during the experiment, due to additional condensation of helium inside the capillary connected to the cell during cooldown as well as potential small leaks of helium gas from the room temperature part of the pressurizing system. The pressure has been recorded for every experimental point, and in the models, we use an interpolation of these pressures (differing from the actual pressures by less then 1 percent) to calculate the correct dissipation rates corresponding to the actual experimental situation

pected to overpredict the emission power slightly, matches the experiment very well even without this correction factor. However this may be simply due to a numerical coincidence as none of these models accounts for the influence of multiple reflections explicitly, which would in effect lead to another constant correction factor.

Considering the large amount of simplifications present in the models themselves and in the complicated description of the reflection of sound waves at the boundary with the aluminium can, the achieved agreement with the data, using only a single fitting parameter, is rather astonishing. Figures 7–9 also show the relative magnitudes of the viscous and acoustic drag forces and a crossover of their mutual importance is seen clearly, except in the high pressure data set.

5 Acoustic Emission by Other Common Oscillatory Structures

Let us give a brief overview of dissipative acoustic properties of other oscillating bodies that have been frequently used as flow generators and detectors in the studies

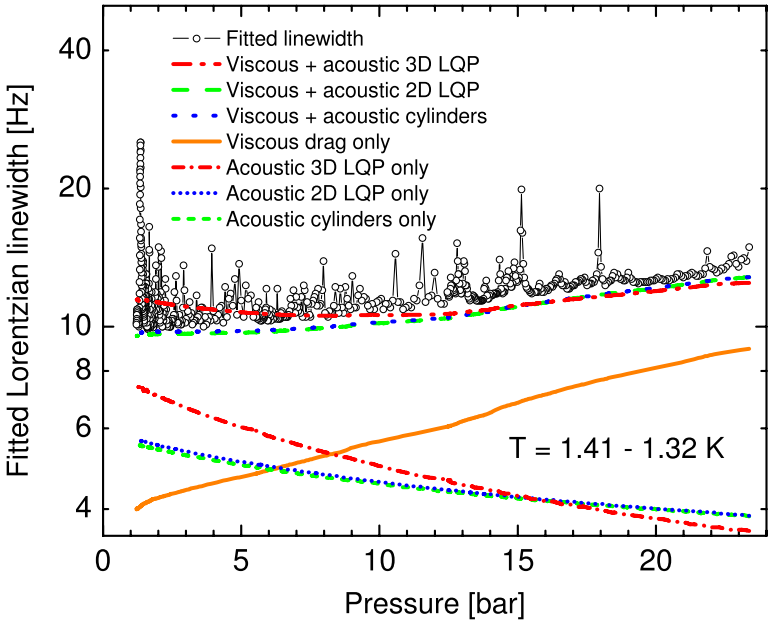

Fig. 9 (Color online) Pressure dependence of the 77 kHz tuning fork linewidth measured at the lowest temperature of our glass cryostat is compared to the results of the three models of acoustic emission. The symbols, line styles and colors are the same as in Fig. 7. The observed linewidth hardly changes due to the balance of two competing effects. The acoustic drag increases with reduced pressure (and lower speed of sound), however, at the same time, the fraction of the normal component decreases significantly and the viscous drag force is thus reduced. Temperature also kept dropping slightly during the experiment due to helium being released from the pressure cell as well as the overall dropping amount of helium in the cryostat bath, but these changes were taken into account during data processing. This figure also illustrates the small differences between the 3D and 2D models of acoustic emission. The experimental data seem to be described better by the 2D models

of normal or superfluid helium (for a review, see Ref. [34]). These include wires [35–40], spheres [41–44] and grids [45–47]. Our aim is to provide quantitative estimates of the respective emission powers and of the influence of acoustic emission on the overall damping the oscillators experience. However, we restrict ourselves by considering application of vibrating structures in cryogenic ^{4}He. Acoustic properties of ^{3}He such as zero sound and various sound modes in superfluid ^{3}He phases as well as Andreev reflection stay outside the scope of this paper.

None of the objects described below can compare with the high frequency tuning forks described in Sect. 4 in terms of the emission power and we believe that none of them will feel a significant measurable acoustic drag force above 1 K in ^{4}He, because it would be *at least* two orders of magnitude lower than the viscous drag force and therefore negligible. However, for some of these oscillators, the situation might be different at lower temperatures where the viscous drag is highly suppressed due to the low fraction of the normal component. Moreover, if the temperature is reduced even further, the hydrodynamic continuum approach is no longer valid and the “laminar” drag force has to be expressed based on the considerations of ballistic

propagation of thermal quasiparticles, in which case the drag force is expected to drop with decreasing temperature as T^4 [4].

There is a principal difference between tuning forks and other vibrating structures as spheres, wires, grids or micromachined sensors in that these are dipolar acoustic sources and our previous models of acoustic emission are thus not applicable for them. On the other hand, it is possible to calculate dipolar acoustic emission in a similar way as shown in Sect. 3. The following (23) represents both the full calculation and the long-wavelength limit for an acoustic dipole. Additionally, analytical solution for a sphere (24), including the effects of the finite viscous boundary layer, is given in Ref. [21]. Both are listed below, giving the respective emission powers as:

$$P = \frac{B^2\rho\omega}{4d}\sum_{\substack{m=1\\ odd}}^{\infty}(2m+1)J_{m+1/2}^2(kd) \approx \frac{B^2\rho\omega^4 d^2}{6\pi c^3}; \tag{23}$$

$$P = \frac{\pi\rho r^6\omega^4 U^2}{6c^3}\left(1+\frac{3}{\kappa}+\frac{9}{2\kappa^2}+\frac{9}{2\kappa^3}+\frac{9}{4\kappa^4}\right), \tag{24}$$

where $2d$ is the distance between the two point sources comprising the acoustic dipole, κ is the ratio of the radius of the sphere to the viscous penetration depth $\delta = \sqrt{2\nu/\omega}$, and all other symbols have the same meaning as in Sect. 3.

5.1 Oscillating Spheres

We consider oscillating spheres such as described by Schoepe et al. [41, 43], Luzuriaga [42] and Hemmati et al. [44]. The emission power was calculated using (24) and the laminar drag was either taken from the experimental data, which might also include the intrinsic damping of the oscillator that would have been observed in vacuum, or estimated using the well-known Stokes formula (taking into account the drag of the normal fluid only) modified for oscillatory flows:

$$F = 6\pi\eta_{\mathrm{n}} r\, U\left(1+\frac{r}{\delta}\right), \tag{25}$$

where η_{n} is the dynamic viscosity of ^{4}He at 1.2 K [48], r denotes the radius of the sphere, and U stands for the velocity amplitude of the sphere, meaning that F also represents the amplitude of the viscous drag force.

For the spheres used in Refs. [41, 43], the acoustic drag was found to be at least 9 orders of magnitude below the laminar drag at 1.2 K; for spheres used by Schoepe et al., this ratio is valid even when compared to the linear drag as measured at 300 mK. For the sphere used by Luzuriaga [42], the ratio was not so huge—acoustic emission was found about four to five orders of magnitude lower than the viscous drag at 1.2 K. It is therefore safe to conclude that for all practical purposes, acoustic emission can indeed be neglected. This holds as well for the niobium sphere used in Ref. [44].

5.2 Vibrating Wire Resonators

For the vibrating wire resonators, we estimate acoustic emission in two different ways. First, we consider the wire as an acoustic dipole consisting of two point sources

in 3D fluid and second, we replace it by a model sphere of the same surface area. The acoustic dipole approach can be justified by the fact that at typical resonance frequencies ($\approx$1 kHz), the size of the wire (usually about 3 mm) is much smaller than the wavelength of sound waves in ^{4}He, which is of order 20 cm. This approach, however, neglects the effects of the viscous boundary layer completely, we therefore additionally use the model of a replacement sphere to estimate its magnitude. We define the acoustic source strength $B = A\,U_{\mathrm{eff}}$, where A is the projected area of the wire on the plane perpendicular to its motion, and U_{eff} is an estimate of the effective velocity along the wire, which we define arbitrarily as $U_{\mathrm{eff}} \approx 0.3\,U$ for the purposes of these order of magnitude estimates. The separation of the two point sources is assumed to be equal to the diameter of the wire.

In some cases the vibrating wire would perhaps be better represented as a long oscillating cylinder with a finite viscous penetration depth. However, we do not discuss such calculations here, as the magnitude of acoustic damping appears to be extremely low for typical vibrating wire resonators (such as described in Refs. [35–40]) and the extra precision in the estimate of emission power would therefore be of little importance. Again, for all the cases considered, the acoustic emission was found very low, about 9 orders of magnitude below the laminar drag force at 1.2 K and therefore negligible for all practical purposes.

5.3 Oscillating Grids

We consider here the case of the Lancaster circular grid of 8 cm diameter driven electrostatically at its resonance frequency about 1 kHz as described in Refs. [45–47]. The emission power was estimated using the acoustic dipole model, where the source strength B was taken as $B = A\,U_{\mathrm{eff}}$, where A is the total projected area of the wires (determined as the area of the grid multiplied by $(1-\tau)$, where τ is transparency of the grid) and U_{eff} is an effective velocity, $U_{\mathrm{eff}} = 0.432\,U$, that takes into account the profile of the fundamental flexural resonance mode of the grid [47] in a form of a zero order Bessel function. We assume the separation of the sources to be equal to the thickness of the grid (6 μm).

When the linewidth due to acoustic emission is compared to the experimental linewidth measured at the base temperature of a dilution refrigerator (about 10 mK), which is very similar to its vacuum value, we find that the acoustic emission contribution is roughly three orders of magnitude lower than this experimentally observed damping. However, in the measured damping, the dominant contribution is the nuisance damping due to the grid material, therefore a direct comparison with viscous/ballistic drag forces is not possible. When separated from the nuisance damping, these losses might in principle turn out to be comparable with the acoustic drag at this very low temperature and, moreover, dispersive effects of sound emission might be observable as well. Still, we believe that it would be an experimental challenge to detect acoustic emission using the vibrating grid of the described geometry.

5.4 Micromachined Devices

Lately, significant effort has been invested in developing very small and highly sensitive vibrating sensors for cryogenic fluid dynamics using technologies such as electron beam lithography and selective etching. With these, it is possible to fabricate

oscillators of micron (MEMS) and recently even submicron (NEMS) sizes. As a representative of these sensors, we consider a $7 \times 3\ \mu m^2$ goal-post shaped oscillator of beam cross-section $220 \times 100\ nm^2$ resonating at 7.1 MHz developed in Grenoble and described by Collin et al. [49].

Even at this high frequency, the oscillator is still smaller than the wavelength of about 30 μm, which justifies the application of the 3D dipole source model to estimate its acoustic emission power. From similar considerations as above, where the 7 μm "paddle" is considered perfectly solid and the two 3 μm "legs" as ideal Euler cantilevers, it follows that the acoustic drag in liquid ^{4}He at 1.2 K is almost three orders of magnitude lower than the viscous drag and therefore does not represent any serious influence on the behavior of the oscillator, unless the temperature is reduced well below 1 K—here a possible influence might be observable depending on the exact geometry and other experimental conditions, especially the nuisance damping. Again, dispersive effects may in principle be seen as well.

5.5 Standard 32 kHz Tuning Forks

In this work we deliberately used high frequency forks in order to make this experimental study feasible. We have already shown that a crossover of the viscous and acoustic drag forces may occur for these forks at temperatures as high as 1.5–2 K. This effectively disqualifies the high frequency tuning forks from use as sensors at very low temperatures below 1 K, as other relevant damping mechanisms (viscous/ballistic/intrinsic drag) will most likely be screened by acoustic emission. It is then natural to raise the question whether a similar phenomenon will take place with the standard 32 kHz tuning forks and at which temperature it might be expected to occur in ^{4}He.

To tackle this problem, we will apply the infinite cylinders model that describes our experimental data obtained with the 77 kHz fork perhaps most accurately. When applied to the 32 kHz forks, it seems that at about 1 K the acoustic drag might be comparable in order of magnitude with the viscous/ballistic dissipation, therefore the final balance of these dissipative mechanisms depends on finer details relevant for acoustic emission, such as the geometry of both the tuning fork and the experiment and the reflectivity of the boundaries. We therefore provide estimates for several types of tuning forks. The forks from Table 1 are complemented by two other types of 32 kHz forks—F32a (large fork) and F32c (small fork)—referred to in [12] as A1 and C3, respectively. For each fork, we list two values of the ratio of acoustic to viscous drag: (i) assuming no reflections at all, and (ii) assuming an overall 99% reflectivity of the container walls. These ought to serve as illustrative examples giving approximate upper and lower bounds for the expected acoustic emission power in comparison to the losses due to viscous drag. We neglect acoustic resonances due to the cell geometry as well as all dispersive effects as well as dissipative processes that are responsible for damping the propagating sound waves inside the liquid helium. The explicit ratios of acoustic to viscous drag force are summarized in Table 2, including the corresponding values for 77 kHz and 100 kHz tuning forks for comparison. To understand Table 2 correctly, we should realize that in practical experiments (maybe except for very large volumes of helium) some finite amount of reflection on the walls will always occur, reducing the resulting emission power and shifting the ratio toward the

Table 2 Estimated ratios of acoustic to viscous drag acting on 32 kHz tuning forks in liquid ^{4}He at 1.2 K and saturated vapor pressure. For experimental conditions where strong reflection on solid boundaries can be expected, such as presented in Sect. 4, one should refer to the values listed in the second column. See the accompanying text for details

Fork type	Acoustic to viscous drag ratio	
	no reflection	99% reflectivity
F32	22	0.22
F32s	0.20	0.0020
F32a	8.9	0.089
F32c	0.21	0.0021
F38	58	0.58
F77	310	3.1
F100	2700	27

value calculated for 99% reflectivity (which more or less corresponds to the situation when the tuning fork is enclosed inside its original can). It therefore follows that in this situation even the large 32 kHz forks will not show strong effects due to acoustic emission at 1.2 K, however, at the same time it is obvious that the ratios of acoustic to viscous drag will change dramatically with the temperature falling below 1 K.

This calculation together with the general formulae given in Sect. 3 shows that it is advisable to use smaller types of tuning forks for sensitive low temperature experiments as they generally display lower losses due to acoustic emission. In order to suppress their acoustic emission even further, we could recommend enclosing them in a sufficiently small experimental volume with highly reflecting walls to minimize the radiation losses as well as the possibility of coupling to acoustic resonances of the cell.

6 Conclusions

We have used a set of quartz tuning forks oscillating at 32, 38, 77 and 100 kHz in experiments aiming to clarify the role of acoustic emission in the overall dissipation experienced by these structures oscillating in cryogenic gaseous and liquid ^{4}He. Thanks to the very steep frequency dependence of the emission power, the high frequency (77 and 100 kHz) forks allowed reliable measurement of acoustic emission even above 1.2 K in a pressure cell placed inside an ordinary helium bath glass cryostat and gave conclusive quantitative evidence of this phenomenon. Level crossing events have been observed both in gaseous and liquid ^{4}He and associated with acoustic resonances due to the geometry of the experimental cell. Additionally, complementary experiments with all the forks have been performed at 350 mK in a dilution refrigerator and provided direct evidence of the acoustic emission and its frequency scaling in the temperature range corresponding to the ballistic drag regime in superfluid ^{4}He.

We have considered three models of acoustic emission by tuning forks—3D quadrupole emission, 2D quadrupole emission and the emission by two infinite transversely oscillating cylinders (also 2D). We have calculated the expected emission powers and compared them with the experimental data taking into account also the

acoustic properties of the boundaries delimiting the fluid volume. While all the models gave reasonable agreement with the pressure and temperature dependences obtained experimentally using the 77 kHz fork, the data are best described by the 2D models, which behave almost identically in the studied range except for the values of their multiplicative parameters. The infinite cylinders model supplemented with the considerations of reflection on the boundaries fits the data obtained in a wide parameter space ($1.3\ \mathrm{K} < T < 4.2\ \mathrm{K}$, $0 < p < 25$ bar) with the precision of about 6% even without any fitting parameter, although this might be due to a numerical coincidence. Nevertheless, these results give us confidence that the same models can be used to predict the significance of acoustic emission for the commonly used 32 kHz forks. Moreover, a similar approach modified for dipole emission has been used to estimate the emission powers of other oscillating structures, such as spheres, wires, grids, MEMS and NEMS, used by others and described in literature.

We hope that these measurements, the proposed models, and the discussion in Sect. 5 will serve other investigators working with tuning forks and other oscillators in liquid helium and provide them with an estimate of the relative importance of acoustic emission in their experiments.

Acknowledgements We are grateful to A. Salmela, S. Babuin, D. Garg, P.V.E. McClintock and W.F. Vinen for stimulating discussions. We also acknowledge the thorough work of all the reviewers who raised a number of useful questions, suggestions and comments that led us to clarify some of the issues under discussion. This research was supported by research plans MS 0021620834 and by GAČR 202/08/0276.

References

1. E.P. Eernisse, R.W. Ward, R.B. Wiggins, IEEE Trans. Ultrason. Ferroelectr. Freq. Control **35**, 3230 (1988)
2. K. Karrai, R.D. Grober, Tip-sample distance control for near-field scanning optical microscopes, in *Near-Field Optics*, ed. by M.A. Paesler, P.T. Moyer. Proc. SPIE, vol. 2535 (1995), p. 69
3. M. Blažková, M. Človečko, V.B. Eltsov, E. Gažo, R. de Graaf, J.J. Hosio, M. Krusius, D. Schmoranzer, W. Schoepe, L. Skrbek, P. Skyba, R.E. Solntsev, W.F. Vinen, J. Low Temp. Phys. **150**, 525 (2008)
4. R. Blaauwgeers, M. Blažková, M. Človečko, V.B. Eltsov, R. de Graaf, J. Hosio, M. Krusius, D. Schmoranzer, W. Schoepe, L. Skrbek, P. Skyba, R.E. Solntsev, D.E. Zmeev, J. Low Temp. Phys. **146**, 537 (2007)
5. P. Skyba, J. Low Temp. Phys. **160**, 219 (2010)
6. E.M. Pentti, J.T. Tuoriniemi, A.J. Salmela, A.P. Sebedash, J. Low Temp. Phys. **150**, 555 (2008)
7. L. Skrbek, M. Blažková, T.V. Chagovets, M. Rotter, D. Schmoranzer, J. Low Temp. Phys. **150**, 194 (2008)
8. M. Blažková, D. Schmoranzer, L. Skrbek, J. Low Temp. Phys. **34**, 380 (2008)
9. E.M. Pentti, J.T. Tuoriniemi, A.J. Salmela, A.P. Sebedash, Phys. Rev. B **78**, 064509 (2008)
10. M. Blazkova, D. Schmoranzer, L. Skrbek, Phys. Rev. E **75**, 025302 (2007)
11. D. Schmoranzer, M. Král'ová, V. Pilcová, W.F. Vinen, L. Skrbek, Phys. Rev. E **81**, 066316 (2010)
12. M. Blažková, D. Schmoranzer, L. Skrbek, W.F. Vinen, Phys. Rev. B **79**, 054522 (2009)
13. G. Sheshin, A.A. Zadorozhko, E. Rudavskii, V. Chagovets, L. Skrbek, M. Blazhkova, J. Low Temp. Phys. **34**, 875 (2008)
14. M. Blažková, M. Človečko, E. Gažo, L. Skrbek, P. Skyba, J. Low Temp. Phys. **146**, 305 (2007)
15. D.I. Bradley, M.J. Fear, S.N. Fisher, A.M. Guénault, R.P. Haley, C.R. Lawson, P.V.E. McClintock, G.R. Pickett, R. Schanen, V. Tsepelin, L.A. Wheatland, J. Low Temp. Phys. **156**, 116 (2009)
16. D.I. Bradley, M. Človečko, E. Gažo, P. Skyba, J. Low Temp. Phys. **152**, 147 (2008)
17. D.I. Bradley, P. Crookston, S.N. Fisher, A. Ganshin, A.M. Guénault, R.P. Haley, M.J. Jackson, G.R. Pickett, R. Schanen, V. Tsepelin, J. Low Temp. Phys. **157**, 476 (2009)

18. D. Schmoranzer, L. Skrbek, J. Phys. Conf. Ser. **150**, 012048 (2009)
19. D.O. Clubb, O.V.L. Buu, R.M. Bowley, R. Nyman, J.R. Owers-Bradley, J. Low Temp. Phys. **136**, 1 (2004)
20. D. Garg, V.B. Efimov, M. Giltrow, P.V.E. McClintock, L. Skrbek, W.F. Vinen, Mutual interactions between oscillating objects in superfluid ^{4}He: critical velocities and the persistence of remanent vortices, Europhys. Lett. (submitted)
21. L.D. Landau, E.M. Lifshitz, *Hydrodynamics*, 2nd edn. (Pergamon Press, New York, 1987)
22. C.L. Morfey, M.C.M. Wright, Proc. R. Soc. Lond. Ser. A, Math. Phys. Sci. **463**, 2101–2127 (2007)
23. K.M. Li, S. Taherzadeh, K. Attenborough, J. Acoust. Soc. Am. **101**, 3343–3352 (1997)
24. K.M. Li, S. Taherzadeh, J. Acoust. Soc. Am. **102**, 2050–2057 (1997)
25. R.M. Sillitto, Am. J. Phys. **34**, 639 (1966)
26. D.A. Russell, Am. J. Phys. **68**, 1139 (2000)
27. I.M. Khalatnikov, *Theory of Superfluidity* (Nauka, Moscow, 1971) (in Russian)
28. S.P. Timoshenko, D.H. Young, *Theory of Structures*, 2nd edn. (McGraw-Hill College, New York, 1965)
29. M. Abramovitz, I.A. Stegun, *Handbook of Mathematical Functions*. Applied Mathematics Series, vol. 55 (National Bureau of Standards, Washington, 1964)
30. P.M. Morse, K.U. Ingard, *Theoretical Acoustics* (Princeton University Press, Princeton, 1986)
31. R.D. McCarty, Thermophysical properties of Helium-4 from 2 to 1500 K with pressures to 1000 atmospheres, Technical Note 631 National Bureau of Standards (1972)
32. V.D. Arp, R.D. McCarty, The properties of critical helium gas, Tech. Rep., U. of Oregon (1998)
33. G.L. Pollack, Rev. Mod. Phys. **41**, 48 (1969)
34. L. Skrbek, W.F. Vinen, The use of vibrating structures in the study of quantum turbulence, in *Progress in Low Temperature Physics*, ed. by M. Tsubota, W.P. Halperin, vol. XVI (Elsevier, Amsterdam, 2009), Chap. 4
35. M. Morishita, T. Kuroda, A. Sawada, T. Satoh, J. Low Temp. Phys. **76**, 387 (1989)
36. H. Yano, A. Handa, H. Nakagawa, K. Obara, O. Ishikawa, T. Hara, M. Nakagawa, J. Low Temp. Phys. **138**, 561 (2005)
37. H. Yano, N. Hashimoto, A. Handa, M. Nakagawa, K. Obara, O. Ishikawa, T. Hata, Phys. Rev. B **75**, 012502 (2007)
38. R. Goto, S. Fujiyama, H. Yano, Y. Nago, N. Hashimoto, K. Obara, O. Ishikawa, M. Tsubota, T. Hata, Phys. Rev. Lett. **100**, 045301 (2008)
39. H. Yano, T. Ogawa, A. Mori, Y. Miura, Y. Nago, K. Obara, O. Ishikawa, T. Hata, J. Low Temp. Phys. **156**, 132 (2009)
40. D.I. Bradley, S.N. Fisher, A.M. Guénault, R.P. Haley, V. Tsepelin, G.R. Pickett, K.L. Zaki, J. Low Temp. Phys. **154**, 97 (2009)
41. J. Jäger, B. Schuderer, W. Schoepe, Phys. Rev. Lett. **74**, 566 (1995)
42. J. Luzuriaga, J. Low Temp. Phys. **138**, 267 (1997)
43. M. Niemetz, H. Kerscher, W. Schoepe, J. Low Temp. Phys. **126**, 287 (2002)
44. A.M. Hemmati, S. Fuzier, E. Bosque, S.W. VanSciver, J. Low Temp. Phys. **156**, 71 (2009)
45. H.A. Nichol, L. Skrbek, P.C. Hendry, P.V.E. McClintock, Phys. Rev. Lett. **92**, 244501 (2004)
46. H.A. Nichol, L. Skrbek, P.C. Hendry, P.V.E. McClintock, Phys. Rev. E **70**, 056307 (2004)
47. D. Charalambous, L. Skrbek, P.C. Hendry, P.V.E. McClintock, W.F. Vinen, Phys. Rev. E **74**, 036307 (2006)
48. R.J. Donnelly, C.F. Barenghi, J. Phys. Chem. Ref. Data **27**, 1217 (1998)
49. E. Collin, T. Moutonet, J.S. Heron, O. Bourgeois, Yu.M. Bunkov, H. Godfrin, A tunable hybrid electro-magnetomotive NEMS device for low temperature physics. J. Low Temp. Phys. **162**, 653 (2011)

Propagation of Thermal Excitations in a Cluster of Vortices in Superfluid ^{3}He-B

J.J. Hosio,[1] V.B. Eltsov,[1,2] R. de Graaf,[1] M. Krusius,[1] J. Mäkinen,[1] and D. Schmoranzer[3]

[1] *Low Temperature Laboratory, P.O. Box 15100, FI-00076 AALTO, Finland*
[2] *Kapitza Institute for Physical Problems, Kosygina 2, 119334 Moscow, Russia*
[3] *Faculty of Mathematics and Physics, Charles University, Ke Karlovu 3, 121 16 Prague, Czech Republic*

(Dated: March 15, 2011)

We describe the first measurement on Andreev scattering of thermal excitations from a vortex configuration with known density, spatial extent, and orientations in ^{3}He-B superfluid. This configuration is created by rotating the ^{3}He-B sample at constant angular velocity. We use two quartz tuning fork resonators embedded inside a blackbody radiator. One resonator creates a controllable density of excitations at 0.2 T_c base temperature and the other records the thermal response. The results are compared to numerical simulations of ballistic propagation of thermal quasiparticles through a cluster of rectilinear vortices. Our studies suggest that the current understanding of Andreev reflection is correct and it can be used as a quantitative tool to visualize vortices in the low temperature limit.

PACS numbers: 67.57.Hi, 67.57.De, 67.30.he

Studies of turbulence in superfluid ^{3}He and ^{4}He have shown that at large length scales quantum turbulence tends to mimic its classical counterpart. Therefore studying complex fluid motion in superfluids could help us to understand turbulence in classical fluids, which still lacks a comprehensive theory. At very low temperatures, in the absence of normal fluid, turbulence in a superfluid condensate consists of a tangle of singly quantized topologically stable vortices with the same core size and circulation. Thus it is, at least on microscopic scales, simpler than turbulence in a normal fluid with eddies at different length scales. Nevertheless, recent studies, both experimental and theoretical, have opened many challenging questions regarding quantum turbulence [1].

Vortex configurations have long been studied in helium superfluids. In ^{4}He the vorticity can be inferred, e.g., from the mobility of charged vortex rings [2], with micron-sized tracer particles [3] or by analyzing the drag force exerted on vibrating structures [4]. In ^{3}He the traditional method to study vortex arrays is nuclear magnetic resonance [5]. The superfluid flow due to quantized vortices modifies the order parameter field and thus, the NMR signal. In uniform rotation a resolution of a single vortex can be obtained in a measurement of the counterflow velocity at temperatures $T > 0.5\ T_c$ [6, 7]. At very low temperatures, in the limit $T/T_c \ll 1$, the most powerful tool is the Andreev scattering of thermal excitations. This technique has been developed and exploited at the University of Lancaster [8].

Hitherto the Andreev scattering technique has only been used to detect disordered vortex tangles, which for interpretation have been assumed to be homogeneous and isotropic, but which in practice are of unknown density and poorly known spatial extent. Thus, it has not been possible to compare theoretical predictions of heat transport in vortex systems directly to experimental results. Our work fixes this deficiency and justifies the use of the Andreev reflection technique as a visualization method of vortices in superfluid ^{3}He-B in the limit of vanishing normal fluid density.

In the ballistic regime of quasiparticle transport the mean free path of thermal excitations is longer than the dimensions of the container. Therefore, thermal equilibrium is obtained via interaction of quasiparticles and container walls and the collisions between excitations can be neglected. In the presence of vortices, the superfluid flow field around the vortex lines can constrain the quasiparticle trajectories.

In the rest frame of the superfluid condensate the BCS dispersion curve $E(\mathbf{p})$ is symmetrical and the minimum energy is the pressure dependent superfluid energy gap Δ. The standard picture of Andreev reflection considers an excitation moving towards an increasing energy gap [9]. In^{3}He-B the superfluid flow field modulates the minimum in the excitation spectrum for an excitation traveling in the condensate. Using the notation by Barenghi *et al.* [10], the energy E of the excitation with momentum $\mathbf{p}$ in the flow field around a vortex is given by

$$E(\mathbf{p}) = \sqrt{\epsilon_p^2 + \Delta^2} + \mathbf{p} \cdot \mathbf{v_s}, \tag{1}$$

where $\epsilon_p = p^2/2m^* - \epsilon_F$ is the effective kinetic energy of the excitation measured with respect to the Fermi energy ϵ_F and $p = |\mathbf{p}|$. Excitations for which $\epsilon_p > 0$ are called quasiparticles and excitations for which $\epsilon_p < 0$ are called quasiholes. For quasiparticles the group velocity $v_g(E) = dE/d\mathbf{p}$ is parallel to the momentum whereas for quasiholes it is antiparallel. At the 29 bar pressure, at which we work, the effective mass $m^* \approx 5.42\ m_3$, where m_3 is the mass of a ^{3}He atom. The superfluid velocity $\mathbf{v_s}$ is proportional to the gradient of the phase φ of the order parameter, i.e., $\mathbf{v_s} = \hbar/(2m_3)\nabla\varphi$. If we consider a vortex oriented along the z axis in cylindrical coordinates (r,ϕ,z) this becomes $\mathbf{v_s} = \kappa/(2\pi r)\hat{\phi}$, where

$\kappa = h/2m_3 \approx 0.662 \times 10^{-3}$ cm^2/s is the circulation quantum and $\hat{\phi}$ the azimuthal unit vector.

The consequence of the interaction term $\mathbf{p} \cdot \mathbf{v_s}$ is that an excitation traveling at constant energy may not find a forward-propagating state due to the superflow gradient ∇v_s along the flight path. When the excitation reaches the minimum of the spectrum the group velocity changes sign and it retraces its trajectory as an excitation on the other side of the minimum. In other words, a quasiparticle Andreev reflects as a quasihole and vice versa with a very small momentum transfer [11].

Let us consider a beam of excitations incident on a single straight vortex. On one side of the vortex the flow parallel to the group velocity of the excitation reflects quasiparticles and on the other side the antiparallel flow reflects quasiholes. An excitation is Andreev reflected if its energy satisfies $E \leq \Delta + p\frac{\kappa}{2\pi b}\sin\theta$. Here θ is the inclination angle of the excitation trajectory measured with respect to the vortex line and b the impact parameter. At temperature T the mean excitation energy is $\tilde{E} = \Delta + k_B T$. In our experiments $k_B T \sim 0.1\ \Delta$ and the momentum p is close to the Fermi momentum $p_F \approx 9.26 \cdot 10^{-25}$ kgm/s, so a typical excitation is reflected if $b < 5 p_F \kappa \sin\theta/(\pi\Delta)$. For an excitation with $\theta \approx \pi/4$ this translates to $\sim 1\mu m$, which is about two orders of magnitude larger than the coherence length $\xi \approx 15$ nm and the vortex core radius. Thus, in a typical experimental situation, where the inter-vortex distance ~ 0.1 mm, the probability of scattering off a vortex core is negligible.

In our experiment we study the heat transported by excitations through a cluster of vortices. Bradley and coworkers did a similar measurement with a vortex tangle created by a vibrating wire resonator as the structure reflecting excitations [12]. Our experiment is made in a quartz glass cylinder filled with ^{3}He. The cylinder is divided in two parts with a 0.7 mm thick quartz division plate. The lower part consists of a 30 mm long, 3.5 mm inner diameter tube, which opens up to a heat exchanger made out of sintered silver. The sinter provides a good thermal contact with the nuclear cooling stage so that the superfluid ^{3}He in the volume can be cooled down to $\sim 0.1\ T_c$. The upper part can be modeled as a blackbody radiator (BBR), an enclosure with a weak thermal link to the outside superfluid ^{3}He via a small orifice in the division plate [13]. Our BBR consists of a 12 cm long section of the quartz tube with 6 mm inner diameter. This volume is furnished with two mechanical resonators, one acting as a thermometer and the other as a heater. The heater is used for generating a beam of ballistic quasiparticles through the orifice.

Our resonators are commercial quartz tuning forks, which have recently been characterized for probing quantum fluids [14, 15]. The forks are made of piezoelectric quartz crystals with electrodes deposited on the surface. When driven with alternating voltage, the two prongs

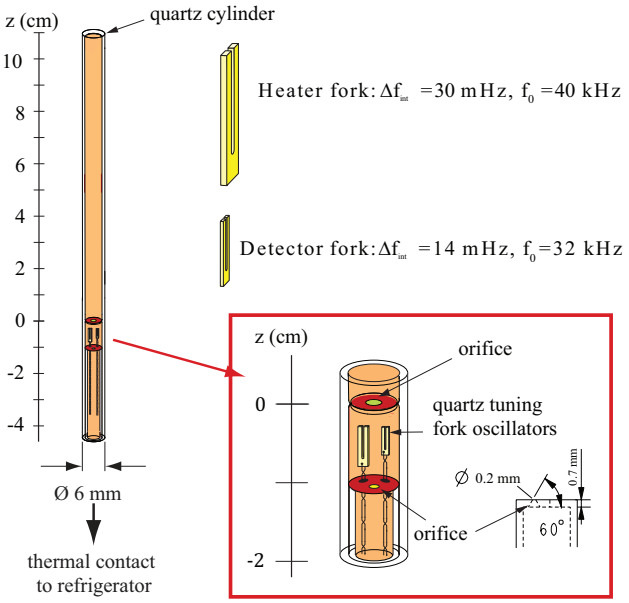

FIG. 1. The experimental setup. The upper experimental volume modeled as a black body radiator is separated from the heat exchanger volume at the bottom by a division plate with a conical orifice with 0.2 mm diameter. The BBR houses two quartz tuning fork oscillators one acting as heater, the other as thermometer.

of the fork start to oscillate in anti-phase producing a current I, which is proportional to the prong velocity v_p. The heater fork signal is amplified with a room-temperature I/V converter [16] before being fed to a two phase lock-in amplifier. This was found to be important in order to reduce the effect of capacitive losses in the signal line, and thus to measure accurately the signal amplitude proportional to the power generated by the fork. The thermometer fork has 32 kHz resonance frequency, a prong cross section of 0.10 mm $\times$ 0.24 mm and a length 2.4 mm. The heater fork has a higher resonance frequency, 40 kHz, to prevent any interference between the forks. The prongs of the heater are 2.9 mm long and the cross section is 0.36 mm$\times$0.44 mm.

In our temperature range the resonance width of the tuning fork depends only on the damping from ballistic quasiparticles. The dependence of the linewidth Δf on temperature and prong velocity is given by

$$\Delta f = \Delta f_{int} + \alpha e^{-\Delta/k_B T}(1 - \lambda \frac{p_F}{k_B T} v_p), \qquad (2)$$

where λ is a geometrical factor close to unity [17]. The velocity-dependent term is due to Andreev reflection of thermal quasiparticles from the potential flow field created by the fork prongs moving the liquid around them. In our experiments v_p is very small and therefore calibrating the fork to act as a thermometer requires determining the geometry-dependent factor α. The thermometer is calibrated at 0.33 T_c against a ^{3}He-melting curve

thermometer, which is thermally coupled to the heat exchanger. Our calibration gives $\alpha \approx$17500 Hz for the detector. The intrinsic damping of the fork was measured to be $\Delta f_{int} \approx 14$ mHz at $T \sim 10$ mK, which translates into the quality factor $Q \sim 2 \cdot 10^6$ in vacuum.

The rough surface of the sinter with the grain size close to the vortex core diameter provides excellent spots for vortices to nucleate. Thus, the critical rotation velocity Ω_c for vortex formation is lower than 0.1 rad/s in the bottom section of the long quartz tube. To create the cluster of vortices, which Andreev reflects a part of the heat back to the BBR, we rotate our system at constant velocity around the axis of the container tube. In the equilibrium vortex state in uniform rotation the sample becomes filled with rectilinear vortices oriented along the rotation axis. The vortex density in the cluster is determined by minimization of the free energy in the rotating frame and is given by $n_v = 2\Omega/\kappa$. The cluster is isolated from the container wall by a narrow annular vortex-free layer. The width of the vortex-free region is only slightly larger than one intervortex distance $\sqrt{\kappa/(\sqrt{3}\Omega)}$ [18].

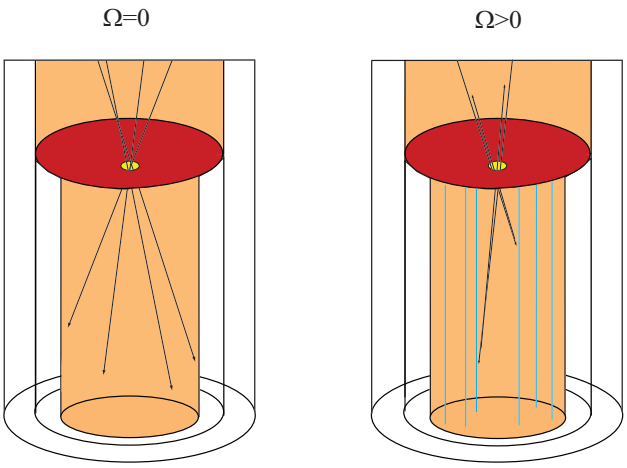

FIG. 2. Sketch of the experiment. In a system at rest (Ω=0) all the excitations which do not migrate back to the black body radiator due to diffuse scattering from the walls are thermalized in the heat exchanger at the bottom. In rotation ($\Omega > 0$), part of the beam is Andreev reflected from the cluster of vortices.

To make sure that we have the equilibrium number of vortices in the container we first rapidly accelerate to some velocity which is much higher than the target velocity for the measurement. Then we decelerate to the final velocity and wait for the system to settle to the equilibrium vortex state via annihilation of the extra vortices.

All the power entering our experimental volume modeled as a black body radiator must leave through the hole at the bottom as a flux of energy-carrying excitations. Assuming thermal equilibrium inside the BBR the power is given by

$$\dot{Q}(\Omega) = \int N(E) v_g(E) E f(E) \mathcal{T} dE dx dy d\phi d\theta, \qquad (3)$$

where $N(E)$ and $f(E)$ are the quasiparticle density of states and the Fermi distribution function, respectively. In the limit $k_B T \ll \Delta$ the latter reduces to the Boltzmann distribution $f(E) = e^{-E/k_B T}$. The transmission function $\mathcal{T} = \mathcal{T}(E, x, y, \phi, \theta, \Omega)$ is equal to one if an excitation leaving the BBR at position (x, y) on top of the orifice to direction (ϕ, θ) reaches the sinter and zero if it is reflected back. The integration goes over the cross section of the orifice, $\phi \in (0, 2\pi)$, $\theta \in (0, \pi/2)$ and $E \in (\Delta, \infty)$. The power generated inside the radiator can now be expressed as the sum of the Ω-dependent heat leak $\dot{Q}_{hl}$ to the BBR and the direct power P_{gen} from the excitations produced by the heater fork as

$$\dot{Q}_{hl}(\Omega) + P_{gen} = \frac{4\pi k_B p_F^2}{h^3} T e^{-\frac{\Delta}{k_B T}} (\Delta + k_B T) A_h(\Omega). \quad (4)$$

Here $A_h(\Omega)$ is the effective area of the orifice, which gets smaller when part of the excitations is scattered back to the BBR. We omit the flow of excitations from the thermal excitation bath in the heat exchanger volume since the quasiparticle density there is at least three orders of magnitude lower than inside the BBR, which is at $0.20\, T_c$. The fraction ν of heat reflected back into the radiator, which we call the reflection coefficient, can be obtained from Eq. 4 as

$$\nu(\Omega) = 1 - \frac{A_h(\Omega)}{A_h(0)}. \qquad (5)$$

In the measurement the heater fork is driven to create the desired excitation beam corresponding to power P_{gen} leaving the radiator. By controlling the rotation velocity, and thus the vortex density, we can control the fraction of Andreev reflected excitations. As shown in Fig. 2, the flow field created by the vortices reflects part of the beam back to the radiator by Andreev scattering. As a consequence, the temperature measured by the thermometer fork increases more than with the same applied heat in the absence of vortices. There is also a vortex cluster inside the BBR, which may cause a small temperature gradient along the cylinder. Nevertheless, the main thermal resistance is still across the orifice and Eq. (5) is valid as long as there is thermal equilibrium inside the radiator.

At each rotation velocity, we apply different power inputs to the radiator and measure the corresponding equilibrium temperature with the thermometer fork. By plotting all the temperature-dependent parts in Eq. (4) as a function of power P_{gen} we get both the effective area A_h and the heat leak $\dot{Q}_{hl}$ from the inverse slope of the obtained line and the intercept with the power axis, respectively (see Fig. 3 for details).

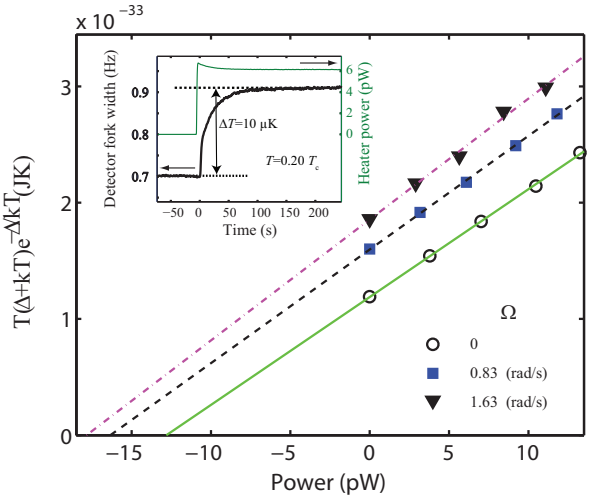

FIG. 3. Temperature dependent part of the power leaving the black body radiator as a function of heating power at three different rotation velocities. The temperature is obtained from the linewidth of the detector fork. The measured points are averaged from a few hundred datapoints measured at the same power. The intercept of the linear fit with the power axis gives the residual heat leak to the sample and the effective area is given by the inverse of the slope. The slope, the heat leak and the scatter in the data all increase with increasing angular velocity. The inset shows an example of a detector response to a heating pulse starting at time $t = 0$.

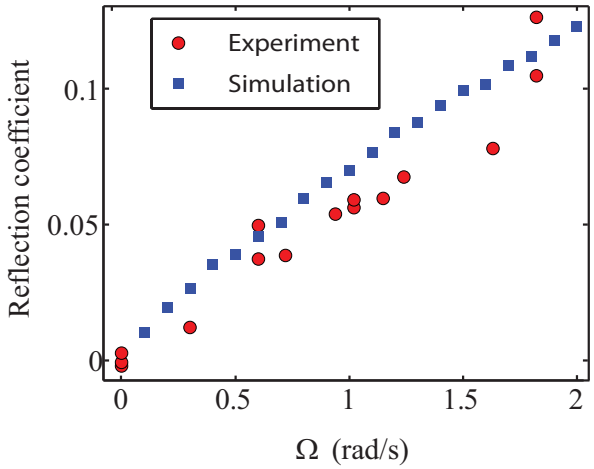

FIG. 4. The fraction of the heat ν Andreev reflected back into the black body radiator. The temperature inside the radiator is 0.20 T_c. The simulation points are obtained by integrating Eq. (3) numerically and solving equations (4) and (5) for ν.

The measurement with no vortices gives $A_h(0) \approx 0.020$ mm^2. This is about half of the geometrical area of the orifice mostly due to diffusive backscattering of excitations from the walls of the 0.7 mm thick division plate and the quartz tube below it. In any case, the absolute value of the the effective area is not an important issue since we are only interested in the relative change of it. The heat leak $\dot{Q}_{hl}$ varies from 12 pW at $\Omega = 0$ to 18 pW at Ω =1.8 rad/s. At high rotation velocities the rotation-induced heat leak fluctuates with variations of about 1 pW. The rotation velocities used in the measurements had to be carefully selected, since due to some mechanical resonances certain velocities show especially high and temporally varying heat leaks.

To test whether our black body radiator works as expected, we can analyze how the system reaches thermal equilibrium when the heater is suddenly switched on. The expected time constant for the thermal relaxation is $\tau = RC$, where the thermal resistance across the orifice $R = (d\dot{Q}/dT)^{-1} \propto A_h^{-1}$ and the heat capacity C is given approximately by [19]

$$C = k_B\sqrt{2\pi}N_F\left(\frac{\Delta}{k_BT}\right)^{\frac{3}{2}} e^{-\frac{\Delta}{k_BT}}\left(1+\frac{21}{16}\frac{k_BT}{\Delta}\right)V. \quad (6)$$

Here $V \approx 3.4$ cm^3 is the volume of the BBR and N_F the density of states at the Fermi level. The measured time constant after a heat input is about 25 s (see inset in Fig. 3), which is in a good agreement (about 80 %) with the expected time constant obtained using the effective area from the calibration described above. This analysis also proves that practically all the heat capacity of the system is in the bulk superfluid ^{3}He. The possible error sources for the effective area are the small statistical error in the determination of the slope (see Fig. 3) and uncertainties in the power calibration, temperature calibration and the value of the gap [20]. The reflection coefficient ν does not depend explicitly on Δ and has a weak logarithmic dependence on the parameter α. The power calibration, if time-independent, has no effect on ν.

Figure 4 shows the reflection coefficient as a function of the rotation velocity together with our numerical simulations. In the measured rotation velocity range the dependence of ν on the vortex density is approximately linear. The measured reflection coefficients are in a good agreement with the simulations. The scatter in the data is mostly due to variation in the power calibration between measurements on different days.

In our numerical calculations we simulate the transmission function $\mathcal{T}$ for our geometry at different rotation velocities and solve the integral in Eq. (3) numerically using Monte Carlo integration with importance sampling. In the simulations diffuse scattering from the container walls is assumed based on the results in Ref. [21] and the fact that the specular scattering model gives completely unrealistic results. We use the exact geometry of our experimental setup including the thickness and the shape of the radiator orifice. Instead of solving for the full equations of motions, which would require too much computing power, only the vortices for which the impact parameter of the excitation is small enough to allow Andreev reflection are considered. We do not assume a perfect retro-reflection but take into account the

small Andreev reflection angle, which for practically all the excitations is $\lesssim 0.1^\circ$ [10].

Recent numerical studies [22, 23] indicate that especially for dense vortex structures, the total reflecting "Andreev shadow" is not necessarily the sum of shadows of single vortices. Our clusters are relatively sparse and moreover, after the first diffuse scattering from the walls the probability for the excitation to migrate back to the radiator is not sensitive to small changes in its trajectory. Thus, we believe that our somewhat simplified model for simulations reproduces the real experimental situation with good accuracy. The simulations were tested at different hole radii and positions. We found that the largest effect on the final result comes from the uncertainty of the radius, of which increasing or decreasing by 50% changes the reflection coefficient by approximately $\pm 10\%$.

Since there is some variation in the rotation velocity on the level of $\Delta\Omega \leq 0.01$ rad/s it is possible that we create helical perturbations on vortex lines, which can end up increasing the total vortex length in our vortex cluster. By modulating the rotation velocity at different frequencies and amplitudes we are able to study whether the presence of these perturbations, which are called Kelvin waves, affects the reflection coefficient. We find that even an order of magnitude larger modulation amplitude compared to the highest noise in the rotation velocity in our measurement barely affects the fraction of transmitted heat flux. Thus, we believe it is safe to omit the effect of Kelvin waves in our analysis.

In conclusion, we describe the first measurement of the interaction between thermal excitations and quantized vortices in a well-defined configuration. Numerical simulations reproduce the experimental results within the margin of uncertainty of our measurements. As quasiparticle beam techniques are at the moment the only practical visualization method of vortices in ^{3}He-B at ultralow temperatures, our studies should make it more reliable than before for probing different vortex structures.

This work is supported by the Academy of Finland (Centers of Excellence Programme 2006-2011 and grant 218211) and the EU 7th Framework Programme (FP7/2007-2013, grant 228464 Microkelvin). JH acknowledges financial support from the Väisälä Foundation of the Finnish Academy of Science and Letters and useful discussions with R. Haley and Y. Sergeev.

[1] W.F. Vinen, J. Low Temp. Phys. **161**, 419 (2010).

[2] P. M. Walmsley, A. I. Golov, H. E. Hall, A. A. Levchenko, and W. F. Vinen, Phys. Rev. Lett., **99**, 265302 (2007).

[3] M. S. Paoletti, Michael E. Fisher, K. R. Sreenivasan, and D. P. Lathrop, Phys. Rev. Lett., **101**, 154501 (2008).

[4] L. Skrbek and W. F. Vinen, in *Prog.Low Temp. Phys.*, Vol XVI, ed. M. Tsubota and W.P. Halperin (Elsevier B.V., Amsterdam, 2009).

[5] V. B. Eltsov, R. de Graaf, R. Hänninen, M. Krusius, R. F. Solntsev, V. S L'vov, A. I. Golov, and P.M. Walmsley, in *Prog.Low Temp. Phys.*, Vol XVI, ed. M. Tsubota and W.P. Halperin (Elsevier B.V., Amsterdam, 2009), arXiv:0803.3225.

[6] V. M. H. Ruutu, U. Parts, J. H. Koivuniemi, N. B. Kopnin, and M. Krusius, J. Low Temp. Phys. **107**, 93 (1997).

[7] R. Hänninen, R. Blaauwgeers, V. B. Eltsov, A. P. Finne, M. Krusius, E. V. Thuneberg, and G. E. Volovik, Phys. Rev. Lett., **89**, 155301 (2002).

[8] S. N. Fisher and G. R. Pickett in *Prog.Low Temp. Phys.*, Vol XVI, ed. M. Tsubota and W.P.Halperin (Elsevier B.V., Amsterdam, 2009).

[9] A. F. Andreev, Zh. Eksp. Teor. Fiz. **99**, 1823 (1964) [Sov. Phys. JETP **99**, 1228 (1964)].

[10] C. F. Barenghi, Y. A. Sergeev, and N. Suramlishvili, Phys. Rev. B **77**, 104512 (2008).

[11] M. P Enrico, S. N Fisher, A. M Guénault, G. R Pickett, and K. Torizuka, Phys. Rev. Lett. **70**, 1846 (1993).

[12] D. I. Bradley, S. N. Fisher, A. M. Guénault, M. R. Lowe, G. R. Pickett, A. Rahm, R. C. V. Whitehead, Phys. Rev. Lett. **93**, 235302 (2004).

[13] A. M Guénault and G. R Picket, Physica (Amsterdam) **126B**, 260 (1984).

[14] R. Blaauwgeers, M. Blažková, M. Človečko, V. B. Eltsov, R. de Graaf, J. Hosio, M. Krusius, D. Schmoranzer, W. Schoepe, L. Skrbek, P. Skyba, R. E. Solntsev, and D. E. Zmeev, J. Low Temp. Phys., **146**, 537 (2007).

[15] D. I. Bradley, P. Crookston, S. N. Fisher, A. Ganshin, A. M. Guénault, R. P. Haley, M. J. Jackson, G. R. Pickett, R. Schanen and V. Tsepelin, J. Low Temp. Phys., **157**, 476 (2009).

[16] P. Skyba, J. Low Temp. Phys., **160**, 219 (2010).

[17] D. I. Bradley, M. Človečko, E. Gažo, and P. Skyba, J. Low Temp. Phys., **151**, 147 (2008).

[18] M. Krusius, J. S. Korhonen, Y. Kondo, and E. B. Sonin, Phys. Rev. B, **47**, 15113 (1993).

[19] C. Bäuerle, Yu. Bunkov, S. N. Fisher, and H. Godfrin, Phys. Rev. B **57**, 14381 (1998).

[20] I. A. Todoschenko, H. Alles, A. Babkin, A. Ya. Parshin, and V. Tsepelin, J. Low Temp. Phys., **126**, 1449 (2002); we use the gap $\Delta(0) = 1.968\ T_c$ at 29 pressure.

[21] M. P. Enrico and R. J. Watts-Tobin, J. Low Temp. Phys., **102**, 103 (1996).

[22] C. F. Barenghi, Y. A. Sergeev, N. Suramlishvili, and P. J. Van Dijk, Phys. Rev. B **79**, 024508 (2009).

[23] C. F. Barenghi, Y. A. Sergeev, N. Suramlishvili, and P. J. Van Dijk, Europhysics Letters **90**, 56003 (2010).